Design and Testing of A Nanoparticle Spectrometer

Simon Box

Darwin College

Supervisor: Nick Collings

Department of Engineering

University of Cambridge

Thesis Submitted to the
University of Cambridge for the degree of
Doctor of Philosophy

November 2005

Abstract

This thesis is concerned with a project to design and test a new Nanoparticle Spectrometer (NPS). The NPS is an instrument designed to make fast measurements of the size distribution and number concentration of aerosol samples containing particles in the size range 5–300nm. The intended application of the NPS is to take time dependant measurements of the aerosols emitted from internal combustion engines. The primary motivation for this work is ultimately the potentially detrimental effects on human health and the environment of combustion generated aerosols.

In common with previous aerosol spectrometers, the Nanoparticle Spectrometer consists of a charger to give particles an electrostatic charge, a classifier, which separates the particles in an aerosol sample according to their electrical mobility (a function of size) and an array of counting devices that count the numbers of particles with different mobilities. The novelty of the NPS is the geometry of the instrument,which, it will be argued, has certain advantages.

The behaviour of particles in the classifier has been modelled numerically and this model has been used to optimise the classifier geometry. Two charger designs were considered, and two analytical charger models developed and compared. The classifier model was combined with the selected charger model to create a simulation of the instrument operation, which predicts the NPS' output signal for a given aerosol sample size distribution and number concentration.

A prototype NPS was designed, built and tested experimentally. The objective of the experiments was to test the validity of the instrument model and compare the performance of the NPS to an established slow response particulate measuring instrument, the SMPS. The experiments showed good agreement between modelled and measured results, as well as close correlation between the NPS and the SMPS results across most of the instruments range.

The experiments also revealed some areas in which the performance of the NPS could be improved; for instance, the modelling of diffusion in the classifier and of the fluid flow in the particle charger.

Acknowledgements

First and foremost I would like to thank my supervisor Nick Collings for proposing this project and providing me with much valued guidance and advice throughout the period of my research. I am also extremely grateful for the invaluable advice provided by Professor Hannes Tammet of the University of Tartu, who consulted on the project.

For help with the design and manufacturing aspects of the project, I owe a debt of thanks to all of the technicians of the Hopkinson Lab at Cambridge University Department of Engineering, in particular Mick Underwood, Rob Leroy, and Trevor Parsons.

Much of the experimental work for this project was carried out at Cambustion Ltd, where I received valuable assistance from most all who work there, but in particular I wish to thank Chris Nickolaus, Kingsley Reavell, John Symmonds and Tim Hands.

Students of the Hopkinson Lab past and present have provided me with a super-abundance of tips on the finer points of LaTeXand Matlab, as well some indispensable help and advice with my project. I would like to thank Alex Darlington, Stuart Swift, Merten Jung, Jason Olfert, Haakon Pedersen and most especially George Biskos.

During the writing of this thesis I received helpful council on medical terminology for which I must thank Gurminder Singh. And finally for proof reading my thesis and for endeavouring to re-educate me in the correct use of the comma I owe inestimable thanks to Anna Wu.

Declaration:

In accordance with the requirements of the board of graduate studies I hear by state: This dissertation is the result of my own work and includes nothing which is the outcome of work done in collaboration except where specifically indicated in the text and does not exceed 65,000 words in length or contain more than 150 figures.

Contents

Nomenclature

Latin Symbols	**Description**	**Alternative**
A	Area	Amps
B	Mechanical mobility	
C_c	Cunningham slip correction factor	
C_p	Charge per particle	
D	Diffusion coefficient	"D" operator
E	Electrical field strength	
F	Force	Volume force field
F_D	Drag force	
F_τ	Frictional force	
G	Dimensionless gravity	
I	Current	
J	Particle flux	
K_E	Constant of proportionality	
Kn	Knudsen number	
N_i	Ion concentration	
P	Pressure	
P_t	Probability of time "t"	
P_n	Probability of "n" charges	
Q	Volume flow rate	
R	Charge separation	
S	Sutherland constant	
T	Temperature	
U	x-wise velocity	
V	velocity (y-wise)	Electric potential
$\mathbf{V}$	3-D velocity vector	
V_{TS}	Terminal settling velocity	

Latin Symbols	**Description**	**Alternative**
W	z-wise velocity	
Z	Electrical Mobility	
a	Particle radius	
b	Collision parameter	
$\bar{c}$	Mean thermal speed	
d	Diameter	Derivative
d_p	Particle diameter	
e	Unit of elementary charge	
f	Function	
f_c	Fraction of charged particles	
g	Acceleration due to gravity	
k	Boltzmann constant	
k_l	Loss correction factor	
m	Mass	
n_i	Fraction of particles with "i" charges	
q	Electrical charge	
r	Radius	
s	Distance	
t	Time	
$\bar{t}$	Average time	
u	Velocity	

Greek Symbols	**Description**	**Alternative**
∇	Vector differentiation operator	
α	Ion flux	
β	Birth an death coefficient	
γ	Collision parameter	Birth an death coefficient
δ	Limiting sphere radius	Birth an death coefficient
ϵ	Dielectric constant	Birth an death coefficient
ζ	Birth an death coefficient	
η	Birth an death coefficient	
θ	Angle	
κ	Image force	
λ	mean free path	

Greek Symbols	Description	Alternative
λ_i	Ionic mean free path	
μ	Dynamic viscosity	
π	3.14159265	
ρ	Density	
σ_g	geometric standard deviation	
τ	relaxation time	
ϕ	Interaction potential	Angle
ω	Filter fibre fraction	

Acronyms

AC	Alternating Current
BC	Black Carbon
CI	Compression Ignition
CPC	Condensation Particle Counter
CPMA	Centrifugal Particle Mass Analyser
CWC	Corona Wire Charger
DC	Direct Current
DAQ	Data Acquisition
DMA	Differential Mobility Analyser
DMS	Differential Mobility Spectrometer
EAA	Electrical Aerosol Analyser
EAD	Electrical Aerosol Detector
EAS	Electrical Aerosol Spectrometer
EEPS	Engine Exhaust Particle Sizer
ELPI	Electrical Low Pressure Impactor
GSD	Geometric Standard Deviation
HC	High Channel
IC	Internal Combustion
LII	Laser Induced Incandescence
MLS	Method of Least Squares
NPS	Nanoparticle Spectrometer
OC	Organic Carbon
PASS	Photo Acoustic Soot Sensor

Acronyms

PM	Particulate Matter
SI	Spark Ignition
SJC	Sonic Jet Charger
SJI	Sonic Jet Ioniser
SMPS	Scanning Mobility Particle Sizer
TEOM	Tapered Element Oscillating Microbalance
TC	Total Current
WAA	Whitby Aerosol Analyser
lpm	Litres Per Minute
rms	Root Mean Square

List of Figures

List of Tables

Chapter 1

Introduction

In 1889 Mr John Aitken presented a new scientific instrument to the Royal Society of Edinburgh [Aitken, 1889], which was one of the earliest particulate measurement devices. The instrument was designed to measure the number concentration of dust particles in the atmosphere. The Aitken counter uses a hand pump mechanism to draw an aerosol sample into a chamber where it is mixed with saturated water vapour; the mixture then undergoes an adiabatic expansion causing dust particles to grow by condensation until gravity causes them to deposit onto a silver plate. Using a magnifier the droplets on the plate are counted manually. Aitkin later used a portable version of his counter to take measurements of atmospheric dust levels throughout the British Isles.

In recent years the ability to take accurate measurements of particulate levels in the atmosphere and at the primary sources of particulate pollution has become of increasing importance. Several independent studies[1] have shown that high levels of particulate pollution are associated with detrimental effects to human health and with climate change.

Internal Combustion engines are a major contributor to particulate background levels, especially in urban areas. Estimations of particulate pollution levels in the environment are rarely clear cut, for example measurements weighted by mass concentration and measurements weighted by number concentration often lead to different conclusions. Investigations carried out in the Los Angeles area have lead to estimates that 50-80% of the airborne particle mass concentration is attributable to vehicle emissions [Pratsinis, 1994, Schauer et al, 1996], while in the greater London area Harrison et al [1999] estimate that 90% of PM_{10} emitted is vehicle related. The overwhelming dominance of vehicle emissions as a source of PM underlines the importance of measuring

[1] See sections 1.1 and 1.2

emissions at the source as well as measuring atmospheric levels.

Modern instruments such as the Differential Mobility Spectrometer (DMS) and the Engine Exhaust Particle Sizer (EEPS)[2] enable time resolved measurements of number concentration and size distribution from an engine's exhaust. A standard emission testing involves the operation of vehicle engines under a simulated "real-life" drive cycle, which includes a significant portion of transient operating conditions. Fast-response instruments can be used to monitor particulate emissions under these transient conditions. The ability to make these measurements is particularly helpful to engine manufacturers in determining which conditions lead to the release of high concentrations of particles and developing hardware and software to ameliorate problematic conditions.

The objective of the project described in this thesis was to design build and test a prototype of a fast response Nanoparticle Spectrometer of novel design. This spectrometer was designed to measure the size distribution of an aerosol sample weighted by number concentration. The instrument was tailored, but not limited, to taking measurements of combustion generated aerosols from IC engines.

In this introduction the effects of particulate pollution on the climate and human health are summarised, and the concept for the Nanoparticle Spectrometer (NPS) is presented.

1.1 Effects of Particulate Pollution on Climate

The earth's atmosphere is densely populated with particles from many sources; large particles ($> 1\mu m$) are generally attributable to sources such as wind blown dust, sea salt, from spray and bursting bubbles, and pollen. Smaller particles are attributable to sulphates from volcanic activity, and to black carbon (BC), organic carbon (OC), and sulphates from the burning of fossil fuels. This section presents some significant research based evidence that variations in the amount of man-made aerosol released into the atmosphere can affect the earth's climate.

The main way in which atmospheric aerosol particles can change the climate is through their effect on the earth's albedo. Aerosols can affect the albedo directly thought the scattering and reflection of light from the sun, typically by sulphates, which causes a cooling effect [Penner et al, 1998]; or by absorption of sunlight by black carbon resulting a radiative heating from the particles causing a warming effect [Jacobson, 2001]. Perhaps more important than the direct albedo effects are the indirect effects due to the aerosol's influence on cloud formation and composition. Particles in the atmosphere provide condensation nuclei for vapour droplets forming clouds, therefore

[2]Descriptions of the DMS and the EEPS are given in Chapter 3

higher concentrations of particles encourage cloud formation, and also result in clouds consisting of more numerous and smaller droplets[Schwartz & Buseck, 2000, Ackerman et al, 2000]. The effect of the increased droplet surface area is to make clouds more reflective, and this creates a cooling effect. An additional effect is enhanced cloud lifetimes, and reduced precipitation [Rosenfeld, 2000]. Overall, atmospheric aerosols are expected to exert a net cooling effect on global climate [Ackerman et al, 2000].

Stanhill & Cohen [2001] conducted research into the levels of solar radiation reaching the earth's surface over the past 50 years and discovered an average global reduction of 2.7% per decade, adding up to a total reduction of $20W/m^2$ over the this period. This phenomenon has been called "Global dimming". Based on current knowledge the most probable cause is increased reflectivity of the earth's albedo caused by man-made aerosols and other pollutants.

Increased levels of greenhouse gases (GHG's) in the atmosphere as a result of man-made emissions are known to cause global warming through the "greenhouse effect". However, the temperature rise has been less than expected. A similar rise in GHG levels during the ice age is thought to have caused a temperature increase 10 times greater than that which is experienced today. Many have attributed this difference to "global cooling" caused by increased aerosol concentrations in the atmosphere, which offset global warming caused by increased GHG levels. Boer et al [2000a,b] devised a theoretical model to investigate the potential climate effects of increased greenhouse gases and sulphate aerosols over a 200 year period (1900-2100). The model simulations for increasing green house gases, and increasing aerosols predicted a significantly lower overall temperature rise than the simulations for increasing greenhouse gases only.

1.2 Effects of Particulate Pollution on Health

Epidemiological studies carried out on the health effects of particulate air pollution can broadly be divided into two types: those that study the effects of chronic exposure, and those that study the effects of acute exposure.

"Chronic" studies aim to evaluate the effects of long term exposure to particles as well as the cumulative effects of repeated exposure to elevated levels of particulate pollution. The methods used for chronic studies generally rely on area to area variations of particulate pollution levels. Instances of health problems such as cardiovascular disease, respiratory disease, lung cancer and lung function are studied in these areas for long periods (1 year or more) and trends between particulate pollution levels, and morbidity and mortality rates are inferred. The data obtained from this type of study can be confounded by other demographic variables such as smoking rates, poverty rates

and housing levels. All studies attempt to correct for these influences. The majority of these studies conclude that there is a positive correlation between mortality rates and air pollution, with the strongest correlation for fine or sulphate particulate matter [Pope, 2000].

Another method used in chronic studies is the individual-based study, whereby community or city wide pollution levels are used but the health data is taken for specific individuals living in these areas. This enables confounding risk factors such as age, sex, or cigarette smoking to be corrected for individually or even controlled, for instance by selecting only non-smokers.

Some reviewers dispute the evidence of a link between long term particulate exposure and health effects noting the problems of confounding variables and suggesting that the number of high quality studies for chronic exposure is much less than that for acute exposure [Vedal, 1997, Gamble, 1998].

Acute exposure studies use short term temporal changes in particulate levels as the source of exposure variability. Observations of health changes are made over a short term period (1-5days) in the area experiencing increased exposure to particulate pollution. The types of health incidents concentrated on in these studies are typically levels of hospitalisation and mortality for respiratory or cardiopulmonary disease and lung function.

These studies have shown mortality rates for respiratory and cardiovascular disease to increase monotonically and in a near linear fashion with particulate mass concentrations. On average daily mortality rates increase by approximately $0.5 - 1.5\%$ per $10\mu g/m^3$ increase in PM_{10} (particles $< 10\mu m$) [Pope, 2000].

Peters et al [2001] conducted research to ascertain whether or not high concentrations of ambient particles can trigger the onset of myocardial infarction (MI). This study involved interviewing MI survivors to ascertain what they did in the short term period leading up to the MI (2 hours and 24 hours) and cross-referencing this data with hourly ambient particulate measurements taken in the area in which the study was carried out. The authors of this study claim to have observed increased probability of MI for patients in the short term period after an exposure to elevated levels of $PM_{2.5}$.

Despite the large body of evidence provided by various epidemiological studies that links nanoparticles to pathophysiology in humans, relatively little is understood about the mechanisms through which exposure to nanoparticles can cause these health effects.

It is widely accepted that smaller nanoparticles ($< 50nm$) pose a greater danger to health [Oberdorster, 1996], which is down to several factors: smaller particles can penetrate deeper into the lungs and because of their higher mobility they are more likely to deposit in the lung [Hinds, 1998]. In addition smaller particles will have a greater

total surface area than the same mass of larger particles providing more opportunity for surface chemistry between the particles and the epithelial cells in the lung.

Experimental studies on rats by Donaldson et al [1998] have shown that rats exposed to small particles ($\approx 20nm$) sustain significantly more lung injury and pathology that rats exposed to the same mass of larger particles ($\approx 250nm$). Interestingly the material of these particles was TiO_2, a substance usually considered biologically inert.

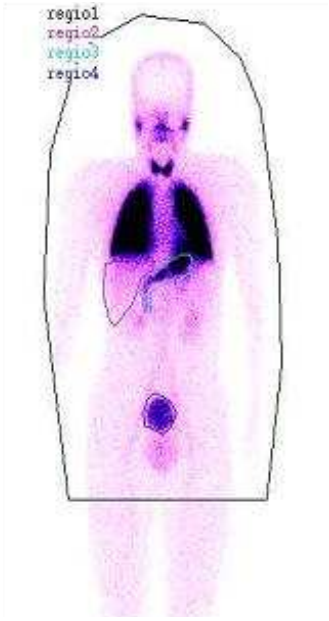

Figure 1.1: Gamma-camera image of radioactivity from inhaled Technegas in a human subject [Nemmar et al, 2001]

Nemmar et al [2001] performed a study to analyse the passage of inhaled particles into the blood. Human volunteers inhaled "Technegas", which is an aerosol consisting of radioactively labelled carbon particles ($< 100nm$). They found that radioactivity in the volunteers' blood was first detected at 1 min after inhalation, reached a maximum at 10-20 mins, and remained at the maximum level for up to 60 mins. Figure 1.1 shows a gamma-camera image of a volunteer taken 60 minutes after inhalation, concentrations of radioactivity can be seen in the sinus, thyroid, lungs, stomach (possibly through swallowing) and the bladder.

1.3 Engines as a Source of Particulate Pollution

Particles emitted from diesel engines mainly consist of solid carbonaceous particles that form in local regions of rich combustion, volatile organic compounds in the form

of unburned fuel and oil, and sulphates (SO_3) oxidised from the sulphur in the fuel. Solid carbonaceous particles will quickly agglomerate to form larger, often irregularly shaped, particles and usually also carry a layer of adsorbed hydrocarbons and sulphates. Fig 1.2 shows the typical particle composition for a heavy duty diesel engine [Kittelson, 1998].

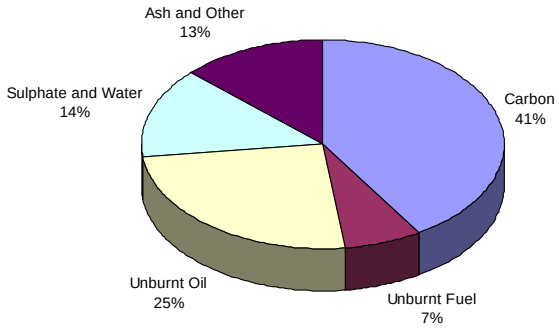

Figure 1.2: Typical particle composition for a heavy duty diesel engine.

Figure 1.3 [Kittelson, 1998] shows the typical Diesel engine exhaust size distribution weighted by both number and mass. The distribution is lognormal and trimodal. The majority of particle number resides in the nucleation mode, these particles consist of volatile organic and sulphur compounds as well as some solid carbon and metal compounds. The majority of particle mass resides in the accumulation mode, these particles are the carbonaceous agglomerates. The largest mode of particles, the coarse mode, is thought to consist of sooty deposits from the inside of the vehicle exhaust that have become re-entrained.

Spark Ignition (SI) engines are also sources of particulate emissions, although in terms of mass emitted they produce significantly less than diesel engines, as the emissions from SI engines are mainly ultra-fine particles. However the number of particles emitted from SI engines can be higher that compression ignition (CI) engines in many cases, leading Kittelson to point out: "if ultra-fine particle number concentration prove to be an important issue for public health then SI engine particle emissions may be of great concern".

Current particulate emissions legislation imposes limits on the mass of PM_{10} or $PM_{2.5}$ particles emitted. The emitted mass is determined by trapping the particles on filters and then measuring the particle mass using gravimetric methods.

It has already been mentioned that the smallest particles are thought to be the most harmful to human health and fig 1.3 shows that the majority number of particles

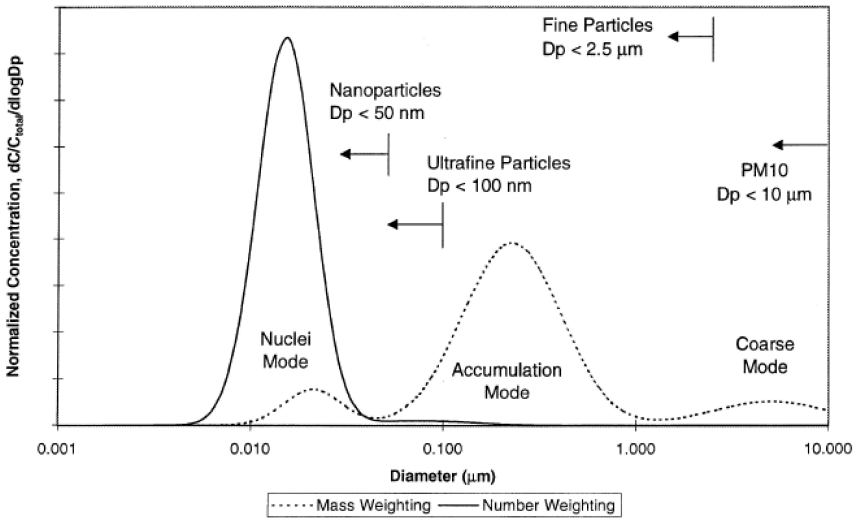

Figure 1.3: Typical Diesel engine exhaust size distribution weighted by number and mass [Kittelson, 1998]

emitted from a typical IC engine are in the nuclei mode, but account for little of the emitted mass. It is therefore possible that successful efforts to reduce the emitted particulate mass by engine manufacturers could result in unchanged, or even increased numbers of nuclei mode particles being produced. This has led many reviewers to suggest that legislation by number may be more appropriate than legislation by mass [Kasper, 2003]. This is an ongoing topic of debate and has, for example, led to the introduction of a Particulate Measurement Programme (PMP), established under the auspices of the United Nations Economic Commission for Europe (UNCE) "Group de Rapporteurs de Pollution et Energie" (GRPE). The purposes of the PMP is to develop a new system for measuring ultrafine particles emitted from heavy duty and light duty vehicles, which could replace or complement the existing particulate mass measurement system [GRPE, 2003].

1.4 Motivation for a New Instrument

Due to the potential effects of particulate pollution on the climate and health, it is necessary to be able to measure the production of particulates from one of its major sources: IC engines. Particle production from IC engines is known to be transient, so the ability to make fast measurements is important. Two very similar instruments exist that can make such measurements of particle number, which many consider the most

relevant particulate measurement metric; these are the DMS and the EEPS. Detailed descriptions of these instruments are given in chapter 3.

The DMS and the EEPS have been shown to be capable of taking very accurate transient measurements of the number concentration and size distribution of particulate matter generated by IC engines, however the instruments have some shortcomings, which make them less suitable for certain applications such as on board vehicle sampling.

The design of the DMS and the EEPS is such that the electrical method of particle detection is vulnerable to interference from electric fields generated within the instruments. In addition to this the instruments are sensitive to vibrations; this and the large size of the instruments is prohibitive to on board vehicle sensing in anything other than a specifically designed test vehicle.

This thesis presents a new Nanoparticle Spectrometer with a novel design that presents potential improvements over the existing instruments in the specific areas mentioned above. More detailed explanations of the shortcomings of the DMS and the EEPS are given with the instruments' description in chapter 3. Also a description of the Nanoparticle Spectrometer (NPS) concept with explanations of the concept's solutions to the above mentioned issues is given in chapter 4

For the project presented in this thesis the NPS concept was modelled in order to test the concept's feasibility, assist in the design of a prototype instrument, and ultimately produce a program that simulates the performance of the NPS. Also a prototype NPS was designed, built and tested. With the aim of verifying the model and showing that the novel concept it indeed a practically feasible spectrometer for making time dependant measurement of aerosol size and number.

1.5 Thesis Outline

The structure of the thesis is as follows: theory relevant to the design and simulation of the NPS is presented in chapter 2. A review of some other important particulate measurement instruments is given in chapter 3 and the concept for the NPS is presented in chapter 4. A model was designed to simulate the performance of the NPS concept, and this is presented in chapter 5. A case study was carried out to compare two types of aerosol charger that could potentially have been used in the NPS, details of this are given in chapter 6. A prototype NPS was designed and built, a description of the prototype can be found in chapter 7. Experiments were carried out on the NPS prototype to verify the performance of the instrument model and compare the

performance of the NPS with another particulate measurement instrument[3], details of these experiments and the results are given in chapters 8 and 9. Finally the accuracy and meaning of the results, the main findings of the project and possible future work are discussed in chapter 10. Also in the discussion is a summary of the main contributions of this project and the main advantages and disadvantages of the NPS compared with existing instrument designs.

[3]The comparison instrument was a TSI SMPS, which is a very accurate but non-time dependant instrument.

Chapter 2

Review of Theory

2.1 Introduction

In this chapter the main theory pertinent to this project and some general aerosol science is introduced. The information presented covers particle dynamics in a gas, the electrostatic forces on particles, and particle dynamics in electric fields. This information is very important in aerosol measurement, as many measurement instruments including the Nanoparticle Spectrometer depend on the electrical mobility of particles as a means of classifying them by size.

Also covered is particle charging theory, this is important for prediction of the charge distribution on aerosols. An inherent problem in differential mobility analysers is the ambiguity arising from the fact that a particle's electrical mobility is a function of both its diameter, and the charge it carries.

Finally some particle filtration theory is discussed. Aerosol filtration is an important part of aerosol measurement and the filtration of aerosols is very different to the filtration of solid particles from a liquid. Thus an understanding of aerosol filtration theory is useful for both the design of filters, and for predicting filtration efficiency.

2.2 Particle Motion

2.2.1 Mechanical Mobility

Stokes Law

For a particle flow situation involving ambient aerosols the motion is usually at low Reynolds numbers due to the small size of the particles. Furthermore the inertia forces are typically so small in comparison to the viscous forces that the viscous drag is equal and opposite to any imposed force, this means that the relaxation time is very short.

The drag forces on aerosol particles under these low Reynolds number conditions are described by Stokes' law.

In 1851 Stokes derived a solution for the Navier-Stokes continuum flow equations for drag forces assuming negligibly small inertial forces compared to viscous forces, incompressible flow, no walls or other particles nearby, and that the particle is a rigid sphere, with no slip at the surface.

The resultant equation for the total force opposing the motion of a particle with velocity V in a fluid is given below.

$$F_D = 3\pi\mu V d_p \tag{2.1}$$

This relationship can be expressed in terms of the ratio of the particle velocity to the drag force opposing that velocity. This is known as the mechanical mobility $B\,(m/Ns)$.

$$B = \frac{V}{F_D} = \frac{1}{3\pi\mu d_p} \tag{2.2}$$

Slip Correction Factor

The assumption of continuum flow in Stokes law does not hold for particles where the particle diameter is of the same order, or smaller than, the mean free path of the gas. Under these conditions molecular slip occurs since the particle no longer moves as a continuum in the fluid, but as a particle among discrete molecules thereby reducing the drag force and increasing the diffusion coefficient. To account for this, a "slip correction factor" must be applied to equation 2.2.

$$B \equiv \frac{V}{F_D} = \frac{C_c}{3\pi\mu d_p} \tag{2.3}$$

where C_c is the Cunningham slip correction factor.

An Empirical equation (2.4) for the Cunningham slip correction factor has been developed based on experimental measurements [Allen & Raabe, 1985].

$$C_c = 1 + \frac{\lambda}{d_p}\left(2.34 + 1.05\,exp\left(-0.39\frac{d_p}{\lambda}\right)\right) \tag{2.4}$$

where λ is the mean free path of the gas.

Settling Velocity

As the inertial forces on small particles are negligible, a particle experiencing a force will almost instantaneously reach terminal velocity where the drag force F_D on the particle

becomes equal and opposite to the applied force. For the case when the applied force is gravity, the terminal settling velocity is defined by equation 2.5.

$$V_{TS} = F_G B = \frac{\rho_g d_p^2 g C_c}{18\mu} \quad \text{for } Re < 1.0 \tag{2.5}$$

2.2.2 Particle Diffusion and Thermal Velocity

Just as with gas molecules, particles in an aerosol will move from areas of high concentration to areas of lower concentration the net transport of these particles within the concentration gradient is known as diffusion. The net number of particles passing through a unit area per unit time is called the particle flux J.

$$J = -D\frac{dn}{dx} \tag{2.6}$$

D is the diffusion coefficient, the larger the value of D the more rapid the transport of particles. For particles suspended in a gas D is given by.

$$D = \frac{kTC_c}{3\pi\mu d_p} = kTB \tag{2.7}$$

where k is the Boltzmann constant, this is known as the Stokes-Einstein equation. It shows that the diffusion coefficient D for a particle is dependant on the particles' mobility, and the temperature of the aerosol. D has units m^2/s. Table 2.1 [Hinds, 1998] shows diffusion coefficients for various particle sizes under ambient conditions.

Particle Diameter (μm)	Mobility (m/Ns)	Diffusion Coefficient (m^2/s)
0.00037[a]	–	2.0×10^{-5}
0.01	1.3×10^{13}	5.4×10^{-8}
0.1	1.7×10^{11}	6.9×10^{-10}
1.0	6.8×10^{9}	2.7×10^{-11}
10	6.0×10^{8}	2.4×10^{-12}

[a]Diameter of an air molecule

Table 2.1: Diffusion coefficients [Hinds, 1998]

The average kinetic energy of a particle is the same as that of the molecules of the gas in which it is suspended ($K.E. = \frac{3kT}{m}$). This is because particles are constantly exchanging energy with surrounding gas molecules by collision. This equation for kinetic energy can be solved to get the root mean squared velocity for a particle of diameter d, and mass m shown in equation 2.8. Similarly the mean thermal velocity of a particle is given by equation 2.9

$$c_{rms} = \left(\frac{3kT}{m}\right)^{1/2} = \left(\frac{18kT}{\pi\rho_p d_p^3}\right)^{1/2} \tag{2.8}$$

$$\bar{c} = \left(\frac{8kT}{\pi m}\right)^{1/2} = \left(\frac{48kT}{\pi^2\rho_p d_p^3}\right)^{1/2} \tag{2.9}$$

2.2.3 Relaxation Time

The relaxation time for a particle is the product of its mass m, and its mobility B. The definition of relaxation time is defined by Hinds [1998] as: the time required for a particle to adjust or "relax" its velocity to a new condition of force.

$$\tau = mB = \frac{\rho_p d_p^2 C_c}{18\mu} \tag{2.10}$$

2.2.4 Particle Brownian Motion and Mean Free Path

An extremely useful tool in characterising the small-scale motion of gas molecules and aerosol particles is the mean free path. For a gas molecule this is simply the average distance a molecule travels before it collides with another molecule. In the case of particles in an aerosol this is different. Particles undergo Brownian motion due to constant bombardment by gas molecules. This means that the path traced by the particle is more of a meandering than the clearly defined ricocheting of a gas molecule (see fig 2.1).

Consequently particle mean free path must be defined differently, and is done so as 'the average distance that the centre of the particle travels between a given origin, and a complete change of direction'. "A complete change of direction" means that the particle has zero component of velocity in the direction it was travelling at the origin i.e. it has turned through 90° (see fig 2.1). This distance is usually called the "stopping distance" of the particle, when travelling at its mean thermal velocity, and can be defined as the mean thermal velocity multiplied by the relaxation time ($\lambda_p = \tau\bar{c}$). Table 2.2 from Hinds [1998] shows typical values for mean free path at various particle diameters.

The pressure and temperature of the aerosol will affect the frequency and velocity of collisions, so Willeke [1976] proposed equation 2.11 to express mean free path in terms of pressure and temperature, relating to a reference mean free path, temperature and pressure (denoted in the equation with subscript r). S is the Sutherland constant.

$$\lambda = \lambda_r \left(\frac{P_r}{P}\right)\left(\frac{T}{T_r}\right)\left(\frac{1+\frac{S}{T_r}}{1+\frac{S}{T}}\right) \tag{2.11}$$

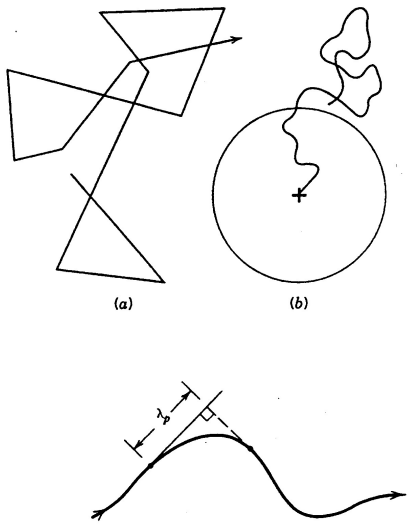

Figure 2.1: Sketches of air molecule motion (a), and particle Brownian motion (b), and also measurement of particle mean free path [Hinds, 1998]

2.3 Electrical Properties of Aerosols

2.3.1 Coulomb's Law

The behaviour of charged aerosol particles in an electric field is of great importance to the problem of aerosol measurement and classification. Many existing aerosol measurement instruments charge the aerosol particles by ionisation for purposes of size classification and/or counting.

In the case of a charged particle in an electric field the electrostatic force on the

$d_p\ (\mu m)$	$\tau\ (s)$	$\bar{c}\ (m/s)$	$\lambda_p\ (\mu m)$
0.00037[a]	–	460.0	0.066
0.01	6.8×10^9	4.4	0.030
0.1	8.8×10^8	0.14	0.012
1.0	3.6×10^6	0.0044	0.016
10	3.1×10^4	0.00014	0.044

[a]Diameter of an air molecule

Table 2.2: Table showing particle mean free paths at standard conditions [Hinds, 1998]

particle is usually the dominant force. The fundamental equation of electrostatics is Coulomb's law (eqn 2.12). F_E is the force between two point charges of like sign separated by a distance R,

$$F_E = K_E \frac{qq'}{R^2} \tag{2.12}$$

where q and q' are the respective charges on the two points, and K_E is a constant of proportionality.

$$K_E = \frac{1}{4\pi\epsilon_0} = 9.0E^9\ Nm^2/C^2 \tag{2.13}$$

ϵ_0 is the permittivity of a vacuum and is equal to $8.85 \times 10^{-12}\, C^2/Nm^2$. The value of gas permittivity ϵ varies according to the species. ϵ is normally given as a multiple of ϵ_0 i.e. $\epsilon = \epsilon_r\epsilon_0$ for most gasses, including air $\epsilon_r \approx 1$.

2.3.2 Electric Fields

Within an electric field there is an electrostatic force acting on charged particles. The intensity of the electric field can be defined in terms of the force per unit charge on a particle.

$$E = \frac{F_E}{q} \tag{2.14}$$

The units of E are N/C. An alternative, and perhaps more practical definition of electric field strength is shown in equation 2.15.

$$E = \frac{\Delta V}{\Delta x} \tag{2.15}$$

Here the field strength between two points is defined as the potential difference between those points, and Δx, the physical distance between them. This equation is very useful for determining something like the electric field between two flat parallel plates with opposite charge. But it can also be modified for more complex geometric configurations. Equation 2.16 gives the electric field strength vector for an electric field varying in three dimensions.

$$E = \frac{\partial V}{\partial x}\mathbf{i} + \frac{\partial V}{\partial y}\mathbf{j} + \frac{\partial V}{\partial z}\mathbf{k} \tag{2.16}$$

where $\mathbf{i}$,$\mathbf{j}$ and $\mathbf{k}$ are unit vectors.

2.3.3 Electrical Mobility

Just as particles have a mechanical mobility B, in an electric field charged particles have an electrical mobility Z where the force is due to the effect of the electric field on the charged particle. Electrical mobility has units m^2/Vs and is given by equation 2.17.

$$Z = \frac{V_{TE}}{E} = \frac{neC_c}{3\pi\mu d_p} \tag{2.17}$$

where V_{TE} is the particle velocity. The charge q is given in this equation as a multiple (n) of the elementary unit of charge $(e = 1.6 \times 10^{-19}C)$. Electrical mobility can also be expressed in terms of particle mechanical mobility B, as shown in equation 2.18.

$$Z = qB = neB \tag{2.18}$$

The component of particle velocity attributed to the force applied by the electric field can be calculated using equation 2.19.

$$V_{TE} = \frac{neEC_c}{3\pi\mu d_p} = neEB \tag{2.19}$$

Equation 2.19 can be useful for predicting the particle trajectories for an aerosol passing through an electric field, such as the situation in a differential mobility analyser. Fig 2.2 shows an aerosol passing between two oppositely charged plates the velocity and trajectory of a particle can be calculated by making a vector triangle using the calculated velocity due to the electric field V_{TE} and the known flow velocity.

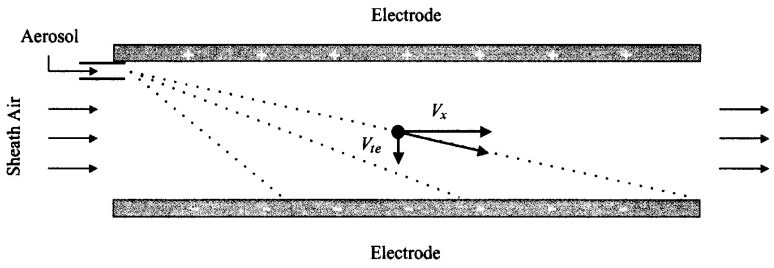

Figure 2.2: Charged particle vectors in an electric field

2.3.4 Van der Waals forces

In addition to the Coulomb force (section 2.3.1) there is another, weaker electrostatic force that is known to act on particles. Van der Waals forces are caused by the random movements of electrons within particles, creating momentary regions of charge concentration called dipoles. These dipoles can produce complimentary dipoles in particles, or surfaces that are in close proximity, thus creating an attractive force. Similarly a charged particle can induce an image force dipole effect in neighbouring particles or surfaces. Dipoles form more easily in materials that are electrically conductive, therefore knowledge of the material dielectric constant (ϵ) is often important in calculating Van der Waals forces.

Detailed in this section are two situations in which Van der Waals forces are important in aerosol science.

Surface Adhesion

Van der Waals attraction is one of the main forces responsible for making particles adhere to a surface. This is important in relation to particle filtration and precipitation. Figure 2.3 shows a particle in contact with a surface; dipole and induced dipole regions are marked. The rough nature of material surfaces at this small scale means that contact between surface and particle is likely to be at a few small points only. The average distance between particle and surface x is also marked on the figure. If the particle charge is neutral the adhesive force is given by equation 2.20 [Hinds, 1998], where A is the Hamaker constant, which is material dependant and varies between $6 \times 10^{-20}\,J$ and $150 \times 10^{-20}\,J$.

$$F_{adh} = \frac{Ad_p}{12x^2} \tag{2.20}$$

In the case that the particle carries a net charge, an image charge is induced on the surface. The electrostatic force resulting from this is given by equation 2.21 [Hinds, 1998], where K_E is the constant of proportionality and x_q is the charge separation, which may be different from the surface separation.

$$F_E = \frac{K_E q^2}{x_q^2} \tag{2.21}$$

Ion-particle image force

Interactions between ions and particles are very important in particle charging. Figure 2.4 shows a situation where a small air ion is passing close by a neutral particle. When

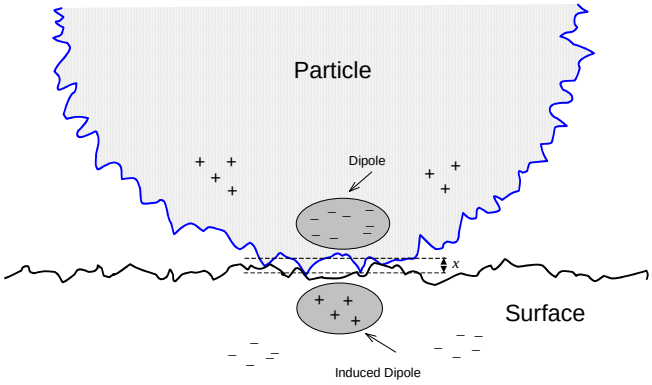

Figure 2.3: Van der Waals forces in surface adhesion

the ion is far away there is no electrostatic force between ion and particle, but as it approaches the positive charge of the ion attracts electrons within the particle to crowd locally on the surface near the ion. This creates a dipole image force that attracts the ion to the particle.

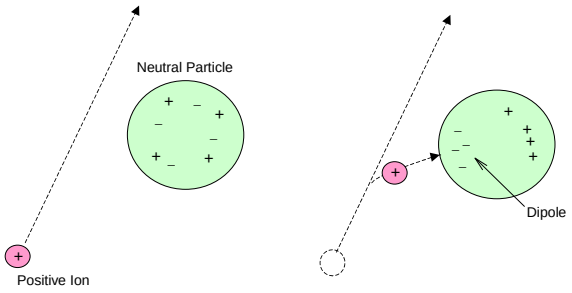

Figure 2.4: Image force dipole between ion and particle

In a particle charging situation the ion flux to particles is a function of the interaction potential (eqn 2.22) where F is the ion-particle interaction force.

$$\phi(r) = \int_r^\infty F\,dr \tag{2.22}$$

$$= K_E\left[\frac{ne^2}{r} - \kappa\frac{a^3}{2r^2(r^2-a^2)}\right] \tag{2.23}$$

This can be expressed as in equation 2.23 where the first term in the parenthesis represents the Coulomb force due to any charge on a particle and the second term represents the image force ($\kappa = \frac{\epsilon-1}{\epsilon+1}e^2$). If there is no charge on the particle the net

force is attractive. If the particle has some charge then the image force will reduce the repulsive force.

2.4 Charging of Particles

2.4.1 Charging Mechanisms

The charging of particles involves bringing them into contact with small ions, which adhere to the particles resulting in a particle with a net positive or negative charge. There are many methods of producing ions; but for the application of charging particles for analysis in particulate measurement instruments, the two most popular methods are corona discharge and ionising radiation.

Corona discharge involves causing a gas (usually air) to undergo electrical breakdown. This is done by creating a strong electric field between a fine electrode, typically a thin wire or a needlepoint, and a larger surfaced electrode, like a flat plate or a concentric tube. When the potential difference between the two electrodes is high enough then a corona region develops around the wire or needlepoint. If a D.C. voltage is applied then ions of the same polarity as the voltage will be produced. An A.C. current will alternately produce positive, and negative ions.

"Ionising radiation" is a term sometimes used for α or β radiation in the application of ionising a gas. High-energy α or β particles collide with gas molecules, upon collision an electron is knocked from the molecule creating a positive ion and a free electron, which can either re-combine and neutralize the molecule, or attach to a nearby neutral molecule leaving two charged ions, one positive and one negative. One α or β particle will generally cause a large number of ion pairs. Consequently ionising radiation produces bipolar ions. Ionising radiation chargers can be made to produce unipolar ions, but this involves precipitating all the ions of the unwanted polarity in an electric field.

Once produced the ions must be introduced to the particles. Here they can be allowed to come together by diffusion (diffusion charging), or the aerosol can be passed through a stream of ions moving in an electric field (field charging). Due to the fast motion of the ions, field charging can result in higher charging levels than diffusion charging.

2.4.2 Charge Distribution

When particles are charged by ions in field or diffusion charging, then larger particles statistically tend to have more collisions with ions and thus pick up more charge. Also a significant fraction of the particles especially at the smallest sizes will not pick up any

charge at all. When a neutral particle acquires an elementary charge it then exerts a repulsive electrostatic force on nearby ions. This reduces the probability of the particle acquiring additional charges. The more charge a particle acquires the more the chance of further charge acquisition is reduced. The upper limit of the number of charges a solid particle can accrue is defined by the surface field required for the particle to begin to spontaneously emit positive ions or electrons, depending on whether the charge is positive or negative respectively. For liquid droplet particles there is an upper charge limit is called the "Rayleigh limit" above this limit the mutual repulsion of charges on the particle surface exceeds the surface tension of the droplet and it disintegrates.

The amount of charge on a particle will affect its electrical mobility, which is used for size classification in many aerosol measurement instruments. Additionally the fraction of particles that are not charged will not be classified or counted. Therefore in order to be able to interpret the output information from the sizing instruments like the SMPS and the DMS described in chapter 3. The charge distribution on the particles exiting the charger must be known.

Bipolar Diffusion charging

Bipolar diffusion charging, often called "neutralisation", produces a charge distribution on the aerosol consisting of fractions of positively and negatively charged particles that are comparable, and a large fraction of uncharged particles. The charge distribution is predicted by Boltzmann's law [Lui & Pui, 1974a,b]. This assumes a symmetrical distribution, however in reality negative ions are slightly more mobile than positive ions giving a slightly asymmetrical distribution with more negatively charged particles[Romay et al, 1994, Clement & Harrison, 1991].

The positive side of the charge distribution produced by the TSI radioactive neutraliser used in the experimental work presented in this thesis, is presented in table 2.3.

Unipolar Diffusion Charging

Pui [1976] postulated equation 2.24 to determine the fraction of particles charged during unipolar diffusion charging.

$$f_c = 1 - exp\left(-\frac{\pi}{4} d_p^2 \bar{c_i} N_i t\right) \tag{2.24}$$

Where N_i is the concentration of ions, t is the residence time of particles with ions, and $\bar{c_i}$ is the mean thermal speed of the ions given by equation 2.25

Particle Diameter	Elec' Mobility(Z)	Fraction of Charged Particles					
(nm)	$(m^2V^{-1}s^{-1})$	+1	+2	+3	+4	+5	+6
1	2.1×10^{-4}	0.0045	0	0	0	0	0
10	2.1×10^{-6}	0.0411	0	0	0	0	0
20	5.4×10^{-7}	0.0846	0.0001	0	0	0	0
40	1.4×10^{-7}	0.1458	0.0031	0	0	0	0
60	6.7×10^{-8}	0.1851	0.0108	0	0	0	0
80	4.0×10^{-8}	0.2046	0.0211	0.0005	0	0	0
100	2.7×10^{-8}	0.2137	0.0317	0.0017	0	0	0
200	8.8×10^{-9}	0.2042	0.0718	0.0153	0.0018	0.0001	0
300	4.9×10^{-9}	0.1782	0.0878	0.0292	0.0068	0.0010	0.0001
400	3.3×10^{-9}	0.1566	0.0910	0.0384	0..0124	0.0030	0.0005

Table 2.3: Positive charge distribution on neutralised particles

$$\bar{c_i} = \sqrt{\frac{8kT}{\pi m_i}} \tag{2.25}$$

The charge distribution from unipolar diffusion charging can be solved with the "birth and death" model [Boisdron & Brock, 1970]. This uses the infinite set of differential equations (2.26) to model the accretion of charge for a certain particle with time. n_i is the fraction of particles with i charges, and α_i is the ionic flux to a particle with i charges.

$$\begin{aligned} \frac{dn_0}{dt} &= -\alpha_0 n_0 \\ \frac{dn_1}{dt} &= \alpha_0 n_0 - \alpha_1 n_1 \\ &\vdots \\ \frac{dn_i}{dt} &= \alpha_{i-1} n_{i-1} - \alpha_i n_i \end{aligned} \tag{2.26}$$

Unipolar diffusion charging, and field charging give a much higher charged fraction of the aerosol than bipolar charging. However, higher charge levels are not necessarily beneficial. Instruments such as the DMA, DMS[1] and the Nanoparticle Spectrometer of this project, rely on differential mobility to identify a particle's diameter. If charging levels become too high, then large particles can accrue enough charge to have the same, or even higher mobility than smaller particles.

[1]The DMA and DMS are described in chapter 3

Figure 2.5 shows a graph plotting electrical mobility against particle diameter for three sources. Firstly the Boltzmann equilibrium distribution [Lui & Pui, 1974b]. Secondly diffusion charging with $N_i t$ of 1×10^7 $ions/cm^3 sec$ [Lui & Bademosi, 1971]. Finally field charging with $N_i t$ of 5.8×10^7 $ions/cm^3 sec$, and a field strength of $8000 V/cm$ [Lui & Kapadia, 1978].

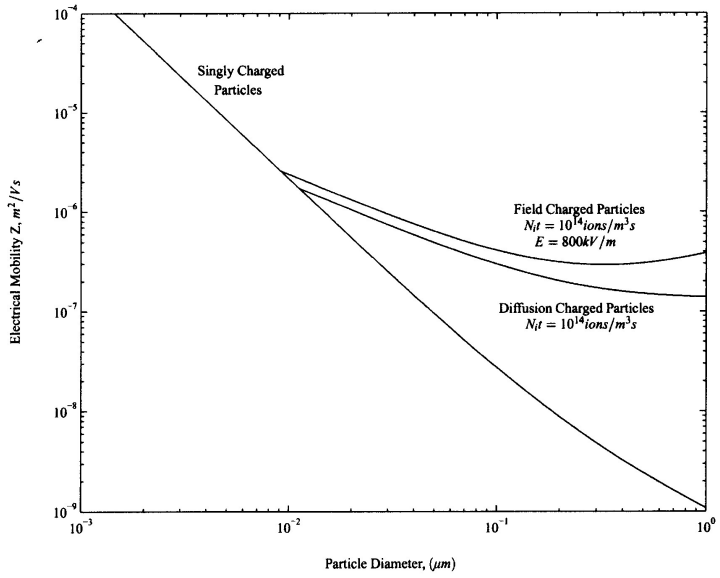

Figure 2.5: Graph showing variation in electrical mobility with particle diameter for diffusion and field charging

It can be seen from figure 2.5 that for small particles all the lines follow the same relationship between size and mobility. This is because at these diameters all charging methods produce particles with just one elementary charge. As the particle diameter increases unipolar diffusion and field charging produce multiply charged particles, and the mobility resolution at these particle sizes reduces. For the case of field charging it can be seen that at diameters above about $300nm$ electrical mobility switches from a decreasing to an increasing function of size, as the ability of larger particles to accrue more charge becomes the dominant factor. This would make field charging only suitable for differential mobility either above or below this change.

2.4.3 Ion Properties and Ionic Flux to particles

Air ions can comprise of many species, among the most common for positive ions is the hydrated proton cluster $H^+(H_20)_6$ [Biskos, 2004]. Water molecules accommodate the formation of these clusters so the humidity of the air can be an important factor in ion generation [Kebarle et al, 1967]. Much experimental work has been carried out to determine the mobility of air ions. The mobility for the $H^+(H_20)_6$ ion has been measured as $Z_i = 1.4 \times 10^{-4}\, m^2 V^{-1} s^{-1}$ [Pui, 1976, Horrak, 2001]

The ion diffusion coefficient can be calculated using the Stokes-Einstein equation (2.27),

$$D_i = \frac{kTZ_i}{e} \tag{2.27}$$

where e is the value of elementary charge ($1.6 \times 10^{-19}\, C$), k is the Boltzmann constant and T is absolute temperature of the gas.

The ionic mean thermal speed is

$$\bar{c_i} = \sqrt{\frac{8kT}{\pi m_i}} \tag{2.28}$$

where m_i is the mass of the ion.

The ionic mean free path can be related to the ion diffusion coefficient by the Maxwell-Chapman-Enskog theory [Biskos, 2004]. This is expressed as

$$D_i = \frac{3}{8}(1 + \epsilon_{i,a})\sqrt{\pi}\lambda_i \left(\frac{m_i + m_a}{m_a m_i} kT\right)^{\frac{1}{2}} \tag{2.29}$$

where $\epsilon_{i,a}$ is a species dependant correction factor ranging from 0.016-0.132, m_a is the mass of the gas molecules and λ_i is the ionic mean free path.

Table 2.4 gives values of the main ionic properties for $H^+(H_20)_6$ ions with mobility $Z_i = 1.4 \times 10^{-4}\, m^2 V^{-1} s^{-1}$.

Property		Value	
Electrical mobility	Z_i	1.4×10^{-4}	$m^2 V^{-1} s^{-1}$
Diffusion coefficient	D_i	0.357×10^{-5}	$m^2 s^{-1}$
Mean thermal speed	$\bar{c_i}$	239	$m s^{-1}$
Mean free path	λ_i	14.5	nm
Mass	m_i	109	amu

Table 2.4: Principle properties for $H^+(H_20)_6$ ions

Ionic Flux to Particles

Ionic flux to particles is a complex process and there is not a single accepted theory available to predict ion flux for all ranges of particle size. Different models for ion flux are used depending on the ratio between the particle size and the ionic mean free path, characterised by the Knudsen number (equation 2.30).

$$\mathrm{Kn} = \frac{2\lambda_i}{d_p} \tag{2.30}$$

There are three transport regimes defined by the Knudsen number: The continuum regime where particles are much larger than the ionic mean free path, the free molecular regime where the ionic mean free path is much larger than the particle diameters and between them the transition regime. Biskos [2004] compiled a comprehensive list of models for ion flux suitable for these three regimes. Some of these models are detailed below.

Continuum Regime (Kn $<<$ 1) An established equation describing ion flux (α) to particle of specific size in the continuum regime is given in equation 2.31.

$$\alpha = \frac{4\pi D_i N_i}{\int_a^\infty \frac{1}{r^2}\left(\frac{\phi(r)}{kT}\right) dr} \tag{2.31}$$

a is the particle radius, r is the distance from the particle centre N_i is the ion concentration and $\phi(r)$ is the interaction potential at a distance r. The interaction potential is defined in equation 2.32

$$\begin{aligned} \phi(r) &= \int_r^\infty F\, dr = K_E\left[\frac{ne^2}{r} - \kappa\frac{a^3}{2r^2(r^2-a^2)}\right] \\ K_E &= \frac{1}{4\pi\epsilon_0} \\ \kappa &= \frac{\epsilon-1}{\epsilon+1}e^2 \end{aligned} \tag{2.32}$$

F is the ion-particle interaction force K_E is the constant of proportionality, n is the number of elementary charges carried by the particle, e is the unit elementary charge ($1.6 \times 10^{-19}\, C$) and ϵ_0 is the permittivity of free space ($8.85 \times 10^{-12}\, C^2/Nm^2$).

The $\frac{ne^2}{r}$ term represents the Coulomb force and the $\kappa\frac{a^3}{2r^2(r^2-a^2)}$ term represents the image force induced by the ion (see section 2.3.4)

Estimating the integral in equation 2.31 is complicated by the fact that the image force at the surface of the particle becomes infinite. However the image force is important only for small particles, and becomes negligible in particles with diameters of

those in the continuum regime. Therefore a solution can be obtained using only the Coulomb force (equation 2.33).

$$\alpha = K_E \frac{4\pi D_i N_i n e^2}{akT\left[\exp(K_E \frac{ne^2}{akT}) - 1\right]} \tag{2.33}$$

For particles in the transition and free molecular regimes the image force effect is not negligible and cannot be discounted from the solution in this way.

Transition Regime (Kn $\approx$ 1) The "limiting sphere theory" [Fuchs, 1963] can be used to model the ionic flux to a particle in the transition regime. The limiting sphere theory uses an imaginary sphere concentric to the surface of the particle. Between the surface and the sphere ion motion is described by the ion-particle interaction potential and the mean thermal speed of the ion. Outside the sphere the motion of the ions is described by macroscopic diffusion theory. Matching the two fluxes at the surface of the sphere gives an expression for ion flux shown in equation 2.34.

$$\alpha = \frac{\pi\gamma\bar{c}_i\delta^2 N_i exp(\frac{-\phi(\delta)}{kT})}{1 + exp(\frac{-\phi(\delta)}{kT})\frac{\gamma\bar{c}_i\delta^2}{4D_i}\int_\infty^r \frac{1}{r^2}exp(\frac{\phi(r)}{kT})dr} \tag{2.34}$$

Where γ is the probability that an ion entering the limiting sphere will collide with and charge the particle, $\bar{c}_i$ is the mean thermal speed of the ions, and δ is the radius of the limiting sphere. The collision probability γ is given by

$$\gamma = \frac{b_m^2}{\delta^2} \tag{2.35}$$

where b_m is the minimum collision parameter, i.e. when $\frac{db^2}{dr} = 0$, b can be calculated by equation 2.36.

$$b^2 = r^2\left[1 + \frac{2}{3kT}[\phi(\delta) - \phi(r)]\right] \tag{2.36}$$

The radius of the limiting sphere δ is given by equation 2.37

$$\delta = \frac{a^3}{\lambda_i^2}\left[\frac{(1 + (\lambda_i/a))^5}{5} - \frac{(1 + (\lambda_i^2/a^2))(1 + (\lambda_i/a))^3}{3} + \frac{2}{15}\left(1 + \frac{\lambda_i^2}{a^2}\right)^{\frac{5}{2}}\right] \tag{2.37}$$

where λ_i is the mean free path of the ions and a is the radius of the particle.

Equations for the ion flux in the transition regime have also been derived using an approximate solution of the Boltzmann collision equation [Huang et al, 1990].

$$\alpha = \pi a^2 \bar{c}_i N_i \left(E_0 - \frac{1}{\tau}E_1\right) \tag{2.38}$$

where τ is the relaxation time of the system given by:

$$\tau = \frac{D_i + D_p}{a}\sqrt{\frac{m_i}{kT}} \tag{2.39}$$

E_0 and E_1 are the zero and first order corrections to the free-molecule flux.

Free Molecular Regime (Kn >> 1) The equations presented for the transition regime take into account image forces, and can to a large extent also be applied to the free molecular regime. However equations exist that are specifically tailored to this area. Equation 2.40 [Keefe & Nolan, 1962] was derived using a Maxwellian distribution of ion velocities. This equation is valid for flux to *uncharged* particles only.

$$\alpha = \pi a^2 \bar{c_i} N_i \left(1 + \sqrt{K_E \frac{\pi e^2}{2akT}}\right) \tag{2.40}$$

2.5 Particle Filtration

Particle filtration is important to this projects as the NPS uses filters to trap and count particles as will be seen later in this thesis.

Unlike liquid filtration of solid particles, aerosol filtration does not rely on sieving, that is using perforated materials with holes smaller than the particles to trap them. Aerosol filters generally use fibrous filters to remove the particles by means of collision with the fibres. Porosity of these filters is typically high ($> 70\%$) and typical spacing between the fibres will be many times larger than the particle diameters.

The number efficiency for an aerosol filter is simply defined as

$$E = \frac{N_{in} - N_{out}}{N_{in}} \tag{2.41}$$

Filter penetration is defined as

$$P = 1 - E \tag{2.42}$$

An "ideal" sieve filter removes 100% of particles larger than the holes irrespective of other conditions. For aerosol filtration using fibrous filters, the probability of a particle colliding with a fibre varies significantly with the flow velocity in the filter. Flow velocity inside the filter is defined as

$$U = \frac{Q}{A(1-\omega)} \tag{2.43}$$

where Q is the volume flow rate through the filter, A is the cross-sectional area and ω is the volume fraction of fibres.

$$\omega = \frac{\text{fibre volume}}{\text{total volume}} \tag{2.44}$$

Often in filter theory the face velocity is used in calculations, this is defined as

$$U_0 = \frac{Q}{A} \tag{2.45}$$

2.5.1 Single-Fibre Efficiency

Fibrous filtration theory concentrates on analysing the collection of a particle on a single fibre to predict the overall filter efficiency. The single fibre efficiency E_Σ is defined as

$$E_\Sigma = \frac{\text{number collected on unit length}}{\text{number geometrically incident on unit length}} \tag{2.46}$$

Single fibre efficiency is related to overall filter efficiency by equation 2.47 [Hinds, 1998].

$$P = 1 - E = \exp\left(\frac{-4\omega E_\Sigma t}{\pi d_f}\right) \tag{2.47}$$

There are five different mechanisms by which a particle can deposit on a filter fibre.

- Interception
- Inertial impaction
- Diffusion
- Gravitational settling
- Electrostatic attraction

Theoretical calculations for the single fibre efficiency for each of these mechanisms have been compiled and combined to give an estimate for overall single fibre efficiency [Hinds, 1998].

Interception

Interception occurs when a particle follows a gas streamline that passes the fibre at a distance of less than the particle radius. If a particle is collected by interception it is assumed that it has followed the streamline perfectly.

The single fibre collection efficiency for interception (E_R) is given by equation 2.48 [Lee et al, 1993]. R is the ratio of particle diameter to fibre diameter $R = \frac{d_p}{d_f}$ and Ku is the Kuwabara hydrodynamic factor. This is very important because it corrects for the effects of flow distortion around the fibres due to the presence of other fibres in flow proximity, so naturally it is a function of the fibre density ω.

$$E_R = \frac{(1-\omega)R^2}{Ku(1+R)} \tag{2.48}$$

$$Ku = -\frac{\ln \omega}{2} - \frac{3}{4} + \omega - \frac{\omega^2}{4} \tag{2.49}$$

Impaction

Impaction occurs when a particle does not follow a streamline that is suddenly diverted around the fibre because of inertia. Consequently the particle crosses the streamlines and collides with the fibre. Impaction is the main collection mechanism for larger particles (typically $> 500nm$).

The single fibre efficiency for impaction (E_I) is given by equation 2.50 [Yeh & Lui, 1974]. The sum of E_I and E_R cannot exceed the theoretical maximum of $1 + R$.

$$E_I = \frac{(Stk)J}{2Ku^2} \tag{2.50}$$

Stk is the Stokes number (equation 2.51), defined as the ratio of the particle stopping distance to the fibre diameter.

$$Stk = \frac{\tau U_0}{d_f} = \frac{\rho_p d_p^2 C_c U_0}{18\mu d_f} \tag{2.51}$$

$$J = (29.6 - 28\omega^{0.62})R^2 - 27.5R^{2.8} \quad \text{for} \quad R < 0.4 \tag{2.52}$$

Diffusion

Collection by diffusion occurs when the Brownian motion of a particle is sufficiently large that that the probability of a particle on a non-intercepting streamline hitting the fibre is greatly increased. This is the main deposition mechanism for small particles (typically $< 100nm$).

The single fibre efficiency for diffusion (E_D) is given by equation 2.53 [Kirsch & Fuchs, 1968]. Pe is the Peclet number.

$$E_D = 2Pe^{-2/3} \tag{2.53}$$

$$Pe = \frac{d_f U_0}{D} \tag{2.54}$$

When estimating overall single fibre efficiency near the point of minimum efficiency it is necessary to include an interaction term (E_{DR}) to account for enhanced collection due to interception of diffusing particles.

$$E_{DR} = \frac{1.24R^{2/3}}{(Ku\,Pe)^{1/2}} \tag{2.55}$$

Gravitational Settling

Deposition due to gravitational settling is a small effect that is only relevant for large particles and a low flow velocity ($< 0.1ms^{-1}$). The effect of gravitational settling on efficiency depends of the direction of flow relative to the direction of gravity. If the flow and the gravity are in the same direction then efficiency is increased (2.56). If the directions are opposed then efficiency is decreased (2.57).

$$E_G \approx G(1+R) \tag{2.56}$$

$$E_G \approx -G(1+R)) \tag{2.57}$$

G is the dimensionless number that controls gravitational settling.

$$G = \frac{V_{TS}}{U_0} = \frac{\rho d_p^2 C_c g}{18\mu U_0} \tag{2.58}$$

Electrostatic Attraction

In the case of a charged particle and a neutral fibre an image force is induced on the fibre causing a small attractive force (see section 2.3.4). The effect of this force on single fibre filtration efficiency has been determined experimentally by Brown [1993], and is given in equation 2.59, where q is the charge on the particle, and ϵ_f is the dielectric constant of the fibre material.

$$E_q = 1.5\left[\frac{(\epsilon_f - 1)}{(\epsilon_f + 1)}\frac{q^2}{12\pi^2\mu U_0\epsilon_0 d_p d_f^2}\right]^{\frac{1}{2}} \tag{2.59}$$

Total Single Fibre Efficiency

The individual efficiencies detailed above are combined to give a total single fibre efficiency [Hinds, 1998], see equation 2.60

$$E_\Sigma = 1 - (1-E_R)(1-E_I)(1-E_D)(1-E_{DR})(1-E_G)(1-E_q) \tag{2.60}$$

Typically the mechanism of diffusion governs the deposition of small particles, while the mechanism of impaction and interception governs the deposition of large particles. It is between these two regions that penetration can occur. Because of this the efficiency curves tend to look like that shown in fig 2.6, where there is a low efficiency size and particles of this diameter have the highest chance of penetrating the filter.

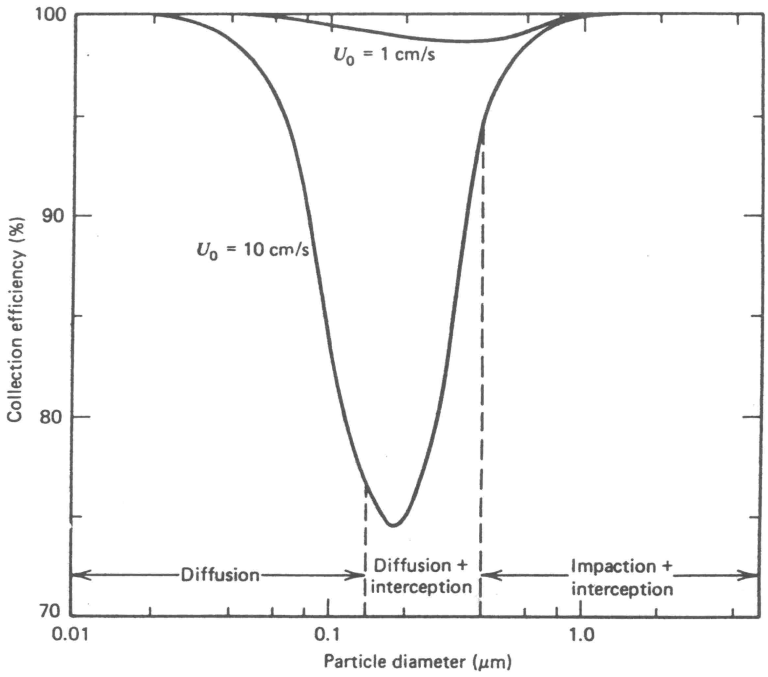

Figure 2.6: Graph showing typical filter efficiency versus particle diameter. [Hinds, 1998]

Chapter 3

Review of Instruments

3.1 Introduction

This chapter will discuss some other particulate measurement instruments and their methods of operation. Some historical instruments, as well as those currently available, and those at the forefront of nanoparticle measurement technology will be considered.

There are many different metrics used to measure aerosols including number concentration, mass concentration, volume concentration and surface area concentration. The NPS is designed to measure number concentration, thus the majority of instruments presented here have this in common although some instruments that measure other metrics are presented for context. The range of particle measurement instruments is wide and so not all instruments are presented here, however some further instruments that may interest the reader are presented in appendix B.

Many particulate measurement instruments use chargers to provide the aerosol sample with an electrostatic charge for purposes of classification or counting or both. Also included in this chapter are descriptions of some various types of aerosol charger.

The following instruments are discussed in this chapter:

- Whitby Aerosol Analyser (WAA)
- Scanning Mobility Particle Sizer (SMPS)
- Electrical Aerosol spectrometer (EAS)
- Differential Mobility Spectrometer (DMS)
- Engine Exhaust Particle Sizer (EEPS)
- Electrical Low Pressure Impactor (ELPI)

- Diffusion battery
- Centrifugal Particle Mass Analyser (CPMA)

3.2 The Whitby Aerosol Analyser (WAA)

One of the earliest particulate measurement instruments to use the techniques of particle charging and differential mobility analysis to establish the size distribution of an aerosol was the Whitby Aerosol Analyser (WAA)[Whitby et al, 1971]. The WAA was designed by Kenneth Whitby at the University of Minnesota and was one of many instruments used in the Los Angeles Smog Project in the early 1970's [Whitby et al, 1972, Hursar et al, 1972]. It was also produced, and sold commercially by Thermo Systems Inc (TSI) as the TSI Model 3000.

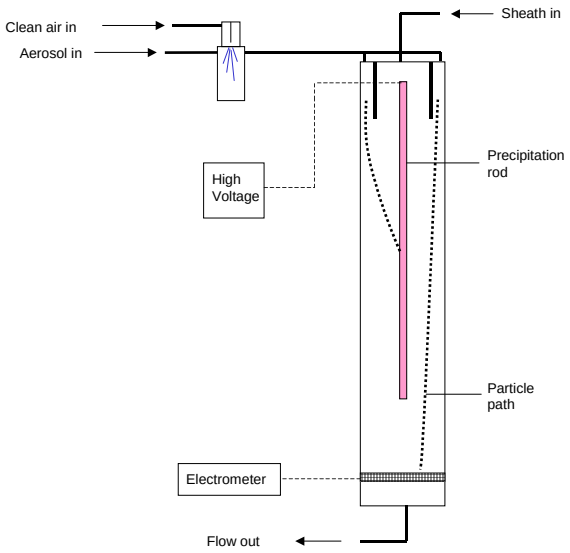

Figure 3.1: Schematic of the Whitby Aerosol Analyser

The principle of operation of the WAA (fig 3.1) is as follows: Particles entering the instrument are charged by a unipolar corona discharge of negative ions. The corona discharge occurs at a needle point which is incident to a flat plate with a large potential difference from the needle. Clean air blows through an orifice in the plate adjacent to the needle creating a jet of negative ions emerging from the orifice. This jet is then mixed with the incoming aerosol stream to charge the particles.

Following charging, the aerosol enters the classification column. This is a long tube

with a concentric rod in the centre. The aerosol enters the column via an annular slit near the inside surface of the tube. Particle-free "sheath" air is passed down the middle of the tube. The flow in the column is laminar. An adjustable voltage difference exists between the tube's inner surface and the central rod; the charged particles are attracted to the rod by electrostatic force. A particle's electrical mobility, that is how quickly it is transported by an electrostatic force, decreases with increasing particle size. Therefore, depending on the voltage, all particles smaller than a critical size will be precipitated on the rod and all those that are larger will flow to the base of the column.

At the base of the column the particles are collected on a filter, which is connected to a sensitive ammeter that measures the small current associated with charged particles landing on the filter. Scanning the voltage on the precipitating rod, and simultaneously measuring the change in current collected on the filter generates data from which the number concentration and size distribution of the aerosol can be inferred.

3.3 The Scanning Mobility Particle Sizer (SMPS)

The SMPS is a system of three commercially available instruments. A bipolar radioactive neutraliser charges the particles, a Differential Mobility Analyser (DMA) classifies the particles by electrical mobility and a Condensation Particle Counter (CPC) counts the particles. This system can measure the size distribution for aerosols weighted by number concentration. The TSI 3080 SMPS has a size range of up to 10-1000nm.

3.3.1 The Differential Mobility Analyser (DMA)

The DMA [Knutson & Whitby, 1975] is the next generation of the classification column seen in the WAA and its construction is very similar (fig 3.2). The aerosol enters at the top, flows into an annular gap outside the column and then enters the main column flow via a circumferential gap in the column wall. Laminar sheath flow in the centre of the column confines the aerosol sample gas flow to a thin region near the inside surface of the column. A voltage on the central rod attracts positively charged particles toward it.

Near the bottom of the precipitating rod is a small circumferential slit through which a small amount of flow is drawn, the rest of the flow is exhausted, or filtered and recycled as sheath air. This feature is the principle difference between the DMA and the WAA because only particles within a narrow mobility band are selected, as opposed to all particles below a critical mobility level.

The voltage on the central rod can be scanned in order to select different mobility bands. The DMA is also useful as a sample preparation tool; with the rod voltage set

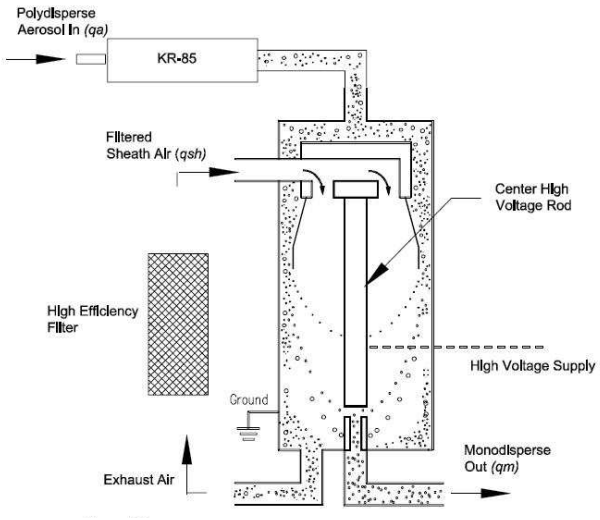

Figure 3.2: Schematic of the Differential Mobility Analyser [TSI, 2005]

to a constant level the output from the DMA is a "monodisperse" aerosol (an aerosol wherein all the particles are of equal size). Monodisperse aerosols are often used in the calibration and testing of other particle measurement instruments; in fact a DMA (TSI Model 3071A) was used to prepare monodisperse samples for testing the NPS discussed in this thesis (chapters 8 and 9).

3.3.2 The Bipolar Radioactive Neutraliser

The TSI model 3080 SMPS uses a bipolar radioactive neutraliser [Lui & Pui, 1974a] that consists of a metal tube containing a radioactive ^{85}Kr source that emits β radiation. The high-energy radioactive particles ionise the gas in the tube producing roughly equal numbers of positive and negative ions. Exposing particles to the ionised gas in the neutraliser results in a bipolar charged aerosol with a charge distribution very close to the Boltzmann equilibrium distribution.

The majority of charged particles produced by this method have a single elementary charge, where as the larger particles charged by corona discharge in the WAA will have several charges, as electrical mobility is a function of both size and charge this leads to a poorer size resolution in the WAA. However only a small fraction of the particles in the sample are charged with the correct polarity when bipolar neutralisation is used.

The bipolar neutraliser can also be used in aerosol sample preparation for experimental work to give a net neutral charge to samples that have obtained a charge distribution with net positive or negative polarity, either in the process of generation

or previous classification. Several bipolar neutralisers were used in the experimental work presented in this thesis.

3.3.3 The Condensation Particle Counter (CPC)

Following classification in the DMA the aerosol sample passes into the CPC for counting [Agarwal & Sem., 1980]. The particles are counted optically, by passing them between a laser or lamp, and a photo detector. There are two modes of detection used in a standard CPC: for particle concentrations below $1000\,\#/cm^3$ the count mode is used, here the photo detector counts the pulses in light extinction caused by single particles passing between the lamp and the detector. For greater concentrations the photometric mode is used, here the light scattering due to several particles passing between the lamp and the detector is measured, and the concentration is inferred.

The particles have to be relatively large in order to be picked up by the optical detector, to this end the particles are "grown" by condensing a vapour on them. The particles entering the CPC pass into a chamber containing a saturated vapour(usually butanol). The saturated sample then passes into a condensation tube where the sample is cooled. This causes the growth of the particles by condensation, to be detected the particles have to be larger than $0.5\mu m$. The growth rate is relative to particle size, with smaller particles growing more slowly. Greater saturation of the vapour in the CPC increases the growth rate, but saturation cannot exceed a critical level above which spontaneous nucleation can occur. Spontaneous nucleation is where fluid droplets form with no particle nucleus, creating a "false" particle. Therefore the CPC has a cut off size below which it cannot detect particles. Most CPC's working under normal conditions have a lower size limit of $7nm$, but some can go as low as $3nm$. The TSI model 3786 uses water as the working fluid, and claims a lower detection limit of $2.5nm$.

The CPC is a very powerful counting method because theoretically it can measure any particle concentration no matter how low, whereas when using an electrometer to count, as in the WAA, below certain concentrations the current is too weak to detect. A CPC (TSI model 3022A) was used in the experimental part of this project.

3.3.4 SMPS System

As a system the three instruments described above are linked together, and a computer is used to control the voltage on the central rod and log readings from the CPC. The aerosol sample is charged in the bipolar neutraliser and passed into the DMA, voltage in the DMA is scanned, and simultaneous CPC measurements of the change in concentration leaving the DMA are taken. The software collates this information and

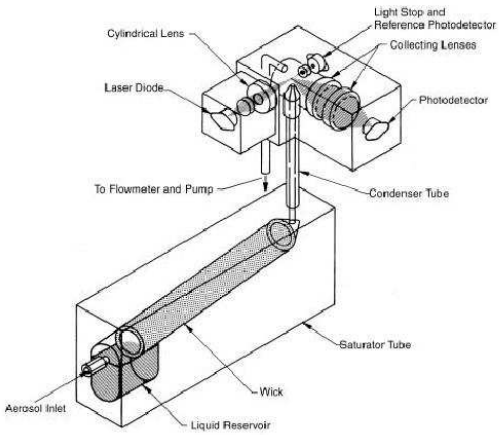

Figure 3.3: Schematic of the Condensation Particle Counter [TSI, 2002]

applies it with a correction function for the charge distribution, giving a final output of size distribution, weighted by number concentration, for the aerosol sample. On average it takes about 60-120 seconds to reliably analyse a sample.

An SMPS (TSI 3080) was used in the experimental testing of the Nanoparticle Spectrometer for results comparison and sample identification.

3.4 The Electrical Aerosol Spectrometer (EAS)

The Electrical Aerosol spectrometer was developed at Tartu University [Tammet et al, 2002], and is used in measurements of atmospheric particle concentrations and size distributions. The EAS has a classifying column like the DMA with a central column carrying a voltage, however in this case the charged aerosol sample enters the column via an annular channel around the central rod and particles are repelled outwards from the rod. This set up can be thought of as an "inside-out" DMA. The Inner surface of the classifying column is divided up vertically into 26 sections and each section is connected to a sensitive electrometer. The current induced by charged particles landing on each of these electrometers can be measured simultaneously; this makes the response of the instrument much faster than a scanning instrument.

The EAS uses two of these classification columns in parallel. The only difference between the two columns is the chargers. One column uses corona discharge to charge the particles by unipolar diffusion charging, while the charger on the other column uses corona discharge and a strong electric field to charge the particles by unipolar field charging.

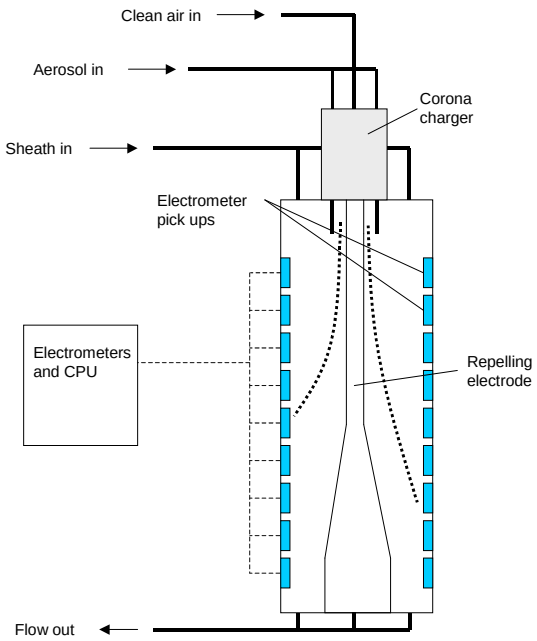

Figure 3.4: Schematic of one Electrical Aerosol Spectrometer column

The column with a diffusion charger is used to analyse particles of up to 500nm, where the mobility of the particles is a decreasing function of size. The column with a field charger is used to analyse particles above 300nm in size, where the mobility of the particles is an increasing function of size due to the field charging. This tandem set up with the two charging methods allows the EAS to analyse a large size range of particles ($10nm - 10\mu m$) with a fast response time ($\approx 1 - 5\,sec$).

3.5 The Differential Mobility Spectrometer (DMS)

The Differential Mobility Spectrometer [Biskos, 2004] is another instrument that measures particle size distribution by number concentration using differential electrical mobility. The DMS is commercially produced by Cambustion (DMS 500); the principle use of the DMS is to measure combustion-generated aerosols.

Particles entering the DMS are charged by unipolar diffusion charging in a corona wire discharge charger similar to that described by Pui [1976]. More details on this charger are given in section 3.10.1

The DMS uses a classifier very similar to that of the EAS. The column is made up of 22 electrometer rings, and the central rod has a varying voltage increasing from top to

bottom. The pressure inside the classification column is about $0.25bar$ (absolute), this increases the particle size range over which electrical mobility is a decreasing function of particle size, enabling the instrument to analyse particles in the size range of $10nm - 1\mu m$.

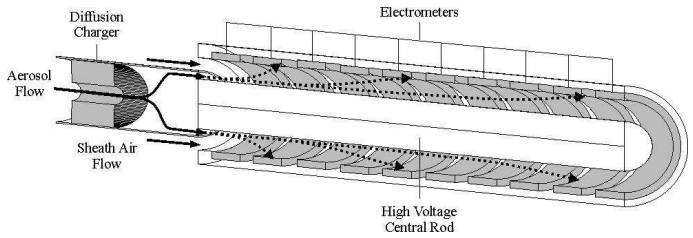

Figure 3.5: Schematic of the Differential Mobility Spectrometer [Biskos, 2004]

The DMS has a very fast response time ($\approx 250\,ms$). This enables the instrument to take transient measurement from combustion aerosol sources such as diesel engines.

As mentioned in the introduction to this thesis, the DMS has some shortcomings which limit its potential applications. As can be seen in fig 3.5 the high voltage rod is in close proximity to the electrometer detector rings. This means that any noise on the voltage signal to the rod can be picked up by the rings. In practice the DMS has a screen not shown in this diagram, which reduces but does not alleviate this problem. In order to have a uniform electric field in the classifier column the central rod must be mounted very accurately as any deviation from the centre will significantly distort the field, this also makes the instrument sensitive to vibrations as the field will change as the rod moves. In order to be able to catch enough charge to produce a detectable signal the electrometer rings must be of a certain width, this is the limiting factor regarding the size of the DMS and makes it comparatively large and heavy.

3.6 The Engine Exhaust Particle Sizer (EEPS)

As the name implies the EEPS is specifically tailored to analyse combustion aerosols from engine exhausts, and is produced commercially by TSI (Model 3090). The design of the EEPS is extremely similar to that of the DMS. The main difference is that the pressure in the classifier is close to atmospheric, and hence the particle size range covered is smaller ($5.6 - 560nm$). Also the EEPS has a negative polarity diffusion charger before the positive one, which makes it less sensitive to existing charge on the

aerosol sample. This is particularly beneficial for the larger particles ($\geq 200\,nm$). Due to its similar design, the EEPS has the same shortcomings as described for the DMS above.

3.7 The Electrical Low Pressure Impactor (ELPI)

All the instruments described so far measure an aerosol sample's size distribution using differential mobility analysis. The ELPI [Marjamärki et al, 2000] operates on a very different principle, it classifies particles by their inertia, which is proportional to their aerodynamic diameter.

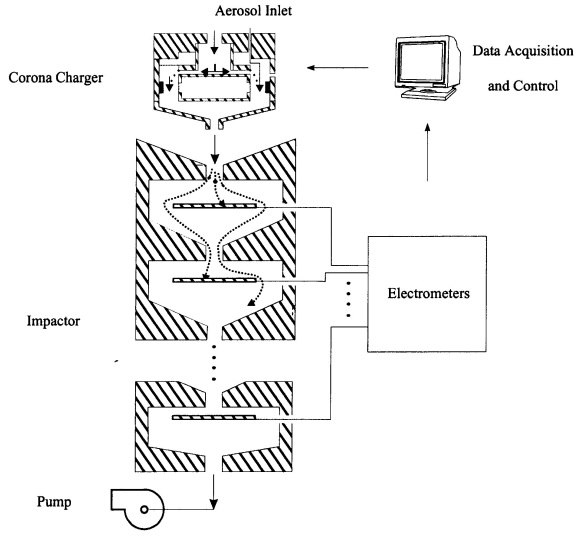

Figure 3.6: Schematic of the Electrical Low Pressure Impactor

Particles entering the ELPI are charged by unipolar corona discharge from a needle, and then flow into the classifier, which consists of a series of stages containing impactor plates (see fig 3.6). The area of the inlet orifice to each stage, and the distance between this orifice and the impactor plate determines the "cut-off" size of the stage. Particles larger than this size will impact on the plate due to inertia while smaller (lower inertia) particles will flow around the plate. Of course particles in the stagnation stream will impact regardless of size and this can be a source of error. The stages are arranged so that the cut-off size decreases incrementally with the flow through the classifier. The final stage is not an impactor but an absolute filter which removes all the remaining particles.

Each Impactor plate, and the filter, is connected to a sensitive electrometer, which measures the current due to the charge depositing on the plate or filter. From this the number of particles landing can be inferred.

The time response of the ELPI is in the order of 2 seconds and the particle size range is $30nm - 10\mu m$. An advantage of the ELPI is that after a sample has been analysed the impactor plates can be removed and further analysis can be performed on the collected particles, such as electron microscopy.

3.8 The Diffusion Battery

The diffusion battery classifies particles by their mechanical mobility (or diffusivity); smaller particles are more mobile in gases than larger ones so therefore precipitate more easily on screens and filters.

The TSI model 3040 diffusion battery consists of 10 stages. Each stage consists of one or more steel mesh screens in series. Between stages some of the sample can be removed for analysis using a CPC. The stages increase in the number of screens and the density of the mesh so that only the most diffusive (smallest) particles precipitate on the first screen, and increasingly larger particles are precipitated on the subsequent screens. From the reduction in concentration between each stage the size distribution of the aerosol can be inferred. The TSI model 3040 diffusion battery classifies particles in the size range of $2 - 200nm$.

Either a single CPC can be used to analyse the concentration of the sample between the stages one by one, which is very time consuming, or multiple CPC's can be used to analyse the concentrations simultaneously, which is relatively expensive.

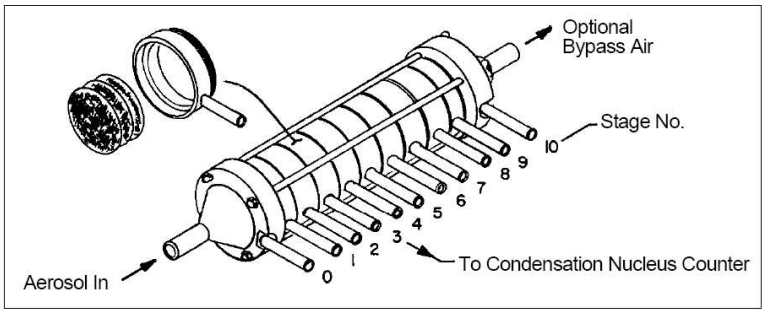

Figure 3.7: Schematic of the Diffusion Battery [TSI, 2000]

Another type of diffusion battery is the Electrical Diffusion Battery [Fierz et al, 2002]. In this design, the aerosol is charged by corona discharge before entering the

diffusion battery and sensitive electrometers are used to measure the current induced by particles landing on the screens in each stage. Using this technique response times of around 20 *sec* have been reported.

3.9 The Centrifugal Particle Mass Analyser (CPMA)

The CPMA classifies particles by mass, and can be used in combination with a charger, and a particle counter such as a CPC to measure an aerosol sample's mass distribution.

The original CPMA[Ehara et al, 1996], consists of two coaxial cylindrical electrodes rotating as a solid body. Pre-charged particles pass between the electrodes where they experience electrostatic and centrifugal forces acting in opposite directions. Thus only particles of a specific mass-to-charge ratio will pass through without precipitating. The classified mass to charge ratio depends on the rotational speed and voltage difference between the electrodes. If the charge on the particles is known then the mass of the classified particle is also known.

In the CPMA an unstable system of forces causes many particles to be lost during classification. The centrifugal force is proportional to r^2 while the electrostatic force is proportional to $\frac{1}{r}$ (where r is the distance from the centre of the CPMA). For a particle of the correct mass-to-charge ratio these forces will be balanced at the 'equilibrium radius', r^*. However, for $r > r^*$ the centrifugal force is greater than the electrostatic force so particles will be forced into the outer electrode and vice versa for $r < r^*$. Therefore, with this system of unstable forces the transfer function is greatly reduced.

An alternative design of CPMA has been presented by Olfert & Collings [2005] that solves the stability issue by running the inner electrode at an increased rotational speed relative to the outer electrode, this causes the centrifugal force decreases with radius. This design has been shown to significantly improve the instrument transfer function.

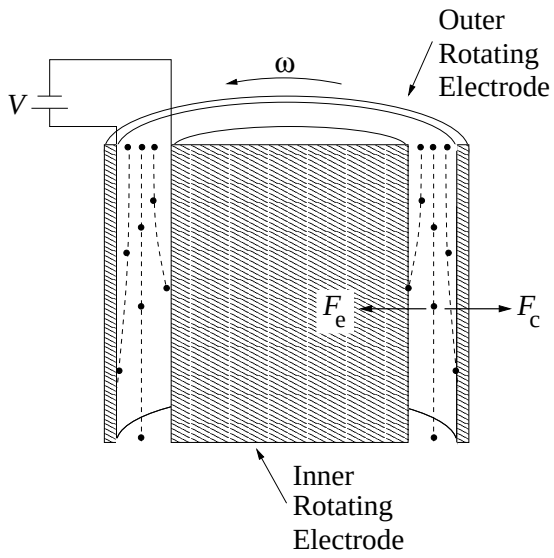

Figure 3.8: Schematic of the CPMA [Olfert & Collings, 2005]

3.10 Aerosol Chargers

The charger is an extremely important part of any differential mobility instrument, as it must charge a significant fraction of the aerosol in the desired particle size range. It must also impart a charge levels than give good mobility resolution across the particle size range and, very importantly, the charge distribution must be predictable.

Presented in this section are some examples of different types of charger design that have been proposed.

3.10.1 Corona wire charger

Several charges of this type have been designed [Hewitt, 1957, Pui, 1976, Biskos, 2004]. In general they consist of two concentric metal cylinders with a fine tungsten wire running through the central axis. This type of charger can be used to generate positive or negative ions, for simplicity only the positive type is described here, but the negative type merely has all the polarities reversed.

A positive high voltage is applied to the corona wire creating a discharge of positive ions. Some of these ions will pass through the screen opening into the annular gap between the cylinders where they will encounter the aerosol sample. Those ions that collide with aerosol particles will normally stick to them giving the particle a net positive charge. The screen has a positive voltage but one that is considerably lower than that of the corona wire and the outer cylinder is grounded. This set up allows the operator

to vary the ion flow through the screen by adjusting the screen voltage. It also creates a field in the charging zone, but one that is low enough that it may still be considered diffusion charging. In the Biskos [2004] design the screen voltage is alternating to make the charged particles move back and forth within the charging zone, reducing the probability of precipitation on the outer wall.

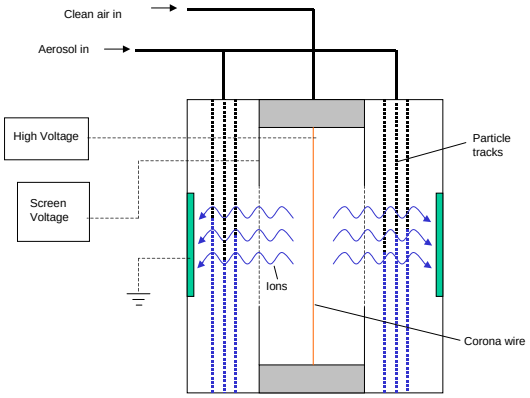

Figure 3.9: Schematic of the Corona wire charger

3.10.2 Twin Hewitt charger

This charger as shown in fig 3.10 was developed by Kruis & Fissan [2001], it uses two fine gold high voltage wires located axially within metal cylinders. Ions are generated by corona discharge from these wires and pass though thin mesh covered slits in the cylinders that are orientated to face each other at a distance of 16mm. The aerosol flows through this gap between the two slits. The wire meshes are connected to square wave generators that supply a voltage difference of $600V$ and are out of phase, so that the voltage alternates from one screen to the other. This produces a high ion concentration in the charging zone, and causes the charged particles to oscillate back and forth, and hence decreases the probability of them precipitating on the mesh.

3.10.3 Unipolar aerosol charger using a radioactive source

Ionising radiation is a popular method for charging particles with a bipolar distribution, but in this charger designed by Chen & Pui [1999] it is applied to unipolar charging. The main aim of this design is to reduce the loss of particles due to space charge precipitation to make longer residence times possible. In all chargers, the efficiency that is $\left(\frac{\text{number charged}}{\text{total number}}\right)$, drops off considerably below sizes of approximately 10nm.

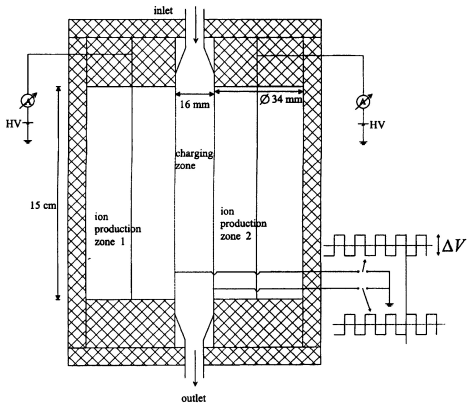

Figure 3.10: Schematic of the Twin Hewitt Charger [Kruis & Fissan, 2001]

This charger has extrinsic charging efficiencies of 22% and 48% at 3 and 5nm which is significantly higher than most other chargers. The charging efficiencies for larger particles are not necessarily higher, but comparable with most chargers.

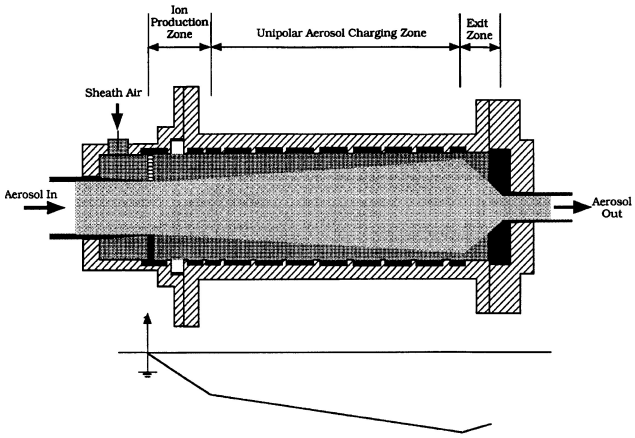

Figure 3.11: Schematic of the Chen Charger [Chen & Pui, 1999]

The charger, shown in fig 3.11 has two concentric inlets at one end: the core flow being the aerosol sample and the annular flow around it being clean sheath air. Downstream of the inlet is a ring containing ^{210}Po sources of α radiation that produce bipolar ions. A D.C. electric field is used to precipitate all the ions of the unwanted polarity

leaving only unipolar ions in the charging zone. Rings around the charging zone have a ramped voltage applied to them to set up a containing field. The containing field combined with the annular sheath airflow and the parallel flow of ions and aerosol, are the key factors that discourage charged particles from precipitating on the walls of the charger.

3.10.4 Medved Needle-plate aerosol charger

This charger designed by Medved et al [2000] is the first of several chargers detailed here that use a Sonic Jet Ioniser [Whitby, 1961]. The construction of the Sonic Jet Ioniser is shown in fig 3.12. Clean air is fed into the ioniser and discharges through a small circular orifice in the face plate at sonic velocity. The point of an axially placed needle is close to the orifice and a high electric potential difference exists between the needle and the plate. This causes a corona discharge at the needle tip, consequently the sonic jet is loaded with unipolar air ions.

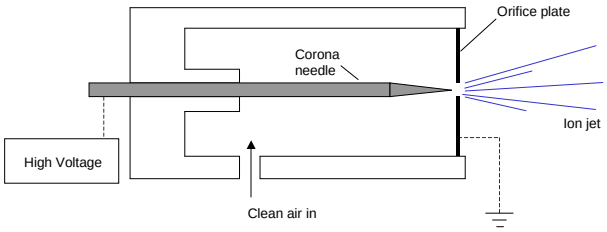

Figure 3.12: Schematic of the Whitby ioniser

The Medved et al [2000] charger (fig 3.13) uses a Whitby type ioniser, being run at atmospheric pressure, discharging into a sub atmospheric chamber at relatively low flow rates ($\approx 0.3\,lpm$) and sub-sonic velocities. The turbulent jet of air containing positive ions impinges directly on a similar turbulent jet of aerosol. Diffusion charging of the particles occurs in the mixing chamber.

3.10.5 Henandez-Sierra Needle-plate aerosol charger

Uniquely among the examples given here this design [Hernandez-Sierra et al, 2003] does not use two gas streams, one for ionised clean air, and one for aerosol particles, but instead relies on ionisation of air within the aerosol sample to charge the particles. The aerosol enters the charger (fig 3.14) from the left hand side where it passes through a perforated PTFE screen that supports the corona needle. The grounded electrode

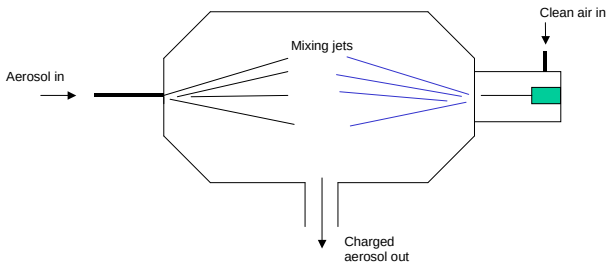

Figure 3.13: Schematic of the Medved Charger

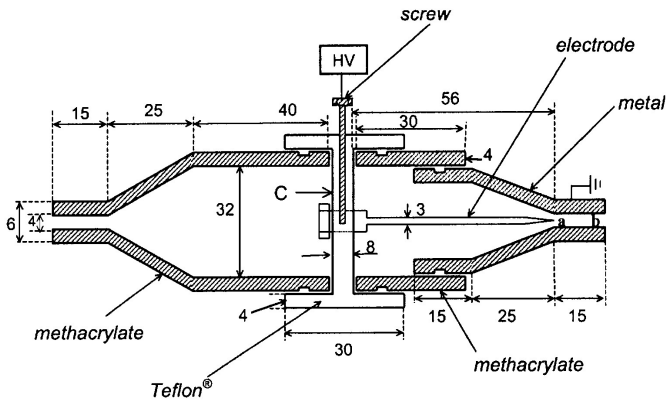

Figure 3.14: Schematic of the Hernandez-Sierra charger [Hernandez-Sierra et al, 2003]

in this charger is not an orifice but a convergent nozzle with the needle tip located at the narrowest point. The convergent nozzle allows the flow of aerosol to be accelerated without the associated pressure loss of an orifice. The high speed flow over the needle point means that the loss of particles through depositions caused by space charge precipitation can be reduced, but as usual there is a trade off with residence time. This charger has comparable particle charging efficiencies to most other unipolar charger designs, but is a good deal simpler in design than many of them.

3.10.6 Bipolar neutraliser using corona needles

This is a slightly different application of the Whitby type ioniser, here it is used to produce bipolar ions for aerosol neutralisation [Romay et al, 1994]. It is possible to generate bipolar ions from a Whitby type ioniser by applying an A.C. current to the

needle, so that the ioniser produces positive ions and negative ions respectively in each half of the A.C cycle. However, due to the fact that negative ions have a slightly higher mobility than positive ions it is useful to be able to produce them in slightly different quantities to offset this difference for neutralisation purposes. This is done here using two needles discharging into a mixing nozzle. One needle is at positive high voltage and one is at negative high voltage. The positive voltage being slightly higher, to produce more ions thus countering the effect of the higher mobility negative ions.

Romay et al [1994] use hard electrode materials to minimise nanoparticle generation by the ioniser through electrode sputtering. They found that by using a tungsten carbide drill bit as the needle and molybdenum for the orifice plate they were able to record lower particle generation than when stainless steel was used.

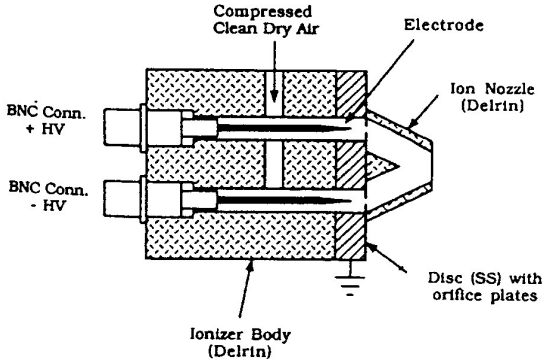

Figure 3.15: Schematic of the Romay neutraliser [Romay et al, 1994]

Chapter 4

Nanoparticle Spectrometer Concept

Here the concept for a new Nanoparticle Spectrometer (NPS) is presented. The instrument was conceived to make time-resolved measurements of the size distribution and number concentration of combustion generated aerosol samples from internal combustion engines. The NPS is a differential mobility instrument, which uses a unipolar diffusion charger to charge the aerosol sample by corona discharge, a classifier that separates the particles out according to their electrical mobility and an array of counting electrometers to count the number of particles with different mobilities. This is the same basic principle of operation that is seen in the EAS, DMS and EEPS (described in chapter 3), but, as will be seen in this chapter, this concept has a very different and novel construction, aimed at solving, to some extent, the deficiencies of existing designs.

4.1 NPS Operation

Fig 4.1 shows a schematic of the NPS concept. Upon first entry to the instrument a unipolar diffusion charger using corona discharge charges the aerosol sample. Following charging the sample flows into the classifier. The classifying region of the instrument is a channel of reducing cross-sectional area, where the base of the channel is a metal plate at a high voltage. The upper surface of the channel is a metal mesh that is grounded. This creates an electric field in the classifier that increases in strength in the x-direction. A flow of particle free "sheath" air is drawn through the classifier in the x-direction with uniform laminar flow at a constant velocity. The charged aerosol enters the classifier at the inlet marked in fig 4.1. The electric field in the classifier imposes a force on the charged particles causing them to travel upwards in the y-direction toward the metal mesh.

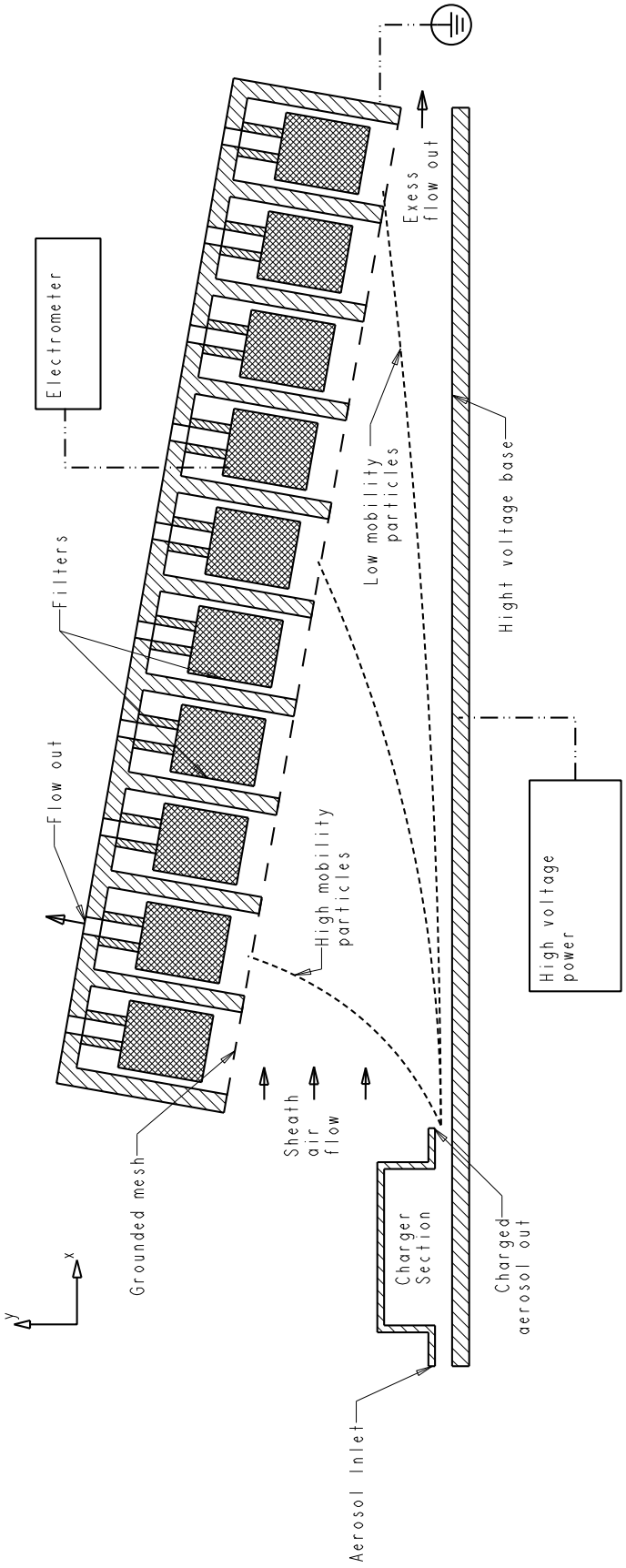

Figure 4.1: Schematic of the NPS concept

The electrical mobility of particles charged in a diffusion charger is a decreasing function of their diameter for particles smaller than a certain size, which depends on the charger $N_i t$ (see section 2.4.2). Therefore it is expected that small (high mobility) particles will be deflected quickly, reaching the mesh early in the classifier and large (low mobility) particles will be deflected more slowly and reach the mesh later in the classifier. Examples of particle tracks are marked on fig 4.1. When particles reach the mesh some will precipitate on it and some will pass through it.

The counting stage of the instrument is downstream of the mesh. This stage is divided into a number of sections, each containing a particle filter through which the flow from the classifier is drawn. The removal of flow from the classifier and through each filter provides control over the flow in the classifier so that the x-wise velocity is maintained approximately constant despite the reducing cross section. The flow also acts to draw the particles through the mesh and trap them in the filters. The filters themselves are connected to sensitive electrometers that measure the current associated with the charged particles entering the filters. Also the filters are electrically floating within earthed metal cases, which act as Faraday cages, screening the filters from external electric fields including the field in the classifier. This keeps unwanted noise on the electrometer signals to a minimum.

Measuring and comparing the currents landing on each filter allows the size distribution and the number concentration to be inferred. Using an array of channels means that the whole size range of the aerosol sample can be analysed simultaneously, this gives the instrument a fast response time making it suitable for transient measurements.

4.1.1 Size ambiguity

There are some issues arising from this particulate measurement technique. In the charger section particles will not accrue a constant level of charge, rather there will be a charge distribution on the particles, this is a known problem for all instruments that use electrical mobility classification. The electrical mobility of a particle is a function of the amount of charge it carries, as well as its diameter. This leads to an ambiguity over where the particle will land in the classifier. The level of charge also affects the amount of current detected by the electrometers when particles land on the filters. Therefore it is important that the charge distribution given to particles by the charger is known. So that the data from the electrometers can be interpreted to give an accurate size distribution and number concentration of the aerosol sample.

4.2 Novel Aspects of the Concept

There are several novel features to this Nanoparticle Spectrometer concept. The reducing cross-section has several positive benefits: it allows flow to be drawn out of the classifier and used to draw the particles through the filters, while maintaining an approximately uniform x-wise flow velocity in the classifier. As flow forces are used to trap the particles on the electrometer filters, no electric field is required to precipitate the particles as is the case in the DMS and the EEPS. Thus the filters can be encased in Faraday cages screening them from external fields, which are a source of noise. The reducing cross section also creates increasing electric field strength in the x-direction, which improves the resolution of the instrument because the gradient of the mobility versus size function decreases with increasing size.

The concept also allows for a relatively compact instrument design meaning that both bench top and on board vehicle use are possible. This is again because flow forces are used to trap the particles on filters, meaning that the NPS is not subject to the same restriction as the DMS and the EEPS, where the rings must be of a minimum width in order catch enough particles to produce a detectable signal.

The two-dimensional design of the NPS means that there is no central rod as in the DMS and the EEPS this means it does not require the very accurate mounting process required to ensure the rod and rings are concentric. The lack or a rod also means that the NPS is potentially a lot less sensitive to vibrations. Also the 2-D design simplifies the task of modelling the instrument's performance.

In addition to the above-mentioned features of the instrument hardware there is also a novel aspect to the instruments post processing software. Here a fast search technique is used to match output signals from the instrument with known signals for aerosol size distributions in a library that has been compiled using a physical model of the instrument and certain assumptions about the particle spectra being measured.

Chapter 5

Simulation and Modelling

5.1 Model of the Charge Distribution

5.1.1 Introduction

Unipolar diffusion charging by corona discharge is the chosen method to charge the aerosol particles for analysis in the Nanoparticle Spectrometer. Unipolar diffusion charging, depending on the $N_i t$ product, results in a charge distribution dependant mainly on particle size. The number of charges carried by a particle affects both its electrical mobility and the current induced when it lands on the electrometer filters. It is therefore very important to be aware of what the charge distribution on particles of a certain size will be. To this end a program has been developed to model the accretion of charge by the particles and predict the charge distribution on particles of a given size.

5.1.2 Accretion of Electrical Charge

Biskos et al [2005] proposed a technique for modelling the charge distribution on aerosols charged by unipolar diffusion that has been proved very effective. This method involves combining two existing models: The "birth and death model" [Boisdron & Brock, 1970] to model the charge accretion rate, and the "limiting sphere model" [Fuchs, 1963], which models the ionic flux to the particles.

The "birth and death" model works on the assumption that particles can only catch one charge at a time; for instance, in the charging region only a particle that has already accrued a single elementary charge can become a particle with two elementary charges and in this way, reduces the number of singly charged particles by one. The same applies for two to three charges, and so on. This "birth and death" process is represented by the infinite set of differential equations below (equation 5.1). Where n_i

is the number of particles with i elementary charges and a_i is the ionic flux to a particle with i elementary charges.

$$\begin{aligned} \frac{dn_0}{dt} &= -\alpha_0 n_0 \\ \frac{dn_1}{dt} &= \alpha_0 n_0 - \alpha_1 n_1 \\ &\vdots \\ \frac{dn_i}{dt} &= \alpha_{i-1} n_{i-1} - \alpha_i n_i \end{aligned} \tag{5.1}$$

There are several existing models for the ionic flux to the particle, for particles in the transition and free molecular regimes the limiting sphere model is the most commonly used. The validity of this model is supported by a large body of research [Pui et al, 1988, Biskos et al, 2005]. As the intended size range of the NPS does not cover particles in the continuum regime this is the only ionic flux model we require.

The "limiting sphere model" assumes two regions separated by an imaginary sphere concentric to the particle. Between this sphere and the particle surface the motion of the ions is determined by the thermal speed and the interaction potential with the particle. Outside this sphere ion motion is described by macroscopic diffusion theory. Matching the two fluxes at the surface of the sphere gives an expression for ion flux shown in equation 5.2 [Fuchs, 1963]

$$\alpha = \frac{\pi \gamma \bar{c}_i \delta^2 N_i exp(\frac{-\phi(\delta)}{kT})}{1 + exp(\frac{-\phi(\delta)}{kT}) \frac{\gamma \bar{c}_i \delta^2}{4 D_i} \int_{\infty}^{r} \frac{1}{r^2} exp(\frac{\phi(r)}{kT}) dr} \tag{5.2}$$

Where γ is the probability that an ion entering the limiting sphere will collide with and charge the particle, $\bar{c}_i$ is the mean thermal speed of the ions, N_i is the ion concentration ($ions/m^3$), k is the Boltzmann's constant, T is the gas temperature, D_i is the ion diffusion coefficient, $\phi(r)$ is the interaction potential at a distance r from the particle and δ is the radius of the limiting sphere.

The collision probability γ is given by

$$\gamma = \frac{b_m^2}{\delta^2} \tag{5.3}$$

Where b_m is the minimum collision parameter, i.e. when $\frac{db^2}{dr} = 0$, b is calculated by equation 5.4

$$b^2 = r^2 \left[1 + \frac{2}{3kT} [\phi(\delta) - \phi(r)] \right] \tag{5.4}$$

The radius of the limiting sphere δ is given by equation 5.5

$$\delta = \frac{a^3}{\lambda - i^2}\left[\frac{(1+(\lambda_i/a))^5}{5} - \frac{(1+(\lambda_i^2/a^2))(1+(\lambda/a))^3}{3} + \frac{2}{15}\left(1+\frac{\lambda_i^2}{a^2}\right)^{\frac{5}{2}}\right] \tag{5.5}$$

Where λ_i is the mean free path of the ions and a is the radius of the particle.

The interaction potential is given by equation 5.6, where $K_E = \frac{1}{4\pi\epsilon_0}$ is the constant of proportionality, n is the number of elementary charges, e is the elementary unit of charge ($1.6 \times 10^{-19}C$), a is the particle radius and κ is the image force parameter for particles with dielectric constant ϵ (equation 5.7).

The first term in the brackets (equation 5.6) corresponds to the Coulomb force between the ion and the particle due to the level of charge on the particle. The second term corresponds to the Van der Waals image force interaction between the ion and the particle. Typically this force is weak compared to the Coulomb force and only significant in the case of particles with a zero or one elementary charge.

$$\phi(r) = K_E\left[\frac{ne^2}{r} - \kappa\frac{a^3}{2r^2(r^2-a^2)}\right] \tag{5.6}$$

$$\kappa = \left(\frac{\epsilon-1}{\epsilon+1}\right)e^2 \tag{5.7}$$

Using the equations 5.2 to 5.7 the ionic flux can be calculated for particles of a certain size with $0, 1, 2, \cdots n$ elementary charges.

5.1.3 Calculating the Charge distribution

Solving the differential equations from the "birth and death" model in equation 5.1 using simultaneous Laplace transforms gives a series of equations for the number of particles that will collect i elementary charges in a time t. The first three steps in this series of equations are shown below.

$$
\begin{aligned}
n_0 &= exp(-\alpha_0 t) \\
n_1 &= \left(\frac{\alpha_0}{\alpha_1 - \alpha_0}\right) exp(-\alpha_0 t) + \left(\frac{\alpha_0}{\alpha_0 - \alpha_1}\right) exp(-\alpha_1 t) \\
&= \beta_0 exp(-\alpha_0 t) + \beta_1 exp(-\alpha_1 t) \\
n_2 &= \left(\frac{\beta_0 \alpha_1}{\alpha_2 - \alpha_0}\right) exp(-\alpha_0 t) + \left(\frac{\beta_1 \alpha_1}{\alpha_2 - \alpha_1}\right) exp(-\alpha_1 t) \\
&\quad + \left(\frac{\alpha_1 \alpha_0}{(\alpha_0 - \alpha_2)(\alpha_1 - \alpha_2)}\right) exp(-\alpha_2 t) \\
&= \gamma_0 exp(-\alpha_0 t) + \gamma_1 exp(-\alpha_1 t) + \gamma_2 exp(-\alpha_2 t)
\end{aligned} \tag{5.8}
$$

Substituting the coefficients in brackets for single letter abbreviations provides a significant simplification of the notation, for use in the subsequent equations. A larger expansion of equation 5.8 can be found in appendix C.

Evaluating the above equations between $i = 1$ and $i = 50$ gives the predicted size distribution for a specified particle size. For the range of particle sizes and residence times used, the probability (as calculated by the charging model) that a particle will accrue as much as 50 charges is effectively zero see fig 5.1).

In order to use this model to represent a specific diffusion charger we have to specify some values. These are the ion concentration in the charging zone N_i and the residence time of particles in the charging zone t. The charge distribution varies according to the product of these two parameters known as the $N_i t$ product. Fig 5.1 shows the charge distributions as calculated by the model for an $N_i t$ of 1×10^{13}.

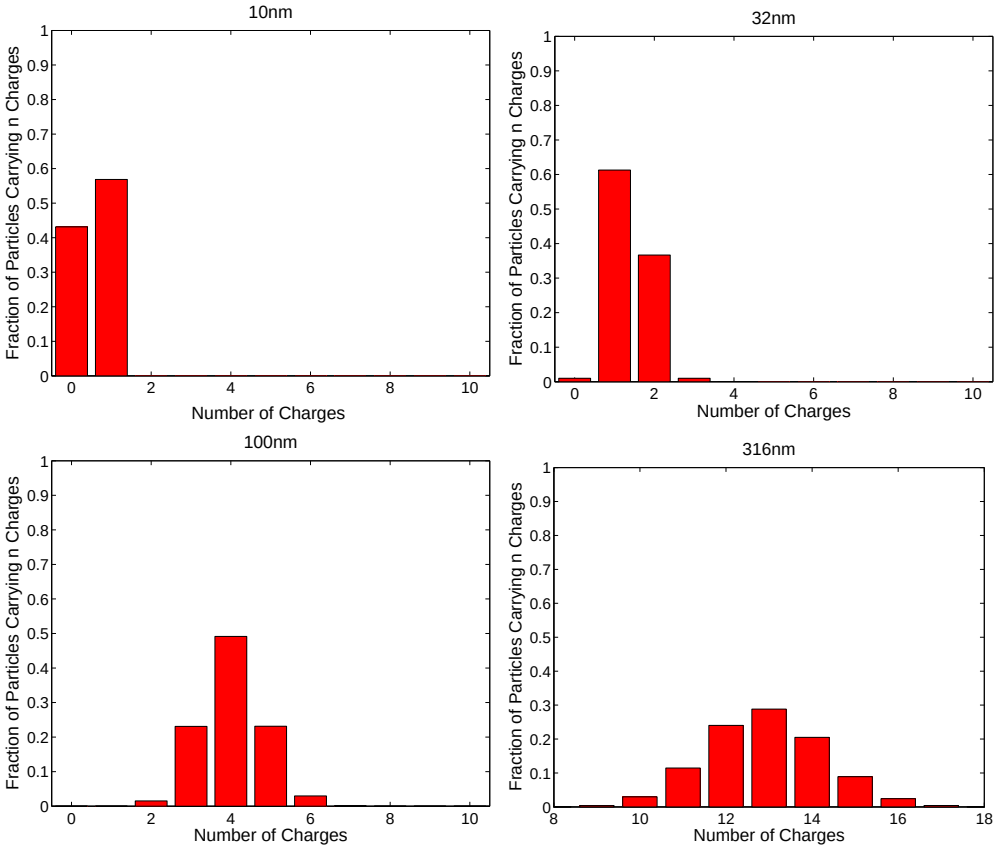

Figure 5.1: Example Charge distributions for various values of d_p. $N_i t = 1 \times 10^{13}$

5.2 Model of the Particle Tracks

This section concerns the simulation of the motion of particles due to the electric field and flow forces in the classifier.

5.2.1 Electric Field

The partial differential equations for the electric field in the classifier were evaluated numerically using the finite element method software "Femlab". A simple 2d geometry like the one in fig 5.2 is used to represent the classifier section.

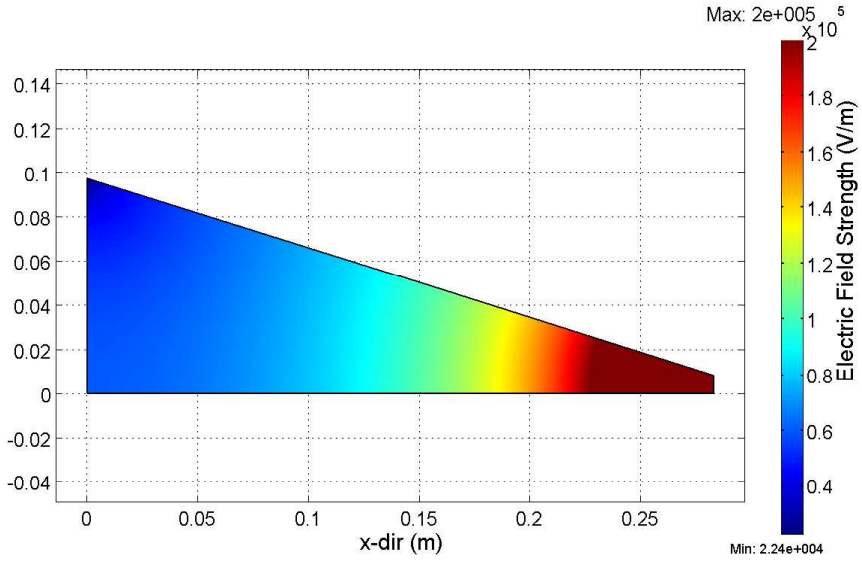

Figure 5.2: Surface plot showing modelled electric field strength (Vm^{-1}) in the classifier cross section

In electrostatics the scalar electrostatic potential V is related to the electric field density E by the relationship shown in equation 5.9.

$$\begin{aligned} E &= -\nabla V \\ E &= -\frac{\partial V}{\partial x}\mathbf{i} - \frac{\partial V}{\partial y}\mathbf{j} \end{aligned} \tag{5.9}$$

This is the equation for the sub-domain of the model. The boundaries can be modelled using either Dirichlet conditions, where the electrostatic potential (V) is specified on the boundary, or Neumann conditions where the surface charge ($n \cdot \nabla V$) is specified.

In the case of the instrument cross-section shown in fig 5.2 the bottom boundary represents the high voltage deflecting plate and is modelled as $V = V$. The upper

boundary represents the mesh screen which is grounded and hence modelled as $V = 0$. The left and right boundaries represent air in the instrument and are modelled as a surface charge of 0.

A different sub-domain equation can be used if it is required to specify the space charge in the classifier. This may be useful because the charged particles in the instrument will introduce a small space charge.

Maxwell's equation for the relationship between the electric displacement field D and the space charge density ρ is shown in equation 5.10. Combining this with the relationship shown in equation 5.11, where ϵ is the dielectric constant of the sub-domain medium, gives the Poisson equation (5.12), which can be used to model the sub-domain with space charge.

$$\nabla \cdot D = \rho \tag{5.10}$$

$$D = \epsilon E \tag{5.11}$$

$$\begin{aligned} -\nabla \cdot (\epsilon \nabla V) &= \rho \\ -\frac{\partial^2 V}{\partial x^2}\epsilon - \frac{\partial^2 V}{\partial y^2}\epsilon &= \rho \end{aligned} \tag{5.12}$$

5.2.2 Calculating the particle tracks

The finite element method model gives a solution for the electric field strength at mesh points across the region. This solution is exported to Matlab where the data is post-processed with a program created to calculate the particle tracks.

The particle tracking program works as follows (see fig 5.3): User specified coordinates define the starting location of the particle, and values of electric field strength in the X and Y directions (E_X, E_Y) are interpolated from the FEM solution. It is assumed that the forces on the particle accelerate it to terminal velocity instantaneously. The terminal velocity of a particle due to electrostatic force is described by equation 5.13.

$$V_{TE} = ZE \tag{5.13}$$

Where E is the electric field strength and Z is the electrical mobility of the particle, as specified by the user. Thus a velocity vector V_{TE} for the velocity due to electrostatic forces on the particle can be calculated. This is combined with the flow velocity U

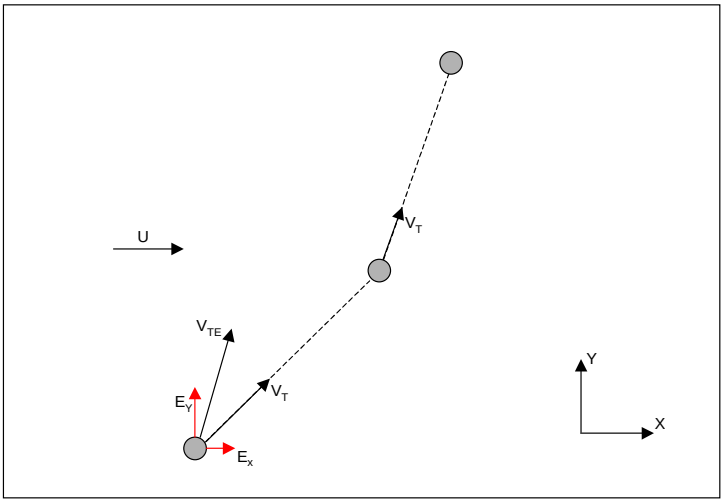

Figure 5.3: Vector modelling of particle motion in the classifier

of the carrier fluid (air) in the X direction to give a final terminal velocity vector describing the particles motion V_T. The particle is assumed to follow this vector for a user prescribed time interval after which the electric field strength is interpolated again at the particles new location and the vectors are re-evaluated. This process is continued until the particle reaches the edge of the modelled region.

Relating Mobility and Particle Size

A particle's electrical mobility is related to its size by the following equation, defined in chapter 2

$$Z = \frac{neC_c}{3\pi\mu d_p} \tag{5.14}$$

The equation used to calculate the Cunningham slip correction factor is an empirical equation [Allen & Raabe, 1985], also defined in chapter 2

$$C_c = 1 + \frac{\lambda}{d}\left(2.34 + 1.05exp\left(-0.39\frac{d}{\lambda}\right)\right) \tag{5.15}$$

The above equations can be used to allow the user of the particle tracking program to input particle diameters as opposed to directly stating the mobility. However this also requires some additional variables to be specified, these are: temperature, pressure of the carrier gas and the number of elementary charges carried by the particle.

As the particle diameter increases electrical mobility decreases, but only up to a point; larger particles also accrue more charge so there is a certain size where the difference between mobilities becomes too small to distinguish. It was found that if atmospheric temperature and pressure are assumed in the classifier, and the charging levels predicted by our theoretical model are correct, then approximately 300nm is the upper size limit before particles become difficult to distinguish. If the pressure in the classifier is reduced then it is possible to go to higher particle sizes. However, combustion generated aerosols in the accumulation mode are rarely larger than 300nm [Collings & Graskow, 2000, Abdul-Khalek et al, 2000]. It was decided that this is an acceptable upper size limit for the instruments range and avoids possible design and operational complications of running at low pressure.

5.3 Optimizing the Classifier

The models described above are useful tools for optimising the classifier. The variables that need to be defined are the size and shape of the classifier, pressure and flow rates of air through the classifier, and the voltage of the deflector plate.

In general, combustion generated aerosols have log-normal size distributions, therefore in order to have the best instrument resolution it is preferable for the particles to be classified by logarithmically increasing size.

In order to visualise approximately where particles of different size will land in the classifier it is possible to use the charging model to predict the average charge level on a range of particle sizes. These particle sizes and their average charge level can then be used as inputs to the particle-tracking model.

Figure 5.4 shows a triangular spaced classifier, with electric field lines plotted. The corresponding particle tracks for a range of logarithmically shaped particle sizes at the average charge level are also shown. The pressure is set as atmospheric, the flow velocity is $0.1ms^{-1}$ in the X-direction and the deflector plate voltage is 5kV.

5.3.1 Analytical Approximation

Adjusting all the available variables in the numerical model by trial and error is a time consuming way to optimise the classifier. To assist in the optimisation an analytical approximation was developed, based on a technique suggested to the author [Kittelson, 2004].

Fig 5.4 shows the curvature of the electric field lines in the classifier cross-section. It can be seen that for a shallow slope, as in this case, the lines are quite close to vertical.

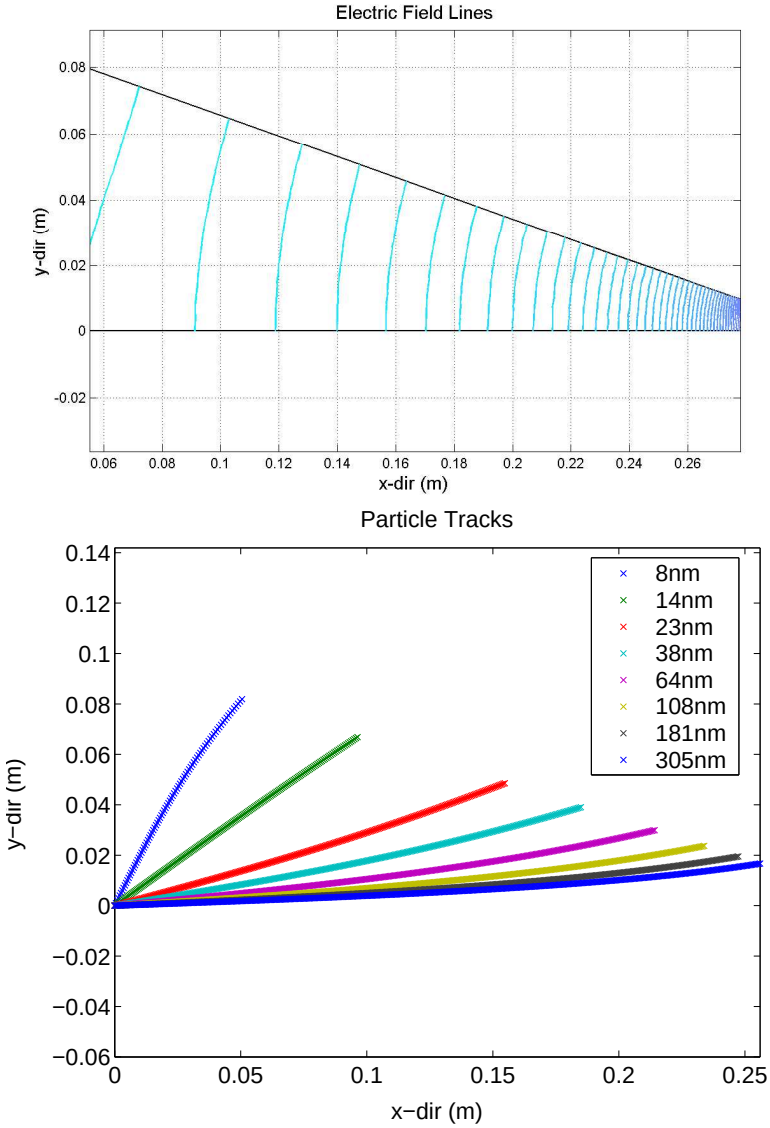

Figure 5.4: Particle tracks for various particle tracks in the classifier shape shown

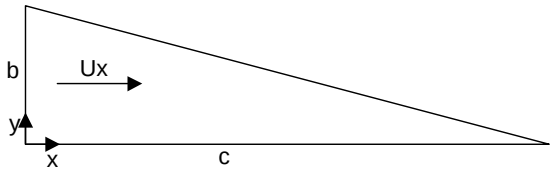

Figure 5.5: Showing the notation for reference with equations describing the analytical approximation

Using a simple analytical model where the field lines are assumed to be vertical it was found that landing positions of particles agreed closely with the numerical model at the low mobility end of the classifier, but were up to 5mm off at the high mobility end (where the field line curvature is more pronounced). This means that the analytical model is not accurate enough for the modelling of actual individual particle landing points. However, it is accurate enough for the purposes of helping in the classifier optimisation.

A simple triangle (fig 5.5) with height b and base c is used to represent the shape of the classifier.

The Electric field is given by:

$$\begin{aligned} E &= \frac{V}{y}, \qquad y = b - \frac{b}{c}z = b\left(1 + \frac{x}{c}\right) \\ E &= \frac{V}{b\left(1 - \frac{x}{c}\right)} \end{aligned}$$

x and y components of velocity of the particle can be written as:

$$U_y = EZ = \frac{VZ}{b\left(1 - \frac{x}{c}\right)}, \qquad U_x = U_x$$

The x position of the particle after a time t is expressed as:

$$x = \int U_x \, dt = Ut, \qquad t = \frac{x}{U}, \qquad dt = \frac{dx}{U}$$

The y landing position of the particle can be expressed thus:

$$y_p = \int U_y \, dt = \frac{VZ}{b} \int \frac{dt}{\left(1 - \frac{x}{c}\right)} = \frac{VZ}{bU} \int \frac{dt}{\left(1 - \frac{x}{c}\right)}$$

using

$$x' = 1 - \frac{x}{c}, \qquad dx' = \frac{-dx}{c}, \qquad dx = -cdx'$$

y landing position can be re-expressed as:

$$y_p = -\frac{VZ}{bU} c \int_1^{x'} \frac{dx'}{x'} = -\frac{VZ}{U}\frac{c}{b} \ln x'$$

Therefore y can be expressed as

$$y = b\left(1 - \frac{x}{c}\right) = b(x') = \frac{-VZc}{Ub} \ln x'$$

using:

$$\begin{aligned} x' &= \frac{-VZc}{Ub^2} l \ln x' \\ -\frac{Ub^2 x'}{VZc} &= \ln x' \\ \frac{-x'}{x_p} &= \ln x' \end{aligned}$$

gives us a dimensionless expression relating the mobility of the particles to its landing position.

$$x_p = \frac{VZc}{Ub^2} \tag{5.16}$$

This value of dimensionless mobility can be plotted against dimensionless position on the x axis (x/c) giving the graph shown in figure 5.6.

What can be seen from the graph in fig 5.6 is that mobility resolution is far better in the centre of the classifier than at the far edges. Using this line, optimal limits of x/c can be chosen. This gives us an upper and lower limit value of x_p. From this comes a value of $\frac{VC}{Ub^2}$ that allows the desired mobility limits that can be matched to the chosen dimensionless mobility limits. The value of $\frac{VC}{Ub^2}$ chosen in this case is 16×10^5 this means values of V, c, b, and U that yield this number must be used.

Imposing this limitation reduces the possible variation in parameters when using the numerical model. It is possible to select the optimum angle of the classifier upper edge with the numerical model. Then select values of V, c, b, and U around this.

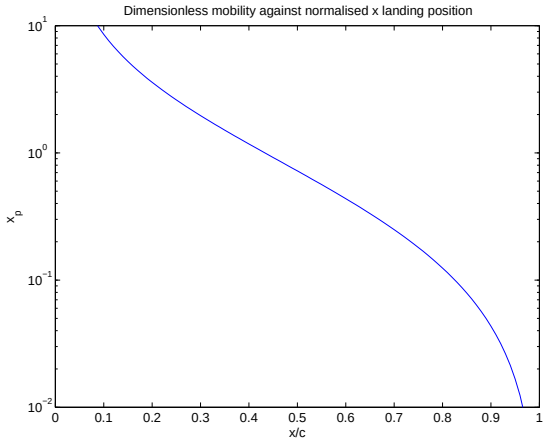

Figure 5.6: Dimensionless mobility plotted against normalised landing position in the classifier

Then the only thing left to choose is the scales of the model. This was done fairly arbitrarily, except for considering factors like ease of manufacture for the prototype, and wall effects on the flow in the classifier.

The Final optimised values selected are given in table 5.1

Variable	Selected optimum
V	$5000V$
U	$0.1ms^{-1}$
b	$96.9(mm)$
c	$314.4(mm)$
angle	17.1°

Table 5.1: Selected optimum parameters for the classifier

5.3.2 More complex geometries

The above optimisation was limited to a situation where the classifier shape is triangular and the deflecting plate is at a constant voltage. Under these conditions it is not possible to have the particles classified perfectly logarithmically by size. Figure 5.7 shows the particle tracks in the optimised triangular classifier. It can be seen that the resolution of the instrument will be better for smaller particles than larger ones.

If more complex geometries are considered then a more logarithmic classification of particles can be achieved. Fig 5.8 shows a classifier geometry where the upper surface

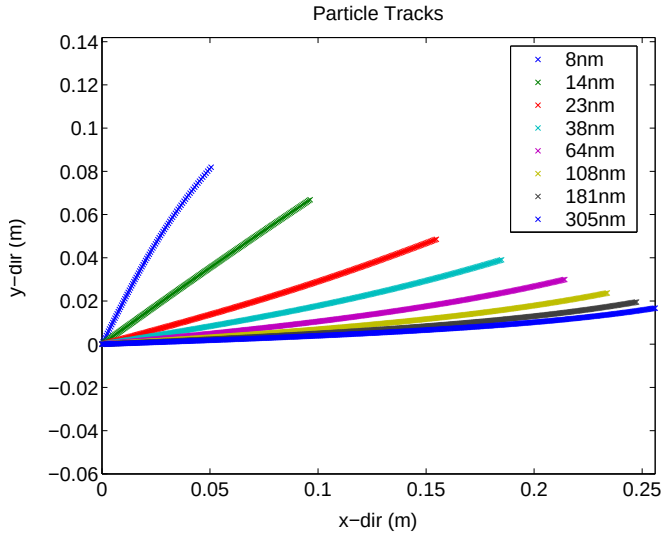

Figure 5.7: Optimised classifier particle tracks

is curved allowing more complex variations of the electric field in the classifier as well as the particle flight distances.

The particle tracks for this geometry are shown in fig 5.9 where it can be seen that the logarithmically increasing particle sizes land evenly spaced in the x-direction.

However, this geometry presents some significant complications to the design of the classifier. Firstly this shape would be difficult, and expensive to manufacture. Also in order to maintain a constant X-wise flow velocity in the classifier different flow rates would have to be drawn through each channel, meaning channels in regions where the angle of the electrode is close to horizontal would have almost no flow through them.

It is also possible to vary the electric field in the classifier by having a varying voltage on the deflecting plate. This could be done by breaking the deflecting plate up into sections and supplying each section with a different voltage. This would also complicate the design but not to the same extent as the curved upper electrode.

It was decided to consider varying voltage on the deflector plate as a re-design option, but to use a constant voltage for the initial instrument prototype.

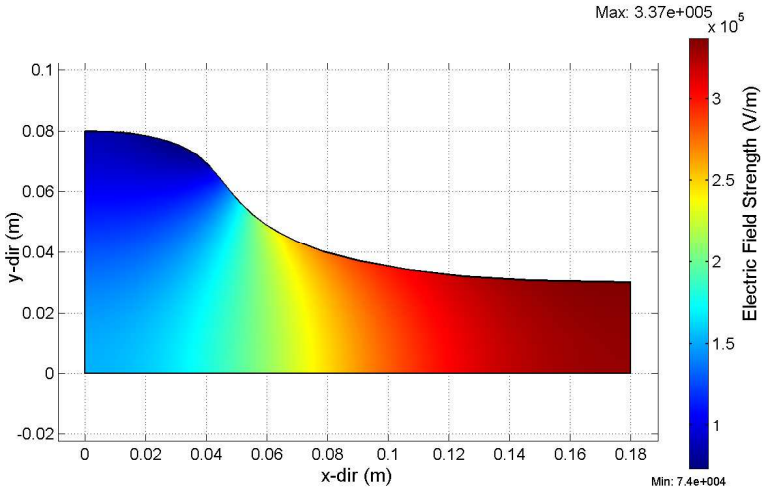

Figure 5.8: classifier with a curved geometry

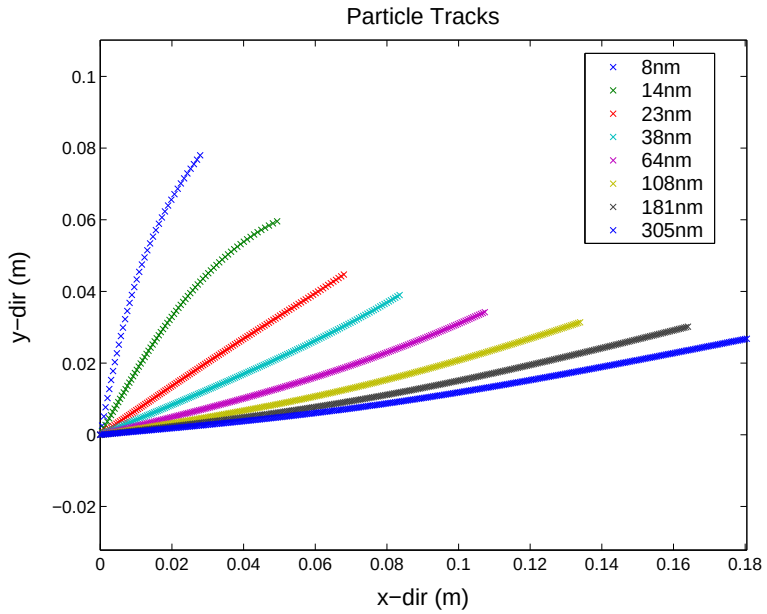

Figure 5.9: Particle tracks for the classifier geometry in fig 5.8

5.4 Model of the Instrument Output

The output signals from the Nanoparticle Spectrometer's electrometers in response to a given aerosol sample can be modelled by combining the charging model described in section 5.1 and the particle tracks model described in section 5.2.

5.4.1 Model Structure

Electrometer Mobility Limits

The boundary representing the ground electrode in the defined instrument cross section (section 5.3) is divided into 16 equal sections representing 16 channels for the electrometers. The numerical particle tracking model described in section 5.2 is used to find the mobilities of particles that would land at the intersections of these sections, thus the mobility limits of each channel are defined. Now if a particle's electrical mobility is known, then the channel where it will land is also known.

Input Distribution

Combustion generated aerosols are nearly always log-normally distributed [Kittelson, 1998]. A sample with a lognormal size distribution can be input by the user specifying the mean particle diameter and the geometric standard deviation. The concentration is normalized because the shape of the signal is dependant only on size distribution.

The program then divides the lognormal into n number of discrete strips along the x axis. Each strip is treated as a mono-disperse sample with diameter equal to that at the centre of the strip. The fraction of area occupied by the strip is retained for later calculation.

Charge Distribution

The charge distribution is calculated using the "birth and death model", described in section 5.1. An $N_i t$ value of 1×10^{13} is used in the data presented in this section as this $N_i t$ produced predicted results with good resolution, and appears to be a reasonable assumption for a diffusion charger according to available literature [Pui, 1976, Biskos et al, 2005].

For each particle size, the fraction of particles with $0, 1, 2, \cdots 50$ elementary charges is calculated. This fraction is multiplied by the fraction of the area occupied by the strip of the lognormal. And finally the combined fraction is multiplied by the number of elementary charges on the particle. This gives number of elementary charges per unit volume, which is proportional to the current that would be induced by the particles

landing on an electrometer. This is done for all n mono-disperse samples relating to the strips of the original log-normal distribution

Classification

Finally for each combination of particle size and number of charges the electrical mobility is calculated.

Knowing the mobility for a specific particles size allows the charge per unit volume for that size to be added to a running total for the corresponding channel in which a particle of that mobility will land.

The final output of the program is a bar graph showing the charge per unit volume in each channel, this is proportional to the current reading on the electrometers for an aerosol sample with the input distribution.

5.4.2 Examples of Modelled Instrument Output

This section presents some examples of outputs produced by the model. For simplicity, the first examples considered are the outputs for aerosol samples where the particles are all the same diameter (monodisperse). Figures 5.10 and 5.11 show graphs of the modelled instrument output and the modelled charge distribution for six particle sizes.

In the case of $10nm$ particles it can be seen that the model predicts that the particles will attain a maximum of one charge and a large proportion of the particles will be uncharged. These uncharged particles will not be classified. The NPS output shows that the singly charged particles are expected to land in channel five.

For $20, 39$, and $76nm$ particles the effects of multiple charging can clearly be seen. The charge distribution for 20nm shows singly charged particles and a small amount of doubly charged particles. The NPS output shows singly charged particles landing in channel 9, and doubly charged particles landing in channel 7. The size of the signal in channel 7 is about twice as large (relative to the singly charged signal) as the predicted fraction of doubly charged, compared to singly charged. This is expected because doubly charged particles induce twice the current per particle of singly charged particles. Similarly the plots for $39nm$, and $76nm$ particles show distinct signals in separate channels representing the 1, 2, 3...etc elementary charges.

In the case of $150nm$ the charge distribution predicts particles with 4-9 elementary charges. However signals are only predicted in channels 14, 15, and 16. This is because particles with different levels of charge are predicted to land in the same channels. There are two reasons for this: The higher numbered channels in the instrument cover a larger mobility range than the lower, and the difference in mobility between two

particle of the same size with n, and $n+1$ charges reduces, as n increases. The same effect is observed for $296nm$.

Observing the outputs for monodisperse samples is useful for the purpose of evaluating the model. However, in general monodisperse samples will not be presented for classification. Figures 5.12 and 5.13 show the predicted NPS output signals for a selection of narrow log-normal distributions (GSD = 1.1). Importantly a unique signal can be seen for each of the lognormals evaluated, and they can be easily differentiated. Between $10nm$ and $39nm$ mean diameter, the spread of channels in which signals are predicted broadens with increasing diameter. Between $39nm$ and $269nm$ the signals narrow again as the wider mobility limits of the channels becomes the dominant factor.

These graphs would seem to indicate that, as predicted by the analytical classifier approximation (section 5.3.1), that resolution will be better for samples landing in the middle of the classifier.

5.5 Signal Variation Analysis

In the previous section some evidence of variation in the signals for samples with narrow distribution has been shown. It is extremely important that the instrument be able to differentiate between the output signals for different aerosol samples and thus identify the sample size distribution correctly.

In order to test this, the model was used to produce predicted output signals for a wide range of log-normal size distributions with mean particle diameter ranging between $10nm$ and $300nm$, and geometric standard deviation ranging between 1.1 and 2. If a signal from this range is taken at random, then the total squared error between this signal, and all other signals in the range can be calculated. Figures 5.14 and 5.15 show surfaces where dp is plotted on the x-axis, GSD is plotted on the y-axis and the squared error between all the signals, and a single selected signal is plotted on the z-axis.

The first thing to notice about these surfaces is that the areas where the squared error is low are confined to the local region around the point being analysed. This is important because it means that if a signal is misidentified, it will likely be mistaken for a signal of similar distribution. This is preferable to the possibility that two very different distributions could be confused.

It can also be seen that the error in the direction of varying GSD than in the direction of varying mean size. From this it can be deduced that the instrument would be more likely to produce a wrong result for the GSD of the distribution than the mean size.

As the lowest squared errors are confined to the region around the point selected

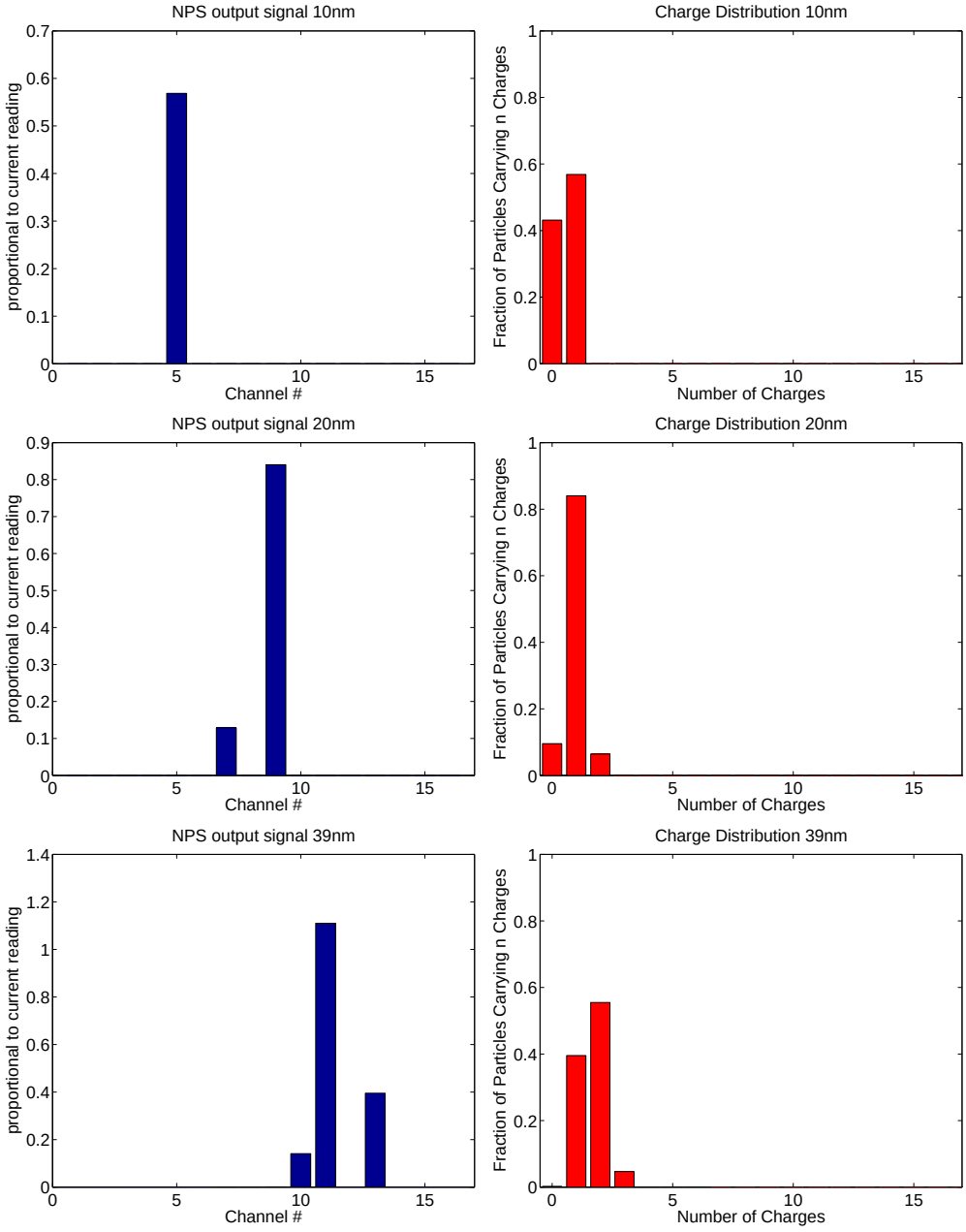

Figure 5.10: Graphs showing modelled instrument output for monodisperse samples

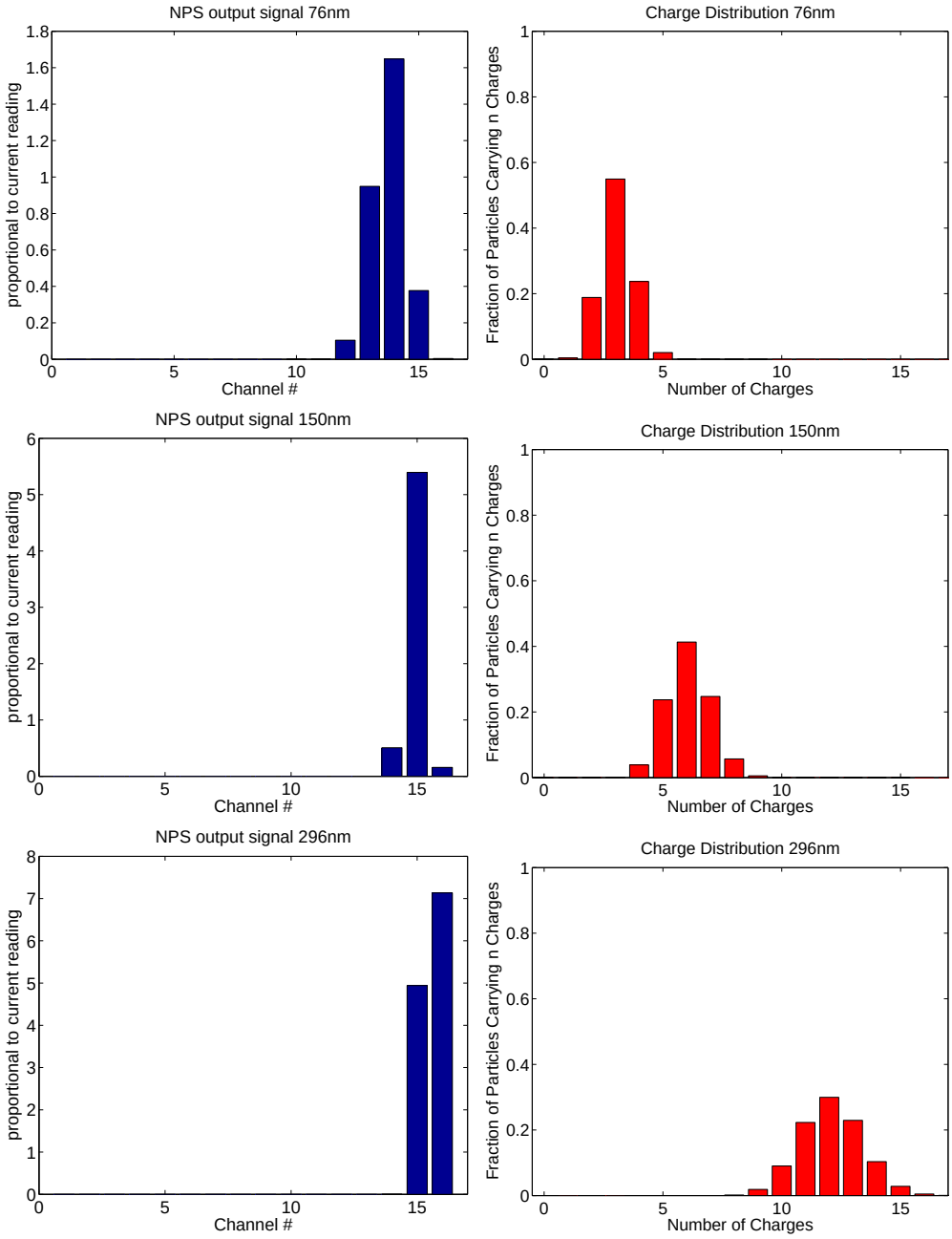

Figure 5.11: Graphs showing modelled instrument output for monodisperse samples

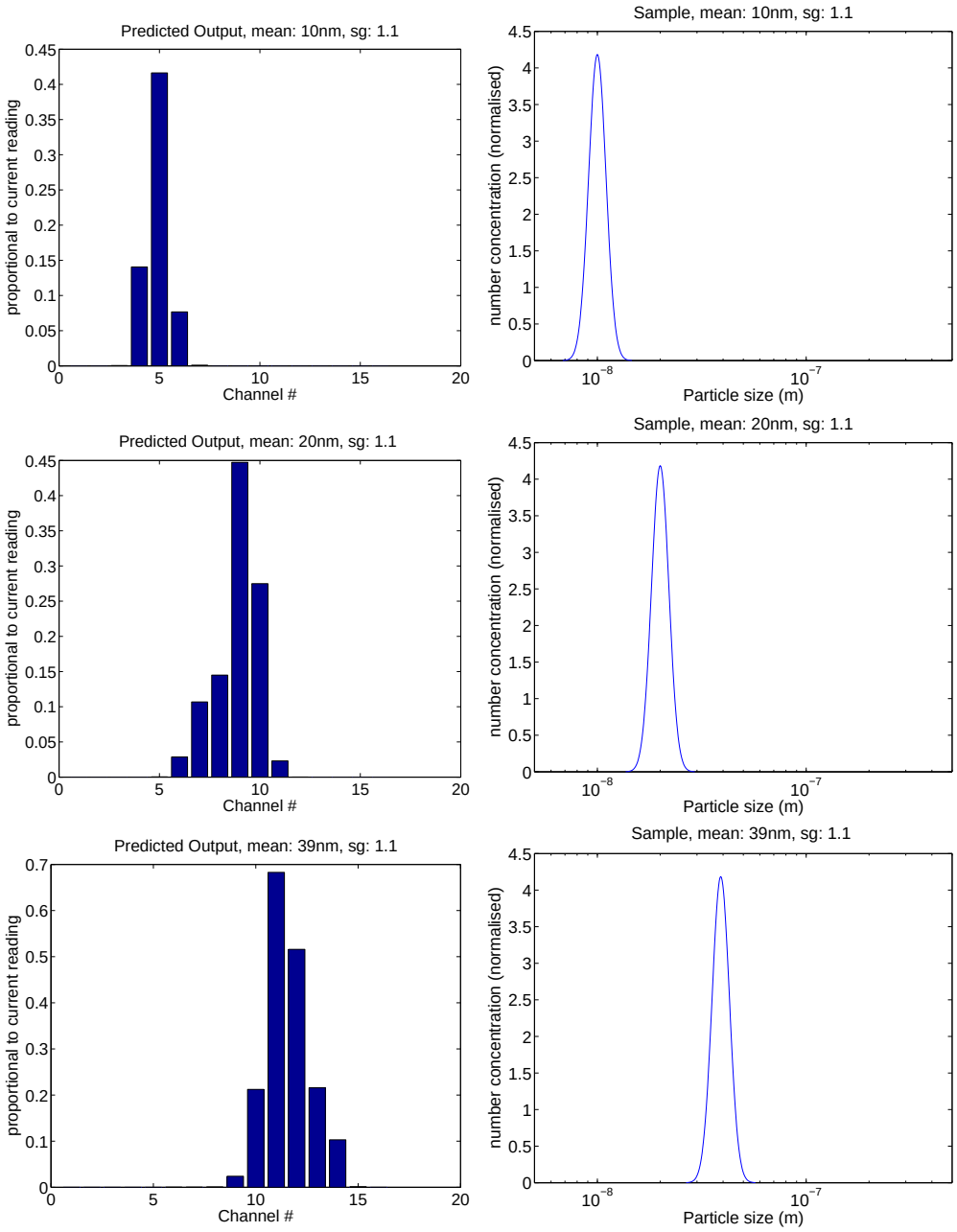

Figure 5.12: Graphs showing modelled instrument output for narrow lognormal samples

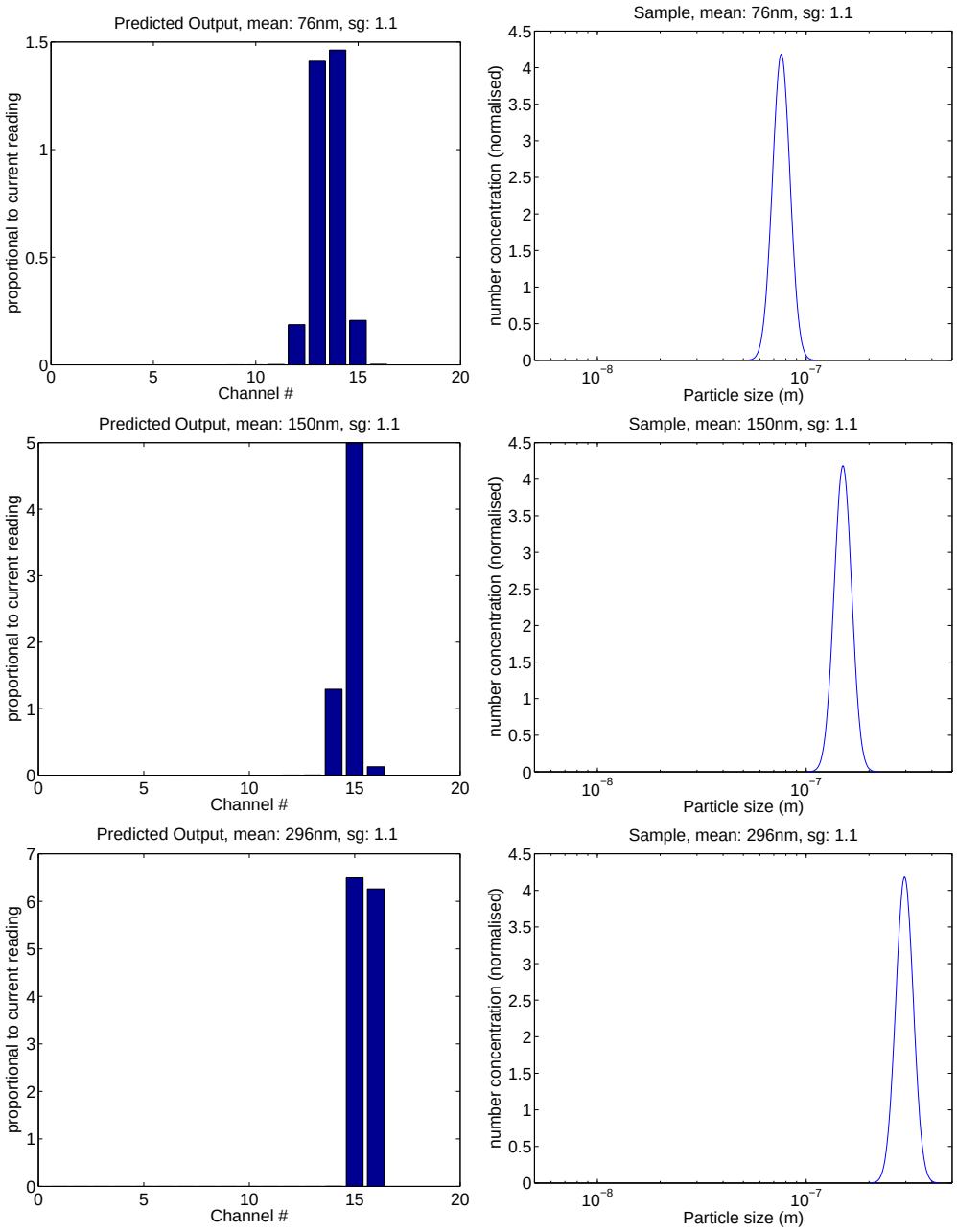

Figure 5.13: Graphs showing modelled instrument output for narrow lognormal samples

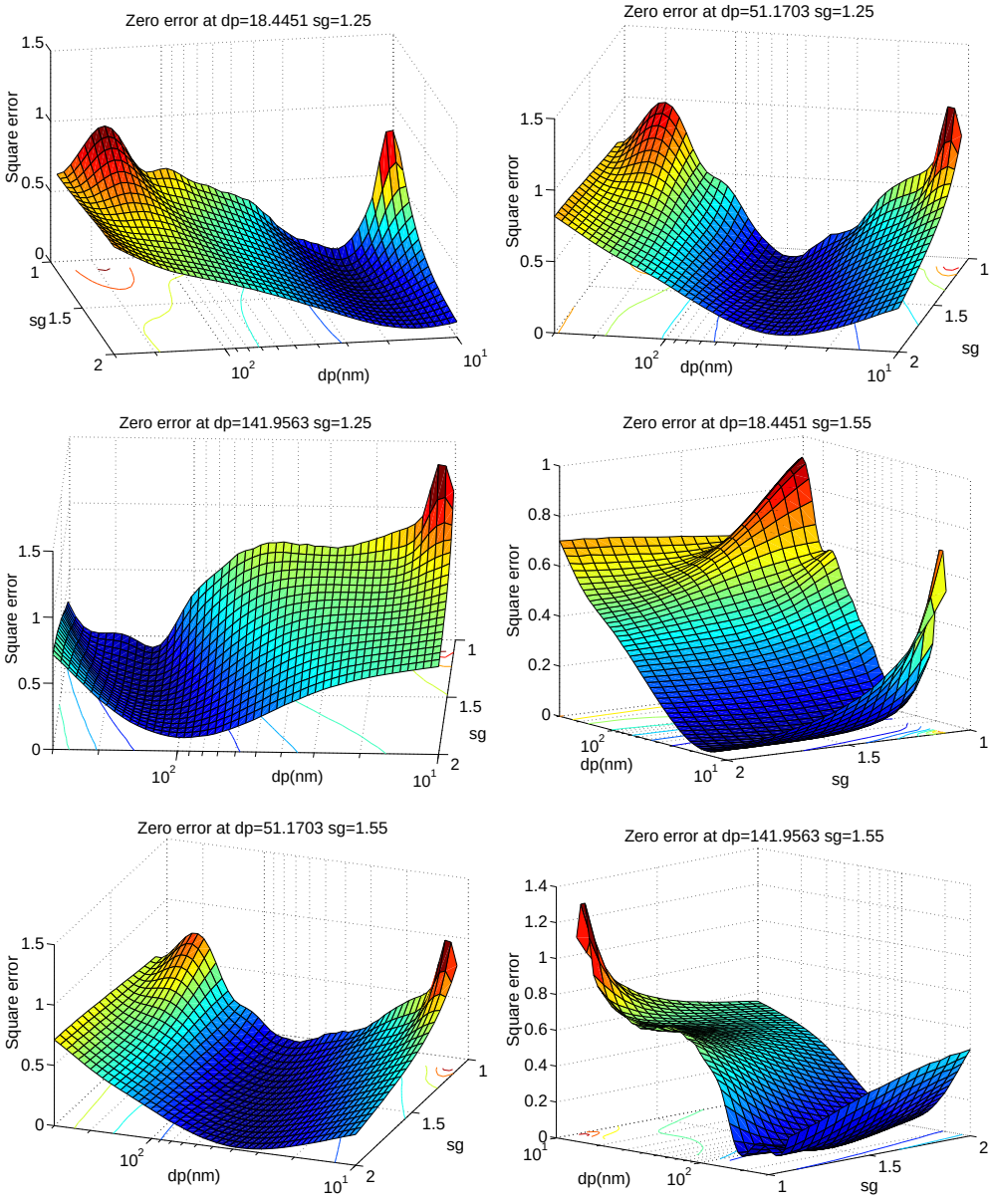

Figure 5.14: Surfaces showing the square error between predicted instrument outputs

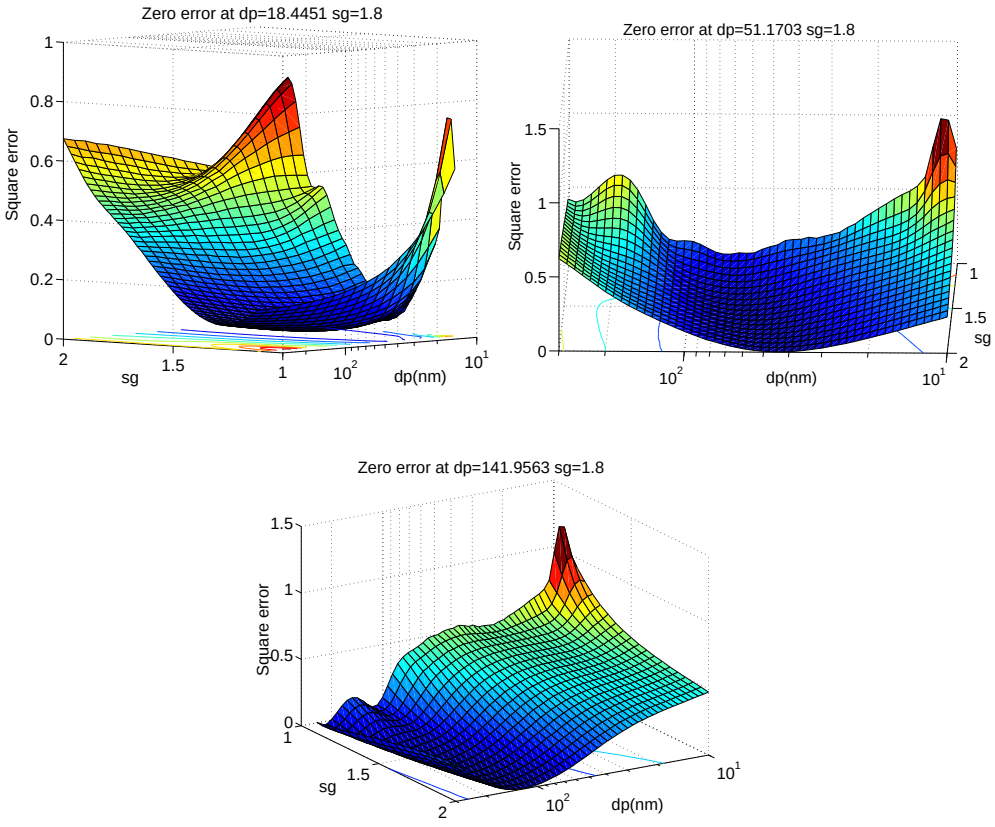

Figure 5.15: Surfaces showing the square error between predicted instrument outputs

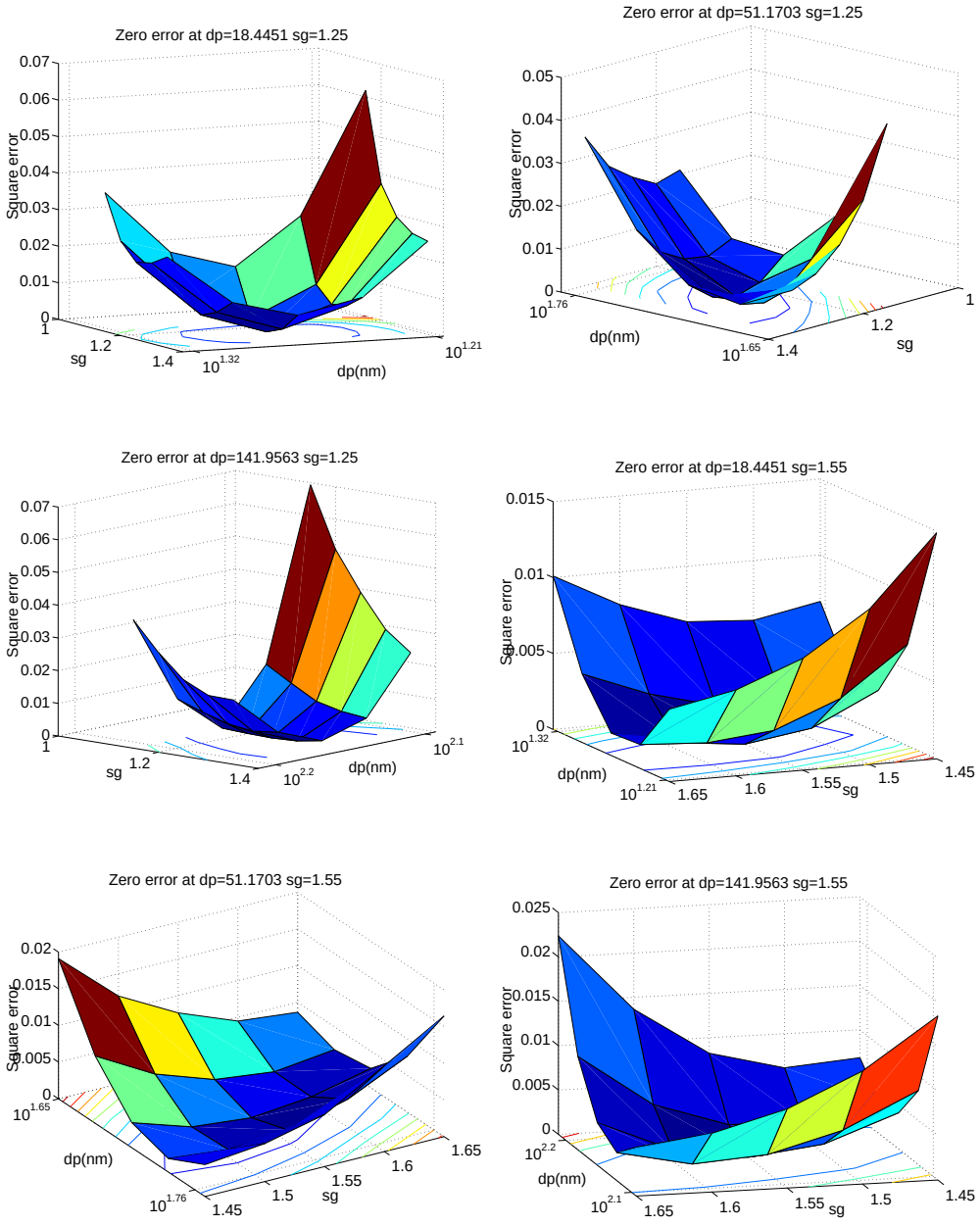

Figure 5.16: Surfaces showing the square error between predicted instrument outputs

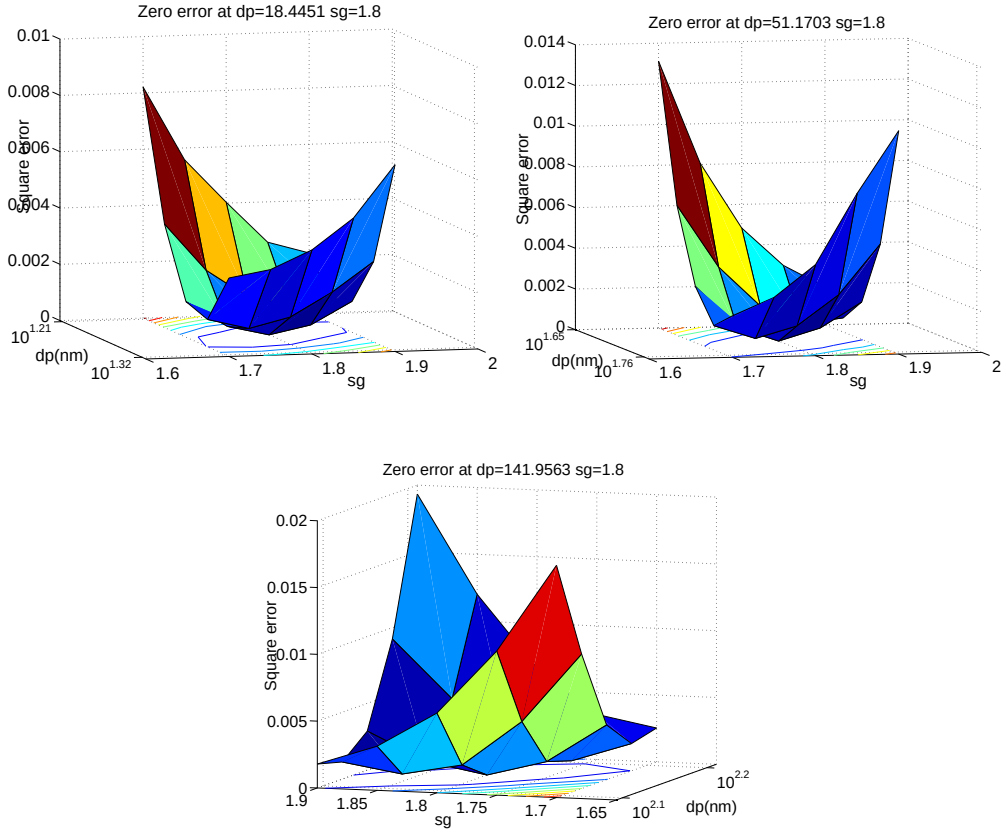

Figure 5.17: Surfaces showing the square error between predicted instrument outputs

for "zero error" it makes sense to look at these areas in more detail. Figures 5.16 and 5.17 show error surfaces for the same points analysed in figures 5.14, and 5.15, except in this case only the immediate area surrounding the zero point is shown.

The local variation seen in these figures shows that some areas have greater variation than others. The highest variation is seen in regions with low GSD and low mean d_p. The lowest variation is seen in areas with high GSD. Again it can be seen that the variation is lowest in the direction of GSD

The smallest error value seen in these plots is $2.9 \times 10^{-4} \left(\frac{\text{elementary charges}}{\text{unit volume}}\right)^2$. In the case of a particle concentration of $6 \times 10^6 \#/cm^3$ the minimum error value quoted above corresponds to a squared error in currents of $1.57 \times 10^{-29} A^2$. If we assume noise on the electrometers of $\pm 3fA$ (which is similar to the noise level on existing spectrometers) and we only analyse channels in which the signal is greater than this noise value, then the squared error produced by this noise would be $7.5 \times 10^{-30} A^2$ i.e. more that a factor of 2 less than the minimum error seen.

5.6 Look-up Table Inversion

Upon sampling an aerosol the instrument will produce an output signal from the electrometers. This signal must be interpreted to give the size distribution and concentration of the aerosol sample.

The problem with this is that a lot of information is lost in the sampling process. Classified particles land on the electrometers and induce a measurable current, but the same level of current will be induced by one large particle with ten elementary charges, as would be induced by ten small particles with one elementary charge. However, if the level of charge given to particles in the charger is accurately known, then statistical methods can be used to make the data inversion possible.

As noted previously, most combustion generated aerosol samples are log-normally distributed. A lognormal distribution can be described by two parameters; the mean and the geometric standard deviation. A large table of predicted output signals was generated using the model for a range of means and GSD's. This is very similar to the table used in the error surface analysis presented in section 5.5.

Each output signal in the look-up table has a value of mean and GSD associated with it. When a sample is analysed by the instrument the output signal can be compared with the predicted signals in the table, and the best fit selected. The mean and GSD associated with the selected signal are returned as the instrument's identification of the sample size distribution.

5.6.1 Look-up Algorithms

Method of Least Squares

This simple method takes the output signal to be tested and calculates the total squared error between this signal and each predicted signal in the look-up table. The signal from the look-up table that returns the lowest squared error is then selected.

Prior to analysis by least squares the test signal and the predicted signals must be normalised. There are two methods available for normalisation. The first is normalisation by "highest channel"; here the highest channel in each of the predicted signals is made equal to 1, as is the highest channel in the test signal. The second normalisation method is "total current". Here the total current for the predicted and test signal are set to 1. Both these methods were tried and are compared below.

Cross Correlation

Cross correlation is a measure of the degree to which two sequences are similar. For two sequences $x(n)$, and $y(n)$ cross correlation produces a sequence $r_{x,y}(l)$ defined by equation 5.17 [Ingle & Proakis, 2000].

$$r_{x,y}(l) = \sum_{n=-\infty}^{\infty} x(n)y(n-l) \tag{5.17}$$

The sequence $r_x, y(l)$ is $2n-1$ numbers long. The highest number is a measure of the similarity of the shape of the two distributions. The higher the number, the more similar the shape. The lag (l) gives the translation of the distributions. If the value l (corresponding to the maximum number in r) equals n then the locations of the distributions are in the same place.

The cross correlation algorithm developed for the NPS compares the test signal with each of the signals in the table in turn. The combination that returns the highest maximum in r at a lag l that is close to n is selected.

As with "least squares" the signals in the table, and the test signals must be normalised. The two normalisation techniques tested for least squares were also used with the correlation algorithm.

5.6.2 Testing the Algorithms

In order to test the above algorithms two levels of testing were employed. First the model was used to generate signals for lognormal distributions with values of mean, and/or GSD that lie between the discrete values in the table. These signals were then

used as test signals in the look-up table to see which signals were selected. The second level of testing was to add simulated noise to the signals generated by the model and again test the look-up algorithm with these signals.

The look-up table used in this case was constructed so that the range of mean sizes and GSD's covered the range of the instrument, and expected distributions. And so that the increments between the values of μ and GSD provided a great enough difference in the signal to be detectable, as estimated by the signal variation analysis. The table was a 51×19 stacked array, with each cell containing the predicted output from the NPS's 16 channels. There are 51 values of mean size increasing logarithmically between $10nm$, and $300nm$, and 19 values of GSD increasing from 1.1 to 2, in increments of 0.05. Twelve signals evenly spaced across the range of the array are selected for testing. The coordinates of these signals are given in table 5.2.

Coordinates of Samples (μ,GSD)		
$18.45, 1.3$	$18.45, 1.55$	$18.45, 1.8$
$36.42, 1.3$	$36.42, 1.55$	$36.42, 1.8$
$72.90, 1.3$	$72.90, 1.55$	$72.90, 1.8$
$142.96, 1.3$	$142.96, 1.55$	$142.96, 1.8$

Table 5.2: Coordinates of samples in the look-up table to be used for comparison

Test signals were generated using the model. These signals were for lognormal distributions that had values of μ and GSD that were between the coordinates of the points shown in table 5.2 and their nearest neighbours in the look-up table, but closer to the values in the table 5.2. Therefore when these test signals are input to the look-up algorithm the desired results would be for the algorithm to select the lognormals in table 5.2. Table 5.3 shows the values of μ, and GSD for the test samples.

Test Samples (μ,GSD)		
$18.88, 1.28$	$18.88, 1.57$	$18.88, 1.78$
$35.62, 1.28$	$35.62, 1.57$	$35.62, 1.78$
$73.59, 1.28$	$73.59, 1.57$	$73.59, 1.78$
$138.85, 1.28$	$138.85, 1.57$	$138.85, 1.78$

Table 5.3: μ and GSD for the test samples

As a measure of the success of the lookup algorithm a numerical value is assigned to each test. If the correct signal is selected the numerical value is 0. If the incorrect signal

is selected then the numerical value is the number of "look-up table" increments between the selected signal and the correct signal, specifically the number of increments in the μ direction plus the number in the GSD direction. Obviously the look-up algorithm that yields the lowest numbers will be the most desirable.

Figures 5.18 and 5.19 show the results for the test samples in table 5.3 analysed with the Method of Least Squares algorithm, with samples normalised by total current and highest channel respectively.

The results for MLS show correct selection occurs in the majority of cases and a result has not been selected that is more that one increment away in the look-up table.

Figures 5.20 and 5.21 show the results for the correlation algorithm, with samples normalised by total current and highest channel respectively. These results show much more frequent and severe miss-selection than the method of least squares. Therefore it was decided that the Method of Least Squares was preferable.

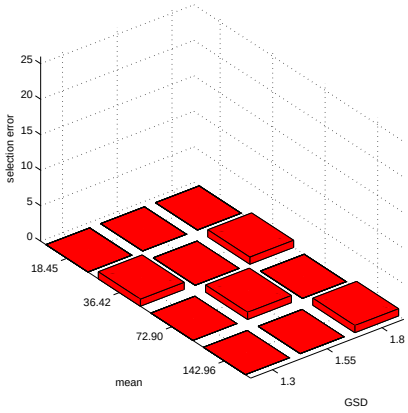

Figure 5.18: Look up algorithm selection error MLS (Total current)

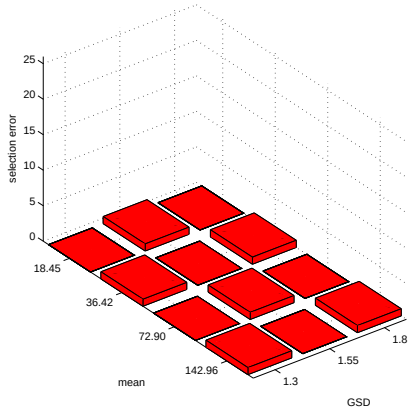

Figure 5.19: Look up algorithm selection error MLS (High channel)

Further analysis of the MLS algorithm was carried out with simulated noise added to the test signals shown in table 5.3. Noise was simulated using a random number generator that generates normally distributed random numbers with mean 0 and variance 1. A multiplication factor was used to scale the generated random numbers to be in the range of $\pm 5fA$ maximum noise. This did not change the results from those seen in Figures 5.18 and 5.19. Therefore the noise was scaled up until an effect was seen. The results of this showed consistently that the algorithm where the samples are normalised by "total current" produced slightly better results than the algorithm using "highest channel". This is unsurprising, as when the signals are scaled by a single channel the noise on that channel is added to all other channels, where as the sum of the noise which is added in the "total current" method is likely to be close to zero. Figures 5.22

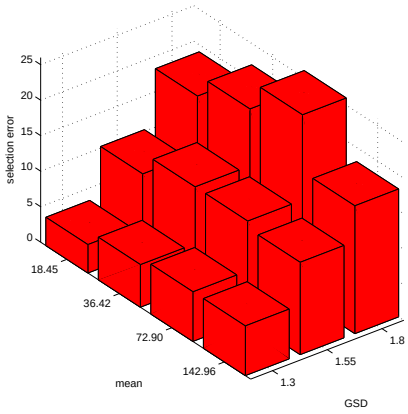

Figure 5.20: Look up algorithm selection error Correlation (Total current)

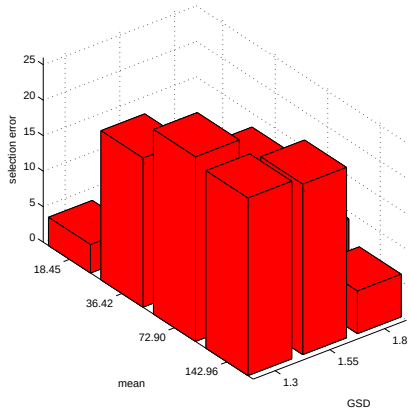

Figure 5.21: Look up algorithm selection error Correlation (High channel)

and 5.23 show typical results from these tests.

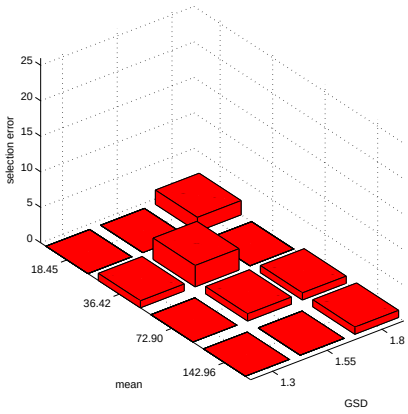

Figure 5.22: Look up algorithm selection error MLS "TC", with simulated noise

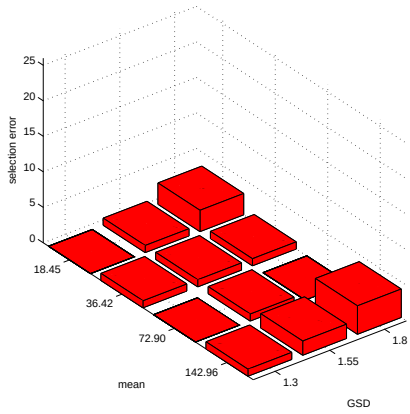

Figure 5.23: Look up algorithm selection error MLS "HC" with simulated noise)

Conclusions

Of the algorithms tested in this way, method of least squares using normalisation by total current made the most accurate selections. Also the time taken to run the algorithm is less than $\frac{1}{10}\,sec$ on a standard desktop PC with a $2.5GHz$ processor, so will not compromise the ability of the instrument to take fast response measurements.

It was concluded that MLS should be used as the initial algorithm, and that any

further improvement of the look-up algorithm would be best carried out using real measurement data from the instrument.

5.6.3 Determining the Concentration

The measured signals from the NPS will have units of Amps. The units of the signals in the predicted table are charge per unit volume. This does not matter when comparing the shapes of the signals in the look-up table, but in order to determine the aerosol concentration $N_p\,(p/cc)$ The units of Amps (C/s) must be converted to charge per volume (C/cc) by dividing by the sample flow rate $Q_A\,(cc/s)$

The lognormal distributions in the look-up table are normalised by concentration, i.e the area under each distribution is 1. The total charge per unit volume of each signal represents a charge per volume per "unit concentration", which is the charge to particle ratio $C_p\,(C/P)$. Varying charge levels on the modelled samples mean that the value of C_p will be different for every lognormal distribution in the table.

When the look-up program is run, the look-up algorithm selects the best match signal, and three values are returned: The mean, the GSD and the C_p for the selected distribution. The total current of the measured signal A_T is divided by the sample flow rate to give measured charge per volume this is divided by C_p to give particles per unit volume, the number concentration (equation 5.18).

$$N_p = \frac{A_T}{Q_A C_p} \tag{5.18}$$

Chapter 6

Charger Case Study: The Sonic Jet Charger

6.1 Introduction

Two types of charger were considered for use in the NPS, the first is the Corona Wire Charger (CWC) described in section 3.10.1. This type of charger has been proven to perform well as a charger for differential mobility instruments, and a variation of this type of charger used in the DMS (described in chapter 3). Work by Biskos et al [2005] has shown that the CWC can be modelled and the performance adequately predicted. These factors suggest that a Corona Wire Charger would be very suitable for application in the NPS.

However the Corona Wire Charger has some shortcomings, it is known to produce low charged fractions of very small particles ($< 15nm$) and the corona wire itself is fragile and prone to breakage. Therefore it was decided to investigate the feasibility of an alternative charger design for use in the Nanoparticle Spectrometer. The alternative design to be investigated is based on the Sonic Jet Ioniser design [Whitby, 1961]. This design has been described in section 3.10.

The Sonic Jet Ioniser produces a jet of air laden with unipolar ions, which lends itself to charging particles by diffusion in a turbulent mixing chamber. A charger of this design has been designed by Medved et al [2000] and used in the Electrical Aerosol Detector (EAD) from TSI (see appendix B.5).

When charging in a turbulent mixing chamber the chamber may be modelled as a well-stirred reactor and thus the residence time of particles in the chamber has a well-defined probability density function. This is a distinct disadvantage compared with the laminar flow charging zone of the CWC. However, in comparison to the CWC the Sonic Jet Charger (SJC) design is robust and simple, also Whitby [1961] has shown that the

SJI can produce very large numbers of ions, meaning that high $N_i t$'s are achievable.

In this chapter details of experiments performed to characterise the performance of the SJI are presented. Using these results a model was developed to simulate the charge distribution on an aerosol sample that a Sonic Jet Charger would produce. This was then used with the existing CWC model to perform a comparison between the two charging techniques.

6.2 Experimental Testing of the Ioniser

A prototype ioniser was designed and built for experimental evaluation. The design of the ioniser is shown in figure 6.1. The main body of the ioniser is constructed from a PTFE tube with a hose connector in the side of the ioniser where air is pumped in. On the front of the ioniser an aluminium orifice plate is screwed on with a gasket to provide a gas-tight seal. The steel corona needle is mounted on a BNC high voltage connector, which is screwed into the back of the ioniser's PTFE body. There are several BNC's with different lengths of needle attached and there are several orifice plates with different orifice diameters, which are interchangeable. A high voltage DC supply is connected to the BNC to apply a voltage to the needle tip and generate unipolar ions for unipolar charging. It is also possible to connect an AC current to generate bipolar ions to make a bipolar charger, although this is not explored in these experiments.

Tests were performed in order to measure the ion production of the ioniser under varying operating conditions. Partly the work consisted of validating Whitby's work, but also it was attempted to determine the governing variables that dictate ion production.

The experiments are divided into two main schemes. In one, air is forced into the ioniser under pressure and allowed to discharge into atmospheric conditions and is described here as High Pressure ('HP') operation. In the other air at atmospheric conditions is drawn through the ioniser, and discharged into a chamber that is at below atmospheric pressure and is described here as Low Pressure ('LP') operation.

The HP experiments were performed first, as the results from these could be compared to the results published by Whitby [1961], which detailed test results for the Sonic Jet Ioniser under HP conditions. In this way the ioniser performance and the experimental procedure can be verified.

6.2.1 Experimental Set up: High Pressure

The number of ions escaping from the ioniser is measured by passing the jet between two parallel plates with a potential difference between them. The positively charged

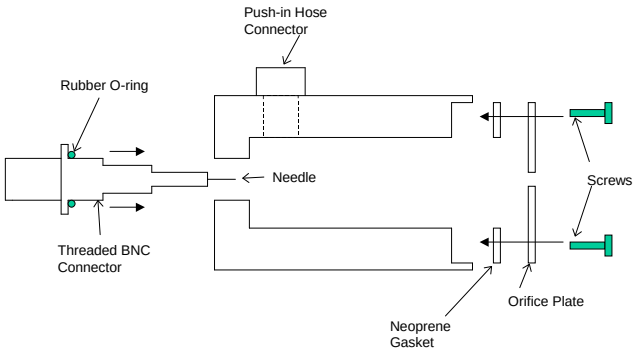

Figure 6.1: Schematic of the Sonic Jet Ioniser

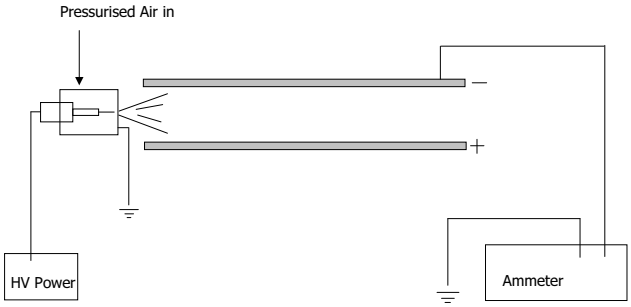

Figure 6.2: Schematic of HP experimental set up

ions are collected on the plate with the negative voltage. This plate is connected to a sensitive micro ammeter, thus the current associated with ions landing on the plate can be measured. Assuming the ions have a single positive elementary charge, the number of ions collected per second can be calculated. Using the flow rate and assuming uniform ion distribution in the jet, the ion concentration in the jet immediately downstream of the orifice can be calculated.

The flow rate of air through the ioniser is measured using a rotameter. The pressure of the air entering the ioniser, the voltage on the needle, and the current flowing to the needle are also recorded.

The potential difference on the plates was sufficient to precipitate 100% of the ions, indicated by the fact that the collected current plateaued before the maximum voltage was achieved.

6.2.2 Experimental Method: High Pressure

The variables in the experiments were:

- Needle spacing (s)
- Orifice diameter (d)
- Inlet air pressure (P)
- Needle Voltage (V)

The procedure for measuring these parameters was as follows: first fixed values of s, d, and P were selected. The needle voltage was then varied in order to determine the lower and upper limits of the available voltage range, defined as the voltage at which a corona discharge starts to occur and the voltage at which arcing occurs, respectively. Between these values readings of needle current and collected current were taken for approximately ten voltages, evenly spread across the voltage range.

This process was then repeated for values of P varying between about $135kPa$, and $310kPa$ (absolute pressure), values of s varying between $1.2mm$ and $3.9mm$ and values of d varying between $0.5mm$ and $2mm$. The flow rate resultant from each combination of P, and d is also recorded at this time.

6.2.3 Results: High Pressure

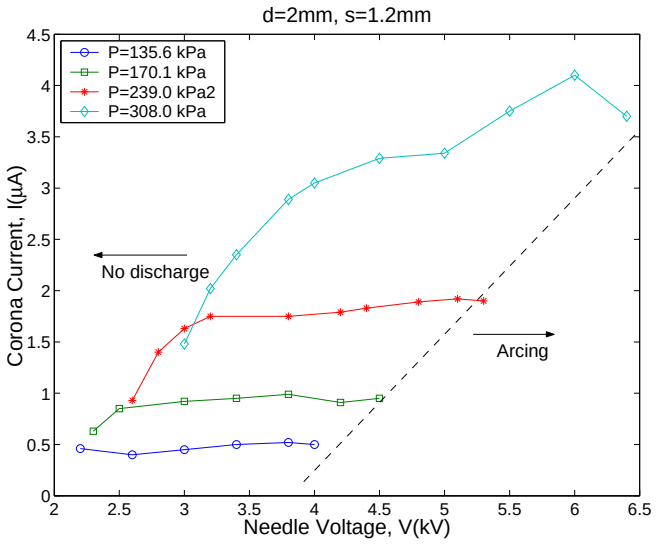

Figure 6.3: Collected ion current vs voltage for various pressures

Graph 6.3 shows the collected ion current against the voltage on the needle tip, for an orifice diameter of $d = 2mm$ and a needle spacing of $s = 1.2mm$, at various inlet pressures. The results show that, at any particular needle voltage, more ions are produced at higher pressures. It is expected that part of this effect is due to the increasing velocity of the air through the orifice, causing the flow forces on particles to increase relative to the electrostatic forces that encourage precipitation. However effects due to the variation in pressure are also present; as the pressure increases the voltage at which the corona becomes established, and the voltage at which arcing occurs, increases. In the results from the LP experiments it will be seen that these effects do not occur when velocity is varied but pressure is constant. It follows that in an atmosphere of higher pressure, air molecules will more frequently enter the small region around the needle tip at which the electric field is strong enough to make ions. This would mean that high pressures could also contribute to the increasing ion output.

The voltages at which corona discharge begins and at which arcing occurs are seen to increase with pressure. The higher number of collisions associated with higher pressures can have a suppressing effect on corona discharge because ions generated at the needle tip more often collide with another molecule before they have been accelerated to a critical velocity above which they cause secondary ionisation upon collision with other molecules.

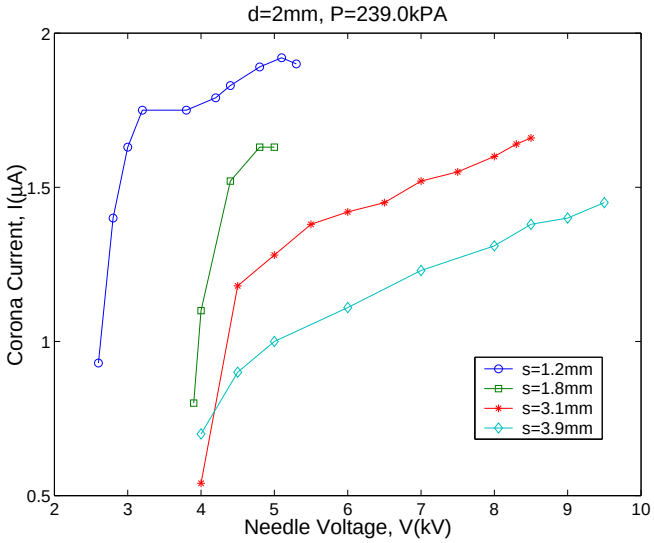

Figure 6.4: Collected ion current vs voltage for various needle spacings

Graph 6.4 shows corona current versus needle voltage for varying values of needle spacing, at constant orifice diameter, of $d = 2mm$, and constant pressure, $P =$

$170.1kPa$. As the needle spacing increases then the electric field around the needle tip with reduce in strength. Therefore it is expected that higher voltage will be required to start the corona and arcing, this effect can be seen in the graph. Also as the electric field strength is reduced it is expected that less ions will be produced and the corona current will be lower, as seen in the graph. Another factor in the variation of corona current is the fact that for smaller needle spacing the ions are generated closer to the orifice, and thus have less distance to travel before being expelled. This means that they will have less time to disperse outwards, and precipitate on the orifice plate.

The shape of the curves seen in graph 6.3 and 6.4 are very similar to those seen in the Whitby [1961] paper, but the numerical value of the collected current is significantly lower.

The efficiency of the ioniser is defined as:

$$\text{Efficiency} = \frac{\text{collected current}}{\text{needle current}} \tag{6.1}$$

Fig 6.5 shows efficiency curves for these tests, and Whitby's tests under similar conditions. A reasonable correlation can be seen, this suggests that the apparatus for collecting the produced ions in these tests is working effectively, but that less ions are being produced at the needle tip than in Whitby's experiments. Factors that could be responsible for this include the sharpness of the needle electrode and the materials used for the electrodes. It can therefore be concluded that the experimental technique used here is suitable for characterising the ioniser designed for these tests.

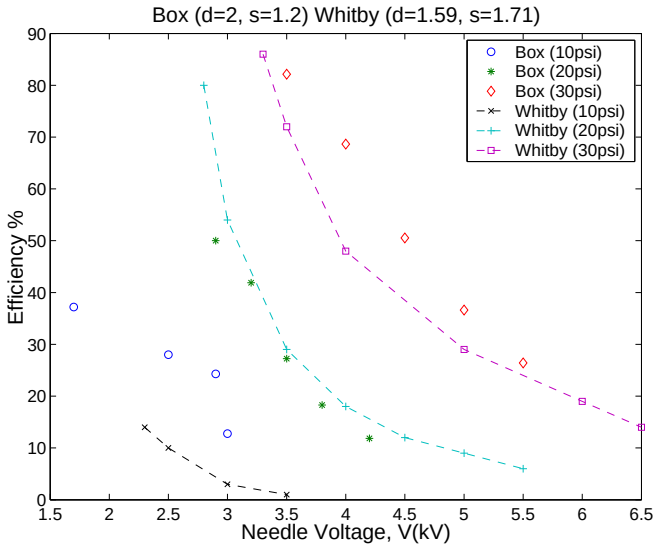

Figure 6.5: Ion production efficiency comparison between two ionisers

6.2.4 Experimental set up: Low Pressure

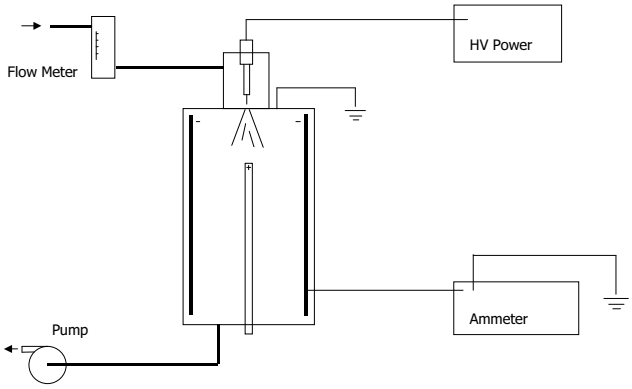

Figure 6.6: Schematic of LP experimental set up

This experiment used the same principles for measuring the ions as the HP experiments, though a different set of measuring apparatus was required. This is because it was necessary for the jet to be discharged into a low-pressure chamber. The chamber is cylindrical with the ioniser mounted at one end, and air drawn through from the other. The inside wall of the cylinder is a set of isolated copper rings, and a steel rod is positioned axially in the centre of the cylinder. The low voltage supply is this time used to apply a potential difference between the central rod, and the outer rings. The ions precipitate on the outer rings, which are connected to to the micro ammeter to detect the ion current. The same procedure as for the HP experiments was followed to ensure there was sufficient voltage to precipitate all of the ions that are in the jet. Again, a rotameter was used to measure the flow rate of air into the ioniser.

6.2.5 Experimental Method: Low Pressure

For these experiments the inlet pressure was constant, at atmospheric pressure. The flow rate of the air was allowed to vary with the different orifice plate sizes, but was also separately controllable by a needle valve placed between the outlet from the vacuum chamber and the inlet to the pump.

The same procedure as that used for the HP experiments was followed for measuring collected current and needle current against needle voltage.

The needle spacing s was again varied between $1.2mm$ and $3.9mm$, but this time the variation of orifice diameter d was refined to be between $0.7mm$, and $1.2mm$ at increments of $0.1mm$. This was done to give smaller increments in change of flow rate,

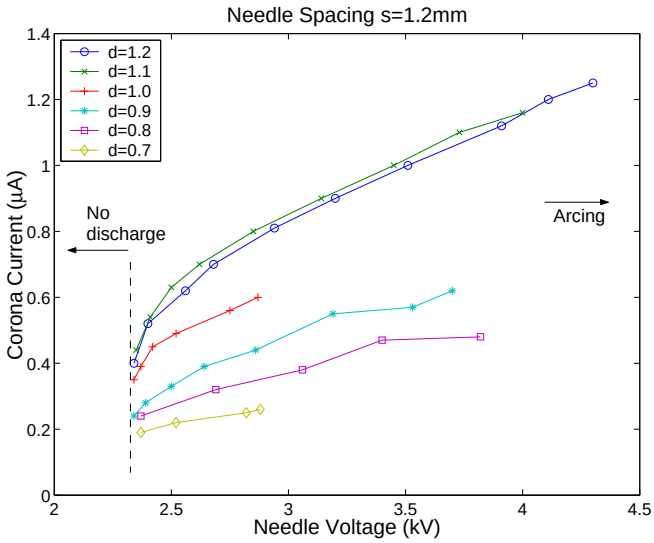

Figure 6.7: Raw data plot of I against V for various values of d at $s = 1.2$

which of course varies significantly with orifice diameter.

6.2.6 Results: Low Pressure

Raw Results

Graphs 6.7 to 6.10 show some raw results from the experiments. The graphs show the collected current against needle voltage for orifice diameter sizes of $0.7 - 1.2mm$. Graph 6.7 is for a needle spacing of $1.2mm$, graph 6.8 is for $s = 1.8$, and graph 6.9 for $s = 2.3$. Graph 6.10 shows collected current against needle voltage for various values of needle spacing, and an orifice diameter of $1.2mm$.

These graphs show that collected current increases with voltage, all following a similarly shaped curve. Generally collected current is increasing with orifice diameter, and decreasing with needle spacing. Predictably, it can be seen from graphs 6.7 to 6.9, that the corona discharge begins at approximately the same voltage regardless of plate size, as the pressure of the gas near the needle tip is constant at atmospheric pressure for all orifice sizes, which was not the case in the HP experiments. The voltage at which arcing occurs does vary but with no apparent correlation to any of the variables considered. Graph 6.10 shows that generally as needle spacing increases, the voltage at which initial corona readings are obtained, and at which arcing occurs, both increase. Although the $s = 1.8mm$ curve does start its corona readings at a higher voltage than the $s = 2.3mm$ curve. This could be due to the fact that the $s = 2.3mm$ needle is

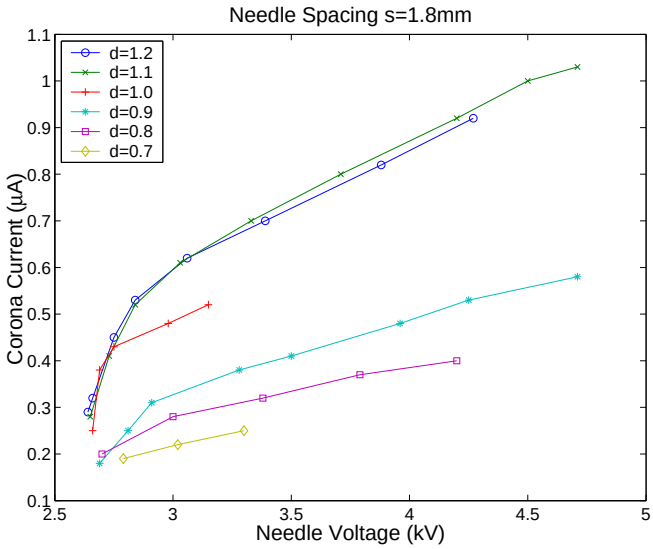

Figure 6.8: Raw data plot of I against V for various values of d at $s = 1.8$

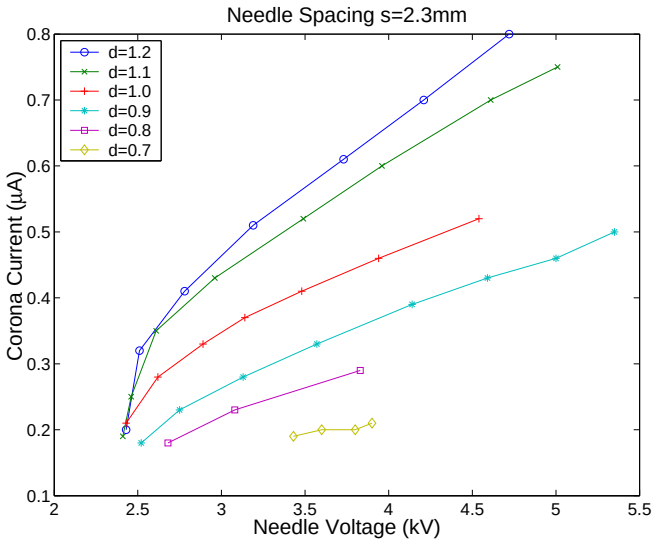

Figure 6.9: Raw data plot of I against V for various values of d at $s = 2.3$

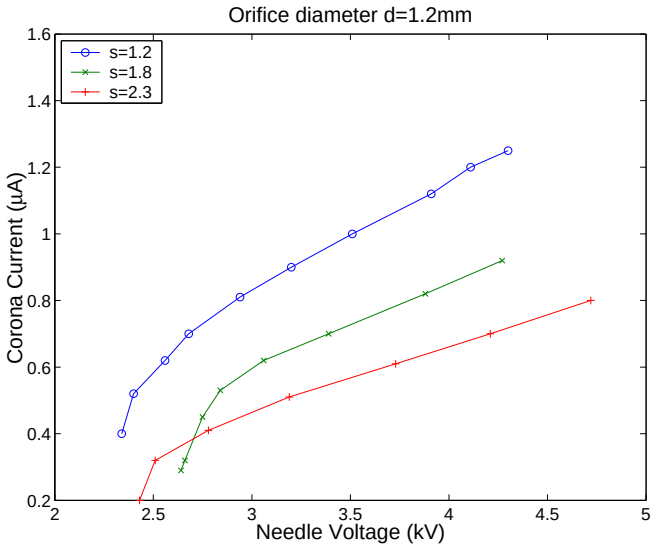

Figure 6.10: Raw data plot of I against V for various values of s at $d = 1.2$

marginally blunter than the others.

An important fact to note from these graphs is that the curves for orifice diameters of $1.1mm$, and $1.2mm$ follow almost exactly the same path, particularly for $s = 1.2mm$, and $s = 1.8mm$.

Repeatability

In order to ascertain the repeatability of these experiments they were repeated on different days. Two typical examples of the experimental repeatability are shown below in graph 6.11.

These two graphs show the agreement between points to be satisfactory, and also the voltages where the corona starts are in close agreement. The one obvious discrepancy however is in the voltage at which arcing occurs. It was typical to find that this would vary from day to day and indeed from test to test on the same day. It is probable that other factors effect the voltage at which arcing occurs, such as atmospheric conditions such as humidity [Kebarle et al, 1967]. Thus it is advisable when choosing a permanent operating condition for the ioniser, to select a voltage that is well below the measured arcing voltage to avoid any chance of arcing occurring. Arcing is considered undesirable, as although ions are produced while the electrodes are arcing the ion production fluctuates wildly and is unpredictable. Also arcing causes rapid erosion to the electrodes, and generates particles.

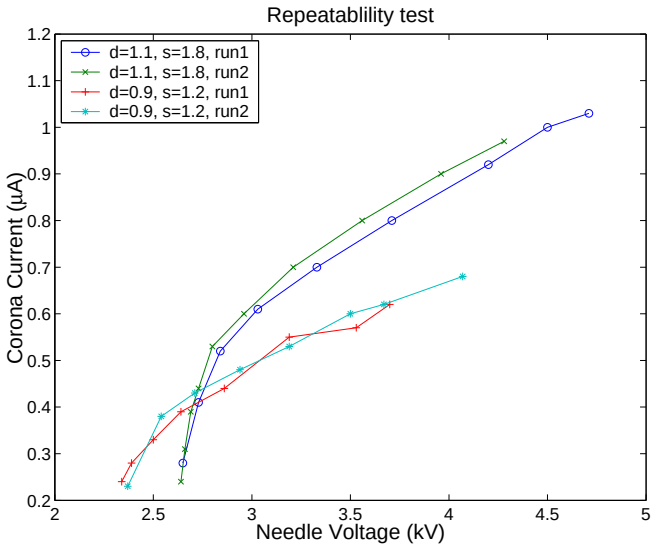

Figure 6.11: Graph showing the repeatability of raw data for two experiments

Analysed Results

Changing the diameter of the orifice in the ioniser also causes several other factors to change; primarily the flow rate of the ionised gas and the velocity of the gas through the orifice. In addition as mentioned above there will also be a slight change in the electric field as the geometry of one of the electrodes has changed.

It is expected that under any operating condition a percentage of the ions produced at the needle tip will be drawn through the orifice by the flow conditions, and a percentage will precipitate on the orifice plate as the ions are attracted to the plate by electrostatic forces.

If the collected current is plotted against plate diameter for a fixed voltage (fig 6.12), a relationship of increasing current with diameter, that appears to be suddenly cut off, can be observed. This corresponds to the earlier observation on graphs 6.7 and 6.8 where we saw the lines for orifice diameters 1.1, and 1.2mm following the same path. It appears as if 100% of the ions are passing through the orifice, however when the results for efficiency are examined it is noted that efficiency at this point is $\approx 20\%$ suggesting that this is not the case.

The same data is plotted against orifice velocity in fig 6.12 and again the same cut off can be seen. In this case the current is decreasing with orifice velocity. This is the opposite effect to that expected, as a higher velocity enables *more* ions to pass through the orifice. In fact this is still the case, it is simply that the flow rate and the orifice

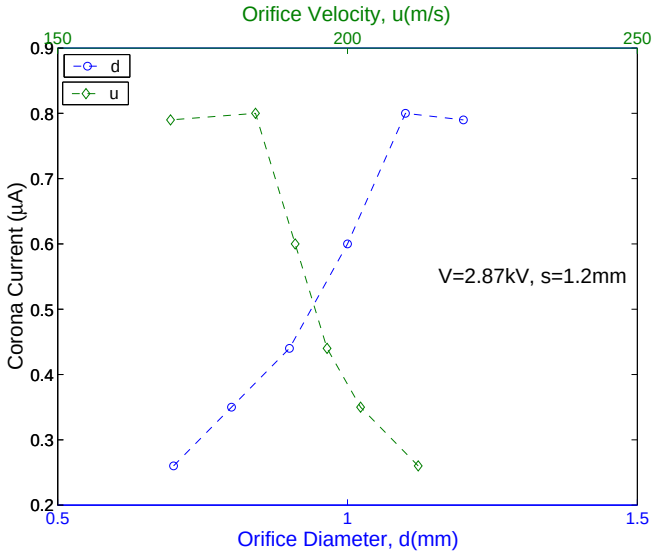

Figure 6.12: Corona current vs orifice velocity and orifice diameter

diameter are increasing at the same time, and these are the dominant variables.

Tests were carried out to determine whether the flow rate can be taken as the single flow variable against which the ion output varies when the orifice diameter is changed. An experiment was performed whereby the flow rate was adjusted using a needle valve restricting the flow out of the low-pressure ion collection chamber, and the orifice size was kept constant. Some results from this are shown in graph 6.13. Here it can be seen that, as the flow rate was reduced the collected current drops off extremely steeply. Flow rate can also be plotted against corona current using the same data seen in fig 6.12, where the orifice diameter was varied; the results of this are shown in fig 6.14.

The behaviour of the corona current variation is significantly different between these two methods of adjusting the flow rate, suggesting that some other variable instrumental in determining ion production is changed when the orifice diameter is changed. Also, the flow rate plotted in fig 6.14 shows the same cut off seen in fig 6.12.

In order to understand the how the variables affect the ion production of the ioniser we must consider the mechanisms within the ioniser. An ion generated at the needle tip is subject to two forces, flow forces and electric field forces. The electric field forces attract the ions to the orifice plate and flow forces act to push the ion through the orifice. For a given electric field, the number of ions that pass through the orifice is determined by the flow forces, and these flow forces are dependent on the orifice velocity, and the size of the orifice. A single dimension (the diameter) describes this size for a circular orifice, where as flow rate is the product of velocity and area. If corona current

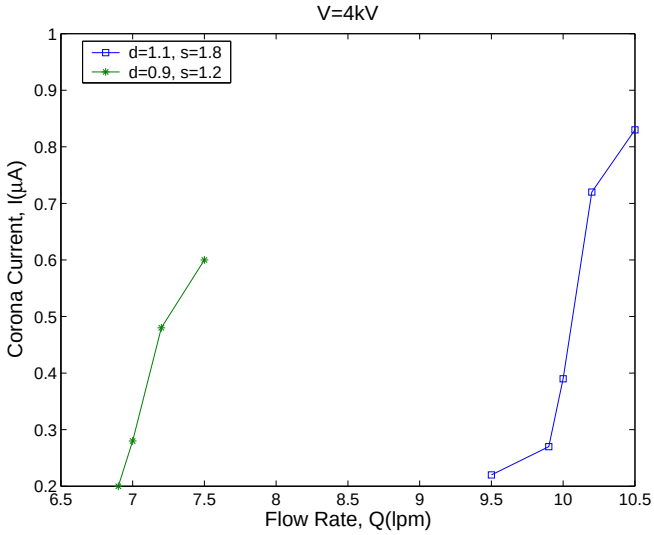

Figure 6.13: Corona current vs flow rate with fixed values of d and s

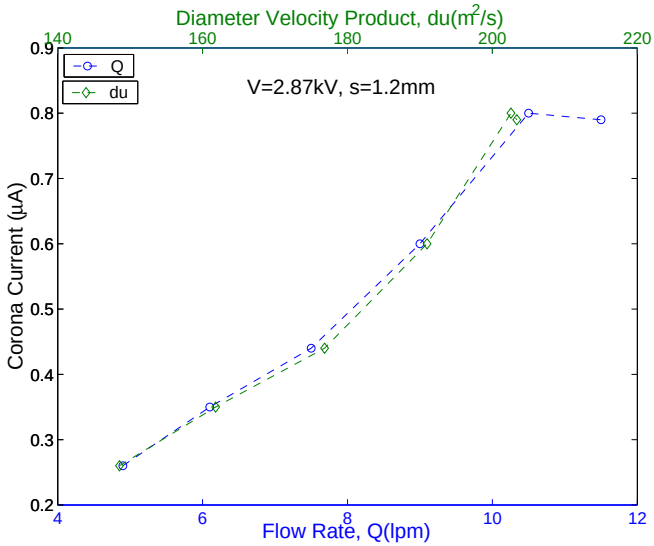

Figure 6.14: Corona current vs flow rate and diameter velocity product

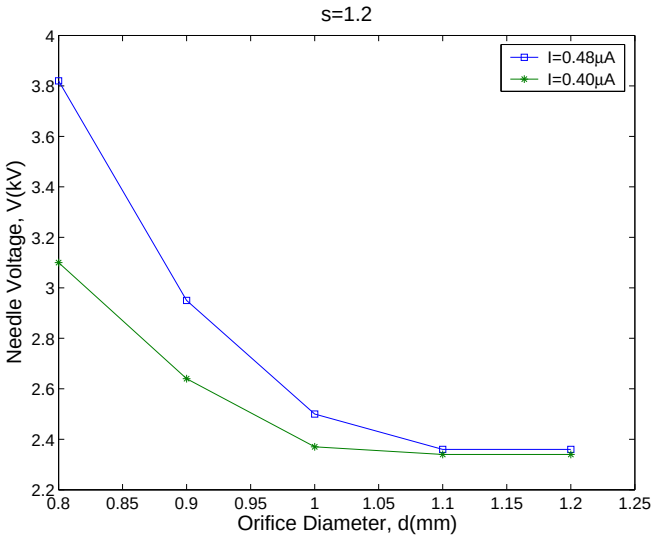

Figure 6.15: Needle voltage vs diameter for constant corona currents

is plotted against the product of orifice diameter and velocity (graph 6.14), then the two points with almost identical corona currents are seen to have almost exactly the same diameter-velocity product and the data follows a constant curve.

The same effect can be seen in graphs 6.15 and 6.16 where two curves showing the voltage required to achieve a fixed current, are plotted against orifice diameter and then again against diameter velocity product.

Characterising the Variables Affecting Efficiency

It has been demonstrated that many factors can affect the actual production of ions from the needle tip including voltage, pressure, and needle sharpness. Many other possible factors can also be implicated, such as electrode material and the humidity of the air. Some of these variables are difficult to quantify. However, by choosing to look at the efficiency of the ion production, only the variables that affect whether or not the ions produced at the needle tip pass through the orifice need to be considered.

Whether or not an ion will pass through the orifice is dependant on the flow forces on the ion, and the electrical forces on the ion. Evidence that the determining variables for the flow forces are the orifice velocity and the orifice diameter has already been presented. The velocity of the ion due to the electrostatic forces on it is dependant on the mobility of the ions Z (m^2/Vs), and the electric field strength E (V/m). The variables in this experiment that affect the electric field strength are the voltage on the needle, and also the spacing between the electrodes. To summarise, the main variables

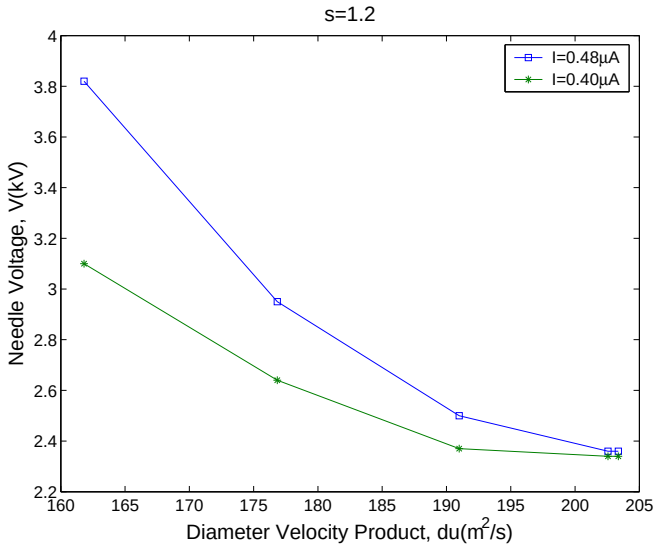

Figure 6.16: Needle voltage vs diameter velocity product for constant corona currents

available to characterise the efficiency are:

- The voltage on the needle V
- The Electrical mobility of the ions Z
- The distance of the needle from the orifice s
- The diameter of the orifice d
- The velocity of the air through the orifice u

Dimensional analysis shows that V,Z,d, and u can be combined to make the following dimensionless group.

$$\frac{VZ}{du} \tag{6.2}$$

Graph 6.17 shows efficiency curves for various operating conditions in the LP mode, plotted against needle voltage. If the same data is plotted against $\frac{VZ}{du}$ (fig 6.18) then the data collapses onto a single curve. Of the four sets of data on the original graph two were at needle spacing 1.2mm and two were at 2.3mm. In this case all the graphs have collapsed onto roughly the same line as the change in efficiency caused by the change in electrode spacing is negligible in this instance. From this result it can be concluded that for constant, or negligible difference in, needle spacing the efficiency of the ioniser

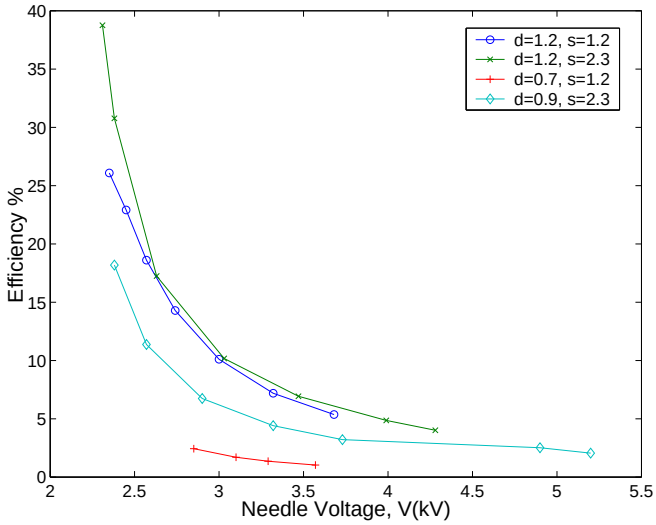

Figure 6.17: Efficiency plots for various experiments

is a function the dimensionless group $\frac{VZ}{du}$. This non-dimensional representation of the charger performance appears useful and does not seem to have been reported previously.

The efficiency graph in figure 6.17 shows a relationship of decreasing efficiency with increasing needle voltage. Conversely the graph measuring raw ion output (figs 6.7 to 6.7) showed that ion output increases with increasing voltage. So despite the reducing efficiency, the ion production at the needle tip is increasing so much that amount of ions in the jet still increases. Therefore, the ideal operating conditions of the ioniser are not necessarily the operating conditions with the highest efficiency.

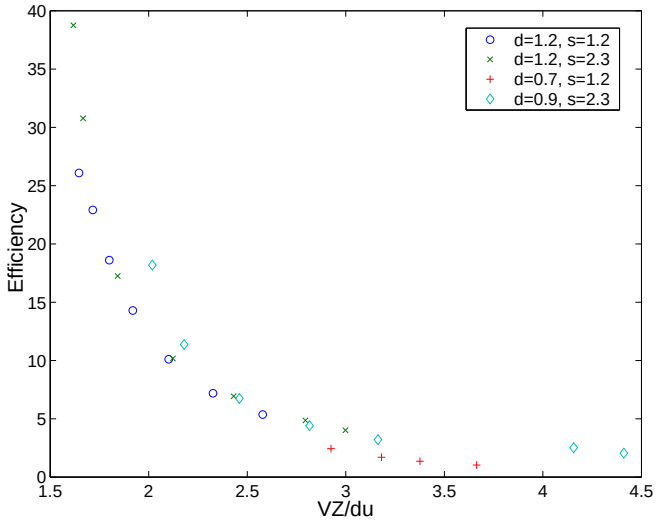

Figure 6.18: Efficiency data from fig 6.17, plotted against $\frac{VZ}{du}$

6.3 Predicting the charge distribution

In a practical embodiment of the Sonic Jet Charger ions are delivered in a high speed turbulent jet into a chamber where they meet a flow containing the aerosol sample. The earthed orifice plate of the ioniser would shield the chamber from the electric field from the needle so the charging process in the chamber can be described as diffusion charging.

In chapter 5 the development of a diffusion charging model was described. The model from chapter 5 assumes that the particles spend a constant amount of time in the presence of ions in the charger. This assumption is reasonable for corona wire charger designs with a laminar flow charging zone. In the case of a sonic jet charger the flow in the charging zone is turbulent and consequently the particle's residence times are distributed.

This section describes how the diffusion charging model was adapted to take into account charging in a turbulent mixing chamber. Modelled results for the charge distribution on aerosols for both corona wire charging and sonic jet charging are presented and compared.

6.3.1 Residence Time Distribution

For continuous flow of fluid through a mixing chamber not all particles in the fluid have the same residence time within that chamber. It is expected that measured values of

residence time would generate a curve like that shown in fig 6.19 where the represented function $f(t)$ is the density function, which can be thought of a probability per unit time. Thus, $\int f(t)\,dt$ is the probability that the residence time falls within the interval between the limits t and $t + dt$.

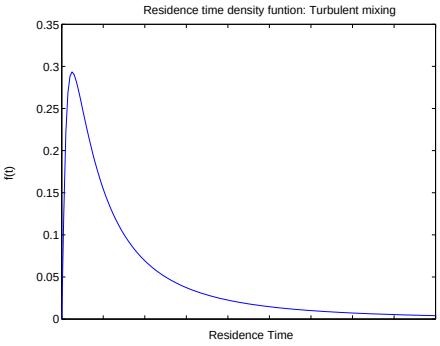

Figure 6.19: Residence time density function for turbulent mixing

If the flow in the mixing chamber is highly turbulent then the mixing may be assumed perfect. This makes the assumption that a parcel of fluid entering the mixing chamber is instantaneously spread evenly through the chamber. This is sometimes referred to as a "well-stirred reactor" The density function for a well-stirred reactor is defined in equation 6.3 [Nauman & Buffam, 1983].

$$f(t) = \left(\frac{1}{\bar{t}}\right) \exp\left(\frac{-t}{\bar{t}}\right) \tag{6.3}$$

where $\bar{t}$ is the mean residence time defined as:

$$\bar{t} = \frac{V}{Q} \tag{6.4}$$

where V is the volume of the mixing chamber and Q is the volume flow rate through the chamber.

The shape of the distribution function for perfect mixing is as shown in fig 6.20. The probability that the residence time will be found between two limiting values of t is of the integral of the density function between those limits, and as such integrating the function between 0 and ∞ gives a value of 1.

$$P_t = \int_0^\infty f(t)\,dt = 1 \tag{6.5}$$

6.3.2 Modifying the Charger Model

The charger model, described in detail in chapter 5, uses the "birth and death" model [Boisdron & Brock, 1970] to simulate the accretion of charge with time. The birth and

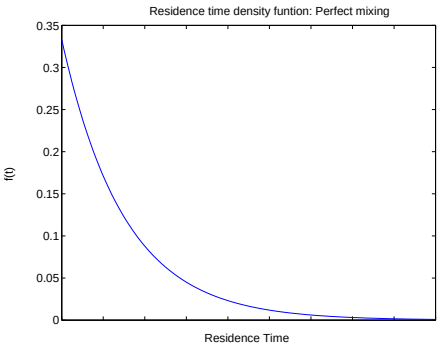

Figure 6.20: Residence time density function for perfect mixing

death model is described by an infinite set of simultaneous differential equations (eqn 6.6).

$$\begin{aligned} \frac{dn_0}{dt} &= -\alpha_0 n_0 \\ \frac{dn_1}{dt} &= \alpha_0 n_0 - \alpha_1 n_1 \\ &\vdots \\ \frac{dn_i}{dt} &= \alpha_{i-1} n_{i-1} - \alpha_i n_i \end{aligned} \tag{6.6}$$

These equations can be solved using simultaneous Laplace transforms to give expressions for $n_o\, n_1 \cdots n_i$ when the residence time has a constant value t (eqn 6.7).

$$\begin{aligned} n_0 &= exp(-\alpha_0 t) \\ n_1 &= \left(\frac{\alpha_0}{\alpha_1 - \alpha_0}\right) exp(-\alpha_0 t) + \left(\frac{\alpha_0}{\alpha_0 - \alpha_1}\right) exp(-\alpha_1 t) \\ &= \beta_0 exp(-\alpha_0 t) + \beta_1 exp(-\alpha_1 t) \\ n_2 &= \left(\frac{\beta_0 \alpha_1}{\alpha_2 - \alpha_0}\right) exp(-\alpha_0 t) + \left(\frac{\beta_1 \alpha_1}{\alpha_2 - \alpha_1}\right) exp(-\alpha_1 t) \\ &\quad + \left(\frac{\alpha_1 \alpha_0}{(\alpha_0 - \alpha_2)(\alpha_1 - \alpha_2)}\right) exp(-\alpha_2 t) \\ &= \gamma_0 exp(-\alpha_0 t) + \gamma_1 exp(-\alpha_1 t) + \gamma_2 exp(-\alpha_2 t) \end{aligned} \tag{6.7}$$

In order to calculate the charge distribution when the residence time is distributed the equations for n_i must be multiplied by the residence time density function, and integrated between the limits of possible residence times $(0 - \infty)$. An example of the integration for n_0 is shown in equation 6.8

$$P_{n_0} = \int_0^\infty n_0 f(t)\, dt = \int_0^\infty \frac{\exp(-\alpha_0 t)}{\bar{t}} \exp\left(\frac{-t}{\bar{t}}\right) dt \tag{6.8}$$

$$= \frac{1}{(\bar{t}\alpha_0 + 1)}$$

Below are the first few expressions for P_{n_i}, that is the fraction of particles with charge i when charged by diffusion charging in a perfectly mixed volume with mean residence time $\bar{t}$.

$$\begin{aligned} P_{n_0} &= \frac{1}{(\bar{t}\alpha_0 + 1)} \\ P_{n_1} &= \frac{\beta_0}{(\bar{t}\alpha_0 + 1)} + \frac{\beta_1}{(\bar{t}\alpha_1 + 1)} \\ P_{n_2} &= \frac{\gamma_0}{(\bar{t}\alpha_0 + 1)} + \frac{\gamma_1}{(\bar{t}\alpha_1 + 1)} + \frac{\gamma_2}{(\bar{t}\alpha_2 + 1)} \end{aligned} \tag{6.9}$$

The charger model was modified so that equations 6.9 were used instead of equations 6.7 to calculate the charge distributions for a give ion concentration N_i and the mean residence time $\bar{t}$ in the mixing chamber. Larger expansions of equations 6.7 and 6.9 can be found in appendix C.

6.3.3 Comparison Between the CWC and SJC Models

Two charger models have been designed; the first, for a Corona Wire Charger (CWC), which assumes a constant residence time in the charging zone, the second, for a Sonic Jet Charger (SJC), which assumes perfect mixing in the charging zone.

Figure 6.21 shows charge distributions predicted with the CWC model at an $N_i t$ of 1×10^{13} (ions $\cdot\, s/m^3$). This is a reasonable assumption for $N_i t$ in a corona wire charger [Pui, 1976, Biskos et al, 2005]. The charge distributions for several particle sizes are plotted against electrical mobility, with the area of the spots representing the fraction of particles with that size-charge combination. The fraction of particles with no elementary charge is not shown.

This graph (6.21) shows that particles with diameters of 5, 8 and 13nm are only singly charged, the area of the spot for 5nm shows that the majority of these particles are uncharged. Multiple charging is seen above 20nm, and at 300nm the charge distribution covers several charge levels, but the mobility range covered is not wide.

In the SJC model an N_i of 2×10^{13} ions$/m^3$ and a $\bar{t}$ of 0.5 s is comparable to an $N_i t$ of 1×10^{13}. Figure 6.22 shows the charge distributions predicted by the SJC model for these settings. Below 30nm the charge distributions look very similar to those seen in figure 6.21. For larger particle diameters the effect of the distributed residence time can be seen in the charge distributions, which are much broader and cover a wide range of mobilities. This would be damaging to the resolution of a differential mobility

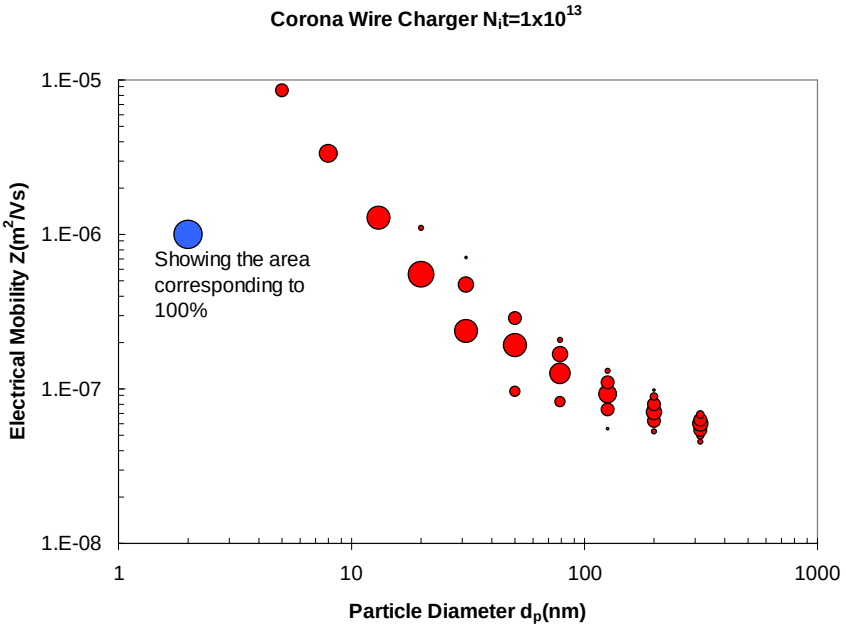

Figure 6.21: Charge distribution and mobility against particle size for a CWC ($N_i t = 1 \times 10^{13}$)

instrument, it can be seen that the main group of $300nm$ particles has the same mobility as singly charged $50nm$ particles.

The real benefit of the Sonic Jet Charging method is the high ion concentrations achievable. Experiments with the Sonic Jet Ioniser have shown that ion concentrations of $N_i = 1 \times 10^{14}$ ions$/m^3$ and higher are achievable. Figure 6.23 shows charge distributions predicted by the SJC model for an N_i of 1×10^{14}. This shows that for small particles $(5 - 13nm)$ the fraction of charged particles is much higher. For the larger particles the charge distributions are still much broader than those produced using the CWC model. Also these particles are more highly charged, this is damaging to resolution, and this effect becomes more severe as N_i is increased further.

6.3.4 Conclusions

Experimental data on the ion production of a Sonic Jet Ioniser has been used in the development of a theoretical model for a Sonic Jet Charger. This model has been compared with a theoretical model for a Corona Wire Charger in order to test the feasibility of using one of these chargers in the Nanoparticle Spectrometer.

Results from the modelling have shown that the SJC can produce high ion levels

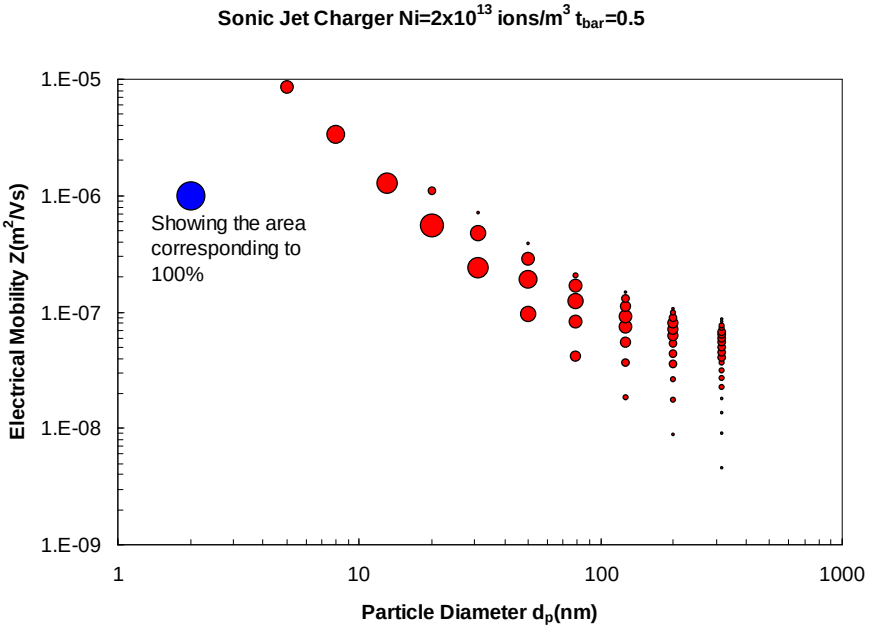

Figure 6.22: Charge distribution and mobility against particle size for a SJC ($N_i = 2 \times 10^{13}, \bar{t} = 0.5$)

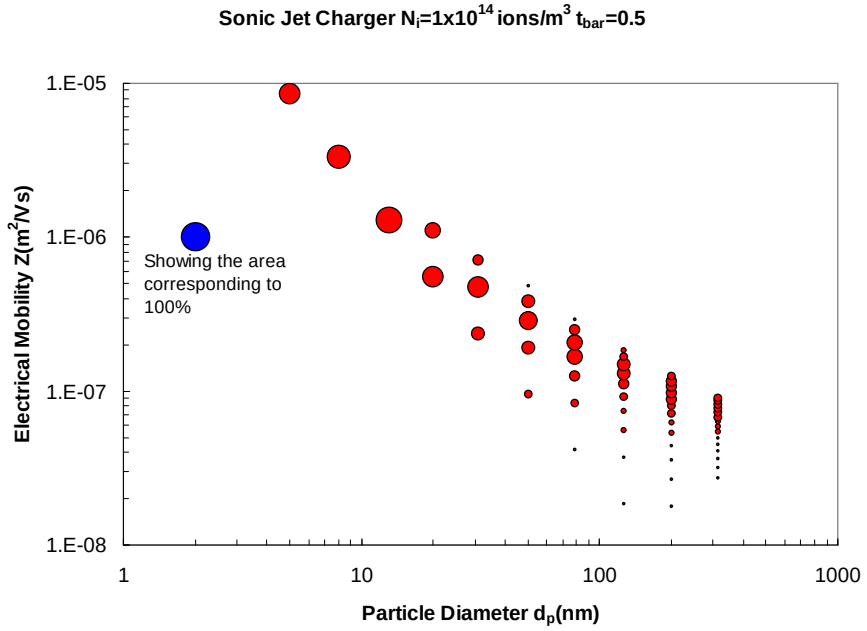

Figure 6.23: Charge distribution and mobility against particle size for a SJC ($N_i = 1 \times 10^{14}, \bar{t} = 0.5$)

and can charge high fractions small particles. However the charge distributions for large particles are much broader than those produced by the CWC. Thus the NPS would have greater resolution at these particle sizes if a CWC is used.

In conclusion, a SJC would be an excellent charger for charging sub $50nm$ particles, but for the broader size range for which the NPS is designed a Corona Wire Charger is more suitable.

Chapter 7

Design of a Prototype NPS

7.1 Introduction

This chapter provides design details of the first prototype Nanoparticle Spectrometer. Some of the dimensions for the NPS have already been decided through the classifier optimisation detailed in chapter 5. However, there are many other aspects of the design that require consideration. This chapter presents details of the most significant design issues, as well as explanations of how the solutions were reached.

The NPS prototype presented here is a one-off build that will require rigorous testing and much assembly and disassembly. Thus the design reflects this fact, and as such aspects of the design will not necessarily be ideal for a production instrument.

Figure 7.1 shows a cross-section through the centre of the prototype parallel to the gas flow and fig 7.2 shows a cross-section through the NPS prototype perpendicular to the gas flow at the point of the aerosol inlet to the classier. Figure 7.3 shows a three dimensional view of the prototype, several walls, and the casing for the filters are not shown enabling one to see inside. These three figures will be referred to throughout this chapter.

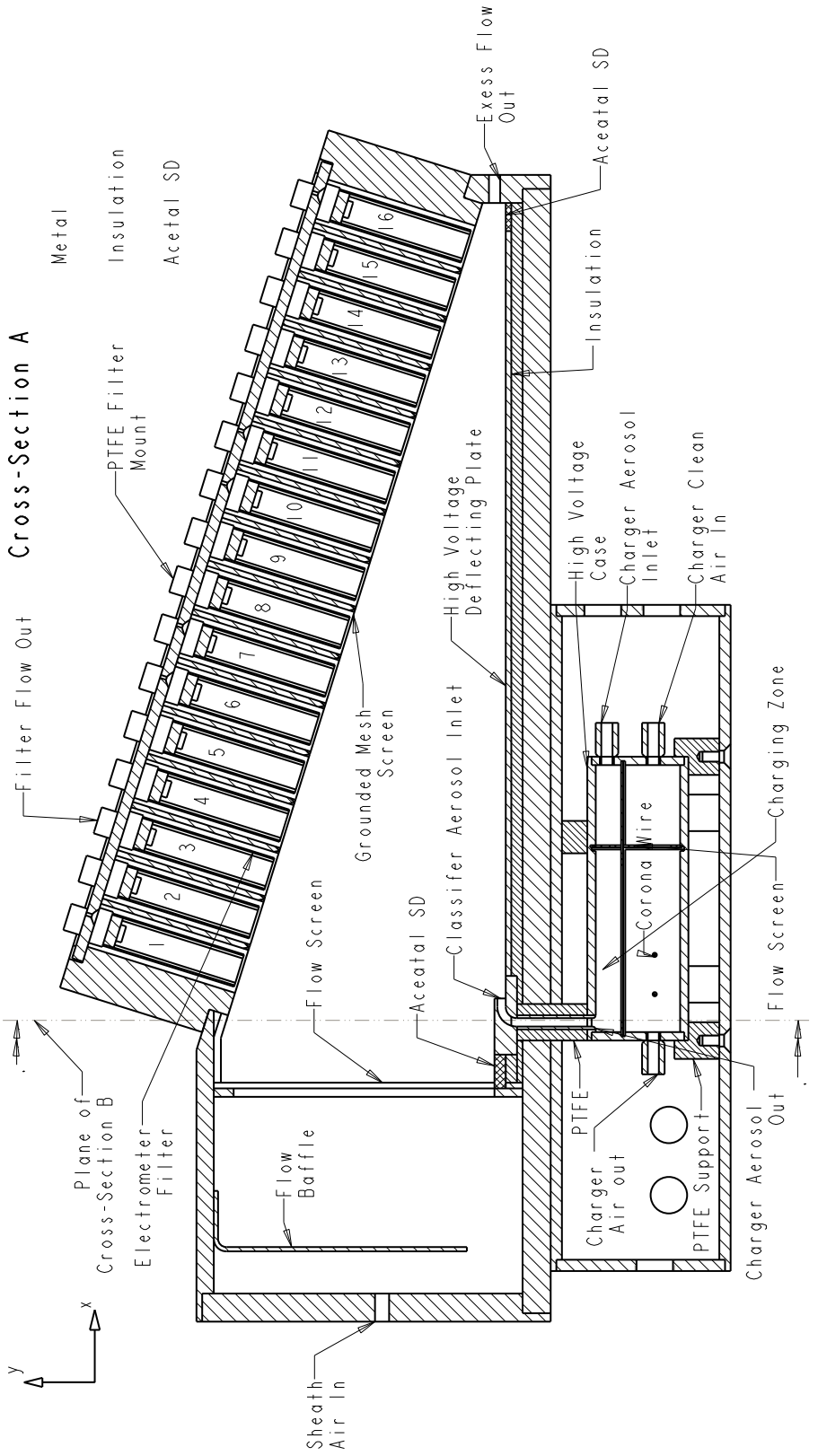

Figure 7.1: Cross Section **A** through the NPS

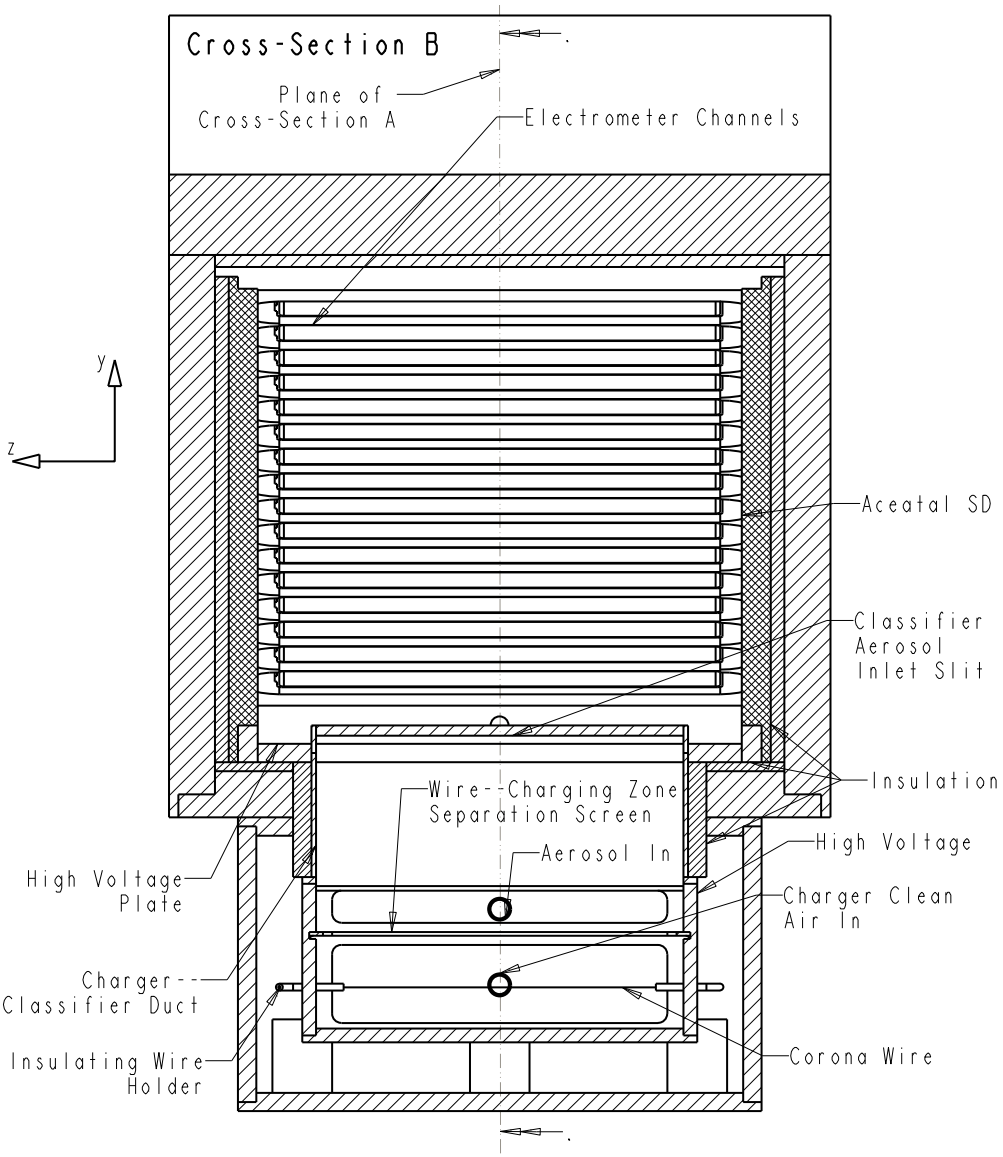

Figure 7.2: Cross Section **B** through the NPS

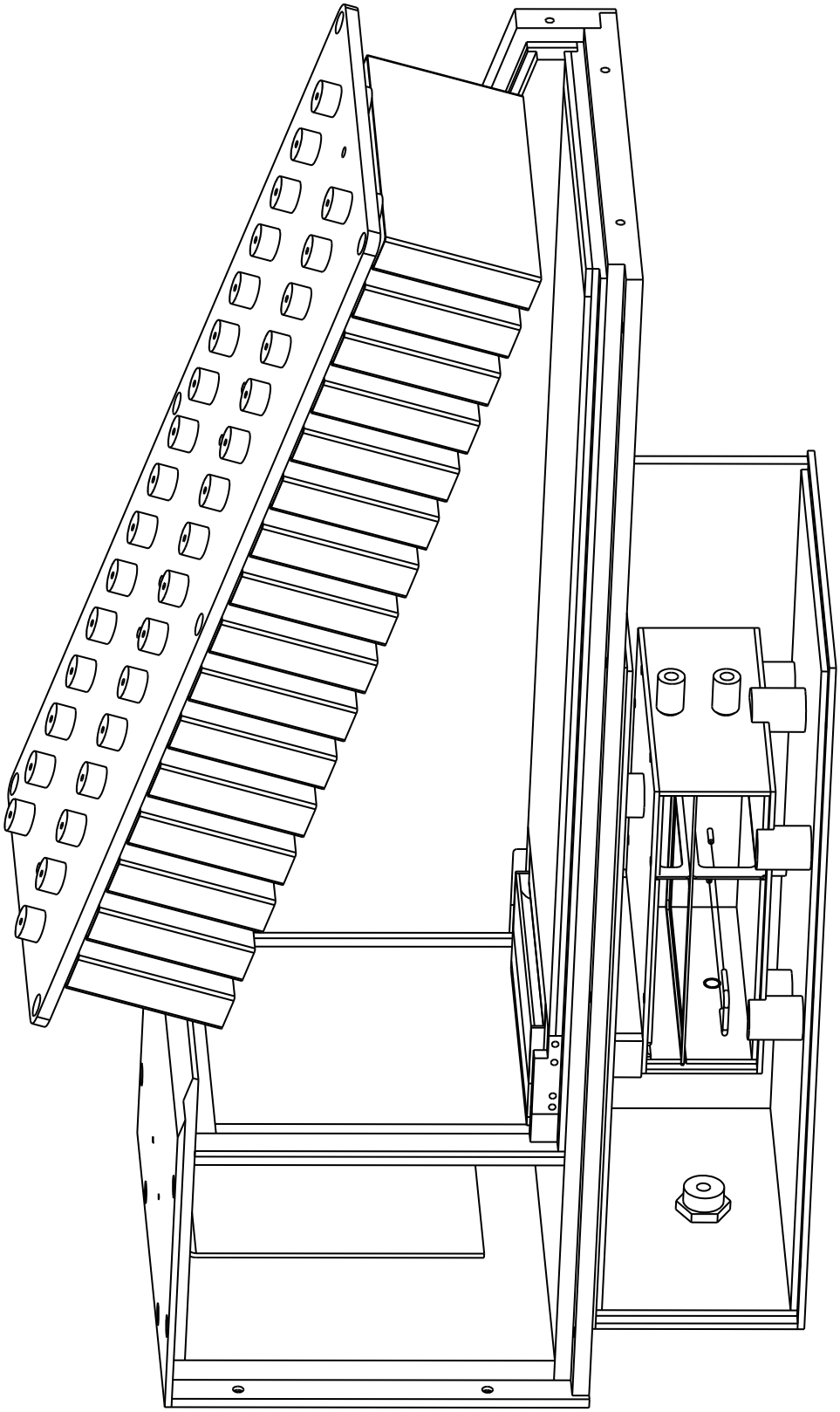

Figure 7.3: 3-D View of the NPS prototype with several walls hidden.

7.2 The Classifier

7.2.1 Side Walls

In Chapter 3 several other differential mobility instruments were described, all of which use a 2-D axis-symmetric column design. The NPS uses a flat two-dimensional design with side walls, the effects of which are not taken into account in the two-dimensional model. As a result the classifier must be designed in such a way that the effects of these walls on both the electric field, and the flow in the classifier will be minimised.

Electric Field Effects

The base of the classifying zone is a high voltage metal deflecting plate, and the upper surface is a grounded mesh. The electric potential in the classifier varies linearly between the base and the mesh. If the side walls are made of conductive material at a constant voltage, and forgetting the insulation issues this raises, they will severely distort the electric field in the classifier. However, most insulating materials can pick up static charge and when exposed to charged particles in the classifier, a standard insulator would over time build up a static charge that will also distort the electric field. Static dissipative acetal is a special plastic that is permanently anti-static. When sandwiched between two conductors at different voltages the surface potential of the acetal will vary linearly between the two conductors. This makes it an ideal material for the application of the classifier side walls.

The acetal-SD side walls are in contact with the high voltage deflector plate at the base and with the grounded mesh on the upper surface. To ensure that the surface potential of the acetal varies linearly between these two surfaces a second wall of standard insulating plastic is placed between the acetal and the metal outer wall of the classifier. This construction can be seen clearly in figure 7.2.

Flow Effects

The flow in the classifier is laminar, and the velocity profile will be like that shown in figure 7.4. Friction between the walls and the gas will create a laminar boundary layer near the walls which will grow in the z-direction Any particles in this boundary layer region will have a slower velocity than that predicted by the model.

To avoid this situation the particle inlet slit does not cover the entire width of the classifier, thus the particles do not flow close to the walls (fig 7.4).

The velocity profile shown in Fig 7.4 will not be constant in the x-direction. The boundary layers will grow as the flow progresses through the classifier. The *Blasius*

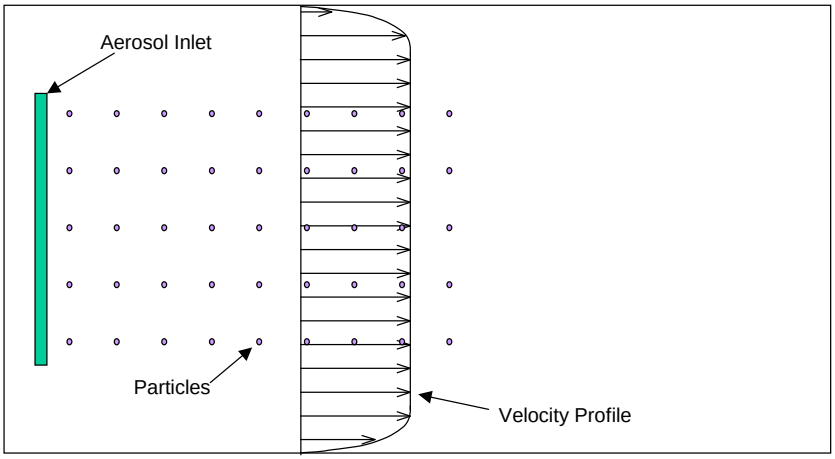

Figure 7.4: Sketch of classifier velocity profile as viewed from above

equation (eqn 7.1) can be used to estimate the thickness of a laminar boundary layer at a flat plate [White, 1999].

$$\delta_t \left(\frac{U}{\upsilon x} \right)^{1/2} \approx 5.0 \tag{7.1}$$

where δ_t is the thickness of the boundary layer where the velocity is 99% of the mainstream velocity and υ is the kinematic viscosity.

Using this equation it can be estimated that at at the end of the classifier the boundary layer will have grown to $10.4mm$ in thickness. The distance between the wall and the edge of the aerosol inlet is approximately $14mm$

There will also be a horizontal boundary layer of similar extent at the deflection plate in the base of the classifier, causing a variation in velocity in the y-direction. Particles will flow in this region, and there will be some effects due to the fact that some particles will spend longer in this region than others. Further investigation of this is needed but the effect will be seen as a broadening of the response, especially for low mobility particles, which spend longer near to the base

7.2.2 Classifier Gas Flow

It is very important that the flow in the classifying region is laminar and has uniform velocity. To this end there is a volume upstream where the entering flow first encounters a baffle, and then a flow screen made of an extremely fine nylon mesh. This is designed to produce a flow entering the classifier, which is uniform and laminar.

In the classifying region the uniform flow velocity is maintained by the carefully controlled gas flow being drawn through the electrometer filters. Drawing a small

amount of the flow out of the classifier at each filter means that a constant velocity can be maintained, despite the reducing cross-section of the classifier. The design velocity for the classifier is $0.1m/s$, which gives a Reynolds number in the classifier of $Re \approx 670$ taking the width of the classifier as the characteristic dimension. The method of flow control used for the filters is discussed in section 7.5. As discussed above, boundary layers will form on the walls and base, but only the latter is of concern, as the sample is introduced in the central portion of the classifier (see fig 7.4).

7.2.3 Screening and Construction

Interference from external electric fields can be a severe source of "noise" on the signals from the sensitive electrometers. To shield the instrument from these fields the outer case is made of aluminium, which is earthed. The aluminium case also provides the main structure of the classifier. It was anticipated that, as a prototype instrument, the NPS would require frequent assembly and disassembly throughout the testing process. To facilitate ease of disassembly and component replacement the internal components of the classifier are all designed to tessellate together in such a way that no internal fixings are required and all the components are held securely in place by the outer case when screwed together.

7.3 The Electrometers

7.3.1 Introduction

Following classification particles in the NPS flow through the mesh screen, and into the channels, which are 16 individual Faraday cages. Within these cages particles are caught on filters. The filter is housed in a metal case, which is electrically isolated from the cage walls. The filter case is connected to a sensitive electrometer, which measures the flow of charge onto the filter. Although aerosol electrometers of this type already exist [Lui et al, 1982, TSI, 2003], the NPS application presents the specific problem of packaging sixteen separate aerosol electrometers into the small space available.

Most aerosol electrometers consist of a "standard" fibrous filter within a metal case that is connected to an electrometer [Lui et al, 1982, TSI, 2003]. A "standard" fibrous filter is usually made of paper, and thus the fibres of these filters are not highly electrically conductive. This does not pose a problem to the detection of the particles as the presence of the charge within the metal case alone will induce a current [Bernigau & Vank, 1989]. However, as the caught particles do not instantly discharge on contact with the fibres, an electric field can build up within the filter. In this case the field would

exert a repelling force on particles trying to enter the filter. This effect is undesirable, so multiple inlet screens are required to contain the field; this could cause a problem when the available space for the filter is limited. If conductive fibres are used, inlet screens are not required, creating more space for filter material.

When filtering particles with a unipolar electrical charge it is possible to use the charge to improve filtration efficiency; there has been a lot of research in this area. An example of this is the use of a blocking electrode downstream of the filter with a voltage of the same polarity as that of the particles; the electrostatic force generated on the particles opposes the gas flow resulting in stronger curvatures of the particle trajectories and higher collection efficiencies [Pnuelil et al, 2000]. Another technique is to pre-treat the filter fibres with anionic surfactants thus giving them a small charge of opposite polarity to the particles, creating an attractive force between the fibres and the particles [Yang & Lee, 2004]. Unfortunately these techniques would be unsuitable for this application, as they would involve using an electric field inside the Farady cages, which would generate unwanted noise on the electrometer signals.

7.3.2 Electrometer Construction

The design of the filter case is shown in figure 7.5, it comprises of a thin walled metal case, which is open at the bottom and can be packed with fibrous filter material. Mounted in the top surface of the case are two PTFE mounts, which serve several purposes. Firstly, they hold the filter in place while keeping it electrically isolated from the rest of the cage. Secondly, both mounts have holes axially through the centre one hole is used to draw the gas flow through the filter, the second provides a route for the wire making the electrical contact with the electrometer circuit.

Figure 7.3 shows the battery of filters mounted in place on the lid for the Faraday cages. The cages surrounding this construction are hidden in fig 7.3, but can be seen separately in fig 7.6

7.3.3 Filter Material

The fibrous filtration theory described in section 2.5 was used to design a "Filtration Efficiency Calculator". This is a simple program used to calculate the theoretical filtration efficiency for the NPS filters given the fibre diameter and the mass and density of the filter material. Knowing the weight of the material and fibre diameter gives all the other parameters required to work out filtration efficiency such as total fibre length and packing density.

Figure 7.7 shows a graph for theoretical filtration efficiency, in which the efficiency

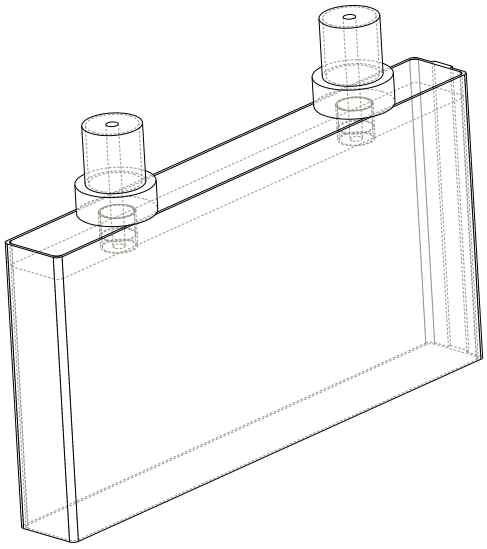

Figure 7.5: Electrometer filter part 3-D View

versus particle diameter plots for several fibre diameters are presented assuming $6g$ of steel wool in each filter as the filtration material.

Analysis of the calculations had shown that the dominant mechanism of collection is diffusion. This explains why efficiency is seen to decrease with particle size. There is a strong correlation between filter efficiency and fibre size, with smaller fibres having better efficiency.

The finest grade of steel wool available is '0000' grade. The steel fibres do not have a constant value of diameter but measurement showed that typical values were in the range of $5\mu m < d_f < 20\mu m$. The data presented in fig 7.7 would suggest that a '0000' grade steel wool filter would probably have some penetration, which would have to be measured and corrected for in subsequent calculations. The graph (7.7) shows greater penetration for larger particle sizes, this would suggest that the penetration would be most likely to occur in the later channels as this is where the larger particles are expected to land.

Despite the possibility of filter penetration it was decided to select '0000' grade steel wool as the initial filter material, as it fills the requirement of an electrically conductive fibrous material. Also the construction of the filter battery makes it very simple to remove and replace the filter material, therefore if steel wool were to be proved unsuitable during instrument testing it would be a simple task to replace it with a different material.

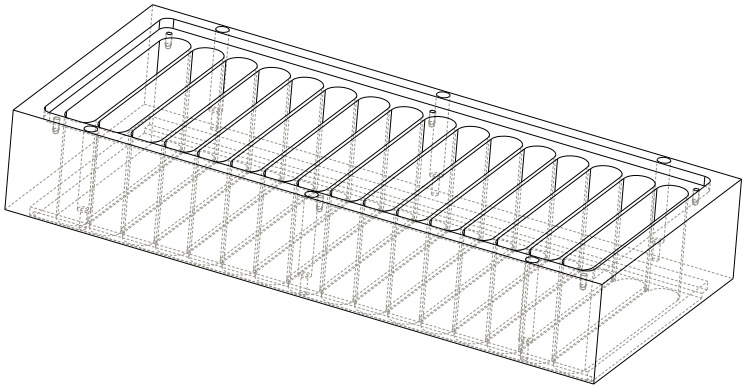

Figure 7.6: Faraday cages part 3-D View

7.3.4 The Electrometer Circuit

Figure 7.8 shows the circuit for the electrometers. The filter cases are electronically connected to the input. The current from the charged particles landing on the filter flows to the negative pin of the operational amplifier LMC6081. This amplifier is used because of its ultra low bias current and high voltage gain. The amplifier balances the voltage on the positive and negative terminals by sending a current from the output terminal and through the feedback loop to cancel out the current coming in to the negative terminal. The voltage on the output terminal will hence be related to the current on the input terminal and the feedback resistance by Ohm's law. The feedback resistor is extremely large so that the very small currents from the landing particles produce a measurable voltage at the output pin. For the $500\,G\Omega$ used the output was $0.5V$ per pA.

The resistor and capacitor on the input protects the op-amp from any surge that might occur, e.g. if there was a discharge between the high voltage deflecting plate and the filters. This resistor and capacitor combination does not constitute a low pass filter, as the output is a virtual earth.

7.4 The Charger

Following the investigation into the Sonic Jet Charger (chapter 6) it was decided that a corona wire charger with a laminar flow charging zone would be the best type of charger design for the NPS. Several designs of this type exist already [Pui, 1976, Biskos, 2004, Kruis & Fissan, 2001] and some are described in section 3.10. These chargers generally consist of a thin corona wire mounted axially within a mesh tube, with the aerosol

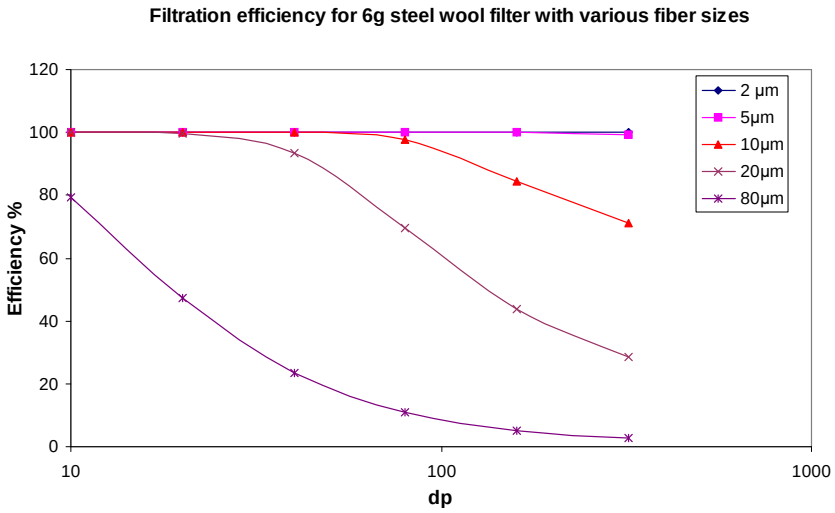

Figure 7.7: Graph showing predicted filter efficiencies for steel wool filter

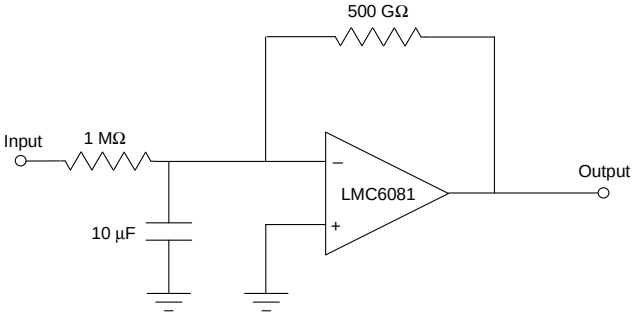

Figure 7.8: Schematic diagram of the electrometer circuit

flowing in an annular region surrounding the tube. This design is very well suited to axis-symmetric column differential mobility analysers. The charger design for the NPS is based on the same principles as these chargers but has a very different construction and layout to facilitate a good interface with the specific classifier design of the NPS.

A cross-section of the charger design is shown in figure 7.1. There are two flows through the charger: the aerosol flows through the upper level of the charger, and particle free sheath air flows through the lower level. Both flows enter the charger at the right hand side, where they pass into individual residence chambers, and then through flow screens to create uniform laminar flow. In the left hand side of the charger a mesh screen separates the upper and lower levels. There are two $16\mu m$ diameter Tungsten corona wires in the lower section, which are both at a voltage $3.5 - 6kV$ higher than the charger casing and thus cause a corona discharge. Streams of ions are generated,

which radiate out in all directions from the wires. Many of the ions travelling upward toward the screen will pass through into the upper level of the charger. The aerosol flowing through this upper level becomes charged by the ions that have crossed into this region. The screen shields the particles from the electric field generated by the corona wires, which can cause charged particles to precipitate. At the far left hand side of the charger the particles pass up into a duct that connects the charger to the classifier, this duct leads to the aerosol inlet slit and delivers the charged particles into the classifying zone. The width of the charger is equivalent to the width of the inlet slit.

7.4.1 Electrostatic Considerations

The use of dual corona wires in this charger allows more ions to be generated and creates a larger ion rich zone in the upper level of the charger. However, care must be taken in the placement of these wires; if the wires are placed too close together then the strong fields can cancel each other out and the corona current will be reduced. Fig 7.9 shows the electric field surrounding the corona wires at $4kV$ as modelled using the finite element package Femlab. The first plot shows the electric field for a single corona wire, the red region shows the strong electric field surrounding the wire. The second plot shows the fields for two corona wires just $5mm$ apart. In this plot it is possible to see how the field between the two wires is reduced and the red regions are slightly smaller. The final plot shows the field for two corona wires $14mm$ apart, here the fields around the individual wires are largely unaffected.

It has already been mentioned that the base of the classifier is at a high voltage ($5kV$) in order to create a deflecting field in the classifier. The charged aerosol must flow from the charger and through an inlet slit in this high voltage plate. If the voltage of the charger case is ground, then at some point in the duct between the charger and the classifier the voltage of the duct must change from $0V$ to $5kV$, creating an electric field in the duct that would retard the motion of the particles. This is an undesirable situation, so it was decided to apply a voltage of $5kV$ to the charger casing and the duct. This way particles are crossing into the high voltage zone on first entering the charger, i.e. before they have become charged. This decision has some ramifications for the charger design. Firstly, the corona wires have to be set at an extremely high voltage ($8.5-11kV$) in order to be at a voltage of $3.5-6kV$ above the casing, and hence provide a corona discharge. Secondly, the charger has to be mounted on electrically insulating supports within an outer earthed metal case. Also, the metal duct between the charger and the classifier must be encased in an insulating sheath.

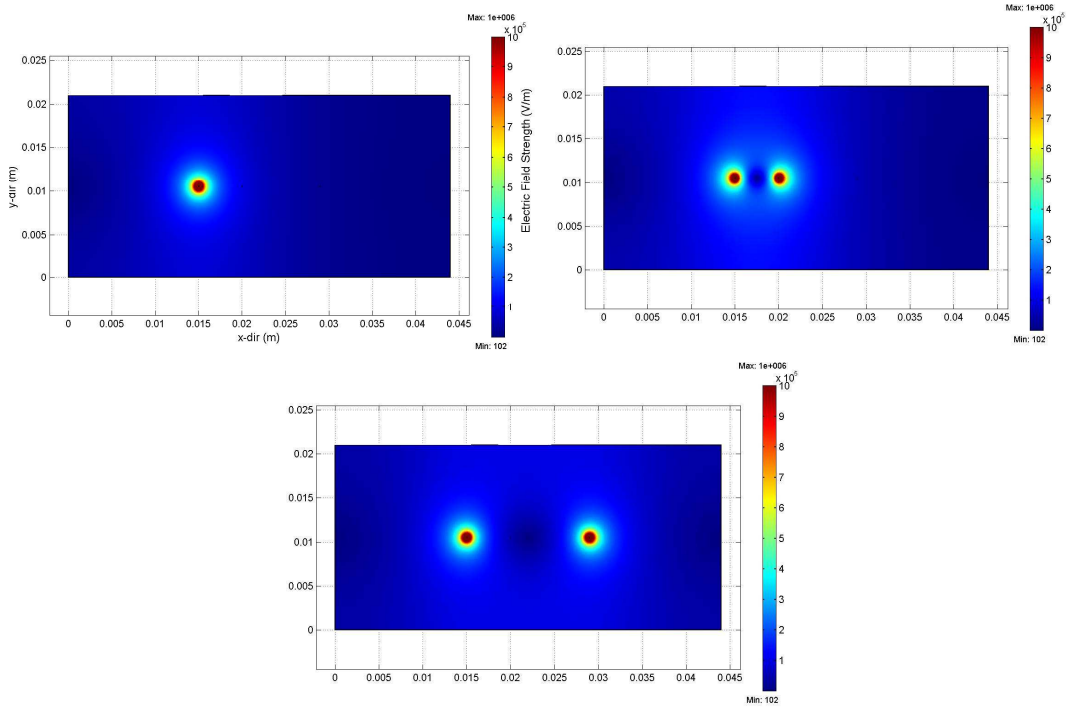

Figure 7.9: Electric field in the charger with different wire configuration's

7.5 Operational Set Up

This section describes how the instrument was set up for testing. This set up is not necessarily indicative of the ideal set up for a production instrument, but instead is designed to have the high flexibility required for experimental testing of the instrument.

7.5.1 Flow set up and control

Figure 7.10 shows the flows to and from the NPS. For this experimental set up the flow is fully controllable. In order to control the flow out of the channels capillary tubes are used, these limit the flow from each channel to $3.38 l/min$. A valve controls the excess flow out of classifier. The inlet sheath flow is controlled with a flow regulator; carefully controlling this flow allows the user to control the suction of aerosol flow into the classifier. The charger sheath flow is set to match the velocity of the aerosol flow in the charger so that there is no pressure gradient across the mesh screen separating the charger wires from the aerosol flow.

There is a flow meter permanently in the instrument sheath air inlet and several other flow meters can be connected to the individual channel out flows, the excess flow, the aerosol in flow and the charger sheath flow. These flow meters are used to periodi-

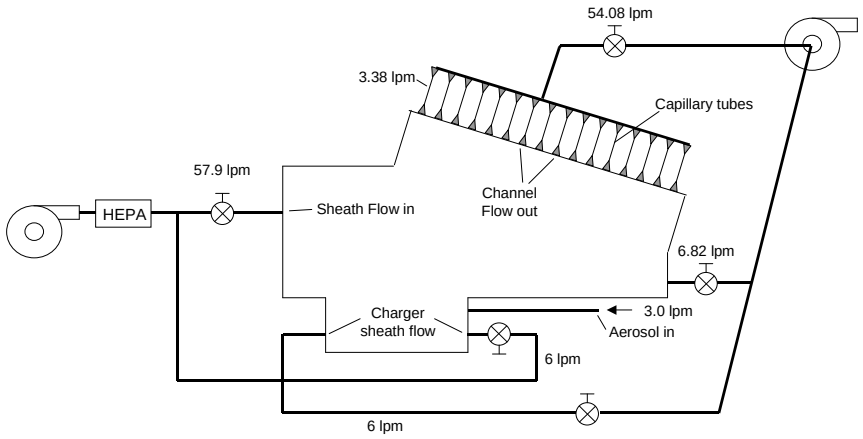

Figure 7.10: Schematic diagram showing the gas flow to and from the NPS

cally check the flow rates, but are not in place during experimentation. Measurements of the flow rates out of each channel show a total range of variation of $0.2l/min$ which is approximately 6% of the flow out of one channel.

7.5.2 Power supply and data acquisition

Power is supplied to the instrument by two HiTek PSM10 high voltage power supplies, one supplying the high voltage to the corona wire, and the other supplying the voltage to the charger case and deflecting plate. The power supplies are computer controlled by analogue signals from a National Instruments DAQ card. The same National Instruments card is used to read the 16 analogue voltages signals from the instrument's electrometers.

Using the National Instruments data acquisition and control software "LabView" an instrument control interface was designed. With this interface it is possible to set the corona wire, and deflecting plate voltages, and monitor the corona current. It is also possible to view real time current signals from the electrometers as well as being able log time averaged signals for post processing with the look-up table.

Power is supplied to the electrometers' operational amplifiers by a separate duel power supply with 5V on the positive rail and -10V on the negative rail.

7.5.3 Rated accuracy of 3rd party components of the NPS

The performance of the HiTek PSM 10 power supply as stated by the accompanying literature is as follows.

- Ripple on the voltage signal $< 1V$ peak to peak

- Voltage monitor accuracy $\pm 2\%$ or $100mV$, whichever is greater
- Current monitor accuracy $\pm 2\%$ or $100mV$, whichever is greater
- The above values are valid after a 1hr warm up period.

The distribution of offset voltages on the LMC6081 op-amps is approximately normal with 95% confidence between $\pm 0.48mv$. However, the instrument control interface is used to "zero" the electrometer signals before each test.

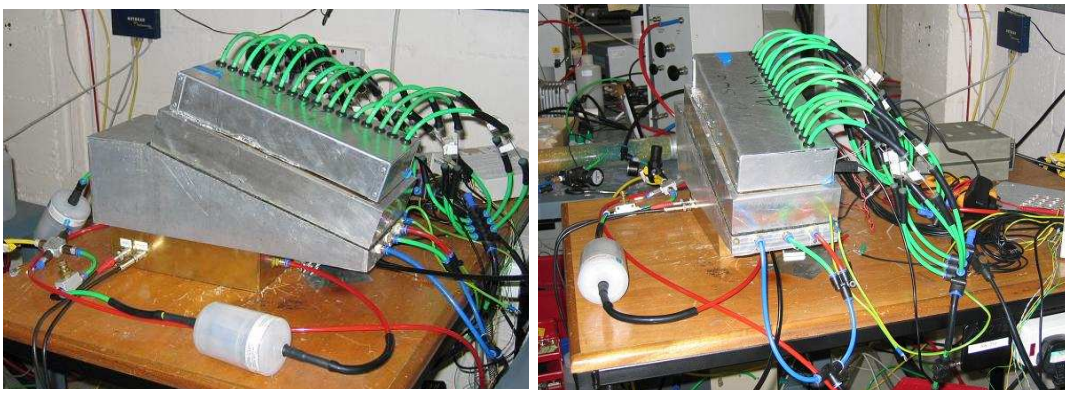

Figure 7.11: Pictures of the NPS prototype test rig

Chapter 8

The Charger: Testing and Results

8.1 Introduction

In this chapter the procedure, and results of tests carried out on the charger are examined. The purpose of these tests was to characterise the performance of the charger, compare it with the theoretical charging model, and select the optimum operating condition for the charger.

8.2 Aerosol Generation

In order to test the charger, and indeed the Nanoparticle Spectrometer as a whole it is necessary to be able to generate an aerosol sample containing particles of the desired size. A Collison nebuliser [May, 1973] was used to generate particles of salt ($NaCl$) or sulphuric acid (H_2SO_4). $NaCl$ aerosols generated with the Collison nebuliser generally have a broad lognormal distribution with a mean between $30 - 70nm$. This sample is useful for all-round testing. H_2SO_4 aerosols can have smaller mean sizes, around $10 - 20nm$ this makes them particularly useful if small particles are needed.

This section details the set up and apparatus for generating $NaCl$ and H_2SO_4 using the Collison nebuliser.

8.2.1 Salt Particles

A Saline solution is prepared using distilled water, and poured into the Collison nebuliser. Compressed air is supplied and a mist of fine saline droplets is generated. The droplets flow from the nebuliser into a volume, where any large droplets are removed by gravity (see fig 8.1). Following this the droplets are passed through a silica gel drier.

The dry atmosphere in the drier causes the droplets to rapidly shrink by evaporation until only the salt particles are left.

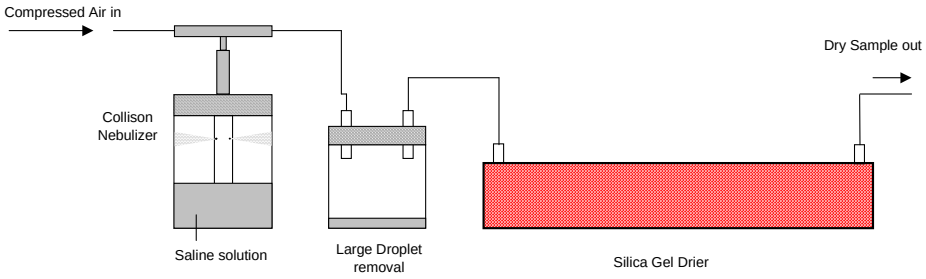

Figure 8.1: Schematic of set up for $NaCl$ aerosol generation

8.2.2 Sulphuric Acid Particles

Sulphuric acid particles are generated using the same procedure as that for salt, but with some extra stages to produce the smallest possible particles, and prepare the sample (see fig 8.2). Following the drier particle pass into a heated tube for evaporation. The sample is then cooled and passed into a further tube for re-nucleation. The sample is diluted with clean "particle free" air, and then aged in a residence tube. Finally the sample is diluted once more by bypass dilution, where a portion of the sample is removed, filtered, and returned to mix with the original sample.

8.3 Charger Initial Tests

It was decided that the best aerosol samples with which to test the charger should be as close as possible to monodisperse. It will be seen in the results presented later, that using a monodisperse sample produces results where the effects of multiple charging are distinguishable, and measurable.

8.3.1 Experimental set up

In order to generate a monodisperse aerosol, first an NaCl aerosol with a broad size distribution is produced using the technique described in section 8.2. The broad sample is then neutralised by exposure to a β radiation source (^{85}Kr), and passed into a Differential Mobility Analyser (DMA), as shown in fig 8.3. The DMA (described in

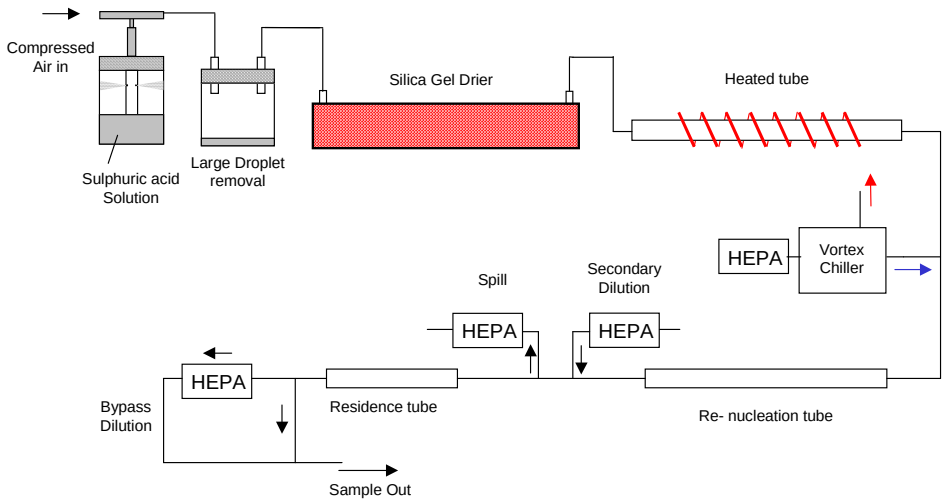

Figure 8.2: Schematic of set up for H_2SO_4 aerosol generation

detail in Chapter 3) selects a very narrow size distribution from the original broad distribution. The experimenter has a larger degree of control over the mean size of this monodisperse distribution, by varying the central rod voltage, and the flow rate in the DMA.

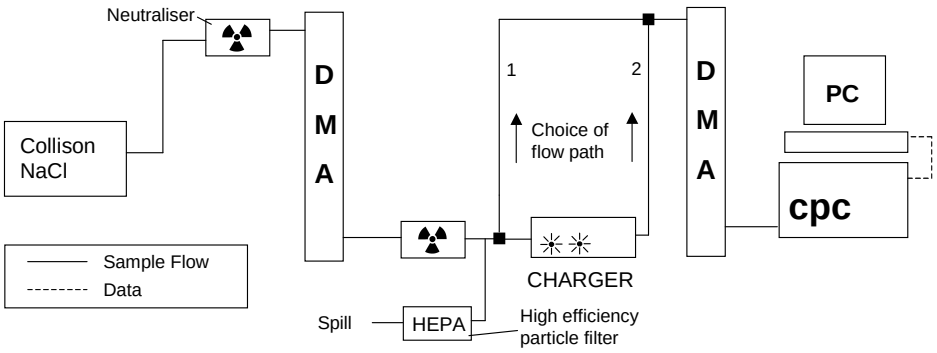

Figure 8.3: Schematic of experimental apparatus for initial charger tests

Downstream of the DMA the monodisperse sample is neutralised again; at this point the sample can be analysed by a Scanning Mobility Particle Sizer (TSI 3081) operating normally (flow path 1), or alternatively it can be passed into the charger, were it is subject to unipolar diffusion charging. The charged sample is then analysed using the SMPS. This is represented in the diagram in fig 8.3 as its component parts:

A DMA, a Condensation Particle Counter (CPC), and a computer. Unlike the normal operation of the SMPS, the sample is not neutralised before entering the DMA. Also the charge correction function on the SMPS is switched off, this means that the SMPS assumes that all the particles counted are singly charged. Knowing the relationship between size and mobility for singly charged particles means this data can be used to make a plot of particle number concentration against electrical mobility.

8.3.2 Experimental Procedure

The procedure for the experiments presented in this section was as follows. The DMA is adjusted to give us a monodisperse sample at the desired size. This sample is then Analysed using the SMPS, and the data stored (path 1 in fig 8.3) . Next the sample path is changed to path 2, the sample passes through the charger with the wire voltage set to 4kV. (The charger case is at ground.) This charged sample is analysed by the SMPS with charge correction disabled, and the data is stored. This is repeated for wire voltages of 5kV, and 6kV. Finally the whole process is repeated for several other monodisperse sample sizes.

8.3.3 Model Predicted Output

The charging model has been adapted to predict what the SMPS data output will be for a sample passing through the charger. The input for the model is the SMPS data for the sample when analysed directly. The data from the model can be plotted as number concentration versus electrical mobility, enabling us to make direct comparisons between predicted and measured data.

The comparison between modelled and predicted results, should be confined to a comparison of the relative shape of the plots, as the overall magnitude of the plots can be affected by factors such as differing rates of sample dilution between direct measurement, and measurement through the charger. The results have not been corrected for these differences, as comparison of relative shapes is all that is required to determine if the measured charge distribution agrees with that of the model.

8.3.4 Results

The results for three different monodisperse samples are presented here in figures 8.4, 8.5 and 8.6. Each set of graphs shows the following:

- The size distribution of the sample as measured by the SMPS.

- The predicted electrical mobility versus concentration plot for that sample with the model $N_i t$ product set to 1×10^{13}.

- The measured electrical mobility versus concentration plots for the charger operating at 4kV, 5kV, and 6kV.

8.3.5 Results Analysis

Sample 1 is a narrowly distributed aerosol sample with mean size $47nm$. The results for this sample are shown in fig 8.4. The graph of the predicted concentration verses mobility shows two peaks. The first peak is at $1.1 \times 10^{-7}\, m^2/Vs$ this is consistent with the mobility of a singly charged 47nm particle. The second peak is at $2.1 \times 10^{-7}\, m^2/Vs$, and *this* is consistent with the mobility of a doubly charged 47nm particle. Therefore in this, and all subsequent graphs, the peaks have been labelled with the number of elementary charges on the sample that they represent.

In the case of the experimental results it can be seen that each graph has two peaks in the same locations as that of the predicted results. However in all cases the doubly charged peak is larger relative to the singly charged peak. This could be seen as evidence that the true $N_i t$ is larger than the one selected due to a higher ion concentration in the charging zone. It can also be seen that the "doubly charged" peak for $6kV$ is larger than $5kV$, is larger than $4kV$. This is to be expected, as a higher voltage results in a higher corona current, which is likely to lead to a greater ion concentration in charging zone.

Sample 2's peak is at $72nm$, and the results for this sample are shown in fig 8.5. Here it can be seen that the predicted data shows mobility peaks for singly and doubly charged particles. The doubly charged peak is this time much larger than the singly charged peak. This is to be expected due to the larger mean size of sample 2. Observing the experimental results, a small peak for triply charged particles can be seen. This would support the idea that the $N_i t$ value used in the model is too low. However these graphs also show a large singly charged peak, not present in the predicted output graph. This suggests a *lower* $N_i t$ than the value used to create predicted output.

A similar effect can be observed for the third sample shown in fig 8.6. Here peaks for 2, and 3 charges can be seen as predicted, but also an unpredicted peak for singly charged particles.

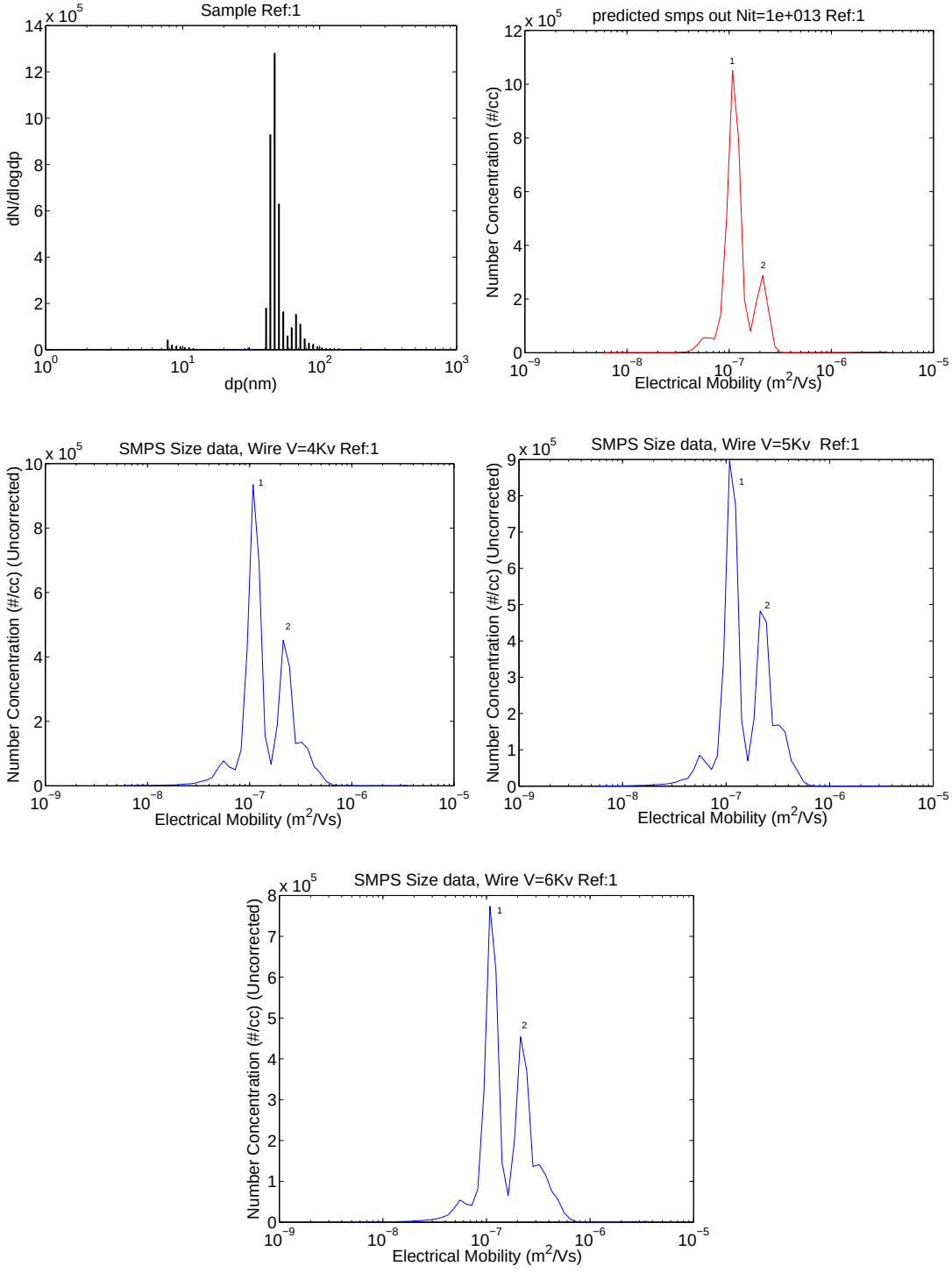

Figure 8.4: Sample, predicted result, and measured results for sample 1

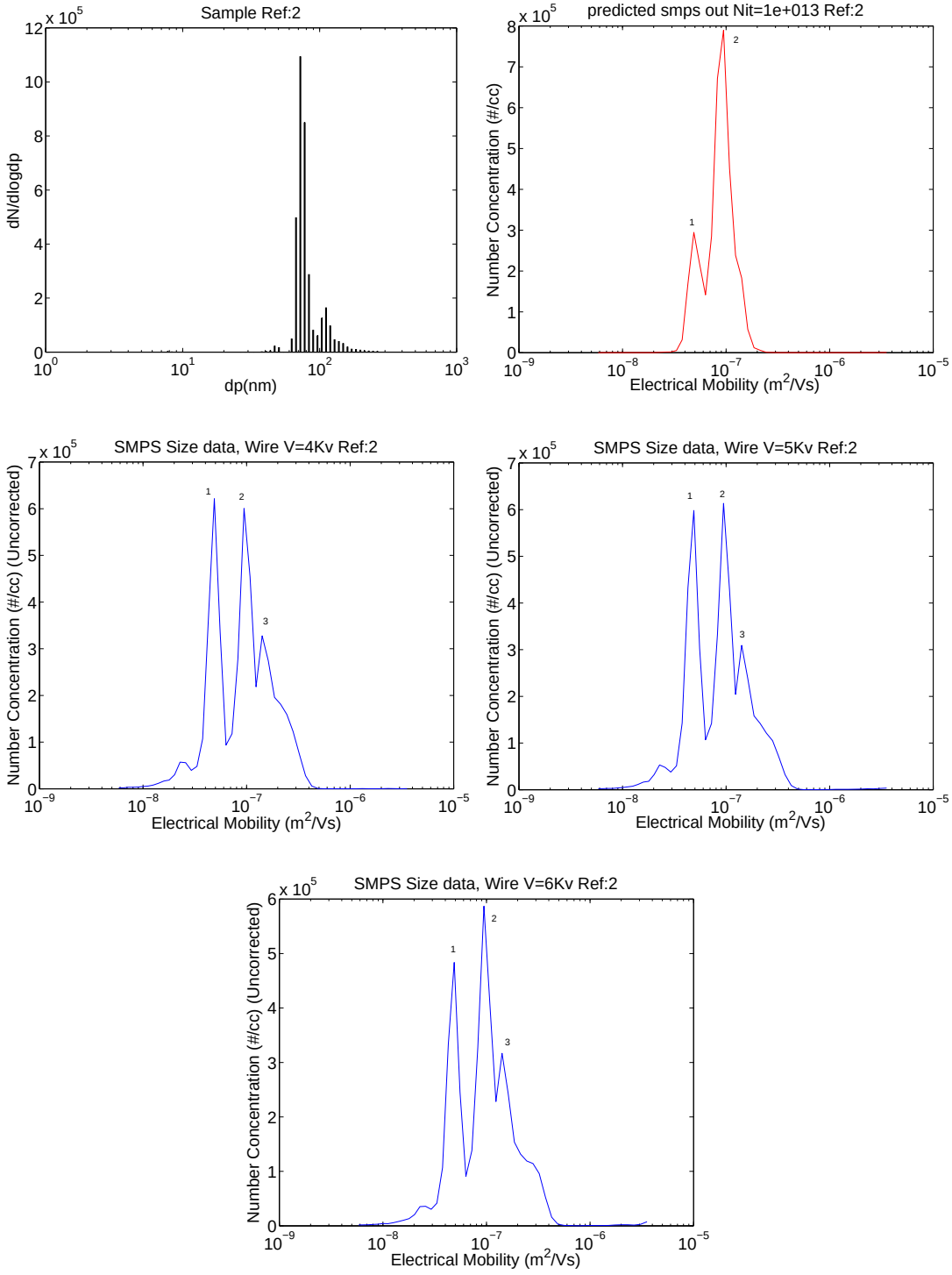

Figure 8.5: Sample, predicted result, and measured results for sample 2

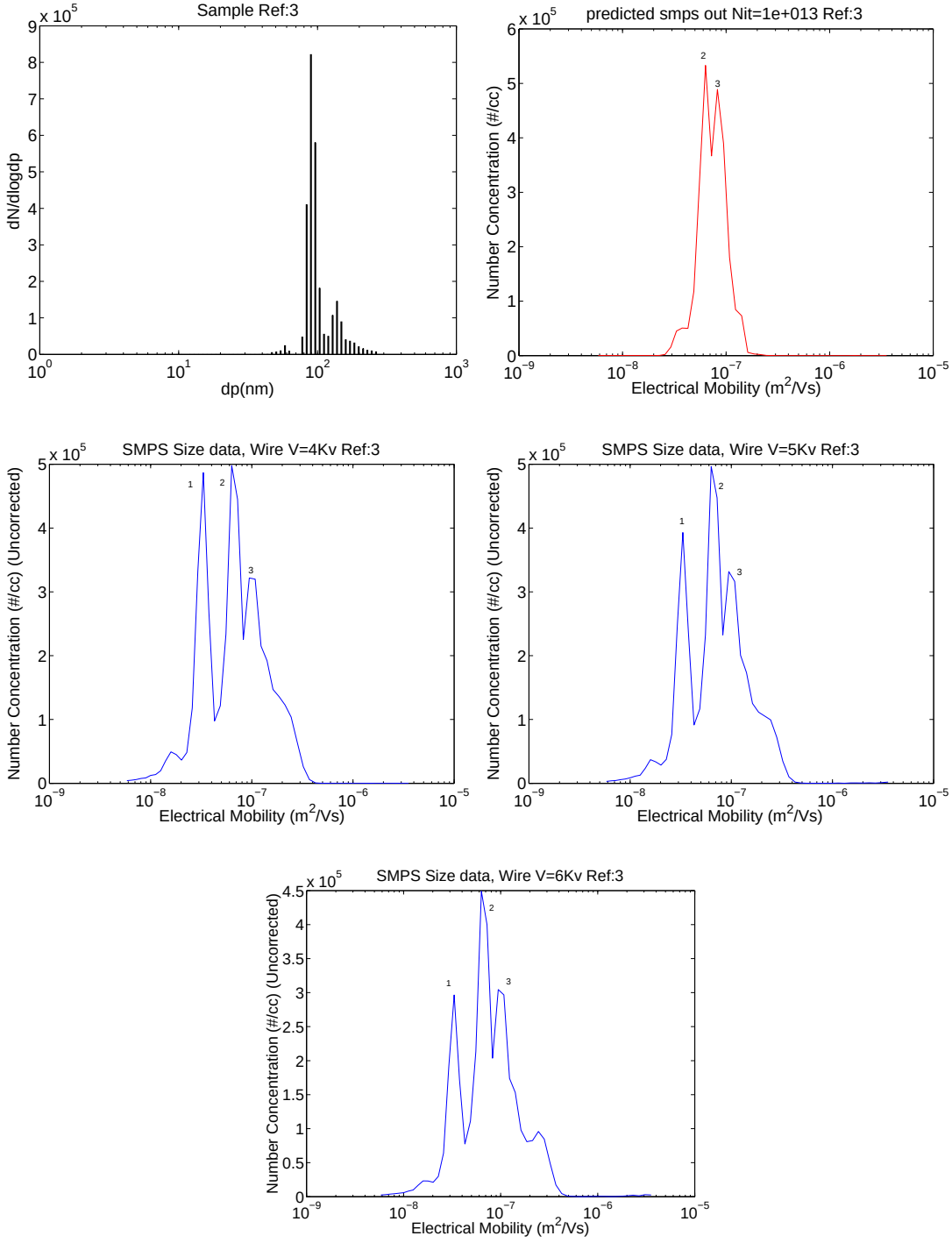

Figure 8.6: Sample, predicted result, and measured results for sample 3

8.3.6 Conclusions

It was suspected that the probable reason for the deviation of the measured results from those predicted was a distribution of particle residence times in the charger. The $N_i t$ is the product of the ion concentration in the charging zone, and the residence time of particles in the charging zone. The charger model assumes $N_i t$ to be constant.

While it is reasonable to assume that the N_i is constant under our operating conditions. It is not reasonable to assume that t is constant unless the flow in the charging region is laminar, and the flow velocity is uniform in the cross-section of the charging zone. A wire mesh screen is used in the inlet of the charger to to encourage uniform flow. In order to test the hypothesis that distributed residence time is in part responsible for the differences between predicted and measured results observed in this section, it was decided to modify he charger by replacing this screen with one of higher blockage, before recommencing the tests.

8.4 Charger Secondary Tests

This section details the tests carried out on the charger following the installation of an improved flow screen in the charger inlet to achieve uniform flow in the charging zone, and consequently a constant residence time for particles in the charging zone.

Some changes were made to the apparatus and procedure for these tests, these are detailed below.

8.4.1 Experimental set up

The experimental set up was changed slightly from the set up detailed in section 8.3. This time the charger is mounted in location in the Nanoparticle Spectrometer. The intention for this change was to ensure that the flow conditions at the charger exit are exactly the same in the test as in normal operation of the instrument.

To extract the sample from the instrument, the Nanoparticle Spectrometer is set up so all the channels except one is blocked off, as is the exhaust flow. A slight sheath flow is added, and the sheath and sample are drawn out of the one open channel, which has had its filter removed. The flows are adjusted so that the flow of sample through the charger is the same as it would be under normal instrument operation. The schematic for this set up is shown in fig 8.7

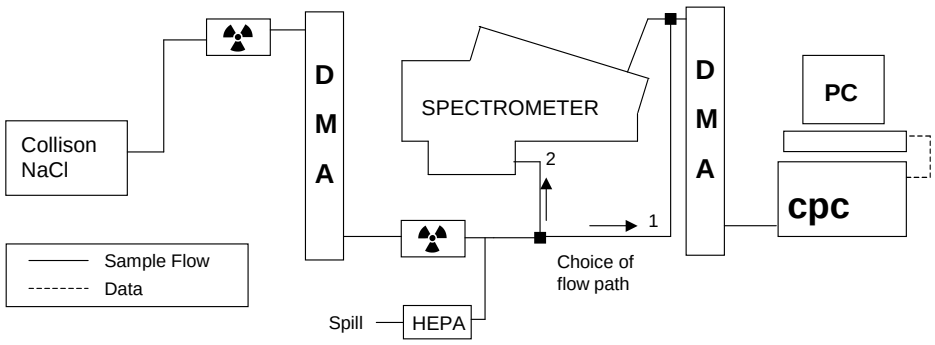

Figure 8.7: Schematic of experimental apparatus for secondary charger tests

8.4.2 Experimental Procedure

The experimental procedure for the tests detailed in this section were as follows. The DMA was set up to produce a monodisperse sample at a desired size. This sample was then analysed directly by the SMPS and stored. The same sample was then passed through the charger with the corona wire voltage set to 3.5kV. The charged sample is passed into the SMPS for analysis, and the data stored. The DMA is then re-adjusted to produce a monodisperse sample of a different size, and the process is repeated. This is done for a total or six different samples. Then the entire process described above is repeated for charger corona wire voltages of 4kV, and 5kV.

This procedure has been changed from that described in section 8.3. This is because when observing the waveform of voltage on the corona wire, it was noticed that immediately after the voltage was set, the waveform was slightly erratic and took a moment to settle into stable operation. It was there deemed inadvisable to adjust the corona voltage during the experiments, and some warm up time was allowed between setting of the voltage and commencement of the tests.

8.4.3 Results

Presented in figures 8.8 to 8.13, are some of the results for testing of the charger at 3.5kV, 4kV, and 5kV. Each fig contains data for two samples, and the graphs shown are:

- The size distribution of the sample as measured by the SMPS.
- The predicted electrical mobility versus concentration plots. The $N_i t$ values for each corona voltage were selected as being the values that gave the best agreement

between predicted and measured results across the whole range of data obtained for each voltage. These values were

- 5×10^{12} for 3.5kV
- 1.2×10^{13} for 4kV
- 3×10^{13} for 5kV

- The Measured electrical mobility versus concentration plots.

8.4.4 Results Analysis

3.5kV Fig 8.8 Shows the results for sample 1 and sample 3. The results for sample 1 show that predicted and measured results agree on a single narrow peak representing singly charged particles. However the measured result shows a second shallow distribution covering a wide range of mobilities. This is evidence of leakage of atmospheric particles into the system, and is present in all measurements, but only visible on plots where the magnitude of the peak is very small. it can also be seen in sample 1 in fig 8.10, and sample 1 in fig 8.12. The results for sample 3 show a good agreement between predicted and measured results, except for the presence of a tiny peak for triply charged particles in the measured data.

Fig 8.9 Shows the results for sample 4 and sample 5. Both show evidence of slightly broader charge distributions than predicted. The shapes of the distributions however are much more closely matched than those seen in section 8.3.

The results for the 3.5kV tests would suggest the new flow screen has improved the problem of distributed residence times, but not eradicated it.

4kV It can be seen that the results for samples, 1 and 2 shown in fig 8.10 show extremely good agreement between predicted and measured data. The same can be said for the results in fig 8.11 for samples 4 and 6, although some slight broadening of the distribution can be seen. The data for sample 6, looks like a single wide peak. It is however made up of particles with 3,4,5 etc elementary charges. However the difference between the mobilities at the higher charge levels is smaller than at lower levels so the peaks merge into one.

Some evidence of broader than predicted distributions can be seen, however the results for 4kV are showing much better agreement with predicted results than those of 3.5kV.

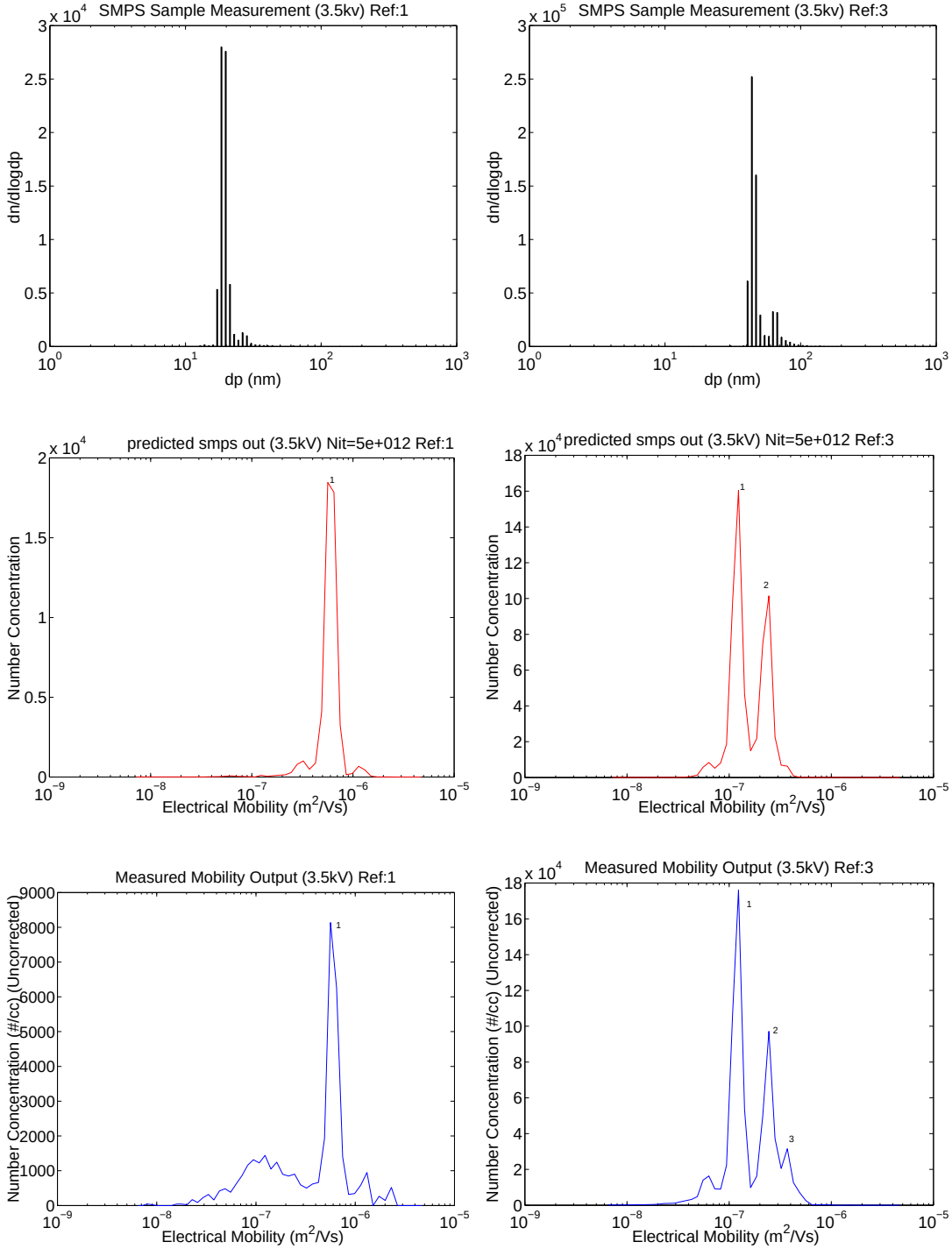

Figure 8.8: Sample, predicted result, and measured results for samples 1 and 3 in the 3.5kV tests

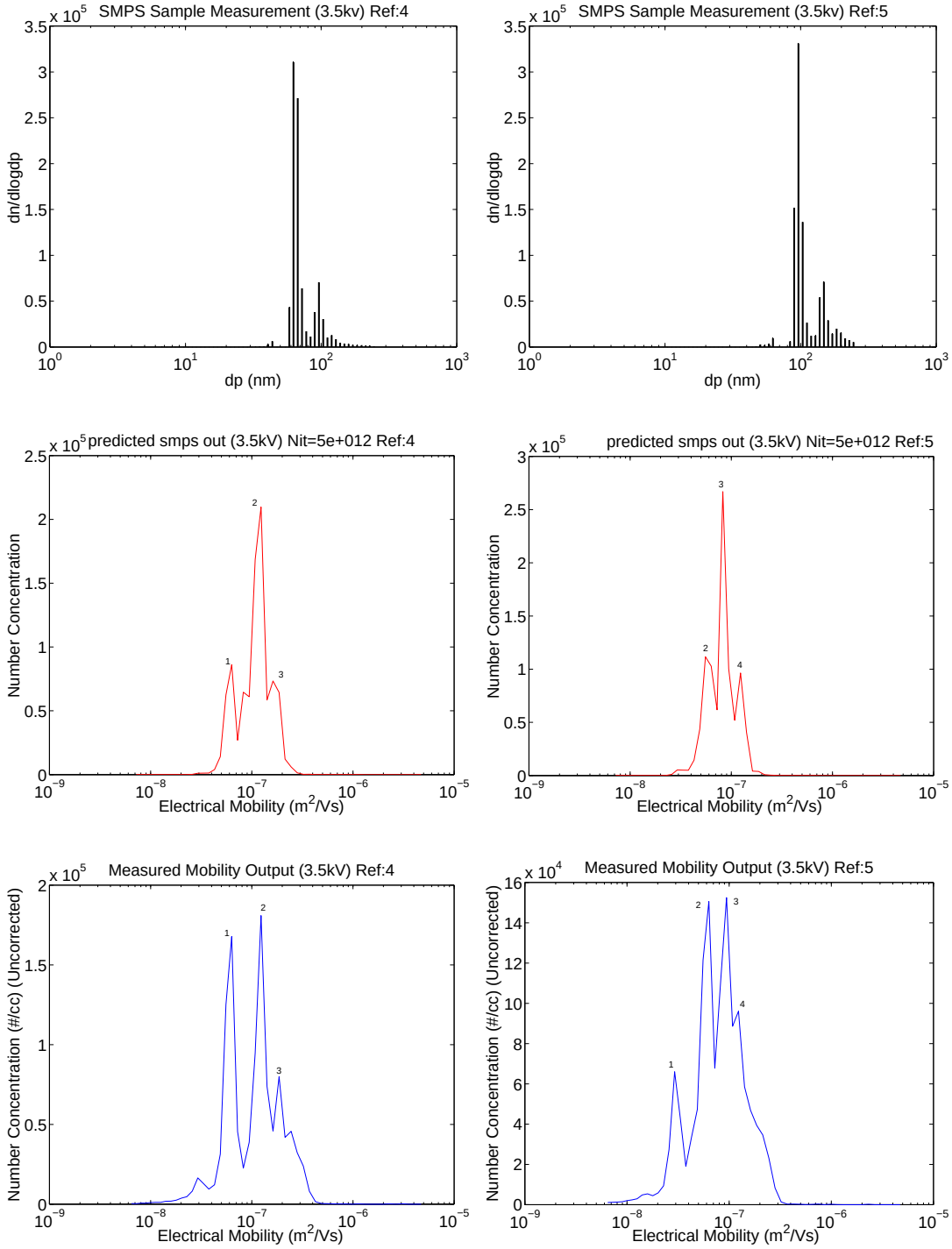

Figure 8.9: Sample, predicted result, and measured results for samples 4 and 5 in the 3.5kV tests

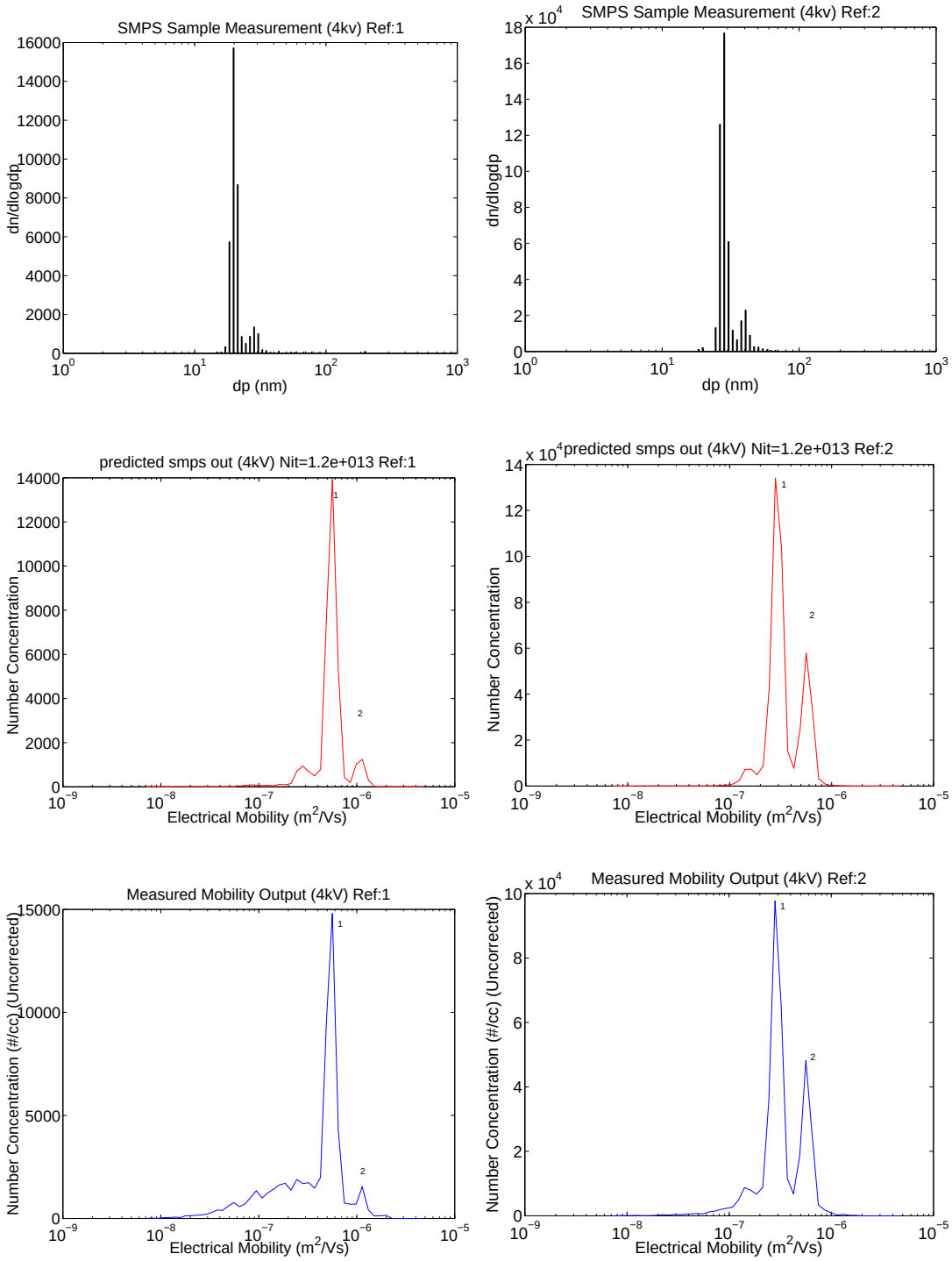

Figure 8.10: Sample, predicted result, and measured results for samples 1 and 2 in the 4kV tests

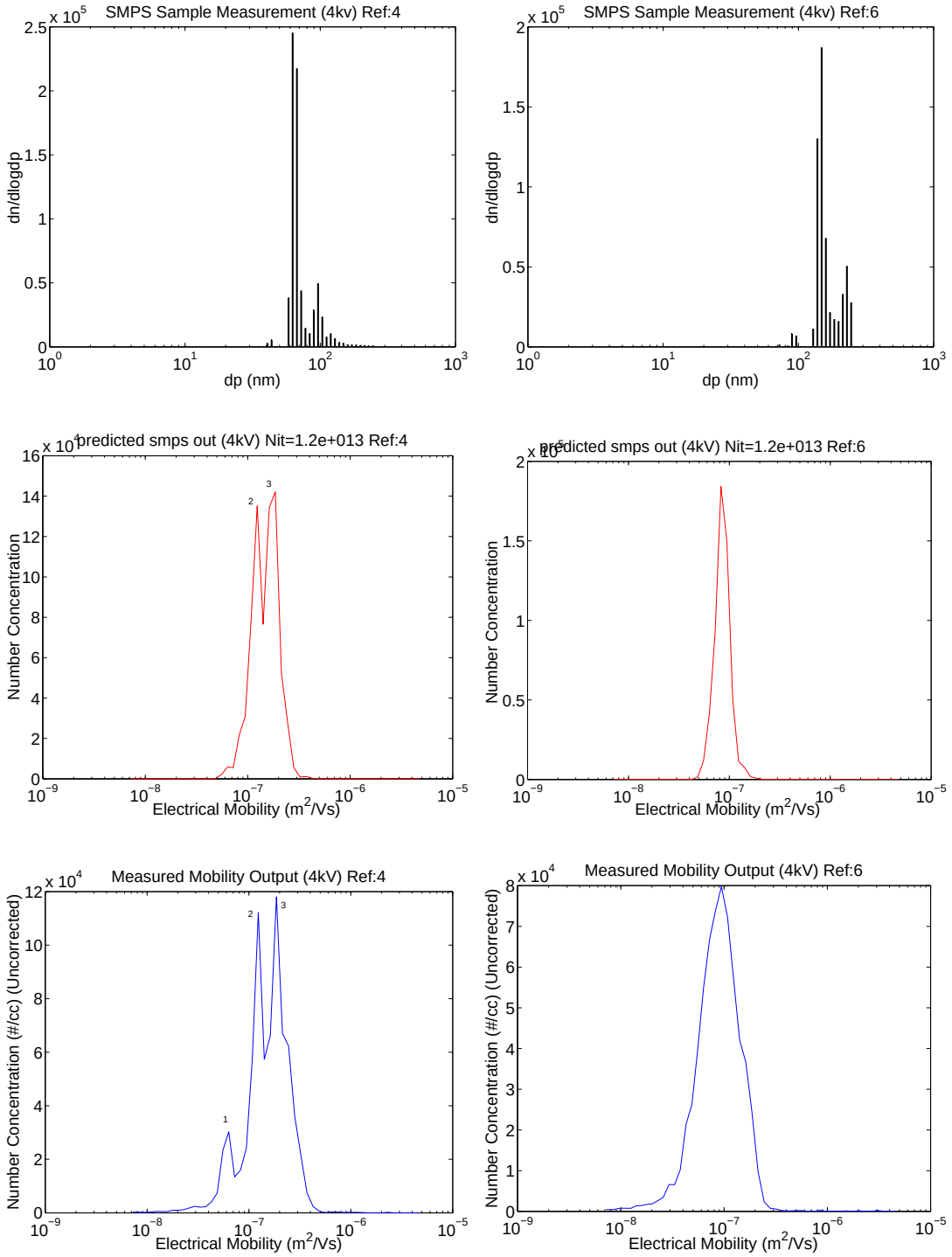

Figure 8.11: Sample, predicted result, and measured results for samples 4 and 6 in the 4kV tests

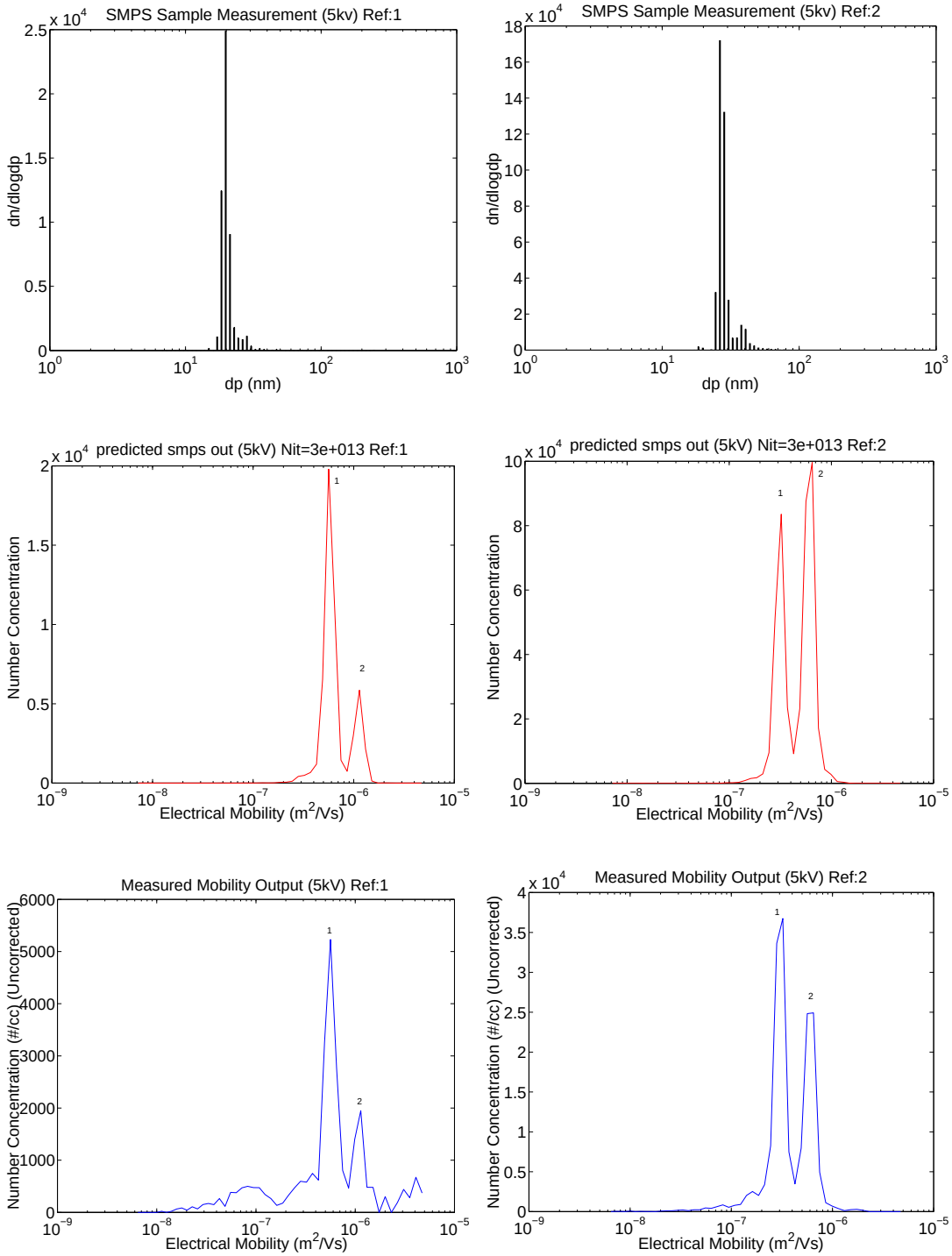

Figure 8.12: Sample, predicted result, and measured results for samples 1 and 2 in the 5kV tests

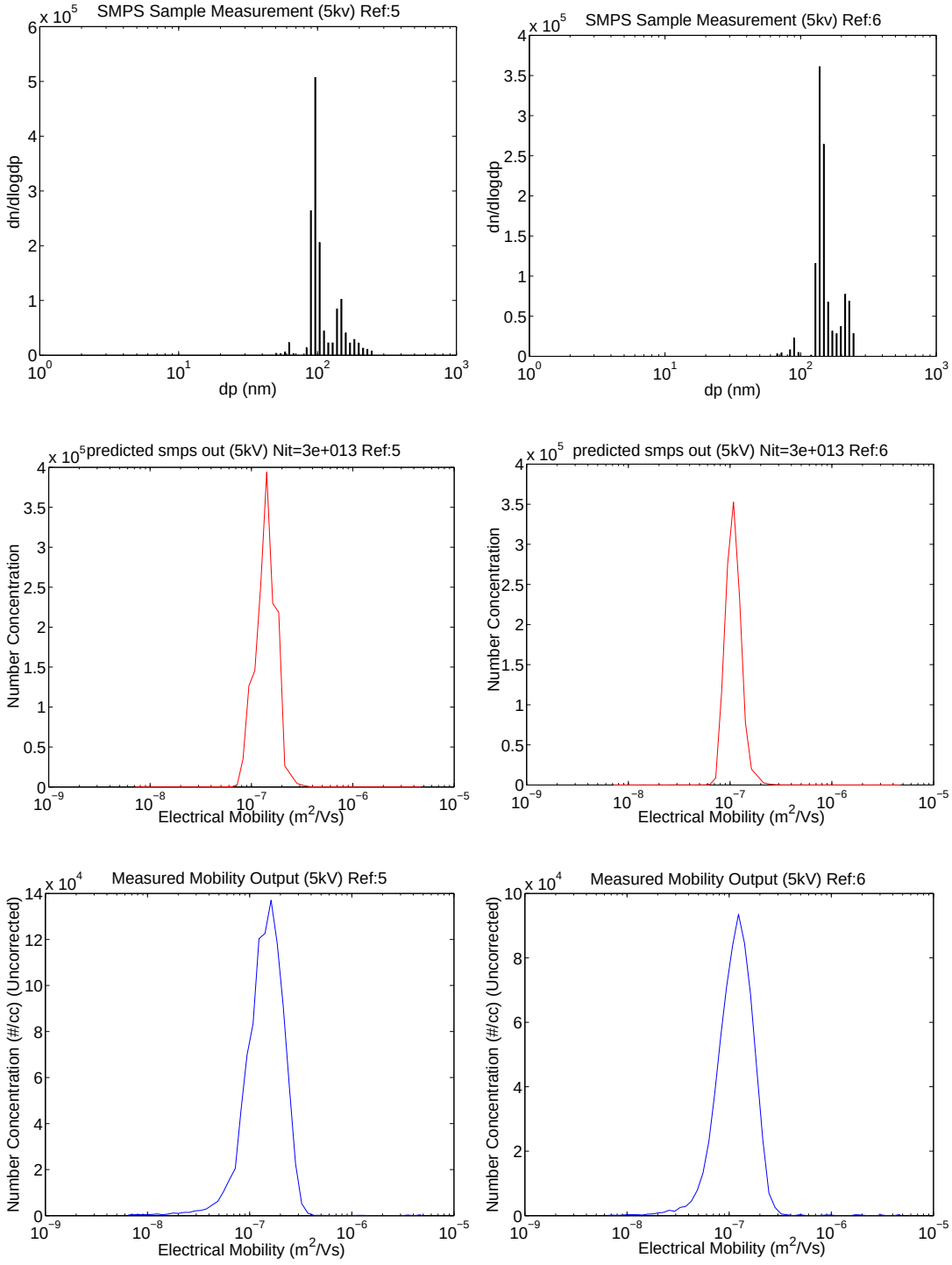

Figure 8.13: Sample, predicted result, and measured results for samples 3 and 6 in the 5kV tests

5kv Figures 8.12, and 8.13, show some results for the charger with the corona voltage set at 5kV. Here a very good agreement between predicted and measured results can be seen, with only very slight evidence of broader measured charge distributions. There is however a further complication arising from these results.

Figure 8.13 shows results for samples 5 and 6. Sample 5 is a monodisperse sample at 96nm. Sample 6 is monodisperse sample at 138nm. There is however very little difference between the mobility plots of the output from the charger. The peak of the mobility plots for sample 5 is $1.23 \times 10^{-7} m^2/Vs$, and the peak for sample 6 is $1.08 \times 10^{-7} m^2/Vs$. It is necessary for different size particles to have different mobilities for the classification part of the Nanoparticle Spectrometer to work. If larger particle accrue too much charge in the charger they can become as mobile as smaller particles. This would be very damaging to the resolution of the instrument.

From the above results it can be concluded that this second set of tests carried out following the installation of a new flow screen to encourage uniform flow in the charging region, have yielded results which agree better with the charging model.

It can also be seen that the problem of measured charge distribution being broader than predicted is present in all results, but appears to be less in the results from the tests with higher corona voltages. The charger theory used in the development of the charger model shows that the probability of a particle with n charges becoming a particle with n+1 charges decreases as n increases. Therefore it stands to reason that the effects of a slightly distributed residence time would be less noticeable when the charger is operating at higher voltages because slightly higher levels of charge are achieved at these voltages.

Operating at higher corona voltages gives a better agreement between predicted and measured results. However it has been seen that if the operating voltage is too high, then the particles become too highly charged and resolution between larger diameter particles is lost. Our tests show that at an operating voltage 4kV there is good agreement between predicted and measured results, and the resolution at large particle diameters is still good, therefore 4kV is selected as the operating voltage for the charger.

8.4.5 Conclusions

From the results of the tests detailed here in section 8.4, it is concluded that the theoretical charging model provides good predictions of the charge distribution on samples charged by the prototype charger. The charger corona voltage selected as optimum is

4kV, and the $N_i t$ used by the model that provides the best predictions for this operating condition is 1.2×10^{13}.

The rationale for the above tests was an attempt to achieve better agreement between measured and modelled data by trying to make the residence time of particles in the charger closer to uniform, as modelled. To have perfectly uniform flow however is an unrealistic expectation for "real world" conditions. Therefore, in order to improve the charging model further consideration would have to be given to modelling the residence times of particles in the charging zone, as well as trying to improve the uniformity of the flow. Possible strategies for further improving the flow uniformity could include flow screens with a still higher blockage, baffles up stream of the flow screen, and also possibly a sheath flow of clean air surrounding the aerosol flow in the charging zone so that the particles do not flow in the boundary layers near the walls where residence times will be longer,

8.5 Additional Charger Data

This section details some additional data, and points of interest relating to the charger that were discovered during these tests.

8.5.1 The Charge Concentration

The $N_i t$ selected for use in the model was chosen on the basis that it was the value that gave us the best results, rather than any measure of N_i in the charging zone. Measuring N_i in the charging zone would be quite challenging, however the current flowing from the corona wires can be measured. The results of this measurement is presented in table 8.1.

Wire Voltage	Measured Current	Elementary charges per Second
$3.5\,kV$	$1\,\mu A$	$6.25 \times 10^{12} \#/s$
$4\,kV$	$4.3\,\mu A$	$2.69 \times 10^{13} \#/s$
$4.5\,kV$	$18\,\mu A$	$1.13 \times 10^{14} \#/s$
$5.0\,kV$	$36\,\mu A$	$2.25 \times 10^{14} \#/s$
$5.5\,kV$	$59.4\,\mu A$	$3.72 \times 10^{14} \#/s$
$6.0\,kV$	$84.5\,\mu A$	$5.28 \times 10^{14} \#/s$

Table 8.1: Measured corona currents at various voltages.

The charger is operating with a sample flow of $3lpm$, and a residence time for particles of about 0.5 sec. Therefore for the values of N_i $(\#/m^3)$ in the charging zone,

that have been used in the model to be correct. Only a small fraction of the ions produced must make it to the charging zone without being precipitated on the walls of the charger or the screen through which the ions must travel.

The table also shows an increase in the ion production of approximately 4 times between 3.5 and 4kV, and approximately 8 times between 4 and 5kV. If the values used in the model are correct then the increase in the charge concentration in the charging zone is 2.4 times between 3.5 and 4kV , and 2.5 times between 4 and 5kV. This would suggest that the ion production efficiency (number of ions that reach the charging zone/number of ions produced) decreases with increasing voltage. This very same trend in ion production efficiency is seen in our tests on the Sonic Jet Charger in chapter 6.

8.5.2 The Image Force Parameter

The charging model contains an expression for the image force (equations 5.6 and 5.7), this is used to model Van der Waals attraction between ions and particles with low, or neutral charge. To model the image force we must specify the parameter given in equation 8.1.

$$\frac{(\epsilon - 1)}{(\epsilon + 1)} \tag{8.1}$$

Where ϵ is the dielectric constant of the particle material.

This parameter only has a significant effect on the prediction of charge distribution on smaller particles. Choosing a value is difficult, as the Nanoparticle Spectrometer is not designed to be able to differentiate particle species. The same charging model used here was tested experimentally [Biskos et al, 2005] for a diffusion charger of similar design. The results in this paper also show good agreement between experimental and predicted results, and the modelled data presented was generated with the image force parameter, set to 1 (i.e. assuming electrically conducting particles).

During the course of our experiments it was also found, through comparison between predicted and measured results, that the best agreement was achieved with the image force parameter set to 1

8.5.3 Accidental Field Charging

The experimental data presented below was obtained during a different set of tests, which are presented more fully in the next Chapter, (section 9.2). However this particular data is presented here as it is most relevant to the charger. (More detailed information about the apparatus and procedure can be found in section 9.2.)

If the Nanoparticle Spectrometer is set up to run with the electrometer filters removed it is possible to divert some of the sample coming out of one of the channels and analyse it in the SMPS. Figure 8.14 Shows the SMPS measured output from channel 3 in the Nanoparticle Spectrometer.

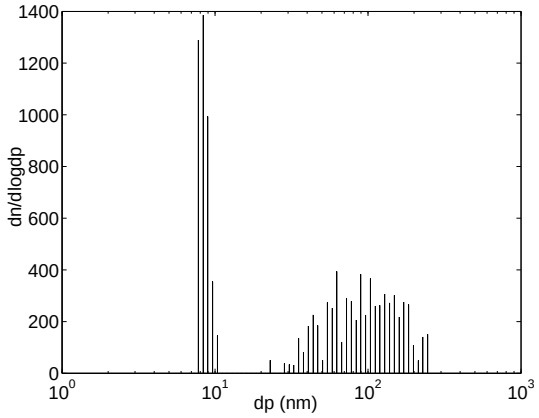

Figure 8.14: SMPS analysis of channel 3 output, with charger sheath flow *in* equal to sheath flow *out*

It is known that only particles of a certain electrical mobility can land on channel 3. It is also known how much charge a particle with a given diameter must have to be of high enough mobility to land in channel 3. The $10nm$ spike in fig 8.14 is expected. This corresponds to singly charged particles of this size. The second small broad peak is not expected, particles of this size would need a lot of charge to be found in channel 3 in many cases in excess of 50 elementary charges are required.

The origin of these particles could be leakage of uncharged atmospheric particles into the instrument. The other possibility is that they are particles that have passed through the screen in the charger that separates the corona wires from the charging zone. If the particles pass into this region they will be subject to field charging, which can result in higher charge levels than diffusion charging.

In order to prevent particles from passing through this screen and becoming field charged, it was decided to adjust the flow rates in the charger, so that the charger sheath flow *in* was slightly higher than the sheath flow *out*. This was intended to create a slight flow of sheath air up through the screen and into the charging zone. Figure 8.15 shows another sample taken from channel 3 after these new flow conditions had been implemented. In this plot no evidence of larger particles can be seen.

Consequently the new flow conditions were adopted, and used in all subsequent

tests.

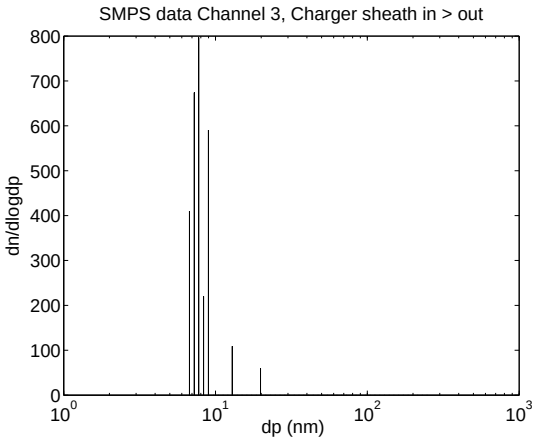

Figure 8.15: SMPS analysis of channel 3 output, with charger sheath flow *in* greater than sheath flow *out*

Chapter 9

The Nanoparticle Spectrometer: Testing and Results

9.1 Introduction

This chapter details the testing carried out on the instrument, and presents the results of these tests. The tests presented here were designed to establish the following.

- Where do particles of a given mobility land within the classifier, and does this agree with the theoretical model?
- What is the output signal from the instrument's electrometers for a given aerosol sample, and does this agree with the theoretical model?
- Can the output signal be used by the look-up program to identify a size distribution for the sample, that is in agreement with that identified by a "standard" SMPS.

In this chapter we seek to present some results, and the analysis of these results with some basic discussion and conclusions. A more detailed discussion on the accuracy and meaning of the results, as well as ideas for future work, is presented in the discussion in chapter 10.

9.2 Channel Mobility Tests

Using the numerical particle tracks model described in chapter 5, it was possible to predict the the mobility limits of each channel. The predicted limits for a deflecting plate voltage of $5kV$ are shown in table 9.1.

In order to verify the predicted channel limits, they were tested experimentally; the details of these tests are given in this section.

Channel #	Lower Mobility Limit	Upper Mobility Limit
1	$2.20 \times 10^{-5} m^2/Vs$	$\infty m^2/Vs$
2	$7.00 \times 10^{-6} m^2/Vs$	$2.20 \times 10^{-5} m^2/Vs$
3	$3.83 \times 10^{-6} m^2/Vs$	$7.00 \times 10^{-6} m^2/Vs$
4	$2.46 \times 10^{-6} m^2/Vs$	$3.83 \times 10^{-6} m^2/Vs$
4	$1.70 \times 10^{-6} m^2/Vs$	$2.46 \times 10^{-6} m^2/Vs$
6	$1.22 \times 10^{-6} m^2/Vs$	$1.70 \times 10^{-6} m^2/Vs$
7	$9.10 \times 10^{-7} m^2/Vs$	$1.22 \times 10^{-6} m^2/Vs$
8	$6.85 \times 10^{-7} m^2/Vs$	$9.10 \times 10^{-7} m^2/Vs$
9	$5.20 \times 10^{-7} m^2/Vs$	$6.85 \times 10^{-7} m^2/Vs$
10	$3.90 \times 10^{-7} m^2/Vs$	$5.20 \times 10^{-7} m^2/Vs$
11	$2.90 \times 10^{-7} m^2/Vs$	$3.90 \times 10^{-7} m^2/Vs$
12	$2.10 \times 10^{-7} m^2/Vs$	$2.10 \times 10^{-7} m^2/Vs$
13	$1.50 \times 10^{-7} m^2/Vs$	$2.10 \times 10^{-7} m^2/Vs$
14	$1.02 \times 10^{-7} m^2/Vs$	$1.50 \times 10^{-7} m^2/Vs$
15	$6.30 \times 10^{-8} m^2/Vs$	$1.02 \times 10^{-7} m^2/Vs$
16	$3.50 \times 10^{-8} m^2/Vs$	$6.30 \times 10^{-8} m^2/Vs$

Table 9.1: Modelled channel mobility limits ($5kV$ field)

Space charge density The model of the electric field in the classifier includes a variable for an average space charge density in the classifier. There will be space charge in the classifier due to the presence of charged particles. However, a value for this variable is very hard to specify, as different samples will introduce different levels of space charge, and space charge will be locally higher in some areas, for instance near the sample inlet.

During these tests it was found that predicted mobility limits generally agreed slightly better with measured mobility values if a small space charge was used in the model. However the number concentrations of the samples used were fairly high and so using the value of space charge used may not be valid for samples with lower concentrations. Therefore the model results presented in this section were generated using a space charge of 0. Nevertheless it is worth considering that if a user of the NPS had some idea about number concentration and charge distribution of the sample they intended to analyse, an approximate value of space charge *could* be used to obtain slightly more accurate results. However, more work would have to be done in this area.

9.2.1 Experimental Set Up and Procedure

Figure 9.1 shows the set up for channel mobility tests. An NaCl aerosol with a broad size distribution was generated using the procedure described in section 8.2. This aerosol was neutralised and then sampled by the Nanoparticle Spectrometer.

The NPS charges, and classifies the aerosol as designed. The electrometer filters are removed, and the classified samples in each channel are simply sucked out. An SMPS can be used to sample the aerosol coming out of one of the channels. If the flow is passed directly into the DMA, bypassing the neutraliser, (flow path 1) then the SMPS data (uncorrected for charge distribution) can be used to obtain a plot of Concentration versus mobility, thus showing us what mobilities of particles are present in that channel.

If the flow is passed into the SMPS via the neutraliser (flow path 2) The SMPS will produce a concentration versus particle size plot, as normal.

Procedure The aerosol generator was set with the NPS classifying the samples. A flow tap is put into the outlet of channel 1 such that the SMPS can sample this flow without affecting the flow rate out of the channel. The sample is drawn into the SMPS via flow path 1, and analysed. This process is repeated for the other 15 channels.

This same test was also done for flow path 2. However, with the exception of the plot shown in section 8.5.3, these results are not presented here, as they simply confirm the performance of the charger, already presented in chapter 8.

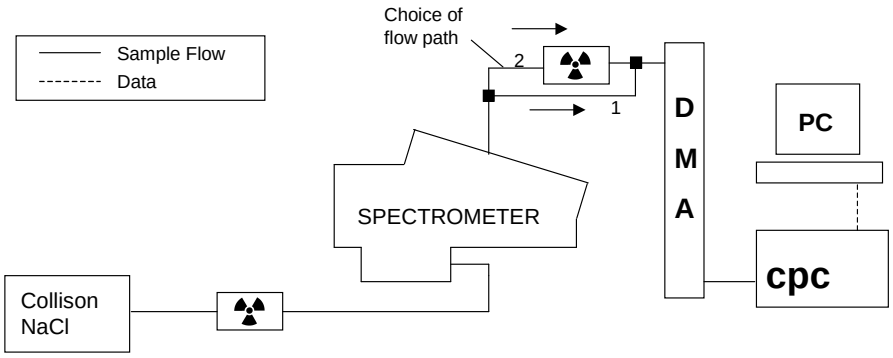

Figure 9.1: Schematic of experimental apparatus channel mobility tests

9.2.2 Results

Figure 9.2 shows the concentration versus mobility plots for the NPS channels, only every other channel is shown to maintain clarity on the graph. There is no data for channels below channel 3 as no signal was detected in these channels. Added to the plots are the predicted mobility channel limits, shown as broken red lines. It can be seen that the peaks of most of these mobility plots lie in the middle of the channel limits for most plots although some slight deviation is seen most notably in channels 11 and 13.

In virtually all cases the range of mobilities in each channel is wider than the predicted limits, and indeed overlapping with the range of mobilities of adjacent channels. This is thought to be due to non-uniformity of the flow in the classifier as discussed in section 7.2.2 and also possibly due to diffusion of the particles in the classifier. Neither of these effects are accounted for in the model. The effects can be seen to be greater in the higher numbered channels. This is because particles destined for these channels have a longer flight time, and also generally spend more time near the base of the classifier where boundary layer effects are the greatest.

Additional Test

Although $5kV$ is the intended operating voltage for the deflecting plate in the classifier, it was decided to test the model further by modelling the channel mobility limits for a deflector plate voltage of $6kV$ and repeating the channel mobility tests at this voltage.

Some results for these tests are shown in fig 9.3. it can be seen that these results

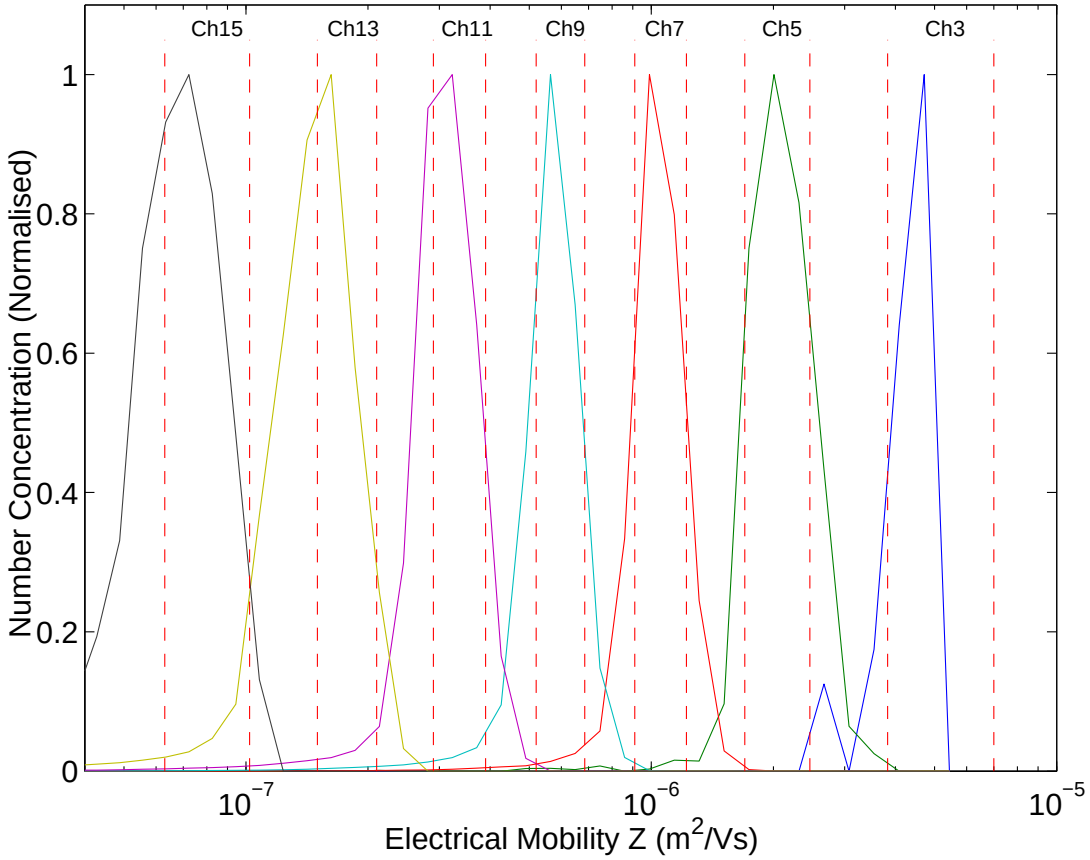

Figure 9.2: Channel mobility plots ($5kV$ field), Channels 3, 5, 7, 9, 11, 13 and 15

show much the same level of agreement with the model, as the $5kV$ results.

9.2.3 Conclusions

The results in this section show that the numerical particle tracks model can accurately predict the landing locations for the majority of particles. It does not however account for the fact that a proportion of particle will stray from their predicted landing positions due to non-uniformity of the classifier flow. This proportion is larger for particles travelling to the higher numbered channels.

9.3 Electrometer Noise Measurements

Tests were carried out in order to determine the ambient noise levels of the electrometers. The procedure for these tests was to set the Nanoparticle spectrometer to run as normal, but with a High Efficiency Particulate Air (HEPA) filter on the sample inlet. Upon first testing high noise levels were recorded. Certain modifications were made to the instrument that were found to reduce the noise: The capacitors in the electrometer between the input and ground were found to be significant source of noise. It is thought that there was some noise on the ground, which was getting onto the input through the capacitors. As the capacitors serve a passive purpose, which is to protect the op-amps from the possibility of a high voltage spark from the deflecting plate in the instrument striking the electrometer filter, it was decided to remove them.

The ends of the electrometer filters in the instrument were only a few millimetres away from the mesh that screens the electrometers from noise from the deflecting plate in the classifier. It was found that shortening the filters by 10mm caused a significant reduction in noise. This was implemented on all channels.

Other practical considerations were implemented such as ensuring, that during testing noise sources in the room such as the Computer monitor, the high voltage power supplies and AC power cables we far away and/or well screened from the instrument.

The final ambient noise levels on the electrometers was on average $4fA$ RMS noise over a sampling time of $\frac{1}{10}$seconds at a sampling rate of $1000Hz$.

9.4 Testing the Instrument Output Signal

9.4.1 Introduction

This section deals with the main tests carried out on the Nanoparticle Spectrometer. The aim of these tests is to take many different aerosol samples and measure them with

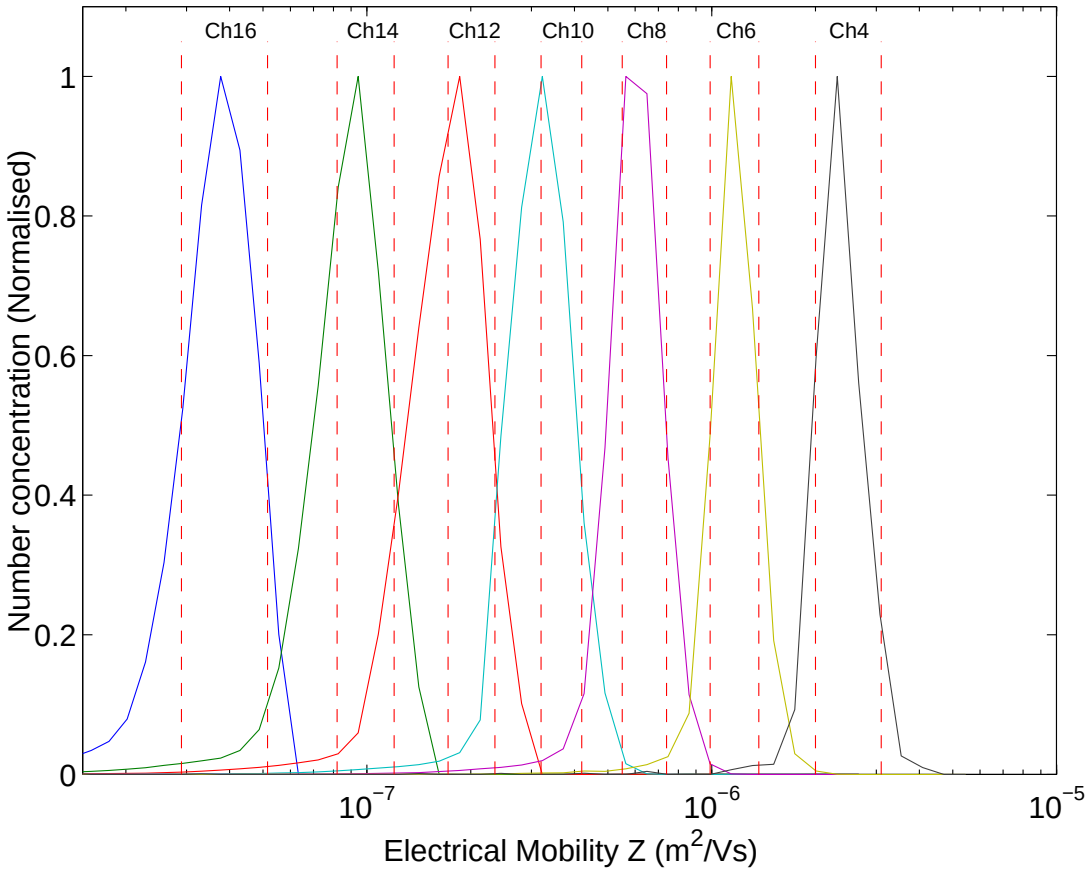

Figure 9.3: Channel mobility plots ($6kV$ field), Channels 4, 6, 8, 10, 12, 14 and 16

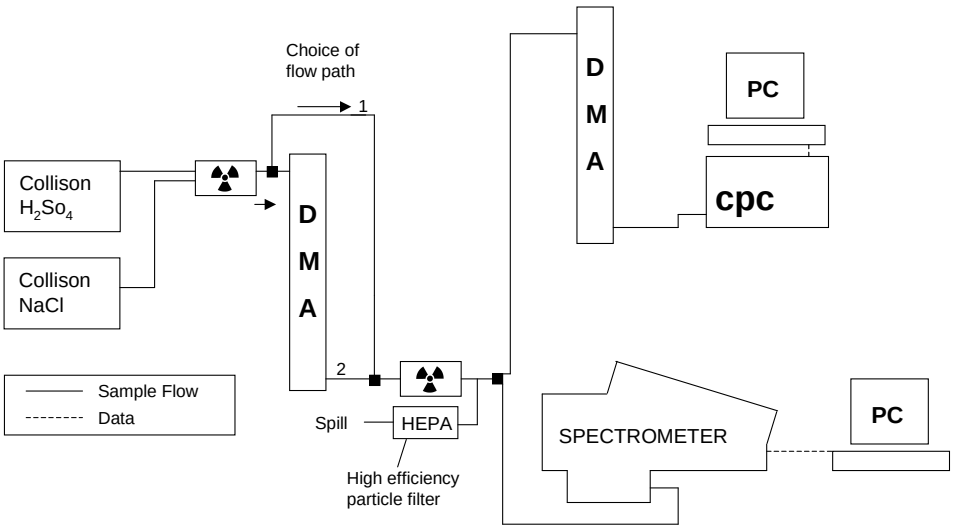

Figure 9.4: Schematic of experimental set up for Instrument signal tests

the Nanoparticle Spectrometer. The same samples are simultaneously analysed by the SMPS. The SMPS data is input into the instrument theoretical model to produce a predicted current output signal for each of the instruments channels. This can then be compared to the measured signal

In total over 50 samples were analysed, the raw results for a selection of these samples are presented in this section, and entire range of results is analysed to produce an error surface showing the squared error between measured and predicted results across the instruments range.

Also discussed in this section are the sources of error between the predicted and measured results, and what can be done about them.

9.4.2 Experimental Set Up

During initial tests on the performance of the instrument it was found that the signals detected in channels 1-6 were close to the noise levels and therefore difficult to detect if the sample concentration was small. As the mobility ranges of these channels are quite narrow compared with the other channels in the instrument it was decided to pair up channels 1 and 2, 3 and 4, and 5 and 6. This was done by connecting the filters of both channels to a single electrometer. The channels now act as a single channel with a larger mobility range, and the signals are, of course higher.

In order to make sample aerosols with a range of distributions, both $NaCl$, and

H_2SO_4 aerosols were generated with the Collison nebuliser as described in section 8.2. Some control over the mean size of the aerosol's distribution is possible by adjusting the flow through the nebuliser, and the concentration of $NaCl$, or H_2SO_4. In the case of H_2SO_4 a little more control is possible by adjusting the temperature of the heated tube. In the case of $NaCl$, the sample can be passed into the Differential Mobility Analyser. Using a DMA, the mean size selected can be controlled using the central rod voltage, and the breadth of the distribution can be controlled by adjusting the sheath/sample flow ratio. However, as will be seen, the DMA does not always produce a lognormal size distribution.

Figure 9.4 shows the schematic of the experiment set up. The aerosol sample is generated (either $NaCl$, or H_2SO_4), this is then neutralised. From here it can either follow flow path 1 and go straight to the instruments, or flow path 2 and be "cut" by the DMA. Following this the sample is simultaneously analysed by the Nanoparticle Spectrometer, and the SMPS.

9.4.3 Experimental Procedure

Direct analysis of the Sample There are many variables available to the experimenter that offer some degree of control over the sample size distribution generated using the Collison nebuliser. These include: Adjusting the pressure of the air supply to the nebuliser, changing the concentration of the fluid in the nebuliser, and adjusting the heated tube temperature. It is very difficult to select a variety of settings to proceed through during the experiment.

Instead various settings are adjusted, and the sample is analysed by the SMPS for observation of the size distribution. The settings can then be re-adjusted, and the sample analysed again, until a desired distribution is achieved. Complete control over the shape of the sample distribution in not possible, so the sample used will be, at best, an approximation to the desired distribution.

Analysis using the DMA The DMA affords the user more control over the sample size distribution. Firstly a sheath/sample flow ratio is set to give a desired breadth of distribution. Then the central rod voltage is set to give a desired mean particle diameter. The sample is checked, by analysis with the SMPS, if acceptable, the sample is then analysed by both instruments. A new rod voltage is then selected and the process is repeated. When the voltage range is covered, a new sheath/sample flow ratio is selected, and the above process is repeated.

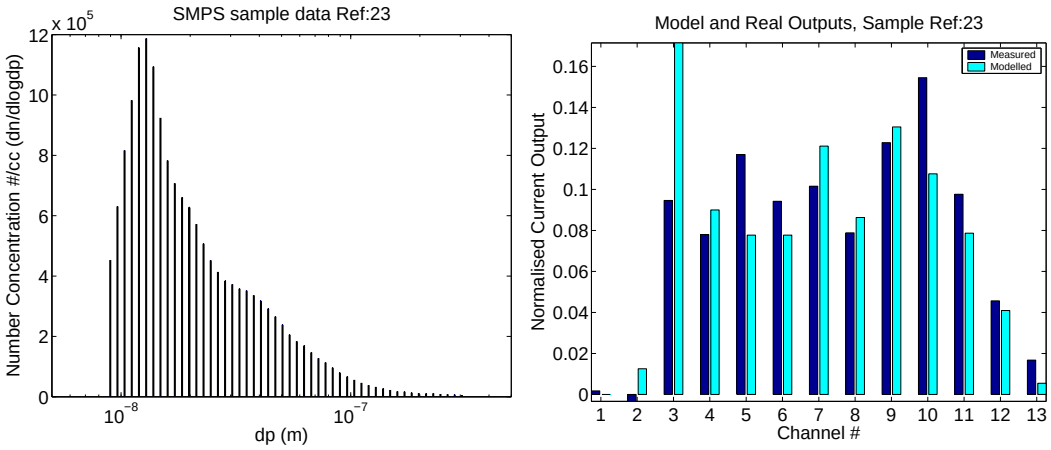

Figure 9.5: Predicted and Measured outputs comparison sample 23

It was intended to produce lognormal samples that covered a wide range of mean diameters, and standard deviations within the instrument's range. Some areas of the range were easier to produce samples for than others. A full presentation of the range samples produced is shown later in this chapter.

9.4.4 Results

Presented in this section is a selection of the results from the tests. Each figure shows an SMPS measured size distribution for the sample being tested. And also a bar graph comparing the measured output signal from the NPS' electrometers when analysing that sample, with the model predicted output for the sample.

The electrometer output currents for the predicted and measured results are normalised by total current in the plots, as this is how samples in the look-up table will be treated.

Fig 9.5 shows an H_2SO_4 aerosol sample. The peak is centred on $12nm$. A strong correlation can be seen between predicted and measured results in channels four to thirteen, however the measured signal in channel 3 is much lower than predicted, and there is no measured signal in channel 2, where a small one is predicted.

Fig 9.6 is another H_2SO_4 sample, this is a log-normal distribution centred around $18nm$. The same trend as was seen in fig 9.5 is present here. The measured signals in early channels (2,3,4) are notably lower than predicted.

Fig 9.7, a third H_2SO_4 sample is centred around $22nm$, the main signals in this slightly larger sample, have moved away from the early channels, and now predicted and measured results, are in largely good agreement, the one notable difference being

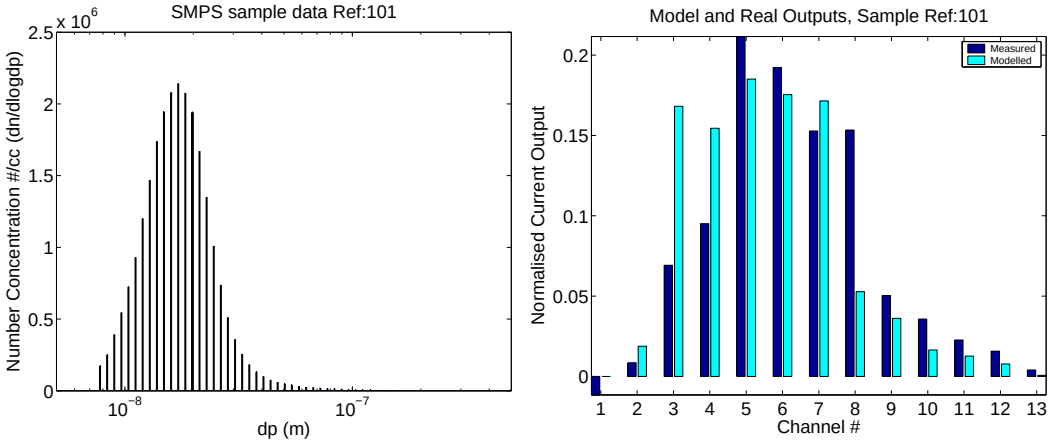

Figure 9.6: Predicted and Measured outputs comparison sample 101

channel 7.

The low measured signals seen in channel 2,3 and 4 could be considered evidence of diffusion losses. These losses are due to particles becoming deposited in the instrument before reaching the electrometers.

Diffusion losses are expected, especially on the mesh screen separating the classifying region from the electrometers. It is also expected that diffusion losses of high mobility particles will be greater, as these particles are more likely to be precipitated. As the early channels are where the high mobility particles land, this is where evidence of diffusion losses will be manifest.

Figures 9.8, and 9.9 show two very similar samples. Both are $NaCl$ aerosols, log-normally distributed with mean of approximately $55nm$ and geometric standard deviation of approximately 2. The peak concentration of sample 13 in fig 9.9 is about $\frac{1}{20}$ that of sample 1 in fig 9.8. The predicted, and measured results for these two samples are very similar. This shows good reproducibility of results, and is also good evidence that the shape of the signal is independent of total concentration.

An apparent difference between predicted and measured results, that is shared by both figures 9.8, and 9.9, is the higher than predicted signal in channel 13.

Figures 9.10 and 9.11 show $NaCl$ samples that have been "cut" with the DMA. The sheath flow rate ratio is close to 1, so the distributions are broad. Each SMPS plot in fact shows two distributions. The selected distribution, at the peak, and in the background a small amount of the original nebuliser sample distribution is getting through.

These figures show good agreement between predicted and measured results, al-

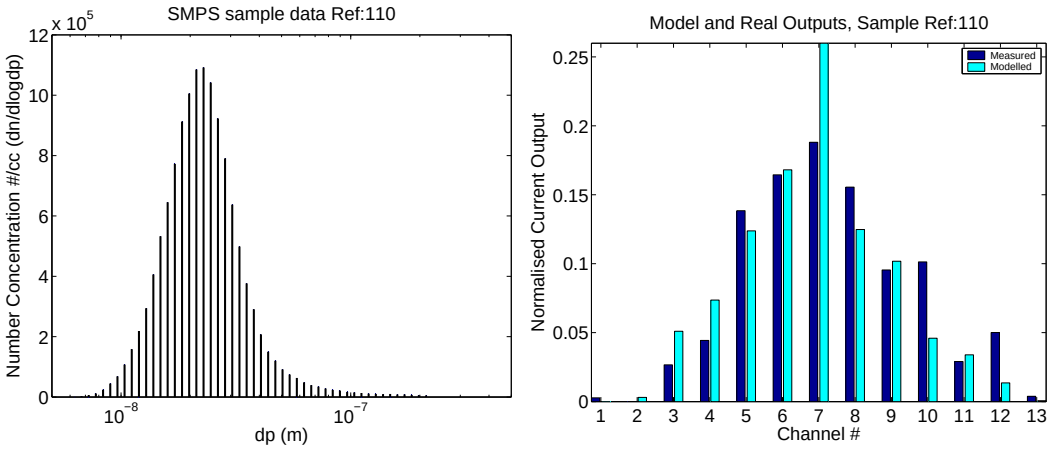

Figure 9.7: Predicted and Measured outputs comparison sample 110

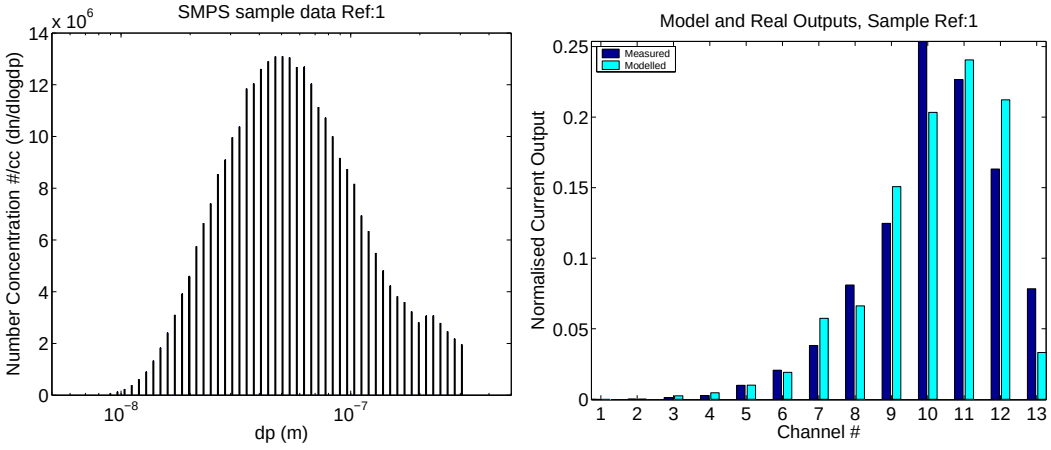

Figure 9.8: Predicted and Measured outputs comparison sample 001

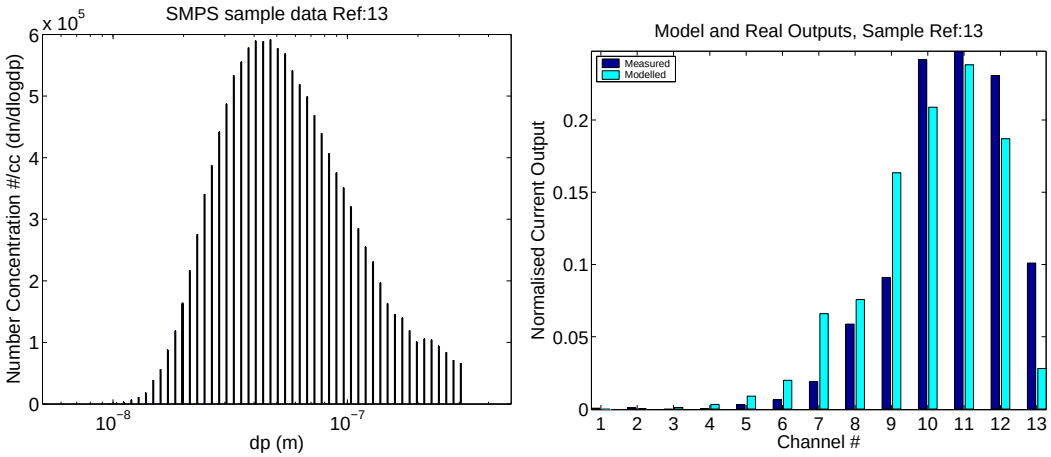

Figure 9.9: Predicted and Measured outputs comparison sample 013

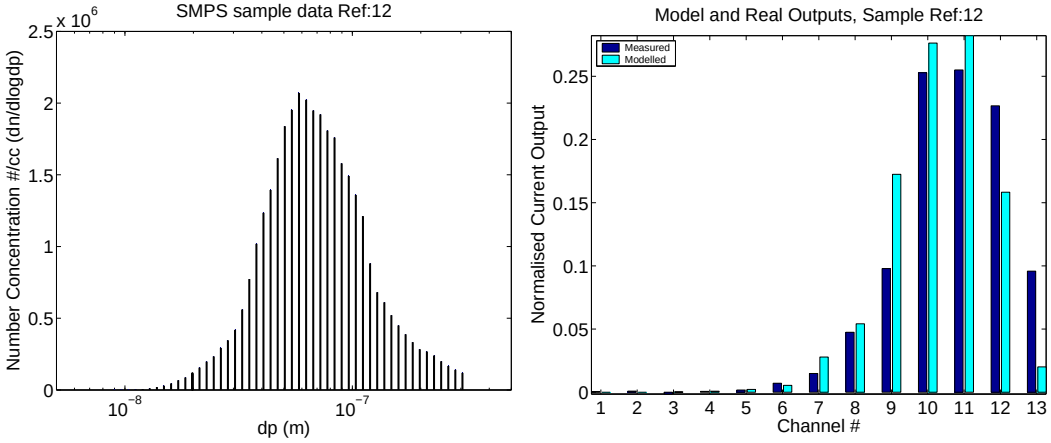

Figure 9.10: Predicted and Measured outputs comparison sample 012

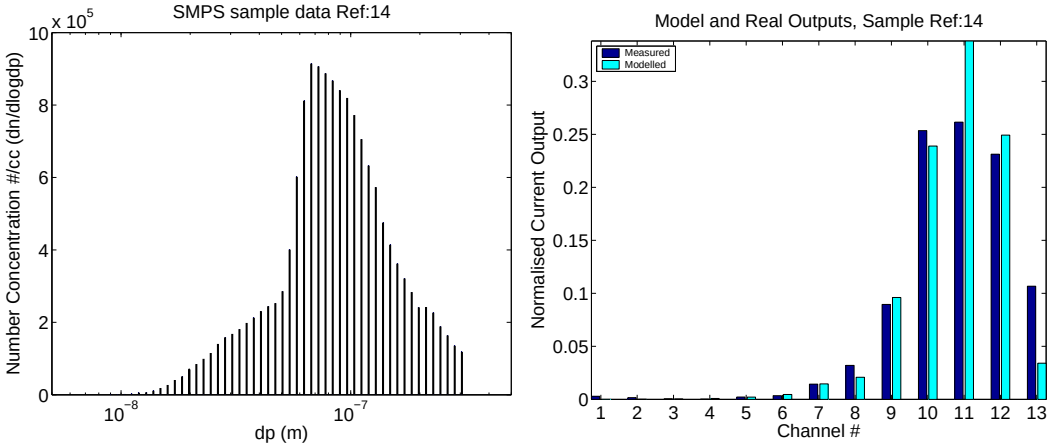

Figure 9.11: Predicted and Measured outputs comparison sample 014

though some broadening can be seen, especially toward the higher channels. This is most probably an effect of the non-uniform flow in the classifier that is not modelled, and also the wider than modelled charge distributions. The same effect is also likely responsible for the higher measured signals seen in channel 13 in figures 9.8, and 9.9.

Figures 9.12 to 9.15 show outputs for $NaCl$ samples that are "cut" with the DMA to give a narrow or "monodisperse" size distributions.

The overall concentration of the sample in fig 9.12 is low, so in the measured output, signal noise can be seen in some channels where there are likely no particles. Outside the noise the correlation between predicted and measured outputs is good.

Figures 9.13 to 9.15 all show measured distributions with peaks in the same location as predicted, but with some degree of broadening. This broadening is more severe for samples with higher mean diameters. Again the broadening is thought to be down to the non-uniform flow in the classifier, and also wider than predicted charge distributions.

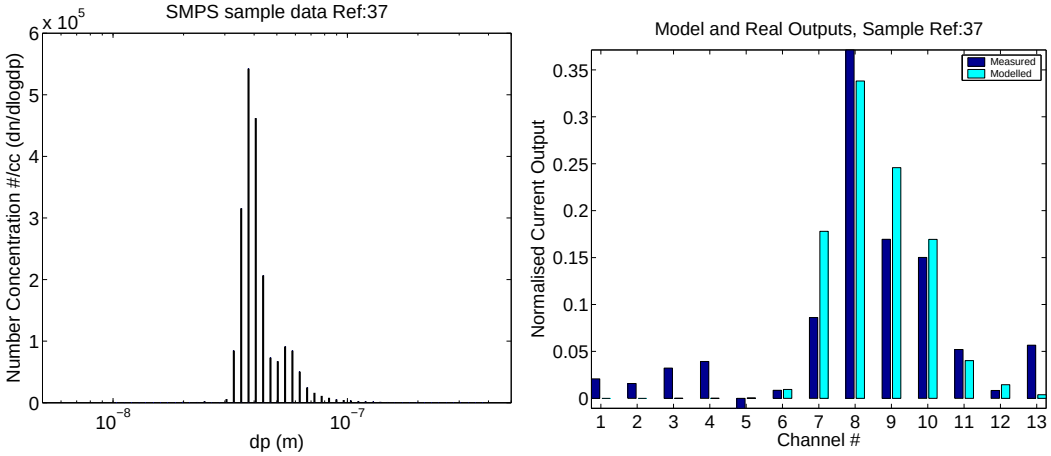

Figure 9.12: Predicted and Measured outputs comparison sample 037

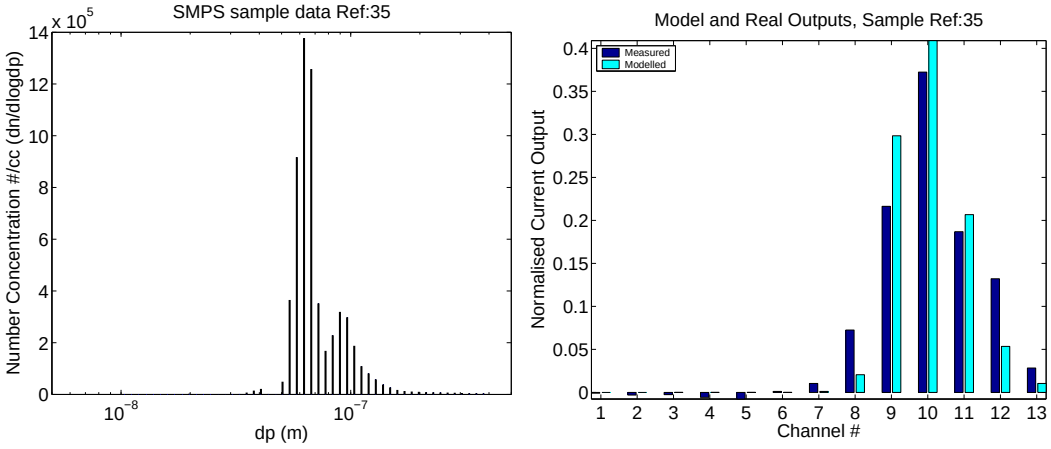

Figure 9.13: Predicted and Measured outputs comparison sample 035

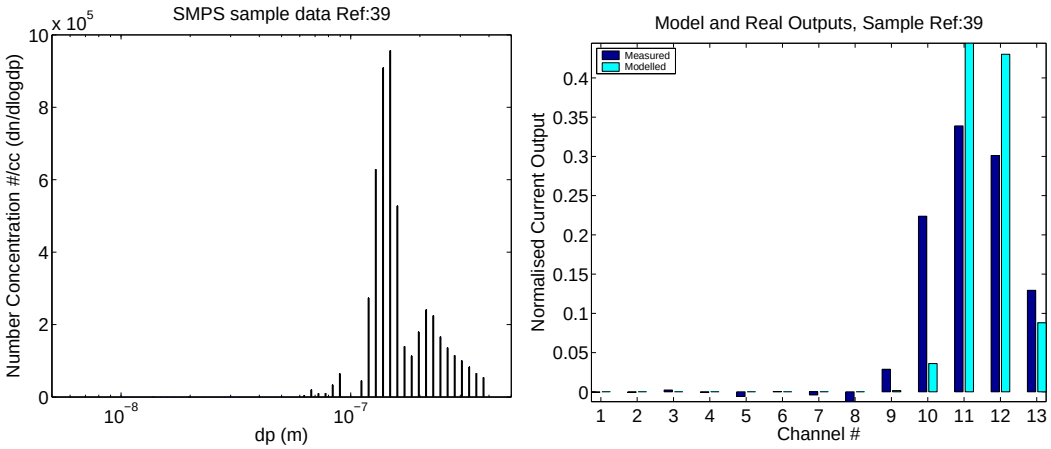

Figure 9.14: Predicted and Measured outputs comparison sample 039

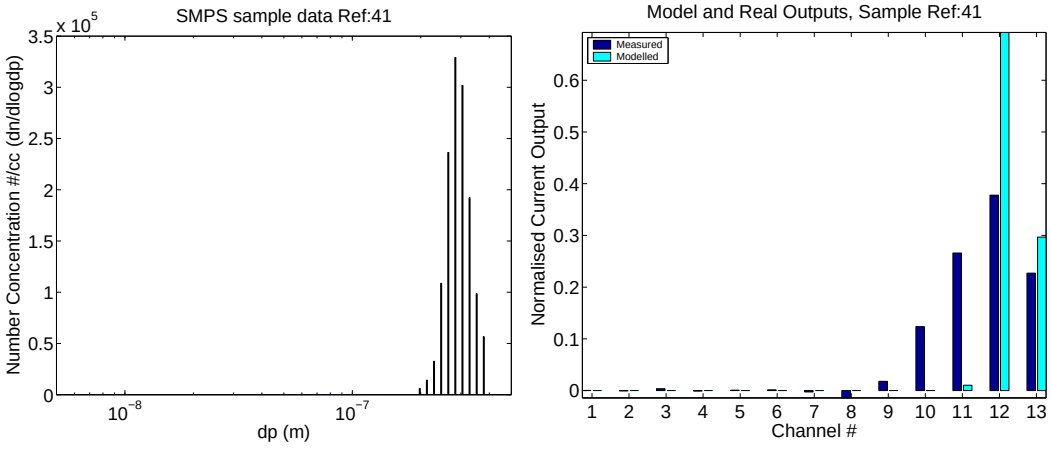

Figure 9.15: Predicted and Measured outputs comparison sample 041

9.4.5 Analysis of Results

There are several sources of error that can result in differences between predicted and measured results. It is convenient to classify these errors into two groups: loss errors, and model errors.

Loss Errors Loss errors are common in existing particulate instrumentation, typically these errors can be empirically characterised, and correction factors can be applied. The Nanoparticle Spectrometer has two sources of loss error. The first of these is diffusion losses through precipitation. Aerosol particles that come into physical contact with walls or screens within the instrument will be deposited, and thus removed from the sample before they are counted.

The main source of precipitation losses in the NPS is the mesh screen between the classifier and the electrometer filters. Charged particles must pass through this mesh, but they are attracted towards it. A large proportion of losses is expected on this screen.

The second source of loss errors is electrometer filter penetration. It is possible for some particles to penetrate the electrometer filters, and hence not be counted. The primary mechanism for deposition on the filters is diffusion; therefore penetration will be higher for larger, less mobile, particles.

The penetration of the filters was tested. An aerosol with a large concentration and wide size distribution was generated and then sampled with the instrument. CPC measurements were taken downstream of the filters and any penetrating particles were counted. Using an estimate for the average elementary charge number for the particles in each channel, and comparing the current signals in each channel with the CPC measurements it is possible to obtain a percentage penetration for each channel. The results of this test are shown in fig 9.16

Fig 9.17 shows the theoretical filter penetration for our filters assuming an average fibre size of $12\mu m$. This was generated using the theoretical model developed to predict filter efficiency described in Chapter 7.

The measured channel penetration seems to follow a similar trend to that of fig 9.17 with the exception of channel 9. The high penetration in this channel could be evidence of leakage in the filter case, allowing flow to bypass the filter material.

Data from the electrometer current measurements presented in section 9.4.4, and SMPS measurements from section 9.2, and also separate CPC measurements made on each channel all agree that there is an overall average loss of particles in the instrument that is 13 times the amount of particles that are actually counted.

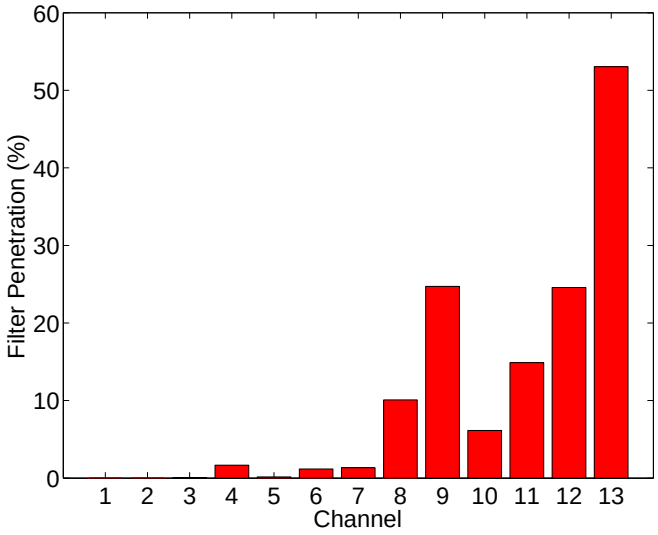

Figure 9.16: Percentage particle penetration for the electrometer filter in each channel

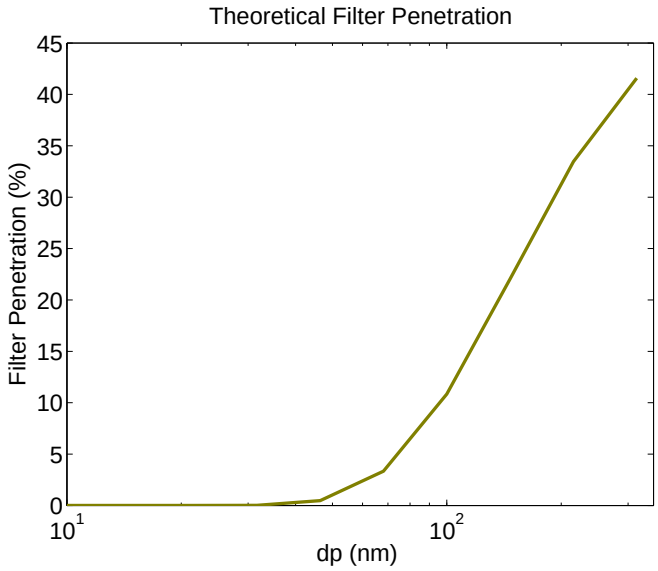

Figure 9.17: Theoretical particle penetration for the electrometer filter against diameter

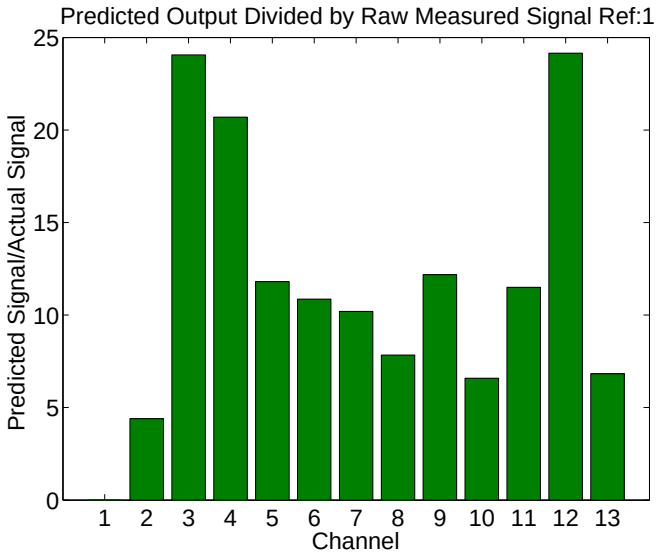

Figure 9.18: Predicted output divided by Measured output sample 1

It is expected that diffusion losses will have a greater effect in the lower channels, and that penetration losses will have a greater effect in the higher channels. Therefore it might be expected that losses are higher than average in the lowest, and highest channels, and perhaps a little lower in those in between.

Fig 9.18 shows the predicted output signal divided by the measured output signal for sample 1. This sample was used as it is the broadest of our samples, and has the highest concentration. The trends discussed above can clearly be seen, there are higher losses in the high and low channels with lower losses in between, with the notable exception of channel 9 which has the suspected "leaky" filter.

Channel 1,2 and 13 appear not to follow the predicted trend in this plot. In the case of channel 1,2 this is because effectively no signal was predicted or measured in these channels. In the case of channel 13, the result is affected by a higher than predicted measured signal in the channel due to diffusion in the classifier (see figure 9.8).

The strategy for dealing with these loss factors would be firstly to look at reducing the losses. Using for example more efficient filter materials, and/or a less dense mesh screen. Inevitably a correction function will have to be applied. This would be determined experimentally and would presumably look similar to the graph shown in fig 9.18. More experimental data would be needed for an accurate correction function. For this reason the data presented later in this thesis uses only a loss correction factor k_l for the overall average loss (13×).

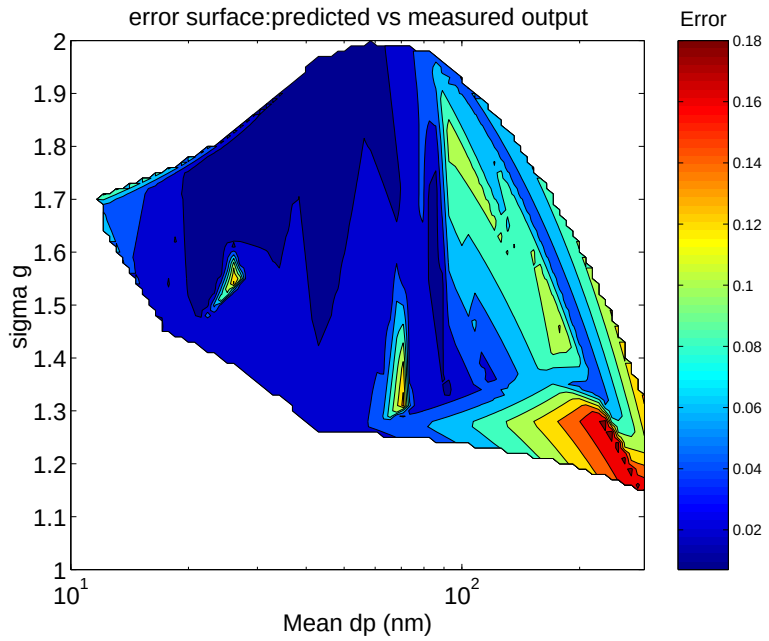

Figure 9.19: Squared error between predicted and measured results across the NPS' range

Modelling Errors The second group of errors between predicted and measured results are modelling errors. These are due to shortcomings in the model. The two main shortcomings have both been discussed previously in this chapter, these are.

1. The assumption that particle residence time in the charging zone of the charger is uniform, when in reality it is not

2. The assumption that the flow in the classifier is uniform, and there is no diffusion

These error sources are only reducible by improvements in the model.

Error Surface in order to understand how the difference between predicted and measured results varies with different type of sample, an error surface was constructed. All the samples generated in the instruments output testing were approximated to be lognormal, and the geometric mean, and geometric standard deviation were noted. The squared error between the normalised measured and predicted results was calculated. This is shown in fig 9.19 plotted against GM and GSD, and interpolated to form the surface.

Due to difficulties generating the desired samples, discussed in section 9.4.3 there were more results in some areas of the instruments range than others. this will effect

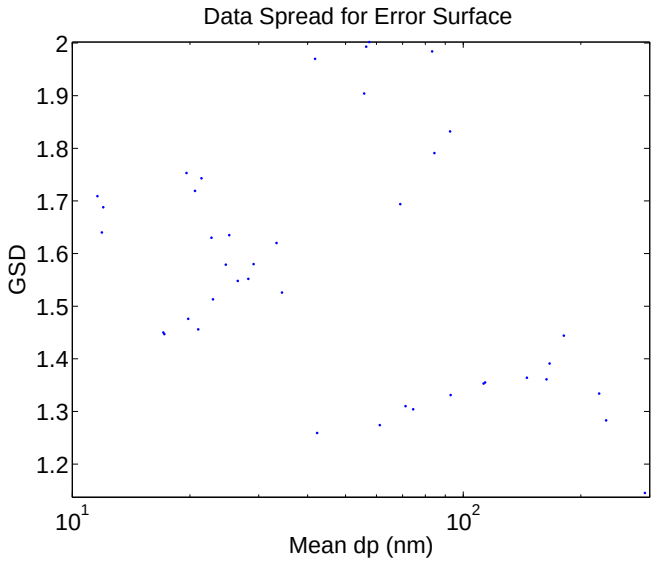

Figure 9.20: Spread of data used to generate fig 9.19

the accuracy of the interpolated error surface. The spread of the data used to generate fig 9.19 is shown in fig 9.20.

The error surface shows that there is a clear "danger" area where the error is higher than others. This is the small region corresponding to monodisperse samples with high mean diameters. This is thought primarily to be down to the unpredicted non-uniformity of flow in the classifier, and the wider than predicted charge distributions, which are expected to be the most severe in the high channels, and the effects of which will be most pronounced on narrowly distributed samples.

A slight increase in error can be seen in the smallest geometric means. This could be due to higher diffusion losses in this region. There is a large yellow area on the right side of the graph. The data spread in fig 9.20 shows that there are few results in this area so no firm conclusions can be drawn about the performance of the instrument in this region.

9.5 Look-up Table Results

9.5.1 Introduction

The previous section dealt with the comparison between the predicted and modelled electrometer output signals for a given sample. This section deals with the post processing of the measured outputs to identify the sample size distribution.

The Instrument model was used to generate a table of predicted outputs for lognormally distributed aerosol samples. The structure of the table is 51 columns for mean diameter, ranging from $10nm$ to $300nm$ in logarithmic increments, and 19 rows for geometric standard deviation ranging from 1.1 to 2 in increments of 0.01. Each cell of the table contains an array of 13 numbers, which are the predicted currents for each channel normalised to a total of 1. The model runs for approximately 40 hours to generate a table this size.

The look-up process involves comparing the normalised output signal, with all the predicted signals in the table. This process takes less than $\frac{1}{10}$ second on a standard desktop PC with a $2.5GHz$ processor. When a matching signal is selected three numbers associated with that signal are returned. The first two are the mean, and the GSD of the lognormal, the third is the charge per particle C_p associated with that distribution. The concentration of the sample N_p is calculated using equation 9.1,

$$N_p = \frac{A_T k_l}{Q_A C_p} \tag{9.1}$$

where A_T is the total measured current, Q_A is the sample flow rate and k_l is the loss correction factor.

The correction factor is only an approximation that requires improvement in the form of a correction function, so the following analysis will focus mainly on the selection of the correct size distribution.

In this section results for some of the samples tested are presented. The SMPS measured distribution is compared to the lognormal distribution selected by the NPS analysis, and any differences are discussed. It must be remembered that differences in the distributions may be down to problems with the modelling and selection process and/or deviation of the sample distribution from lognormal.

9.5.2 Results

The results presented in this section are selected to show an accurate as possible picture of the performance of the look-up table selection process across the range of the instrument. To this end, the results have been divided into three sections: Narrow distributions, medium distributions, and broad distributions. The samples in each section cover a range of mean sizes.

Narrow Distributions

Narrow distributions in the lower half of the mean size range show very good agreement between NPS, and SMPS. Fig 9.21 shows that the correct GM and GSD has been

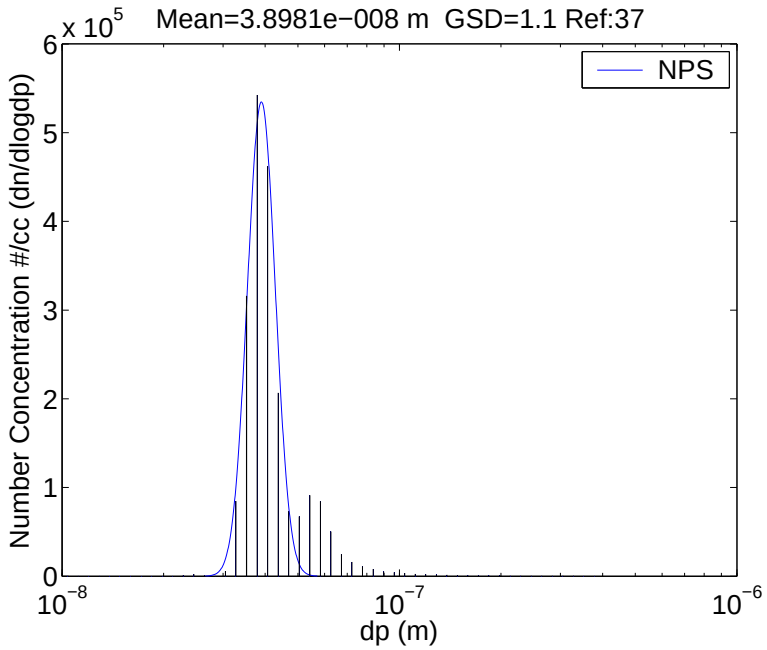

Figure 9.21: NPS and SMPS analysis, Sample 37

selected from the look-up table, and the amplitude is also in agreement. As the mean increases, The NPS look-up program has a tendency to select wider distributions than the SMPS, although the selection of the mean is in agreement. (fig 9.22). At the highest mean values, there is not a close agreement. Here samples selected are generally much broader than the SMPS results, and the mean is at a slightly lower size (fig 9.23). Throughout all testing, the NPS results for samples with narrow distributions and high means had the least agreement with SMPS data. This is in agreement with the error plot for the instrument in fig 9.19.

Figure 9.24 shows the measured and predicted outputs for sample 38, and also the signal from the look-up table that was selected. Visual assessment of the signals shows that the measured and selected signals are not very alike. Therefore it is possible that with modifications to the look-up program, a better result could be selected.

Medium Distributions

The sample distribution in fig 9.25 crosses the lower range of detection for the SMPS, so a comparison between the two instruments cannot be made for the smaller size end of the selected distribution. However, from the right hand side it looks as if the correct GSD has been selected. The mean is also a good selection although at a slightly larger

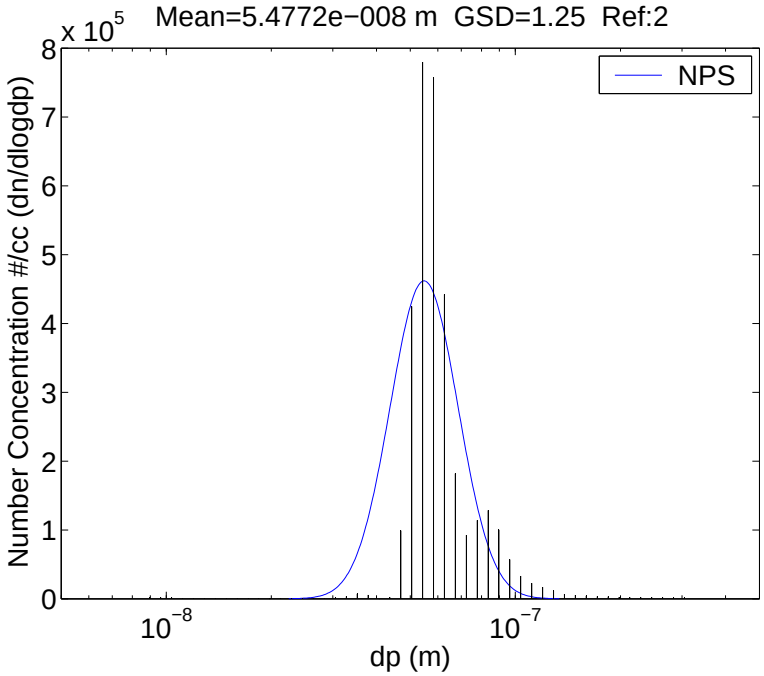

Figure 9.22: NPS and SMPS analysis, Sample 2

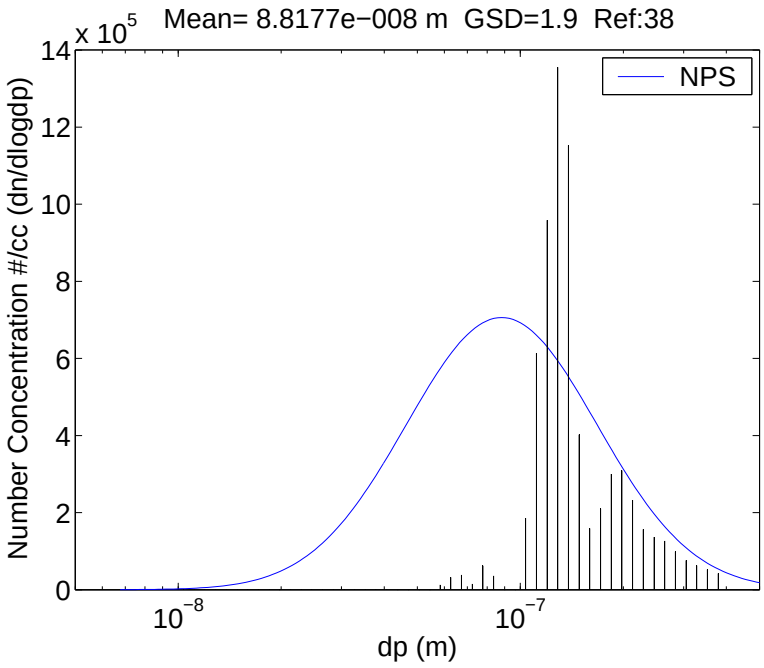

Figure 9.23: NPS and SMPS analysis, Sample 38

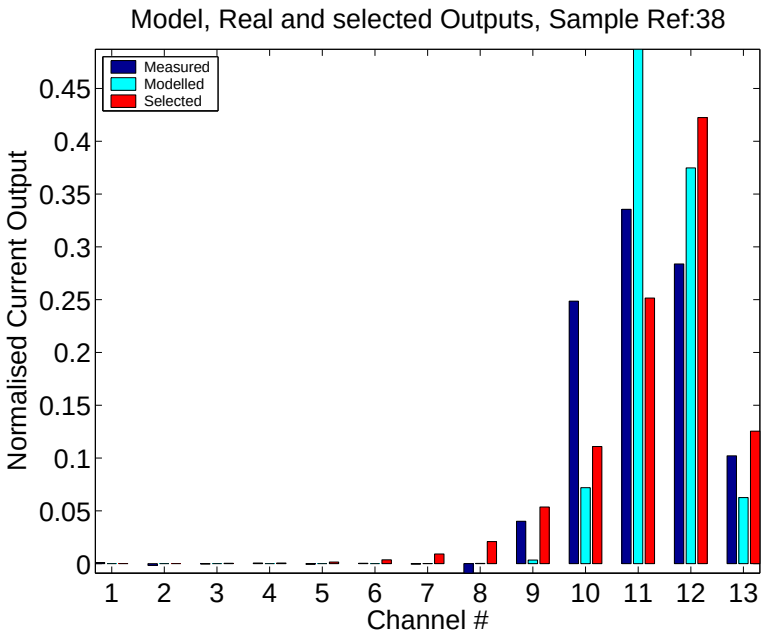

Figure 9.24: Comparing predicted, measured, and selected signals for sample 38

value that that of the SMPS geometric mean. This could be due to higher diffusion losses of smaller particles in the very early channels biasing the distribution to the right.

The overall concentration appears to be slightly underestimated; this could be because the correction factor applied to the measured data is the average for the whole range, but losses are known to be higher for small particles.

Fig 9.26 is for a sample with a geometric mean of $22nm$ the log-normal distribution selected is a very good match. Again the overall magnitude is slightly underestimated.

Sample 12 in fig 9.27 is a good example of a non log-normal distribution produced when the sample is cut with the DMA. Considering the non lognormal shape of the sample, the distribution selected from the lookup table is a good approximation.

Sample 3 in fig 9.28 is also selected using the DMA, and also not a perfect log-normal. The selected distribution has the correct mean. The GSD agrees reasonably well with the right hand side of the sample distribution, but overall is a little too wide. This could be a less severe example of the broadening seen in the monodisperse samples with larger means.

Broad distribution

The selected log-normal distributions for broad distributions were in very good agreement with the SMPS distributions, see figures 9.29 and 9.30. This is because the NPS

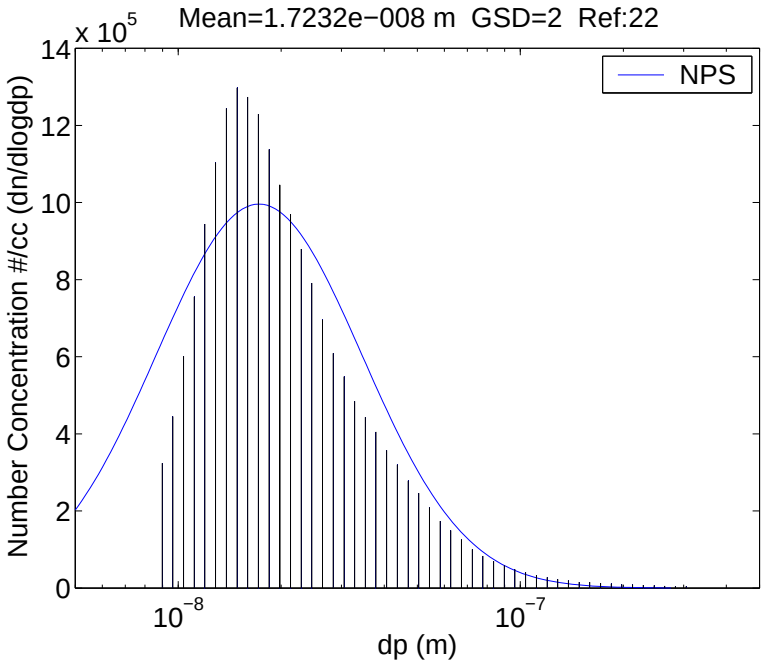

Figure 9.25: NPS and SMPS analysis, Sample 22

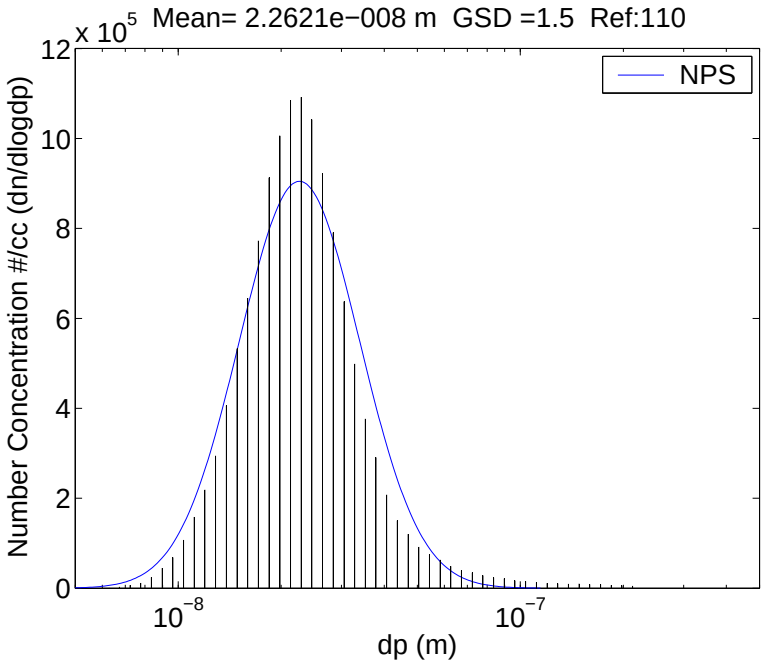

Figure 9.26: NPS and SMPS analysis, Sample 110

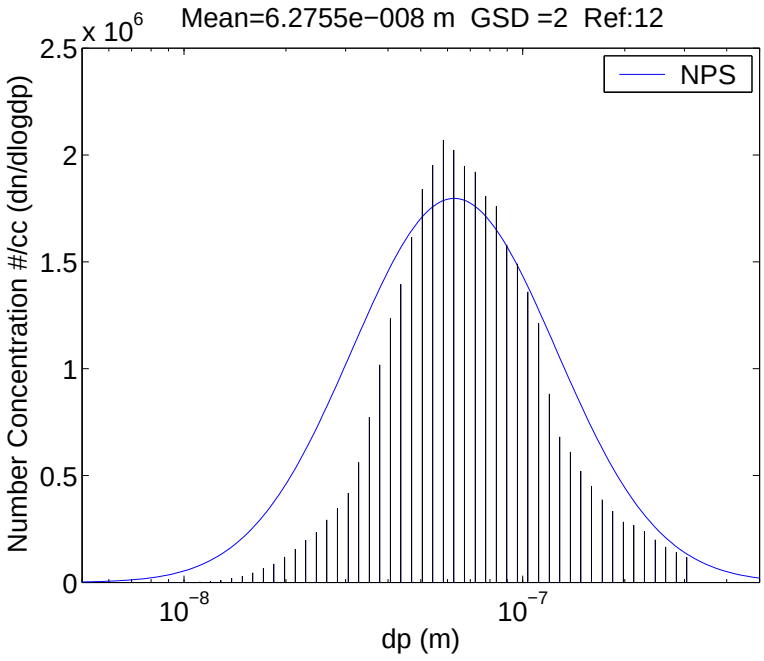

Figure 9.27: NPS and SMPS analysis, Sample 12

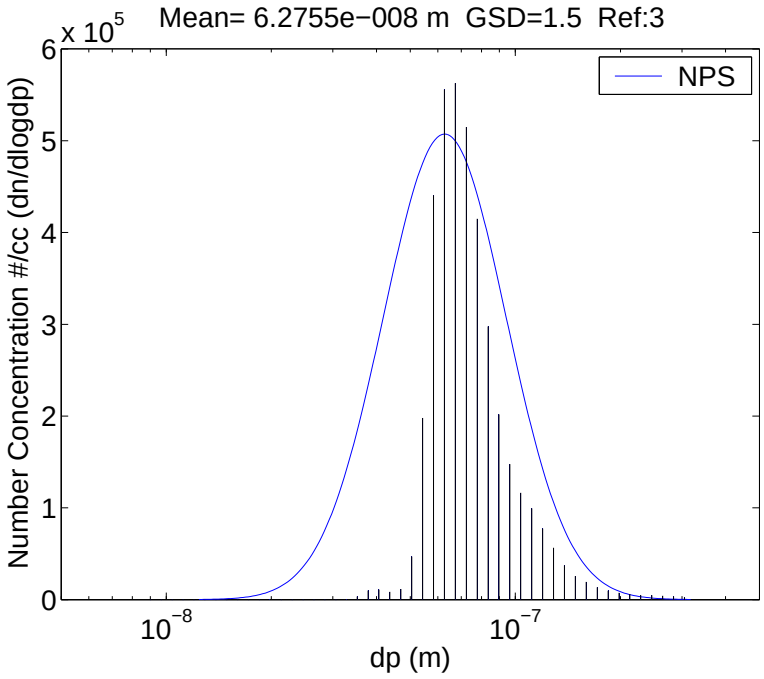

Figure 9.28: Comparing predicted, measured, and selected signals for sample 3

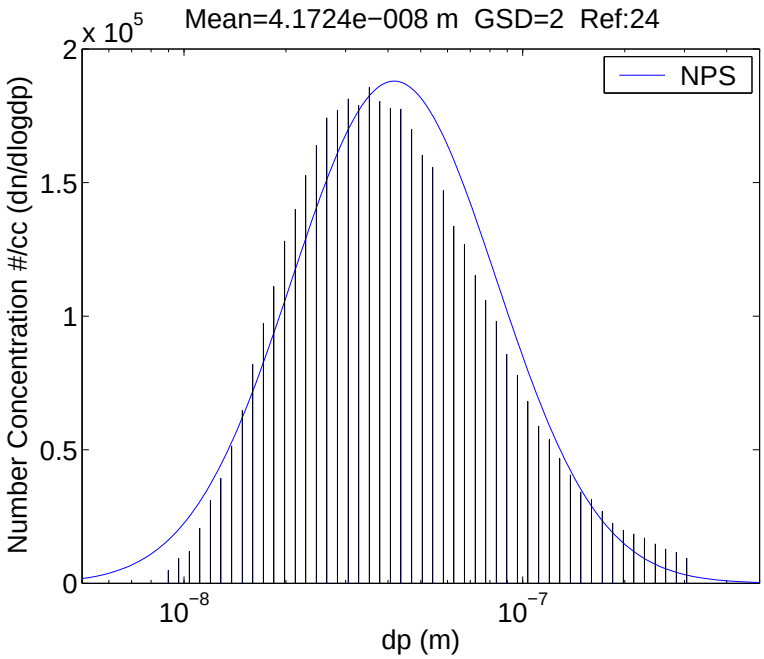

Figure 9.29: NPS and SMPS analysis, Sample 24

generally has a large amount of information about these distributions, with signals in almost every channel. Therefore errors in the signals in one or two channels are unlikely to affect the overall result significantly.

9.5.3 Conclusions

The accuracy of the distributions produced by the least squares look up system tally well with the error surface plot shown in fig 9.19. Samples with high mean sizes, and narrow distributions are shown as the region with the highest error in the plot, and indeed these samples have been shown to have the worst results with the look-up table.

The NPS produces good size distribution matches outside this small region and excellent matches for samples with broad distributions, and samples with means in the middle (logarithmic) of the size range of the instrument.

The overall concentration of the sample can be underestimated, but this is not due to the performance of the lookup system, this is down to the accuracy of the loss correction factor.

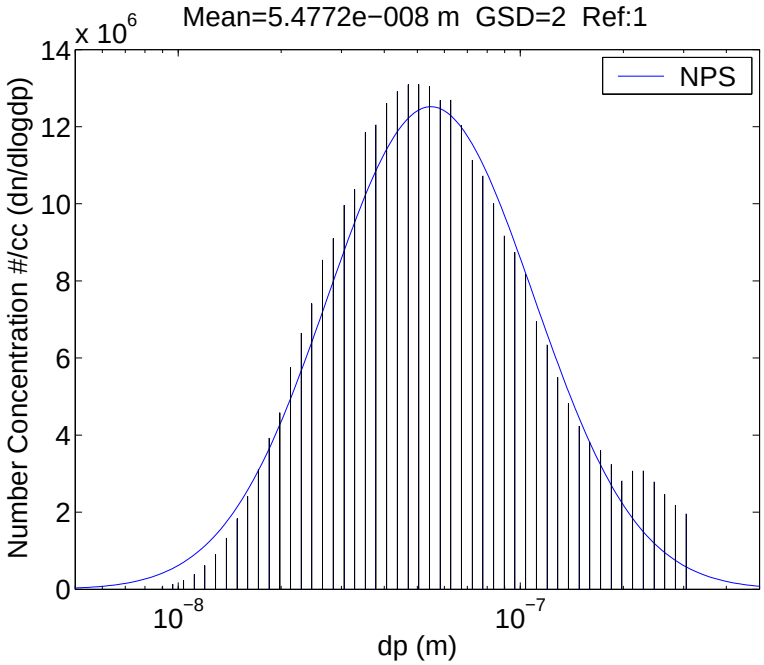

Figure 9.30: NPS and SMPS analysis, Sample 001

Chapter 10

Discussion

In this final chapter several arising from the experimental testing of the Nanoparticle Spectrometer are considered. Firstly, sources of error in the experimental results and uncertainties arising from factors that were not tested are addressed. Secondly some the known issues with the performance of the NPS that have been uncovered by the tests are discussed. Considering these issues some strategies for future work on the NPS are suggested and finally, the main conclusions of the project are presented.

10.1 Possible Sources of Error and Uncertainty

Aerosol Generation

The intended application of the NPS is the transient measurement of aerosol samples from an engine exhaust. During the course of the experiments carried out on the NPS, combustion aerosols were not measured; the aerosols used were salt ($NaCl$), and sulphuric acid (H_2SO_4). Sulphuric acid particles are spherical liquid droplets and salt particles are roughly cubic. Therefore the assumption of spherical particles used in the charging model is reasonable for the aerosols tested. However a large fraction of the the particles in engine exhaust are carbonaceous agglomerates, which can have irregular shapes [Rogak & Flagan, 1993]. The particle diameter 'd_p' is less easily defined for an irregular shaped particle, and the shape of the particle can have an effect on the accretion of charge [Biskos, 2004]. Therefore in future testing the performance of the NPS would also have to be validated for combustion generated aerosols.

Through the process of generating particles the Collison nebuliser can also generate ions and hence charge the particles. The size of the droplets that come out of the nebuliser can be up to $10\mu m$ and can therefore pick up many elementary charges. When the droplets have shrunk due to evaporation the charge will remain, leaving

small particles with high charge levels, assuming the Rayleigh limit is not reached[1]. This can lead to problems because the charging model assumes a neutral charge level on samples entering the charger. Therefore the samples generated by the nebuliser have to be neutralised before being used for testing.

Initial Charge

A properly functioning bipolar neutraliser will always give an aerosol sample the same charge distribution, regardless of the initial charge levels on the aerosol, provided that the aerosol resides for long enough in the charging zone. A unipolar charger will only add charge to any existing charge level of the same polarity on the aerosol sample hence the initial charge state of the aerosol is important. IC engines are known to produce charged particles [Collings et al, 1986] therefore this may effect the charge distribution on combustion generated aerosols analysed within the NPS. Work by Biskos [2004] showed close agreement between modelled and experimental results for diffusion charging of combustion generated aerosols, when the model assumed no initial charge. However, if the initial charge on combustion generated aerosols was shown to affect results in the NPS then either the sample would have to be neutralised before analysis in the NPS, or the charging model would have to incorporate an estimate of the initial charge levels.

Multi-modal Lognormals

The size distributions of the aerosol samples used in the tests described in this thesis were all approximately uni-modal and lognormal. As such the look-up table compiled for this work contained only signals for uni-modal lognormal distributions. Many combustion generated aerosol samples are bi-modal, therefore it would be useful if the NPS could also analyse multi-modal distributions. In principle this is quite possible for the instrument hardware, or model, but would require a significant expansion of the look-up table, which could slow down the speed of the look-up algorithm and create increased possibilities for signal miss-selection. It is likely that the look-up algorithm would require a significant re-design in order to accurately process multi-modal lognormal distributions. Some strategies for this are discussed in section 10.3.

[1] See section 2.4.2 for an explanation of the Rayleigh limit

10.2 Known Issues with the NPS

The experimental testing of the Nanoparticle Spectrometer highlighted several areas in which the performance of the instrument could be improved. This section summarises these main issues and section 10.3 describes some strategies to improve the performance of the NPS system in future work.

Charger Residence Time

The residence time in the charger is modelled as constant, where as in reality it is slightly distributed due to the non-uniform velocity of the aerosol in the charging zone. The effect of this is to make the charge distribution broader than predicted, with the effect being greater for larger particles because they can accrue more charge. This issue can be addressed by attempting to improve the flow in the charger with a re-design, and also by incorporating the distributed residence time into the charging model.

Flow in the Classifier

The model used to simulate the particle tracks in the classifier predicts a "top hat" shaped transfer function in each channel of the NPS, whereas in reality the function has an approximately triangular shape and its mobility range overlaps with that of adjacent channels (fig 10.1).

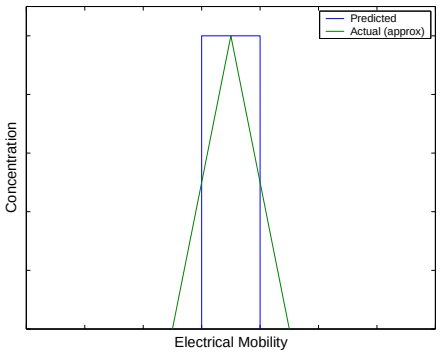

Figure 10.1: Examples of NPS channel transfer functions, modelled and real.

It is thought that the main reasons for this are diffusion and non-uniformity of the flow in the classifier. The effects are more pronounced in the later channels, which could probably due to the longer flight times of particles and also could be due to a less-uniform velocity profile later in the classifier due to the growth of the laminar

boundary layer. Also flow effects due to the exhaust flow at the end of the classifier could have an effect on the final channels.

The effect of this is to make the output signals of the NPS broader than predicted; particularly in the case of aerosols with narrow size distributions that have large mean sizes. Taking steps to study and improve the flow in the classifier may yield performance improvements. Any diffusion effects that remain after this step has been taken can be accounted for by incorporating diffusive effects into the instrument model transfer function.

Particle Losses

A particle entering the NPS can avoid detection by one of three ways. It can fail to become charged in the charger, it can be lost though precipitation, or it can penetrate the electrometer filter. The charge levels on the aerosol are characterised by the charging model. Precipitation and penetration losses must first be minimised and then characterised empirically so that they can be corrected for.

Precipitation losses in aerosol instruments are mainly a problem due to particles of different mobilities precipitating in different ways. High mobility particles are more diffusive, and are more likely to precipitate through diffusion. Low mobility particles are more likely to precipitate through impaction when the aerosol flow is forced to change direction by a wall or a pipe bend. As particles of different mobilities are lost in different proportions, the size distribution of the aerosol will be affected as well as the overall concentration. Therefore detailed knowledge of the precipitation losses inside a particulate measurement instrument are required in order to accurately correct for them.

The experimental testing of the NPS has revealed high precipitation losses. There are small losses in the charger, but the main losses are occurring on the mesh that separates the classifier from the electrometer filters. Particles are electrostatically attracted to this mesh and the flow forces are relied upon to draw the particles through the mesh. However in the current design more than 90% of the particles precipitate on the mesh. Losses at this high level can are a serious problem, especially at low sample concentrations. Therefore it would be beneficial to reduce these loss levels.

The experiments have also shown evidence of higher precipitation losses among more mobile particles. Characterising the relationship between particle losses and mobility is a priority for determining an accurate loss correction function for the instrument.

Penetration of the electrometer filters was also detected in the NPS though these losses could be reduced by improved filter design.

Noise

The noise levels on the electrometers in the prototype NPS were recorded as 4fA RMS. These noise levels are acceptable and did not prove problematic for the majority of samples used in the experiments presented in this thesis. However, lower noise levels may be achievable through changes in the instrument design. The main source of interference with the electrometers is the high voltage plate in the classifier. Measures that could reduce the noise include smoothing the voltage signal on the deflection plate and improving the screening between the electrometers and the classifier.

Presently the screening is provided by the mesh screen between the classifying region and the electrometers. Using a more dense mesh for this screen would reduce the noise on the electrometers. However, as mentioned in the previous section the mesh screen is a cause of precipitation losses and increasing the density of the mesh would result in even more losses. Therefore there either has to be a trade off between noise and losses, or a re-design to this section of the instrument.

10.3 Future Work

10.3.1 Design Changes

This section contains ideas for the re-design of the next prototype NPS that could improve, the accuracy of the NPS and alleviate some of the problems mentioned in this chapter.

Filter Segregation

Particle precipitation losses on the mesh between the classifier and the electrometer have been shown to be high; reducing the density of the mesh will reduce these losses but also make the mesh less effective at screening the electrometers from the interference of the voltage signal on the deflecting plate.

Figure 10.2 shows a sketch of a possible design change to the filter section of the NPS. Here the filters are not directly behind the mesh but enclosed more completely in an earthed metal case with a single small inlet for the aerosol. This would make the filters more completely screened from all sources of interference, resulting in lower noise levels on the electrometer signals.

In this design the purpose of the mesh is simply to create the desired electric field in the classifier. Therefore the mesh can be of a very low density, which will result in lower precipitation losses.

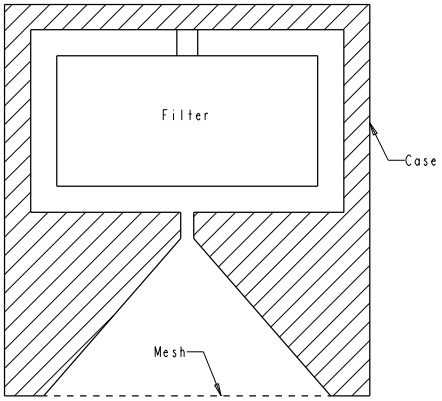

Figure 10.2: Integrated design for improved filter screening

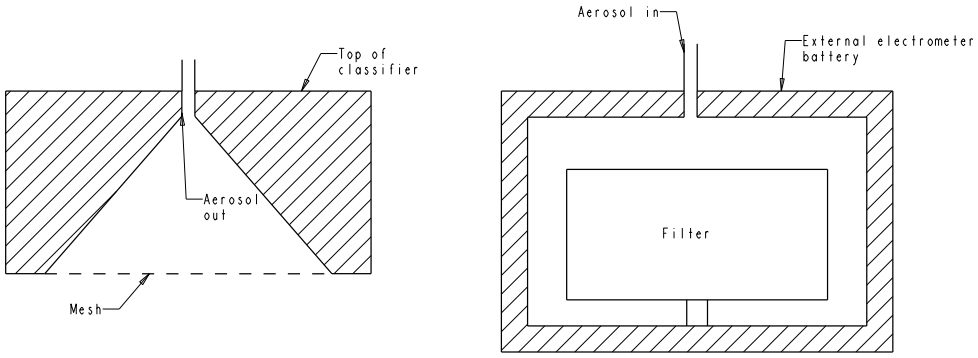

Figure 10.3: Separate design for improved filter screening

The integrated design shown in fig 10.2 would be suitable for an NPS where a compact design is required, for instance in an on-board vehicle application. For laboratory based work a design where the classifier and the electrometer are separated, as in figure 10.3, might be more suitable. One advantage of a separate electrometer battery is that some space for the filters is freed up, allowing potentially more effective filter designs to be used. A further advantage of this design is that it would allow different counting devices to be connected to the classifier. Optical counting devices such as the CPC are preferable to electrometers when analysing aerosols with very low concentrations and this feature would make the NPS a more versatile instrument for laboratory use.

Using a Mesh Voltage

If the above design change is implemented then the mesh would no longer form part of the Faraday cage around the filters. This means that the mesh can be offset to a higher voltage, which would significantly reduce particle losses. In this situation, as particles approach the mesh the ground voltage on the walls behind the mesh imposes a field helping to draw the particles though the mesh without precipitating.

A model has been designed to explore the potential benefits of this effect. Fig 10.4 shows the electric field in the region of a course mesh at an offset voltage, and also flow velocity vectors for an air flow in the x-direction through the mesh. Vectors for flow velocity and the velocity due to the electric field on particles can be interpolated across the modelled region to build particle tracks.

Fig 10.5 shows particle tracks for two different simulations. Simulation 1 uses a voltage of $5000V$ on the left boundary of the modelled region, and $0V$ on the right boundary, the Mesh is also at $0V$. Simulation 2 uses $5500V$ on the left boundary, 0V on the right boundary, and $500V$ on the mesh. Both models have a gas flow of $0.05m/s$ in the x-direction.

The particle tracks shown are for singly charged $18nm$ particles that have trajectories that are incident with gap between two mesh wires. The particle tracks suggest that many more particles will pass through the mesh when the mesh voltage is offset as in the simulation on the right. In fact assuming that particles are evenly distributed in the flow, these simulations show 45% of particles incident on the gap between the wires passing through in the simulation with the grounded mesh, and 80% of incident particles passing through in the simulation with the offset voltage mesh. More details on the model used for this simulation can be found in appendix A.

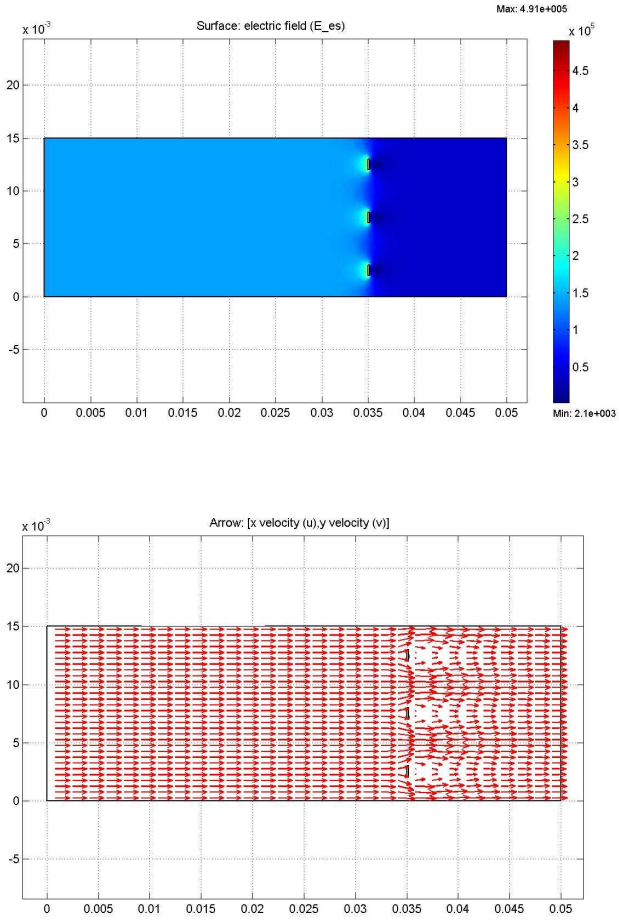

Figure 10.4: Field and flow visualisations from the mesh model

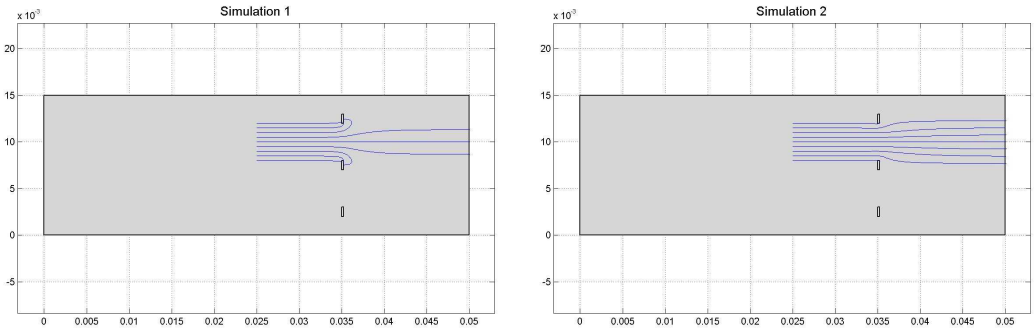

Figure 10.5: Particle tracks in mesh model

Classifier Flow

The resolution of the NPS is highly dependant on the flow in the classifier being laminar with a uniform velocity distribution. Testing has highlighted non-uniformity, and diffusion in the classifier as being responsible for reducing the resolution of the NPS.

The flow inside the classifier can be studied in more detail, by modelling using Computational Fluid Dynamics (CFD). Additionally the temporary replacement of one of the classifier walls with a transparent acrylic or glass wall would enable the flow inside the classifier to be visualised using smoke. These tests would highlight any changes that may be required to the internal geometry of the NPS to improve the flow in the classifier.

As well as design changes to improve the flow, such as better control over the flow out of the channels would be of great benefit. The current system uses capillary tubes to control the flow rate out of the channels. Measurements of the flow rates out showed a total variation of $0.2l/min$ which is approximately 6% of the flow out of one channel.

Charger Flow

Details of changes made to the charger design in order to improve the flow in the charger were given in chapter 8. The aim of improvements to the charger flow is to give a constant residence time of particles in the charging zone, which makes the charge distribution narrower and more predictable. CFD modelling of the flow in the classifier could highlight potential changes in the design that may make the residence time more uniform. These changes could include introducing a baffle upstream of the flow screen, changes to the profile of the charged sample outlet, or further changes to the type of flow screen.

Charger Field

Experimental work on corona wire chargers has shown that using an A.C. current to apply a small alternating field in the charging zone can produce higher charging efficiencies and lower precipitation losses [Kruis & Fissan, 2001, Biskos et al, 2005]. This design change would be simple to implement in the NPS' charger and could improve performance.

10.3.2 Model Changes

The problems of distributed residence times in the charger and diffusion and non-uniform flow in the classifier may be helped by design changes, but they can never

be eradicated. In order to completely eliminate the problem their effects must be accounted for and this means incorporating them into the instrument model.

Charger Residence Time

The charging model has already been adapted to include a residence time function for the Sonic Jet Charger, as described in chapter 6. Here the residence time function for a well-stirred reactor was used. Study of the flow in the charger would have to be carried out to determine a suitable function for the residence time in the NPS' charger and then this could be incorporated in the charger model in the same way.

Diffusion Modelling

Incorporating a model for diffusion into the numerical particle tracks model would be one way of modelling the diffusion in the classifier. However, it may be simpler to use empirically determined transfer functions for each channels like those measured in the channel mobility tests described in chapter 9. The empirically determined transfer functions could be combined with the existing model to give output signals with diffusion taken into account.

10.3.3 Changes to the Look-up Algorithm

There are two motivations for making changes to the look-up algorithm: firstly if the look-up table is expanded to contain multi-modal lognormal distributions then a faster algorithm may be required. Secondly, testing has shown the current algorithm to misselect under certain conditions.

A detailed study of the look-up algorithm would be an important part of the future work as there are many possibilities to be explored, such as different search methods to the ones investigated in this thesis and different ways of preparing the signals for analysis.

One strategy that could be useful in improving both the speed and that accuracy of the look-up algorithm is to include a number of logical statements to refine the area of the look-up table that is to be searched.

Figure 10.6 shows an example of how logical steps could be implemented before the search is run. Certain details about the shape of the signal are ascertained using questions, for instance about the location of the peak signal and the range of channels covered by the signal. Each possible combination of answerers corresponds to a specific region of the look-up table, which is selected and this area alone is searched.

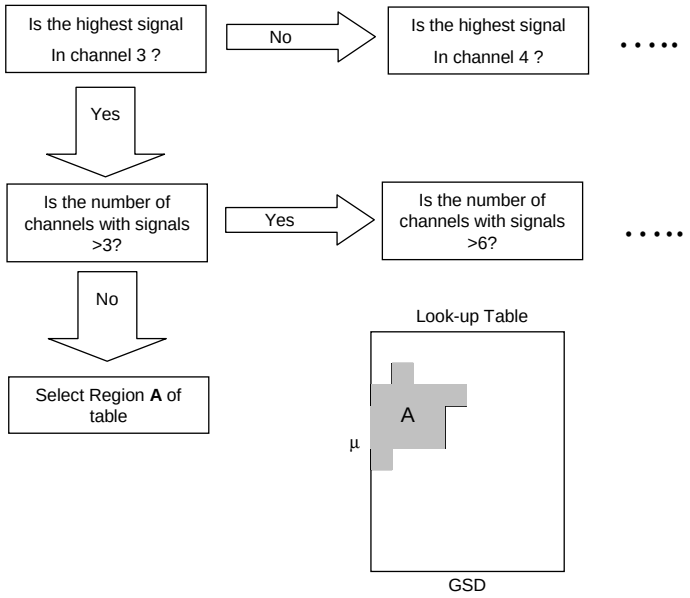

Figure 10.6: Example of the use of logical decisions in look up algorithm.

In the case of a large look-up table such as would be required for analysing multi-modal lognormal distribution the benefit of this would be that the algorithm would run much faster if the search area could be significantly reduced. However, this method could also be used to improve the accuracy of selection. Fig 10.7 is a repeat of figure 9.24 from chapter 9. This shows the predicted, measured, and selected signals for a sample which the look-up table mis-selected. It shows that there are some obvious differences between the measured and selected signal, such as the channel in which the peak signal occurs, and the range of channels, which the signals cover. It is possible that this situation could be improved by selecting a different search system to the method of least squares, but logical statements could also be used to assist the algorithm by limiting the choices available to a small area that is close to the measured signal.

10.3.4 Additional Testing

As part of the future work of this project some additional testing would be required to asses the suitability of the NPS for the specific application for which it has been designed, that is transient measurements of combustion generated aerosols from I.C. engines.

Combustion generated aerosols generated from engines were not tested for this

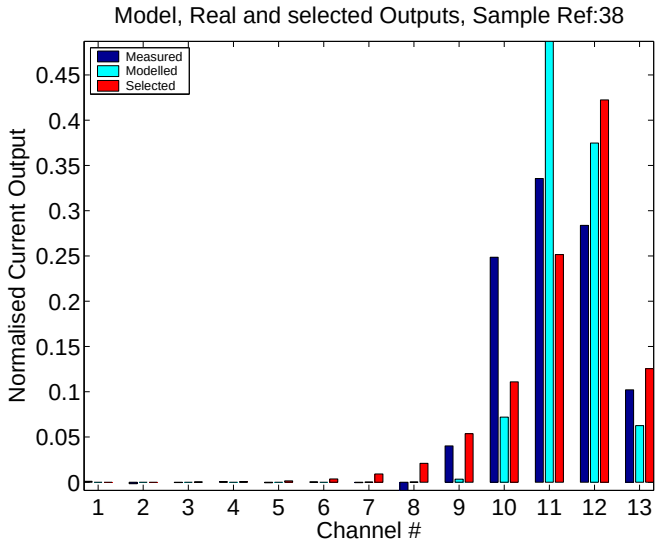

Figure 10.7: Comparing predicted, measured, and selected signals for sample 38

project as the scope of this project covers only the development and initial testing of the NPS. For the purposes of initial testing salt and acid particles generated with a Collison nebuliser provide an extremely stable source of approximately spherical aerosol particles with a uni-modal lognormal size distribution. It is appropriate when initially testing a new instrument to verify its performance first with aerosol samples of this type before moving on to combustion generated particles, which pose the further complications of irregularly shaped particles, multi-modal distributions, and transient distributions and concentrations.

In the testing of the NPS with combustion generated aerosols it would be advisable to initially use aerosols of a steady concentration and size distribution. This way it can be verified whether or not the performance is the same as for the case of the salt and acid particles used in the project to date.

Once the performance of the NPS with combustion generated aerosols is verified then testing of transient aerosol samples from engine exhausts can commence. Here the speed of response of the instrument can be tested.

Other tests that could be carried out include tests for sensitivity of the NPS to vibrations so as to ascertain the feasibility of using the NPS as an on-board vehicle instrument. Long running tests could also be used to determine if and how the performance of the NPS is affected by long periods of continuous operation.

10.4 Conclusions

In the course of this project the concept of the Nanoparticle Spectrometer has been explored using theoretical modelling, as well as experimental testing of a prototype Instrument. The work presented in this thesis has proven the NPS concept to be viable by both theoretical and empirical methods. The prototype instrument has performed well in preliminary tests, by successfully identifying the size distribution of the majority of the aerosol samples tested. However, the tests have also highlighted several areas in which the performance of the NPS can be improved and in this chapter these areas have been highlighted, and strategies for improving the performance suggested. In conclusion this section summarises the main contributions of this work and the potential advantages and disadvantages of the NPS compared to other particulate measurement instruments.

10.4.1 Main Contributions

1. A numerical model was developed to simulate the particle tracks within the NPS classifier. The electric field strength in the classifier was modelled using finite element method, and then particle tracks were calculated using a time-marching technique.

2. The Numerical model was combined with an analytical charging model to create a model that could simulate the performance of the NPS and predict the output signal for any given input aerosol size distribution.

3. Experimental work characterised the performance of the Sonic Jet Ioniser. And the dimensionless group $\frac{VZ}{du}$ was derived, which determines the efficiency of the ioniser.

4. The charger model was combined with the residence time probability density function for a well stirred reactor in order to develop a model that predicts the charge distribution for diffusion charging in a turbulent mixing chamber.

5. A look-up algorithm was developed in order to search a table of aerosol size distributions for comparison with the instrument output distribution. In the development of the look-up table a number of strategies were tested before one was selected.

6. A Prototype Charger was built, and the performance of the charger determined by experimental testing.

7. Testing of the prototype charger was used to verify the performance of the charging model.

8. Tests were carried out on a prototype NPS to characterise the transfer functions of the instrument's channels and to verify the performance of the numerical particle tracks model.

9. Tests were carried out on a Prototype NPS using aerosol samples with uni-modal lognormal distributions. The tests showed that unique output signals were produced for each sample and the accuracy of model predictions was determined.

10. The look-up table inversion method was tested using the real-life data from the NPS and the performance of the system was established

10.4.2 Five Advantages and Five Disadvantages of the NPS

Advantages

1. Other multi-channel spectrometers like the DMS, EEPS, and EAS use ring electrodes to precipitate and count the particles. The minimum size of these instruments in thus limited by the minimum ring width that gives an acceptable signal. The NPS uses a flow to draw the particles onto electrometer filters so it is not subject to this limitation and can be very compact.

2. Using a flow to draw particles into the channels also enables the use of electrometer filters inside Faraday cages as no field is required to precipitate the particles. The extra screening of the Faraday cage means that low noise levels on the electrometers are achievable.

3. As the NPS is the only single-instrument multi-channel spectrometer that uses a flow through the channels it presents a unique opportunity to combine the NPS with other instruments. For example, it could be set up so that part of the flow from each channel went to the electrometers, and part went for further analysis, e.g. electron microscopy, or mass spectrometry.

4. The two-dimensional shape of the NPS simplifies the task of modelling the instrument, making accurate simulations more feasible.

5. The simple compact design and robust look-up table inversion method make the NPS a possible candidate for on board vehicle measurements.

Disadvantages

1. The Use of a screen in the NPS causes high particle losses. Although it is highly likely that these losses could be significantly reduced with future re-designs.

2. The NPS has a relatively small size range compared with other aerosol spectrometers this somewhat limits its possible applications. Although the range is sufficient for intended application of engine exhaust measurements.

3. The use of electrometers in the NPS limits the sensitivity of the instrument when analysing samples with low concentrations.

4. The look-up table inversion means that only distributions contained in the table can be correctly identified, thus an anomalous distribution will not be detected.

5. The NPS has many separate gas flows which require a large amount of flow control compared to other instruments.

Appendix A

Mesh Penetration Model

In section 10.3 a model was presented to illustrate the effects of a voltage applied to the mesh between the classifier and the electrometers on particle losses in the Nanoparticle Spectrometer. The model was adapted from the particle tracking model for the classifier described in section 5.2, this appendix outlines how the model works.

A.1 Model PDE's

As with the model described in section 5.2 finite element method is used to solve the two dimensional partial differential equation for electric field strength in the model sub-domain. This PDE is given in equation A.1

$$E = -\nabla V \tag{A.1}$$

Finite element method is also used to solve the incompressible Navier Stokes equations (shown below) in the model's sub-domain to simulate the gas flow through the mesh.

$$-\nabla \cdot \mu(\nabla u + (\nabla u)^T) + \rho(u \cdot \nabla)u + \nabla p = F \tag{A.2}$$

$$\nabla \cdot u = 0 \tag{A.3}$$

μ is the dynamic viscosity, ρ is the density, u is the velocity field, p is the pressure, and F is the volume force field.

A.2 The Boundary Conditions

Figure A.1 shows the sub-domain of the mesh penetration model with a colour surface visualisation of the gas flow velocity. The mesh wires are represented by the small

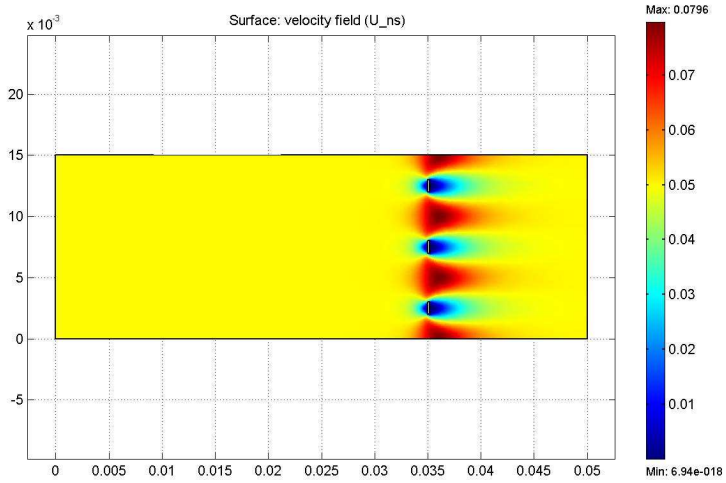

Figure A.1: Mesh penetration model sub-domain with flow velocity visualisation.

rectangular boxes.

In the case of the flow model the left hand boundary of the sub-domain is modelled as a uniform velocity in the x-direction of $0.05m/s$, and the right hand boundary is modelled as a pressure, in this case a gauge pressure of 0. The upper and lower boundaries are symmetry or "slip" boundaries, and the mesh wires themselves are wall or "no-slip" boundaries.

In the case of the electrostatics model there are two different boundary settings for two simulations. In the grounded mesh simulation the left hand boundary of the sub-domain is modelled as a constant voltage condition at $5000V$, and the right hand boundary is modelled as ground ($0V$). The upper and lower boundaries are symmetry or insulation boundaries, and the mesh wires themselves are at a constant voltage of $0V$. In the offset mesh voltage simulation the Voltage on the left hand boundary is increased to $5500V$ and the voltage on the mesh wires is increased to $500V$.

A.3 Particle Tracks Modelling

The particle tracks are modelled using the same time marching technique described in section 5.2. A starting location for the particle is chosen by the model user, then x and y vectors for the electric field strength and the gas flow velocity are interpolated at this point. The vectors for electric field strength are used to calculate velocity vector for a

particle moving in that field, which are then combined with the gas flow velocity vectors to give a final particle trajectory. The particle is assumed to follow this trajectory for a prescribed time step, at the particles new location the vectors are interpolated again and the particle trajectory is re-assessed.

By varying the starting position of the particles tracks it is possible to determine which trajectories will result in particles precipitating on the mesh and which trajectories will result in particles passing through. The results of this analysis have been presented in section 10.3

Appendix B

Additional Review of Instruments

A review of instruments was presented in the main thesis chapter 3, this contained reviews of the particle instruments that are most relevant to the project. This Appendix presents a review some additional instruments that may be of interest to the reader.

B.1 Laser Induced Incandescence (LII)

Laser induced incandescence is a measurement technique that allows transient measurements of the volume concentration of Black Carbon in diesel exhaust to be made. A high energy pulsed laser beam is used to rapidly heat BC particles up to the carbon sublimation temperature ($\sim 4000K$). The emitted thermal radiation is detected, there is a linear relationship between emitted radiation and volume concentration of BC [Witze et al, 2004].

When the laser is modulated the decay of radiation in the "off cycle" can be measured. There is a relationship between the rate of decay of radiation and particle size, so some limited size information can be inferred from this.

LII can only detect black carbon, volatile particles are evaporated very quickly by the laser, as is volatile material condensed on the outside of BC particles.

B.2 Photo Acoustic Soot Sensor (PASS)

The photo acoustic soot sensor [Haisch et al, 2004] is designed to measure the mass fraction of black carbon (BC) particles in Diesel exhaust.

The detection method for the PASS uses a photo acoustic effect. When BC particles are exposed to a high power laser beam they will heat up very rapidly. If the beam is quickly modulated on and off with a square wave, then the particles will heat during the "on cycle" and cool during the "off cycle". This results in a pressure wave that

is detectable with a microphone. A linear relationship exists between the microphone signal and the mass concentration of BC in the measuring volume.

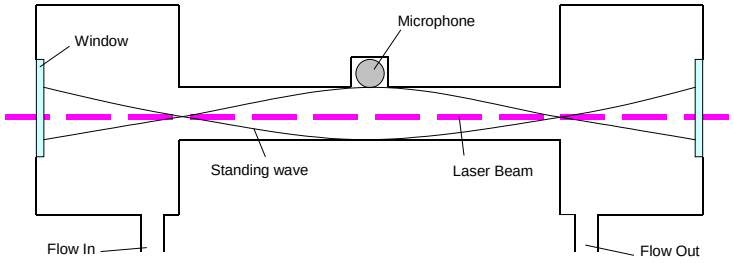

Figure B.1: Schematic of the PASS.

Figure B.1 shows a schematic of the PASS. The instrument consists of a longitudinal resonating tube with a volume at either end. The resonant frequency is determined by the tube length. Transparent windows at either end of the cell allow the modulated laser beam to pass down the axis of the tube. The resultant standing acoustic wave has two pressure minimums at either end of the resonator tube, and three pressure maximums, two at the window, and one in the centre of the tube where the microphone is located.

A problem with the PASS is that the soot build up on the windows over time and degrades the signal, therefore the windows require frequent cleaning.

B.3 Tapered Element Oscillating Microbalance (TEOM)

The tapered element oscillating microbalance is a device that can be used to measure particulate mass in diesel exhaust in real time. A particle filter substrate is mounted on the tip of a tapered hollow tube. As particulate mass accumulates on the filter tip the natural oscillating frequency of the tube is changed. This frequency can be constantly monitored, and hence real time information about the cumulative mass on the filter is recordable. The derivative of this data can be taken to deduce the transient particulate mass emissions [Witze et al, 2004].

TEOM measurements are sensitive to water in the exhaust. The filter can absorb water, adding to the mass, and also water can evaporate from the filter causing the mass to reduce. Fluctuations in the temperature and pressure in the exhaust can also affect TEOM measurements.

B.4 Electric Aerosol Analyser (EAA)

The electric aerosol analyser is essentially the generation of differential mobility instruments that came between the WAA and the SMPS[1].

The main changes in the design from the WAA is that a corona wire charger is used instead of a needle point charger, and the construction of the column is slightly different, with the sheath flow entering through the precipitating rod (see fig B.2). Otherwise the operation of the EAA is the same as that of the WAA. That is that the charged aerosol flow in an annular region at the periphery of the column, and the sheath flows down the centre, all particles above a critical mobility precipitate on the central rod, while the remainder are caught on an aerosol electrometer filter. The rod voltage is scanned to vary the critical mobility and from the corresponding change in current measured on the filter the size distribution, and concentration of the aerosol sample is inferred. [Hinds, 1998].

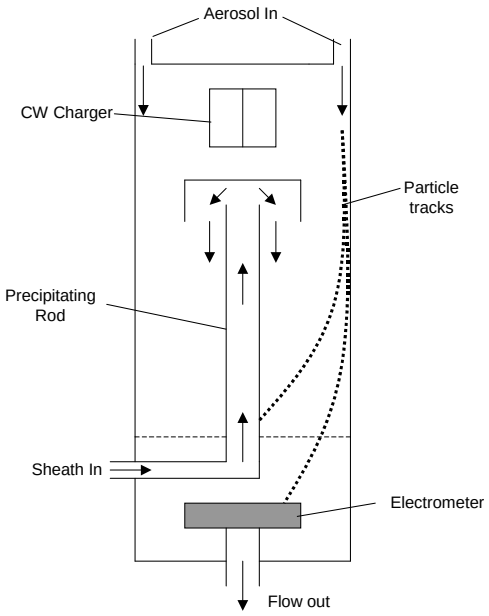

Figure B.2: Schematic of the EAA.

[1]The WAA and the SMPS have been described in chapter 3

B.5 Electrical Aerosol Detector (EAD)

The EAD measures a parameter called total aerosol length (mm/cm^3) this falls some where between number concentration ($\#/cm^3$) and surface area concentration (mm^2/cm^3) [TSI, 2005b]. The instrument uses a needle point Charger of the design presented by Medved et al [2000] and described in section 3.10. Downstream of the charger an aerosol electrometer measures the charge on the particle flowing out of the charger. The current measured on the electrometer is proportional to the aerosol length. A recent version of the EAD called the nanoparticle surface area monitor has been shown to produce an electrometer signal that correlates linearly with the surface area concentration of aerosol deposited in a human lung [TSI, 2005c].

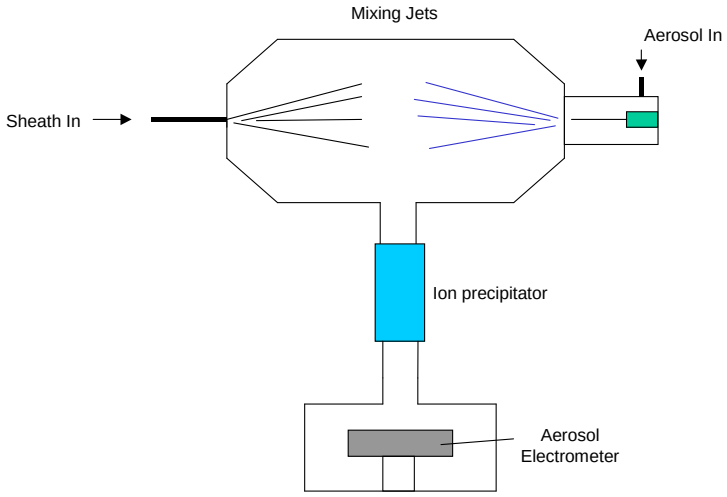

Figure B.3: Schematic of the EAD.

Appendix C

Expansion of Birth and Death model Equations

The "Birth and Death" model Boisdron & Brock [1970] was used in the charging models for both the laminar flow charging zone on the CWC (section 5.1) and the turbulent charging zone of the SJC (section 6.3). In sections 5.1 and 6.3 only the first three steps of the infinite set of birth and death model equations were shown. Presented here are the equations for charging in a laminar flow charging zone, and in a turbulent flow charging zone are presented expanded to seven steps in order to better show the pattern of the equations.

Equation C.1 shows the equations for the laminar flow charging zone, here the cumbersome coefficients of each term are show both in full and also simplified to a single Greek letter with a subscript. Equation C.2 shows the equations for the turbulent flow charging zone, here only the simplified notation is shown as the full coefficients are the same as those shown in equation C.1.

$$
\begin{aligned}
n_0 &= \exp(-\alpha_0 t) \\
n_1 &= \left(\frac{\alpha_0}{\alpha_1-\alpha_0}\right)\exp(-\alpha_0 t)+\left(\frac{\alpha_0}{\alpha_0-\alpha_1}\right)\exp(-\alpha_1 t) \\
&= \beta_0\exp(-\alpha_0 t)+\beta_1\exp(-\alpha_1 t) \\
n_2 &= \left(\frac{\beta_0\alpha_1}{\alpha_2-\alpha_0}\right)\exp(-\alpha_0 t)+\left(\frac{\beta_1\alpha_1}{\alpha_2-\alpha_1}\right)\exp(-\alpha_1 t)+\left(\frac{\alpha_1\alpha_0}{(\alpha_0-\alpha_2)(\alpha_1-\alpha_2)}\right)\exp(-\alpha_2 t) \\
&= \gamma_0\exp(-\alpha_0 t)+\gamma_1\exp(-\alpha_1 t)+\gamma_2\exp(-\alpha_2 t) \\
n_3 &= \left(\frac{\gamma_0\alpha_2}{\alpha_3-\alpha_0}\right)\exp(-\alpha_0 t)+\left(\frac{\gamma_1\alpha_2}{\alpha_3-\alpha_1}\right)\exp(-\alpha_1 t)+\left(\frac{\gamma_2\alpha_2}{\alpha_3-\alpha_2}\right)\exp(-\alpha_2 t)+\left(\frac{\alpha_2\alpha_1\alpha_0}{(\alpha_0-\alpha_3)(\alpha_1-\alpha_3)(\alpha_2-\alpha_3)}\right)\exp(-\alpha_3 t) \\
&= \delta_0\exp(-\alpha_0 t)+\delta_1\exp(-\alpha_1 t)+\delta_2\exp(-\alpha_2 t)+\delta_3\exp(-\alpha_3 t) \\
n_4 &= \left(\frac{\delta_0\alpha_3}{\alpha_4-\alpha_0}\right)\exp(-\alpha_0 t)+\left(\frac{\delta_1\alpha_3}{\alpha_4-\alpha_1}\right)\exp(-\alpha_1 t)+\left(\frac{\delta_2\alpha_3}{\alpha_4-\alpha_2}\right)\exp(-\alpha_2 t)+\left(\frac{\delta_3\alpha_3}{\alpha_4-\alpha_3}\right)\exp(-\alpha_3 t) \\
&\quad +\left(\frac{\alpha_4\alpha_3\alpha_2\alpha_1\alpha_0}{(\alpha_0-\alpha_4)(\alpha_1-\alpha_4)(\alpha_2-\alpha_4)(\alpha_3-\alpha_4)}\right)\exp(-\alpha_4 t) \\
&= \epsilon_0\exp(-\alpha_0 t)+\epsilon_1\exp(-\alpha_1 t)+\epsilon_2\exp(-\alpha_2 t)+\epsilon_3\exp(-\alpha_3 t)+\epsilon_4\exp(-\alpha_4 t) \\
n_5 &= \left(\frac{\epsilon_0\alpha_4}{\alpha_5-\alpha_0}\right)\exp(-\alpha_0 t)+\left(\frac{\epsilon_1\alpha_4}{\alpha_5-\alpha_1}\right)\exp(-\alpha_1 t)+\left(\frac{\epsilon_2\alpha_4}{\alpha_5-\alpha_2}\right)\exp(-\alpha_2 t)+\left(\frac{\epsilon_3\alpha_4}{\alpha_5-\alpha_3}\right)\exp(-\alpha_3 t)+\left(\frac{\epsilon_4\alpha_4}{\alpha_5-\alpha_4}\right)\exp(-\alpha_4 t) \qquad \text{(C.1)} \\
&\quad +\left(\frac{\alpha_5\alpha_4\alpha_3\alpha_2\alpha_1\alpha_0}{(\alpha_0-\alpha_5)(\alpha_1-\alpha_5)(\alpha_2-\alpha_5)(\alpha_3-\alpha_5)(\alpha_4-\alpha_5)}\right)\exp(-\alpha_5 t) \\
&= \zeta_0\exp(-\alpha_0 t)+\zeta_1\exp(-\alpha_1 t)+\zeta_2\exp(-\alpha_2 t)+\zeta_3\exp(-\alpha_3 t)+\zeta_4\exp(-\alpha_4 t)+\zeta_5\exp(-\alpha_5 t) \\
n_6 &= \left(\frac{\zeta_0\alpha_5}{\alpha_6-\alpha_0}\right)\exp(-\alpha_0 t)+\left(\frac{\zeta_1\alpha_5}{\alpha_6-\alpha_1}\right)\exp(-\alpha_1 t)+\left(\frac{\zeta_2\alpha_5}{\alpha_6-\alpha_2}\right)\exp(-\alpha_2 t)+\left(\frac{\zeta_3\alpha_5}{\alpha_6-\alpha_3}\right)\exp(-\alpha_3 t)+\left(\frac{\zeta_4\alpha_5}{\alpha_6-\alpha_4}\right)\exp(-\alpha_4 t) \\
&\quad +\left(\frac{\zeta_5\alpha_5}{\alpha_6-\alpha_5}\right)\exp(-\alpha_5 t)+\left(\frac{\alpha_6\alpha_5\alpha_4\alpha_3\alpha_2\alpha_1\alpha_0}{(\alpha_0-\alpha_6)(\alpha_1-\alpha_6)(\alpha_2-\alpha_6)(\alpha_3-\alpha_6)(\alpha_4-\alpha_6)(\alpha_5-\alpha_6)}\right)\exp(-\alpha_6 t) \\
&= \eta_0\exp(-\alpha_0 t)+\eta_1\exp(-\alpha_1 t)+\eta_2\exp(-\alpha_2 t)+\eta_3\exp(-\alpha_3 t)+\eta_4\exp(-\alpha_4 t)+\eta_5\exp(-\alpha_5 t)+\eta_6\exp(-\alpha_6 t) \\
n_7 &= \left(\frac{\eta_0\alpha_6}{\alpha_7-\alpha_0}\right)\exp(-\alpha_0 t)+\left(\frac{\eta_1\alpha_6}{\alpha_7-\alpha_1}\right)\exp(-\alpha_1 t)+\left(\frac{\eta_2\alpha_6}{\alpha_7-\alpha_2}\right)\exp(-\alpha_2 t)+\left(\frac{\eta_3\alpha_6}{\alpha_7-\alpha_3}\right)\exp(-\alpha_3 t)+\left(\frac{\eta_4\alpha_6}{\alpha_7-\alpha_4}\right)\exp(-\alpha_4 t) \\
&\quad +\left(\frac{\eta_5\alpha_6}{\alpha_7-\alpha_5}\right)\exp(-\alpha_5 t)+\left(\frac{\eta_6\alpha_6}{\alpha_7-\alpha_6}\right)\exp(-\alpha_6 t)+\left(\frac{\alpha_7\alpha_6\alpha_5\alpha_4\alpha_3\alpha_2\alpha_1\alpha_0}{(\alpha_0-\alpha_7)(\alpha_1-\alpha_7)(\alpha_2-\alpha_7)(\alpha_3-\alpha_7)(\alpha_4-\alpha_7)(\alpha_5-\alpha_7)(\alpha_6-\alpha_7)}\right)\exp(-\alpha_7 t) \\
&= \theta_0\exp(-\alpha_0 t)+\theta_1\exp(-\alpha_1 t)+\theta_2\exp(-\alpha_2 t)+\theta_3\exp(-\alpha_3 t)+\theta_4\exp(-\alpha_4 t)+\theta_5\exp(-\alpha_5 t)+\theta_6\exp(-\alpha_6 t)+\theta_7\exp(-\alpha_7 t)
\end{aligned}
$$

$$
\begin{aligned}
P_{n_0} &= \frac{1}{(\bar{t}\alpha_0+1)} \\
P_{n_1} &= \frac{\beta_0}{(\bar{t}\alpha_0+1)} + \frac{\beta_1}{(\bar{t}\alpha_1+1)} \\
P_{n_2} &= \frac{\gamma_0}{(\bar{t}\alpha_0+1)} + \frac{\gamma_1}{(\bar{t}\alpha_1+1)} + \frac{\gamma_2}{(\bar{t}\alpha_2+1)} \\
P_{n_3} &= \frac{\delta_0}{(\bar{t}\alpha_0+1)} + \frac{\delta_1}{(\bar{t}\alpha_1+1)} + \frac{\delta_2}{(\bar{t}\alpha_2+1)} + \frac{\delta_3}{(\bar{t}\alpha_3+1)} \\
P_{n_4} &= \frac{\epsilon_0}{(\bar{t}\alpha_0+1)} + \frac{\epsilon_1}{(\bar{t}\alpha_1+1)} + \frac{\epsilon_2}{(\bar{t}\alpha_2+1)} + \frac{\epsilon_3}{(\bar{t}\alpha_3+1)} + \frac{\epsilon_4}{(\bar{t}\alpha_4+1)} \\
P_{n_5} &= \frac{\zeta_0}{(\bar{t}\alpha_0+1)} + \frac{\zeta_1}{(\bar{t}\alpha_1+1)} + \frac{\zeta_2}{(\bar{t}\alpha_2+1)} + \frac{\zeta_3}{(\bar{t}\alpha_3+1)} + \frac{\zeta_4}{(\bar{t}\alpha_4+1)} + \frac{\zeta_5}{(\bar{t}\alpha_5+1)} \\
P_{n_6} &= \frac{\eta_0}{(\bar{t}\alpha_0+1)} + \frac{\eta_1}{(\bar{t}\alpha_1+1)} + \frac{\eta_2}{(\bar{t}\alpha_2+1)} + \frac{\eta_3}{(\bar{t}\alpha_3+1)} + \frac{\eta_4}{(\bar{t}\alpha_4+1)} + \frac{\eta_5}{(\bar{t}\alpha_5+1)} + \frac{\eta_6}{(\bar{t}\alpha_6+1)} \\
P_{n_7} &= \frac{\theta_0}{(\bar{t}\alpha_0+1)} + \frac{\theta_1}{(\bar{t}\alpha_1+1)} + \frac{\theta_2}{(\bar{t}\alpha_2+1)} + \frac{\theta_3}{(\bar{t}\alpha_3+1)} + \frac{\theta_4}{(\bar{t}\alpha_4+1)} + \frac{\theta_5}{(\bar{t}\alpha_5+1)} + \frac{\theta_6}{(\bar{t}\alpha_6+1)} + \frac{\theta_7}{(\bar{t}\alpha_7+1)}
\end{aligned}
\tag{C.2}
$$

Bibliography

Abdul-Khalek, I.S., Kittelson, D.B. and Brear, F. (2000) Nanoparticle growth during dilution and cooling of exhaust: experimental and theoretical assessment. *International Society of Automotive Engineers technical paper 2000-01-1515.*

Aitken J. (1889) On improvements in the apparatus for counting the dust particles in the atmosphere. *Journal of Proceedings of the Royal Society of Edinburgh V.16*

Ackerman, A.S., Toon, O.B., Stevens, D.E., Heymsfield, A.J., Ramanathan, V. and Welton, E.J. (2000) Reduction of Tropical Cloudiness by Soot. *Science V.288 pp.1042-1047.*

Agarwal, J.K. and Sem, G.J. (1980) Continuous flow, single-particle-counting condensation nucleus counter. *Journal of Aerosol Science V.11 pp.343-357.*

Allen, M.D. and Raabe, O.G. (1970) Slip correction factor measurements of spherical solid aerosol particles in an improved Milikan apparatus. *Aerosol Science and Technology V.4 pp.269-286.*

Arendt, P. and Kallman, H. (1925) The mechanism of charging of mist particles. *Zeitshrift fur Physik V.35 pp.421-441.* in Biskos [2004]

Bernigau, N.G. and Vank, R.M. (1989) Time varying charge levels as an alternative approach for aerosol concentration Measurements. *Journal of Aerosol Science V.20 pp.1497-1499.*

Biskos G. (2004) *Theoretical and Experimental Investigation of the Differential Mobility Spectrometer.* PhD Thesis, University of Cambridge.

Biskos, G., Reavell, K. and Collings, N. (2005) Unipolar diffusion charging of aerosol particles in the transition regime *Journal of Aerosol Science V.36 pp.247-267.*

Bricard, J. (1949) L'equilibre ionique de la bassa atmosphere. *Journal of Applied Physics V.54 pp.39-52.* in Biskos [2004]

Brown, R.C. (1993) *Air Filtration: An Integrated Approach to the Theory and Applications of Fibrous Filters.* Pergamon, Oxford.

Boer, G.J., Flato, G., Reader, M.C. and Ramsden D. (2000) A transient climate change simulation with green house gas and aerosol forcing: experimental design and comparison with the instrumental record in the twentieth century. *Climate Dynamics V.16 pp.405-425*

Boer, G.J., Flato, G. and Ramsden D. (2000) A transient climate change simulation with green house gas and aerosol forcing: climate to the twenty-first century. *Climate Dynamics V.16 pp.427-450*

Boisdron, K. and Brock, J.R. (1970) On the stochastic nature of the acquisition of electrical charge and radioactivity by aerosol particles. *Atmospheric Environment V.4 pp.35-50.*

Chen, D. and Pui, D.Y.H. (1999) A high efficiency high throughput unipolar aerosol charger for nanoparticles. *Journal of nanoparticles research V.1 pp.115-126.*

Clement, C. F. and Harrison, R.G. (1991) The charging of radioactive aerosols. *Journal of Aerosol Science V.23 pp.481-504.*

Collings, N., Baker, N. and Wolber W.G. (1986) Real-Time Smoke Sensor for Diesel Engines. *SAE 860157*

Collings, N. and Graskow, B.R. (2000) Particles from internal combustion engines — what we need to know. *Phil. Trans. R. Soc. London A V.358 pp.2611-2623*

Donaldson, K., Li, X.Y. and MacNee, W. (1998) Ularafine (nanometer) mediated lung injury. *Journal of Aerosol Science V.29 pp.553-560.*

Ehara, K., Hagwood, C. and Coakley, K.J. (1996) Novel method to classify aerosol particles according to their mass-to-charge ratio - aerosol particle mass analyser. *Journal of Aerosol Science V.27 pp.217-234.*

Fierz, M., Scherrer, L. and Burtscher, H. (2002) Real-time measurement of aerosol size distributions with an electrical diffusion battery *Journal of Aerosol Science V.33 pp.1049-1060.*

Fuchs, N.A. (1963) On the stationary charge distribution on aerosol particles in a bipolar ionic atmosphere. *Geofiscia Pura e Applicata V.56 pp.185-193.*

Gamble, J.F. (1998) $PM_{2.5}$ and Mortality in Long-Term Prospective Cohort Studies: Cause-Effect or Statistical Associations? *Environmental Health Perspectives V.104 pp.838-850* in Pope [2000]

GRPE (2003) *Particulate Measurement Programme (PMP)* Published by the UK Department for Transport.

Haisch, C., Beck, H.A. and Niessner, R. (2004) A Photoacoustic Sensor for Time Resolved Quantification of Diesel Soot Emissions. *SAE 2004-01-0968*

Hernandez-Sierra, A., Alguacil, F.J. and Alonso, M. (2003) Unipolar diffusion charging of nanometer aerosol particles in a corona ioniser. *Journal of Aerosol Science V.34 pp.733-745.*

Hewitt, G.W. (1957) The charging of small particles for electrostatic precipitation. *AIEE Transactions V.76 pp.300-306.*

Hinds, W.C. (1998) *Aerosol Technology. Properties, Behaviour, and measurement of Airborne Particles.* John Wiley and sons inc.

Horrak, U. (2001) *Air ion mobility spectrum as a rural area.* Dissertationes geophysicales universitatis tartuensis.

Huang, D.D., Seinfeld, J.H. and Marlow, W.H. (1999) BKG equation solution of coagulation for large Knudsen number aerosols with a singular attractive contact potential. *Journal of Colloid and Interface Science. V.140 pp.258-276.* in Biskos [2004]

Husar, R.B., Whitby, K.T. and Lui, B.Y.H. (1972) Physical mechanisms governing the dynamics of Los Angeles smog aerosol. *Journal of Colloid and Interface Science V.39 pp.211-224.*

Ingle, V.K. and Proakis, J.G. (2000) *Digital Signal Processing using Matlab.* Brooks/Cole

Jacobson M.Z. (2001) Strong radiative heating due to the mixing state of black carbon in atmospheric aerosols. *Nature V.409 pp695-697*

Kasper M. (2003) *The Number Concentration of Non-Volatile Particles: Design Study for an Instrument According to the PMP Recommendations.* Presentation given at The 7th ETH Conference on Combustion Generated Nanoparticles, Zrich.

Kebarle, P., Searles, S. K., Zolla, A., Scarbrough, J., and Arshadi, M. (1967) The solvation of hydrogen ion by water molecules in the gas phase. Heats and entropies

of solvation of individual reactions.*Journal of the Americal Chemichal Society. V.89 pp.6393-6399* in Biskos [2004]

Keefe, D. and Nolan, P.J. (1962) Combination coefficient of ions and nuclei. *Proceedings of the Royal Irish Academy V.66 pp.17-29* Biskos [2004]

Kirsch, A.A. and Fuchs, N.A. (1968) Studies of Fibrous Filters - III: Diffusional Deposition of Aerosols in Fibrous Filters. *Ann. Occup. Hyg. V.11 pp.299-304.*

Kittelson, D.B. University of Minnesota *–Private Communication*

Kittelson, D.B. (1998) Engines And Nanoparticles: A Review. *Journal of Aerosol Science V.29 pp.575-588.*

Knutson, E.O. and Whitby, K.T. (1971) Aerosol Classification by Electric Mobility: Apparatus Theory and Applications. *Journal of Colloid and Interface science V.39 pp.136-162*

Kruis, F.E. and Fissan, H. (2001) Nanoparticle charging in a twin Hewitt charger. *Journal of nanoparticles research V.3 pp.39-50.*

Lee, K.W. and Ramamurthi, M. (1993) Filter Collection. in Willeke, K. and Baron, P.A. (Eds) (1993) *Aerosol Measurement: Principles, Techniques, and Applications.* Van Nostrand Reinhold, New York.

Lui, B.Y.H. and Bademosi, F. (1971) *Diffusion Charging of Knudsen aerosols.* Theoretical technical report 156, University of Minnesota.

Lui, B.Y.H., Pui, D.Y.H., McKenzie, R.L., Agarwal, J.K. Jaenicke, R., Pohl, F.G., Preining, O., Reischl, G., Szymanski, W. and Wagner, P.E. (1982) Intercomparison of different "absolute" instruments for measurement of aerosol number concentration *Journal of Aerosol Science V.13 pp.429-450.*

Lui, B.Y.H. and Kapadia, A. (1978) Combined field diffusion charging of aerosols in the continuum regime. *Journal of Aerosol Science V.9 pp.227-242.*

Lui, B.Y.H. and Pui, D.Y.H. (1974a) Electrical Neutralisation of Aerosols. *Journal of Aerosol Science V.5 pp.465-472.*

Lui, B.Y.H. and Pui, D.Y.H. (1974b) Equilibrium bipolar charge distribution of aerosols. *Journal of Colloid and Interface Science V.49 pp.305-312.*

Lui, B.Y.H. and Pui, D.Y.H. (1974c) A Submicron aerosol standard and the primary, absolute calibration of the condensation nuclei counter. *Journal of Colloid and Interface Science V.47 pp.155-171.*

Marjamärki, M. Keskinen, J. Chen, D. and Pui, D.Y.H. (2000) Performance Evaluation of the Electrical Low Pressure Impactor. *Journal of Aerosol Science V.31 pp.249-261*

Marquard, A., Ehouarn, P. and Kasper, G. (2002) *Designing a unipolar corona charger with maximum efficiency and minimum losses of nanoparticles.* Universitat Karlsruhe, Germany.

May, K.R. (1973) The Collison Nebulizer. Description, Performance & Application. *Journal of Aerosol Science V.4 pp.235-143.*

Medved, A., Dorman, F., Kaufman, S.L. and Pocher, A. (2000) A new corona based charger for aerosol particles. *Journal of Aerosol Science V.31 pp.616-617.*

Nauman, E.B. and Buffam, B.A. (1983) *Mixing in Continuous Flow Systems.* John Wiley and Sons.

Nemmar, A., Hoet, P.H.M., Vanquickenborne, B., Dinsdale, D, Thomeer, M., Hoylaerts, M.F., Vanbilloen H., Mortelmans, L. and Nemery, B. (2001) Passage of Inhaled Particles Into the Blood Circulation in Humans. *Circulation V.105 pp.411-414.*

Harrison, R.M., ApSimon, H., Clarke, A.G., Derwent, R.G., Fisher, B., Hickman, J., Mark, D., Murrells, T., McAughey, J., Pooley, F., Richards, R., Stedman, J., Vawada, Y., Williams, M., Coster, S., Mayland, R., Prosser, H., and McMahon, N. (1999) *Source apportionment of airborne particulate patter in the United Kingdom.* Technical report, Department of Environment, Transport and the Regions, the Welsh Office, the Scottish Office and the Department of the Environment(Northern Ireland)

Oberdorster, G. (1996) Significance of particle parameters in the evaluation of exposure-dose relationships for inhaled particles. *Inhalation Toxicology V.8 pp.S73-S90.*

Olfert, J.S., and Collings, N. (2005) New method for particle mass classification - the Couette centrifugal particle mass analyser. *Journal of Aerosol Science.* (in press)

Penner J.E. Chuang C.C. and Grant K. (1998) Climate forcing by carbonation and sulfate aerosols. *Climate Dynamics V.14 pp.839-851.*

Peters, A.P., Dockery, D.W., Muller J.E. and Mittleman, M.A. (2001) Increased Particulate Air Pollution and the Triggering of Myocardial Infarction. *Circulation V.103 pp.2810-2815.*

Pnueli, D., Gutfinger, C., Moldavsky, L., Shuster K. and Fichman, M. (2000) Electrostatic Porous Filter with a Blocking Electrode. *Journal of Aerosol Science V.31 pp.1371-1379.*

Pope, C.A. (2000) Review: Epidemiological Basis for Particulate Air Pollution Health Standards *Aerosol Science & Technology V.32 pp.4-14*

Pratsinis, S.E. (1994) Motor vehicle contributions to fine carbonaceous aerosol in Los Angeles. *Aerosol Science & Technology V.21 pp360-366.*

Pui, Y.H. (1976) *Experimental study of diffusion charging.* PhD thesis, University of Minnesota.

Pui, D.Y.H., Fruin, S. and McMurry, P.H. (1988) Unipolar Diffusion Charging of Ultrafine Aerosols *Aerosol Science and Technology V.8 pp.173-187.*

Rogak, S.N. and Flagan, R.C. (1993) The Mobility and Structure of Aerosol Agglomerates. *Aerosol Science & Technology V.18 pp.25-47*

Romay, F.J., Lui, B.Y.H. and Pui, D.Y.H. (1994) A Sonic Jet Corona Ionizer for Electrostatic Discharge and Aerosol Neutralisation. *Aerosol Science and Technology V.20 pp.31-34.*

Rosenfeld, D. (2000) Supression of rain and snow by urban and industrial air pollution. *Science V.287 pp.1793-1796*

Schauer, J.J., Rogge, W.F., Hildemann, L.M., Mazurek, M.A., Cass, G.R. and Simoneit, B.R.T. (1996). Source appointment of airbourne particulate matter using organic compounds as tracers. *Atmospheric Environment V.30 pp.3837-3855.*

Schwartz, S.E., and Buseck P.R. (2000) Atmospheric Science: Absorbing Phenomena. *Science V.288 pp989-990.*

Stanhill, G. and Cohen, S. (2001) Global dimming: a review of the evidence for widespread and significant reduction in global radiation with discussion of its probable causes and possible agricultural con sequences. *Agricultural and Forest Meteorology V.107 pp.255-278.*

Tammet, H. (1992) *Air ions and electrical aerosol analyser.* Tartu University.

Tammet, H., Mirme, A. and Tamm, (1998) E. Electrical aerosol spectrometer of Tartu University. *Journal of Aerosol Science V.29 pp.S427-S428.*

Tammet, H., Mirme, A. and Tamm, E. (1998) Electrical aerosol spectrometer of Tartu University. *Atmospheric research V.62 pp.315-324.*

TSI (2000) *Model 3040/3041 Diffusion Battery Instruction Manual.*

TSI (2002) *Model 3022A Condensation Particle Counter Instruction Manual.*

TSI (2003) *Model 3068A Aerosol Electrometer Instruction Manual.*

TSI (2004) *Model 3090 Engine Exhaust Particle Size Spectrometer Operational Manual.*

TSI (2005) *Series 3080 Electrostatic Classifiers Instruction Manual.*

TSI (2005b) *Model 3070A Electrical Aerosol Detector Instruction Manual.*

TSI (2005c) *Model 3550 Nanoparticle Surface Area Monitor Spec Sheet.*

Ambient Particles and Health: Lines that Divide. *Journal of Air & Waste Management Assoc. V.47 pp.551-581.* in Pope [2000]

ang, S.C. and Flagan, R.C. (1990) Scanning electrical mobility spectrometer. *Aerosol Science and Technology V.13 pp.230-240.*

Whitby, K.T. (1961) Generator for producing high concentrations of small ions. *Review of scientific instruments V.32 N.12.*

Whitby, K.T., Lui, B.Y.H., Husar, R.B. and Barsic, N.J. (1971) The Minnesota Aerosol-Analysing System Used in the Los Angeles Smog Project *Journal of Colloid and Interface science V.39 pp.136-162.*

Whitby, K.T., Husar, R.B. and Lui, B.Y.H. (1972) The aerosol size distribution of Los Angeles smog. *Journal of Colloid and Interface V.39 pp.136-164.*

White, F. M. (1999) *Fluid Mechanics.* McGraw Hill International.

Willeke, K. (1976) Temperature dependence of particle slip in a gaseous medium. *Journal of Aerosol Science V.7 pp.381-387.*

Witze, P.O., Chase, R.E., Maricq, M.M., Podsiadlik, D.H. and Xu, N. (2004) Time-Resolved Measurments of Exhaust PM for FTP-75 Comparison of LII, ELPI and TEOM Techniques. *SAE 2004-01-0964*

Yang, S. and Lee, G.W.M. (2004) Filtration characteristics of a fibrous filter pretreated with anionic surfactants for monodisperse solid aerosols. *Journal of Aerosol Science V.36 pp.419-437.*

Yeh, H.C. and Lui, B.Y.H. (1974) Aerosol filtration by fibrous filters. *Journal of Aerosol Science V.5 pp.191-217.*